Evaluation and Extension of the Monte Carlo Code Toolkit Geant4 for Fusion Nuclear Analyses of DEMO

Zur Erlangung des akademischen Grades einer

DOKTORIN DER INGENIEURWISSENSCHAFTEN (Dr.-Ing.)

von der KIT-Fakultät für Maschinenbau des

Karlsruher Instituts für Technologie (KIT)

angenommene

DISSERTATION

von

M.Sc. Elena Nunnenmann

Tag der mündlichen Prüfung:
25.07.24

Hauptreferent:
Prof. Thomas Müller

Korreferenten:
Prof. Anton Möslang, Prof. Xu Cheng

Hiermit erkläre ich, dass ich die vorliegende Arbeit selbständig angefertigt und keine anderen als die angegebenen Quellen und Hilfsmittel benutzt sowie die wörtlich und inhaltlich übernommenen Stellen als solche kenntlich gemacht und die Satzung des Karlsruher Instituts für Technologie (KIT) zur Sicherung guter wissenschaftlicher Praxis in der jeweils gültigen Fassung beachtet habe.

Karlsruhe, den 28.03.2024 Elena Nunnenmann

Abstract

The Monte Carlo particle transport code Geant4 was originally developed for high energy particle physics. In the meantime, it has been expanded to support the transport of neutrons in the energy range below 20 MeV based on evaluated nuclear cross section libraries. Therefore it is considered a potential alternative for the standard code MCNP (Monte Carlo N-Particle) for fusion neutronics applications.

This thesis presents the investigation of Geant4 for neutronics analyses of the DEMO nuclear fusion reactor. On the one hand, it is investigated if Geant4 provides the necessary functionalities for neutronics analyses and on the other hand, the reliability of the calculated results for various important physical quantities are assessed.

Necessary functionalities are the ability to support complex geometry descriptions and the option to automatically convert geometry descriptions from the Computer Aided Design (CAD) syntax into the code-internal format. Furthermore, the code needs to be able to represent the characteristics of complex neutron sources such as the fusion plasma of the DEMO reactor or the neutron generators used in experiments.

The flexible toolkit structure of Geant4 is used to program missing functionalities. This includes a functionality to create reflecting surfaces, which allow the simplification of symmetrical geometries, and a functionality to calculate energy dependent quantities derived from the particle flux such as the reaction rate.

Several benchmarks are used to assess the reliability. Initially, the basic functioning is verified in comparison with the well-validated code MCNP, which is used as a standard in fusion neutronics. For this, very simple geometries and neutron source descriptions are used. In the first set-up, results are compared after a single material interaction and in the second set-up after multiple interactions.

Subsequently, experimental benchmarks taken from the Shielding Integral Benchmark Archive and Database (SINBAD) are used. In this part, results of calculations with Geant4 are compared with the experimental results and the results of calculations with MCNP. SINBAD provides input files for MCNP, which describe the parameters of the experiment. These are converted for Geant4. The benchmarks cover the neutron transport in the most important structural material iron, the calculation of the Tritium Breeding Ratio (TBR) in a Test Blanket Module (TBM), and a shielding calculation with combined neutron and photon transport and variance reduction.

Finally, Geant4 is applied to a TBR calculation for a DEMO reactor model with integrated tritium breeding blanket of the type Helium Cooled Pebble Bed (HCPB). For this, the description of the fusion plasma neutron source available for MCNP as a subroutine is converted and validated. The reactor geometry is represented in a simplified way by a 10° sector to whose bounding surfaces the reflecting surface functionality is applied. Despite this, the geometry description is still large and complex. The calculations are also performed with MCNP using an available input file and the results are compared.

This thesis shows that Geant4 can be applied to DEMO design analyses only in a limited way: reliable results can be expected for neutron transport and related nuclear responses, as long as they are not too affected by deep penetration transport. The benchmarks revealed issues in photon production and variance reduction, which prevent the reliable application to nuclear heating and shielding calculations. However, the developments in this thesis have created the necessary requirements to enable the application to DEMO design analyses provided these issues are resolved. Further progress of Geant4 can be monitored using the benchmark applications developed in this thesis.

Zusammenfassung

Das Monte-Carlo-Teilchentransportprogramm Geant4 wurde ursprünglich für Hochenergie-Teilchenphysik entwickelt, aber es unterstützt mittlerweile auch den Transport von Neutronen im Energiebereich $< 20\,\text{MeV}$ auf Basis von evaluierten nuklearen Wirkungsquerschnitts-Bibliotheken. Daher kommt es möglicherweise als Alternative für das Standard-Programm MCNP (Monte Carlo N-Particle) für Kernfusions-Neutronik-Berechnungen in Frage.

Diese Dissertation präsentiert die Untersuchung von Geant4 für neutronenphysikalische Analysen des DEMO Kernfusionsreaktors. Einerseits wird untersucht ob Geant4 notwendige Funktionen bereitstellt, die für Neutronik-Analysen benötigt werden, und andererseits wird die Verlässlichkeit der erzielten Ergebnisse für verschiedene wichtige Berechnungsgrößen überprüft.

Notwendigen Funktionen sind die Fähigkeit, komplexe Geometrien darzustellen und die Möglichkeit Geometrie-Beschreibungen aus der Computer Aided Design (CAD) Syntax automatisch in das interne Format des Programms konvertieren zu können. Außerdem sollen die Profile komplexer Neutronenquellen, wie das Fusionsplasma des DEMO-Reaktors, oder bei Experimenten eingesetzte Neutronengeneratoren repräsentiert werden können.

Die flexible Toolkit-Struktur von Geant4 wird genutzt um fehlende Funktionen zu programmieren. Dies beinhaltet eine Funktion für reflektierende Oberflächen, welche es ermöglicht symmetrische Geometrien vereinfacht zu repräsentieren, und eine Funktion zur Berechnung vom Teilchenfluss abgeleiteter, energieabhängiger Größen wie der Reaktionsrate.

Zur Prüfung der Verlässlichkeit wurden mehrere Benchmark-Tests eingesetzt. Zunächst wurde die grundlegende Funktion des Programms durch Berechnungen im Vergleich mit dem standardmäßig eingesetzten und gut validierten Programm MCNP getestet. Hierzu werden sehr einfache Geometrien und Neutronenquellen verwendet. Im ersten Aufbau werden Ergebnisse nach einer Material-Interaktion verglichen und beim zweiten Aufbau nach vielen Interaktionen.

Danach kommen experimentelle Benchmark-Tests aus der Shielding Integral Benchmark Archive and Database (SINBAD) zum Einsatz. Hier werden Berechnungen mit Geant4 mit den experimentellen Ergebnissen und Berechnungen mit MCNP verglichen. SINBAD stellt MCNP Eingabe-Dateien zur Verfügung, die das Experiment beschreiben, welche für Geant4 konvertiert werden. Die eingesetzten Benchmark-Tests behandeln den Neutronentransport im wichtigsten strukturellen Material Eisen, die Berechnung der Tritiumbrutrate (TBR) in einem Test-Brutblanket-Modul (TBM), und eine Abschirmungsberechnung mit kombiniertem Neutronen- und Photonentransport und Varianzreduktion.

Abschließend wird Geant4 auf eine TBR-Berechnung für ein DEMO-Reaktor-Modell mit Brutblanket des Typs Helium Cooled Pebble Bed (HCPB) angewendet. Dazu wird die Beschreibung der Fusionsplasma-Neutronenquelle, die für MCNP als Unterprogramm vorliegt, umgewandelt und validiert. Die Reaktorgeometrie wird vereinfacht durch einen 10°-Sektor dargestellt, an dessen Grenzflächen reflektierende Oberflächen angebracht sind. Die Berechnung wird außerdem mit einer bereits vorliegenden Eingabe-Datei mit MCNP durchgeführt und die Ergebnisse verglichen.

In dieser Arbeit wird gezeigt, dass Geant4 nur begrenzt auf DEMO-Designanalysen angewendet werden kann: verlässliche Ergebnisse können für den Neutronentransport und abgeleitete nukleare Größen erwartet werden, wenn diese nicht zu stark von tief eindringendem Transport abhängen. Die Benchmark-Tests zeigen Probleme in der Gamma Produktion und in der Varianzreduktion auf, welche die verlässliche Anwendung von Geant4 auf nukleare Aufheizung und Abschirmrechnungen verhindern. Jedoch haben die Neuentwicklungen im Rahmen dieser Arbeit die notwendigen Voraussetzungen für DEMO-Designanalysen geschaffen, sobald diese Probleme behoben sind. Die weiteren Fortschritte von Geant4 können mithilfe der entwickelten Benchmark-Anwendungen kontrolliert werden.

Contents

List of Abbreviations

ACE	A Compact ENDF
CAD	Computer Aided Design
CIEMAT	Centro para Investigaciones Energéticas, Medioambientales y Tecnológicas
CSG	Constructive Solid Geometry
D	Deuterium
DEMO	DEMOnstration Fusion Power Reactor
ENDF	Evaluated Nuclear Data Format
ENEA	Agenzia nazionale per le nuovetecnologie, l'energia e lo sviluppo economico sostenibile
EU	European Union
F90	Fortran90
FNG	Frascati Neutron Generator
FOM	Figure of Merit
GDML	Geometry Description Markup Language
HCPB	Helium Cooled Pebble Bed
IAEA	International Atomic Energy Agency
IPPE	Institute of Physics and Power Engineering
ITER	International Thermonuclear Experimental Reactor
JAEA	Japan Atomic Energy Agency
JEFF	Joint Evaluated Fission and Fusion File
KIT	Karlsruhe Institute of Technology
MC	Monte Carlo
McCad	Monte Carlo geometry conversion tool
MCNP	Monte Carlo N-Particle
NDS	Nuclear Data Services
OECD/NEA	Organization for Economic Cooperation and Development / Nuclear Energy Agency
SDEF	MCNP Source Definition Card
SINBAD	Shielding Integral Benchmark Archive and Database
SS316	Stainless Steel AISI 316 type
SuperMC	Super Multi-functional Calculation Program for Nuclear Design and Safety Evaluation

T	Tritium
TBM	Test Blanket Module
TBR	Tritium Breeding Ratio
TOF	Time of Flight
TSL	Thermal Scattering Law
TUD	Technical University Dresden
VOV	relative Variance Of the Variance
V&V	Verification and Validation
WCLL	Water Cooled Lithium Lead

Chapter 1

Introduction

With growing electrical energy demand and the need to phase out fossil fuel sources due to climate change, alternative energy sources such as renewables, nuclear fission, and nuclear fusion are required. In comparison with the main renewable sources solar and wind, fusion has the advantage of being scheduable. In comparison with fission, fusion has the advantage of producing much less long-lived nuclear waste and having no risk of reactivity accidents. These reasons make fusion a promising candidate to play a part in the future energy mix.

The successful running of a fusion power plant is a complex task, which requires further research in many fields of physics and engineering. An important part is played by nuclear analysis codes which are used to monitor the adherence of new developments to the design requirements. This thesis presents the investigation and extension of the particle transport code Geant4 for use in the fusion neutronics field. In the following, the basic concepts of fusion energy production are introduced and the search for alternative fusion neutronics codes are explained.

1.1 Basic Concepts of Fusion Energy Production

The energy released in fusion reactions can be derived from the basic properties of nuclei. The nuclear binding energy B is the energy which would be needed to break up a stable nucleus into individual nucleons (Masterson, 2017). In figure 1.1, the average binding energy per nucleon B/A is plotted against the number of nucleons A. It can be seen that B/A is highest for nuclei with intermediate mass such as Fe-56 and lower both for smaller and larger nuclei. Amongst the smaller nuclei, He-4 has a particularly high binding energy.

The released energy Q of a nuclear reaction is the difference between the binding energies of the final and initial nuclei:

$$Q = \sum_f B_f - \sum_i B_i \tag{1.1}$$

and exothermic reactions occur when B/A of the reaction products is larger than for the initial products (Atzeni and Meyer-ter-Vehn, 2004). Nuclear fission is using the increase in B/A between large and intermediate nuclei by splitting large nuclei into smaller ones and nuclear fusion is using the increase in B/A from the lightest nuclei to intermediate nuclei.

There are several potential energy-releasing reactions between light nuclei, for example Wu (2017) describes:

$$\begin{aligned}
\mathrm{D{+}D} &\rightarrow \mathrm{He\text{-}3}\ (0.82\,\mathrm{MeV}) + \mathrm{n}\ (2.45\,\mathrm{MeV}) \quad , && (1.2)\\
\mathrm{D{+}D} &\rightarrow \mathrm{T}\ (1.01\,\mathrm{MeV}) + \mathrm{p}\ (3.02\,\mathrm{MeV}) \quad , && (1.3)\\
\mathrm{D{+}T} &\rightarrow \mathrm{He\text{-}4}\ (3.52\,\mathrm{MeV}) + \mathrm{n}\ (14.06\,\mathrm{MeV}) \quad , && (1.4)\\
\mathrm{D{+}He\text{-}3} &\rightarrow \mathrm{He\text{-}4}\ (3.67\,\mathrm{MeV}) + \mathrm{p}\ (14.67\,\mathrm{MeV}) \quad . && (1.5)
\end{aligned}$$

The value in brackets is the released binding energy Q, which is distributed among the final products according to the law of momentum conservation.

For a fusion reaction to happen, the Coulomb barrier between the positively charged nuclei needs to be overcome. Due to the quantum mechanical tunneling effect, this can already happen below the Coulomb energy threshold and the probability for such reactions to happen depends on the energies of

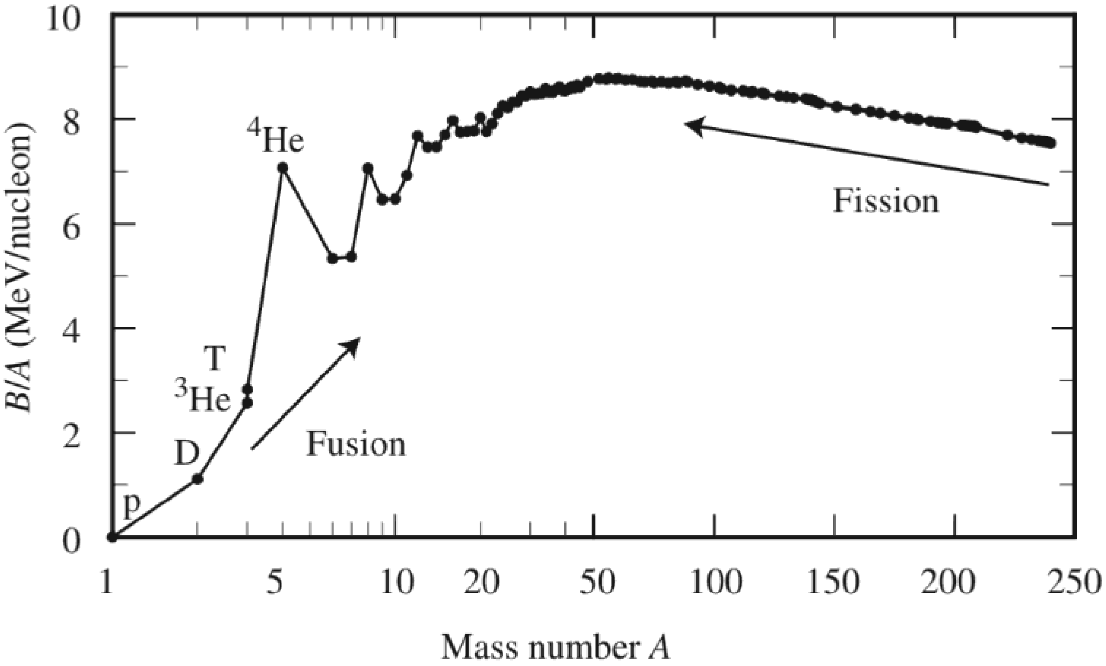

Figure 1.1: The nuclear binding energy per nucleon B/A plotted against the mass number A (Atzeni and Meyer-ter-Vehn, 2004).

the initial particles. This probability is denoted by the nuclear reaction cross-section σ. In figure 1.2, the reaction cross-sections for the previously mentioned reactions are displayed.

In a reactor setting, the material is brought to a certain energy level through heating. Since 10 keV is equivalent to the extremely high temperature of approximately 10^8 K, it is apparent that the fusion reaction with the highest cross-section at the lower range of the temperature is the most easily achievable one. Therefore, the D-T reaction is the primary fusion reaction.

Due to the high temperatures the fuel cannot be kept in any container in contact with any material. It exists in the plasma state, which means the positively charged nuclei are separated from their negatively charged electron shells and can therefore be contactlessly confined by magnetic fields.

There are many different magnetic confinement concepts. One of them is the tokamak concept (see figure 1.3). The fact that charged particles follow magnetic field lines is used by turning those field lines into a loop to avoid end losses. The resulting torus shape leads to a radial magnetic field gradient, which causes particle drifts that ultimately break the confinement. To avoid this, an additional field component which twists the magnetic field lines in poloidal direction has to be introduced.

A tokamak is using simple electromagnetic coils to create the toroidal confinement field component. Additionally, it is ramping up and down a current through the central solenoid, a coil which is aligned along the centre of the plasma torus. This changing current is creating a changing magnetic field along the torus centre, which in turn is inducing a toroidal current in the plasma. This toroidal current in the plasma is creating the intended poloidal magnetic field, which combines with the toroidal magnetic confinement field. Since the central solenoid current has to be constantly ramped up or down, this concept can only operate in pulsed mode.

The EUROfusion consortium, the umbrella organisation of Europe's fusion research laboratories, has published a roadmap for the realization of fusion electricity (Donné, 2019). It discusses the milestones which have to be reached on the path to fusion power. The aim is to demonstrate commercial electricity production from magnetically confined fusion.

The next important step is the ITER (International Thermonuclear Experimental Reactor) facility currently under construction in Cadarache, France. ITER will be a tokamak type reactor aiming to demonstrate fusion by producing net energy.

The next step after ITER will be the demonstration reactor DEMO. The main DEMO criteria are a closed tritium fuel cycle with tritium self-sufficiency and electricity generation with a target of 300–500 MW$_{el}$ (Donné, 2019).

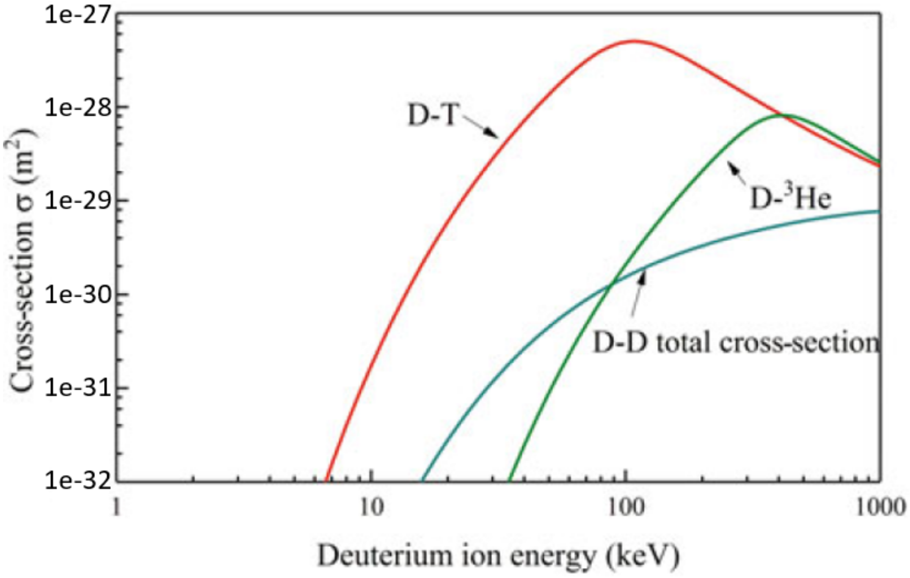

Figure 1.2: The reaction cross-section for different fusion reactions plotted against the deuterium ion energy (Wu, 2017).

An important criterion for a future power plant is tritium self-sufficiency. For ITER, tritium will be provided externally. However, as tritium has the short decay time of 12.32 a, it does not occur readily in nature (Donné, 2019). The main source of commercially available tritium are heavy water moderated nuclear fission reactors of the CANDU type. The available amount by 2055 is estimated to be between 0 and 30 kg, which causes concerns whether this will even be enough for the start up of one or more DEMO plants (Kovari et al., 2017).

In a scenario where fusion is part of commercial energy production with multiple plants in operation at the same time, the necessary amount of tritium would by far exceed what is procurable. To illustrate, the European DEMO power plant with a planned fusion power of 2 GW is estimated to need 111.2 kg tritium per full power year (Fischer et al., 2020). For this reason, future fusion power plants will have to produce their own tritium during operation.

To do this, the plasma chamber is surrounded with a blanket containing lithium. When the neutrons created in the fusion plasma impact on the lithium isotopes Li-6 and Li-7, the possible reactions include ones which produce tritium (Wu, 2017):

$$\mathrm{Li\text{-}6} + \mathrm{n} \quad \rightarrow \quad \alpha + \mathrm{t} + 4.8\,\mathrm{MeV} \quad , \tag{1.6}$$

$$\mathrm{Li\text{-}7} + \mathrm{n} \quad \rightarrow \quad \mathrm{n'} + \alpha + \mathrm{t} - 2.5\,\mathrm{MeV} \quad . \tag{1.7}$$

The cross-section for the tritium production of Li-6 increases with decreasing neutron energy while Li-7 can only produce tritium when interacting with neutrons with an energy above a threshold of 3.15 MeV (Wu, 2017). Therefore, Li-6 achieves the higher tritium yield, because it can still produce tritium with neutrons which have lost energy in multiple material interactions. Due to this, the lithium used in breeding blankets is usually enriched to contain more Li-6 than in nature.

Multiple breeder blanket concepts are under development. In ITER, the tritium production capabilities of several Test Blanket Modules (TBM) will be tested under real fusion reactor conditions. These include the European Helium-Cooled Pebble Bed (HCPB) and water-cooled lithium lead (WCLL) concepts (Donné, 2019).

The quantity used to estimate whether tritium self-sufficiency is achieved is the tritium breeding ratio (TBR). The TBR is the ratio between the tritium produced in the blanket and the tritium burned up in the plasma (Wu, 2017). Since a fusion reaction in the plasma uses up one triton and produces one neutron, the number of used up tritons is equal to the number of produced neutrons N_{tot}. The amount of tritium produced depends on the number density n of Li-6 or Li-7 nuclei in the breeder material, the cross-section of the tritium producing reaction σ and the neutron flux in the blanket volume Φ:

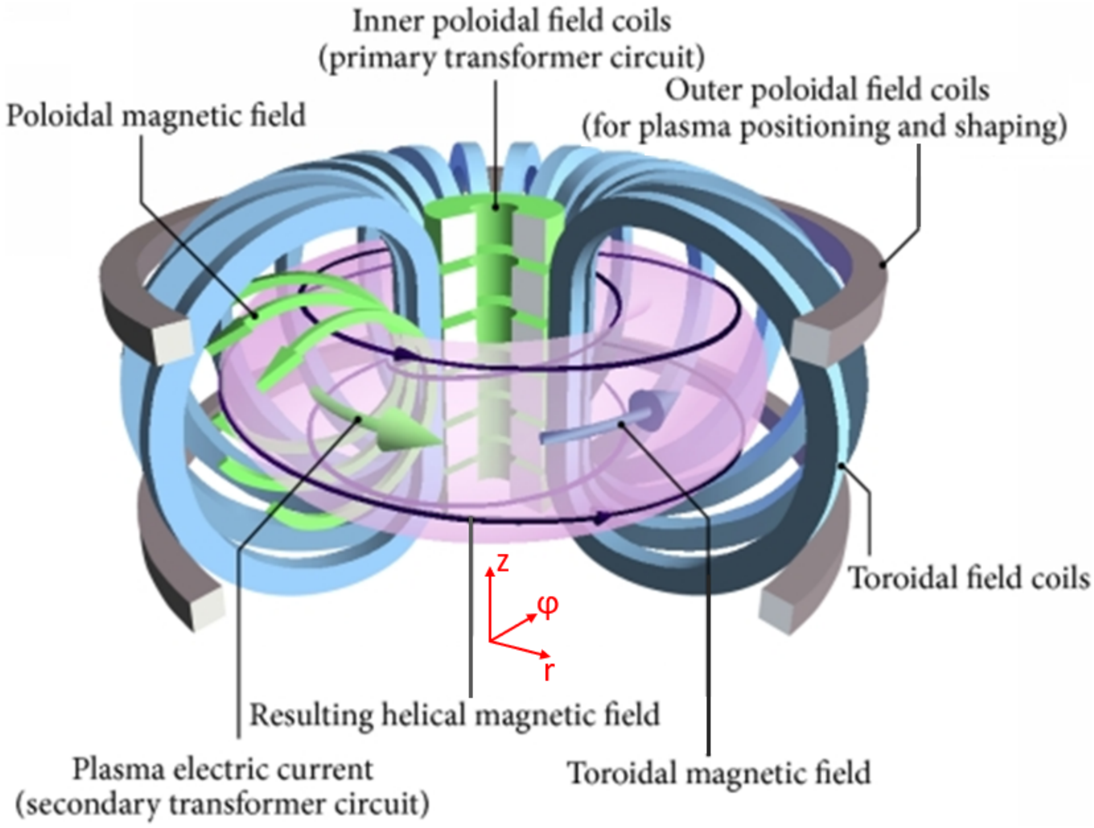

Figure 1.3: The tokamak concept for magnetically confining fusion plasmas (Li et al., 2014).

$$TBR = \frac{\int\int n_{\text{Li-6}}\sigma_{\text{Li-6}}(E)\Phi(E,V)\mathrm{d}E\mathrm{d}V + \int\int n_{\text{Li-7}}\sigma_{\text{Li-7}}(E)\Phi(E,V)\mathrm{d}E\mathrm{d}V}{N_{tot}} \quad . \tag{1.8}$$

Neutron transport calculations are used to estimate the TBR of different breeder concepts. Fischer et al. (2020) present an assessment of the required DEMO TBR. The factors which necessitate a $TBR > 1$ are the uncertainties in the neutronics calculation, the loss budget of the fuel cycle, and the tritium decay (5.5 % per year). Furthermore, a slight surplus of tritium needs to be generated to ensure operational availability through interruptions of the schedule, and to accumulate a store of tritium to allow successor plant to start up. The final requirement is $TBR \geq 1.05$ for the DEMO blanket, and a design target of $TBR \geq 1.15$, which includes margins for calculation uncertainties and incomplete models.

Parts of the reactor, for example the magnetic coils, are sensitive to radiation and the design requirements specify thresholds below which the neutron and secondary photon radiation levels have to be. To this end, shielding configurations to attenuate the radiation coming from the fusion plasma are designed and have to be verified by neutronics calculations.

1.2 Search for Alternative Fusion Neutronics Codes

The standard neutronics code for monitoring whether design goals are reached during the development process was for a long time the MCNP (Monte Carlo N-Particle) code (Brown et al., 2003), which continues to be developed at Los Alamos National Lab, US. It has been continuously validated against experimental benchmarks. However, in recent years, the European fusion community grew concerned over the export control by the US Department of Energy, which limits access to executables and in particular the source code.

Due to this, it is a long-term goal to evaluate alternative codes so that the number of available and reliable analysis tools can be increased. In a first step, multiple codes were assessed by Pampin et al. (2012). As a first criterion, only codes were included which had ongoing development and maintenance and were not under export or military control. The shortlisted codes were: Tripoli4, Serpent-2, Mcbend11, PHITS, MCU5, FLUKA, and Geant4.

The assessment included both an evaluation of criteria and a simple benchmark calculation. Geant4 was deemed promising in terms of the criteria, but the benchmark calculation could not be performed due to the toolkit nature of Geant4. Geant4 does not provide a standard executable and instead the user has to build an application tuned to their requirements out of parts of the toolkit. This requires a certain level of user expertise and is time-consuming, which is why it fell outside of the scope of the investigation by Pampin et al. (2012).

Therefore, the aim of this thesis is to continue the investigation of the suitability of Geant4 for fusion neutronics applications. In the meantime, the investigation of the other alternative codes is also ongoing and comparisons with published results of this are part of this thesis.

In a previous PhD thesis, Qiu (2016) developed geometry representation and conversion functionalities to convert CAD-based geometry descriptions for Geant4. This is applied to more complex geometry configurations in this thesis.

1.3 Objectives and Organisation of the Thesis

The objective of this thesis is to investigate the suitability of Geant4 for DEMO fusion neutronics analyses and extend the code with new developments for missing functionalities. The work can be separated into the following parts:

1. **Development of missing functionalities:** The flexible toolkit nature of Geant4 is exploited to develop new functionalities which are needed during the investigation and are also important for the wider application in fusion neutronics.
   (a) **Reflective boundaries:** The rotationally symmetric fusion reactor geometry can be represented by a sector by using reflective boundaries at the side surfaces of the sector. This standard practice strongly reduces the computational costs, making the reflective boundary function an important requirement for a fusion neutronics code.
   (b) **MCNP-equivalent tallying:** Geant4 has basic functionalities to detect physical quantities such as the average neutron flux in a volume, but not for derived quantities such as reaction rates. Since the comparison with MCNP is an important part of this work, the development of MCNP-equivalent tallying functions, which detect all required physical quantities, is necessary.
   (c) **Variance reduction methods:** Fusion neutronics calculations are used to assess the neutron shielding capability of geometry configurations. Since the aim of the shield is to let as little radiation through as possible, this poses difficulties for the statistics of Monte Carlo tallies. To alleviate this issue, variance reduction techniques for coupled neutron-photon transport are applied and are therefore a requirement for a successful fusion neutronics code.
2. **Three-level investigation strategy:**
   (a) **Verification and validation with code-to-code benchmarks:** The basic neutron transport behaviour of the Geant4 code in two simple geometries is compared with the standard code MCNP. The first benchmark verifies that the Geant4 application built out of the toolkit for this thesis performs consistently with previously published Geant4 results. The second benchmark validates Geant4's calculation of neutron flux, gamma flux, and energy deposition in fusion-relevant bulk materials.
   (b) **Validation with experimental benchmarks:** Geant4 is validated with data from experimental benchmarks from the Shielding Integral Benchmark Archive and Database (SINBAD). The chosen experiments are about the bulk structural material iron, the reliability of the tritium breeding estimation and coupled neutron-photon transport with variance reduction. MCNP is also used for comparison.
   (c) **DEMO nuclear analysis:** A DEMO design model is converted to confirm Geant4's ability to represent the large-scale, complex geometry and the plasma neutron source subroutine. As an example evaluation, the TBR is calculated in comparison with MCNP.

The thesis is structured in the following way:

- **Chapter 2** introduces the basic principles of nuclear analyses of fusion reactors. It starts with the underlying physics of neutron interactions with matter, illustrates the organisational principles of nuclear data libraries, and finishes with the mathematical representation by the Monte Carlo method.
- **Chapter 3** explains the reasoning behind the verification and validation strategy. Furthermore, the benchmarks and their MCNP representations are described and the conversion for Geant4 is delineated. The development of code functionalities necessary for these benchmarks is presented.
- **Chapter 4** covers the creation and conversion of neutron source representations and their validation.
- **Chapter 5** contains the analysis of the verification and validation of Geant4 with code-to-code benchmarks in comparison with MCNP.
- **Chapter 6** presents the validation of Geant4 against experimental data from SINBAD and in comparison with MCNP.
- **Chapter 7** covers the application to DEMO. TBR and neutron flux spectrum results are analysed and compared with MCNP. Finally, a verdict is made on the suitability of Geant4 for fusion nuclear analyses of DEMO.
- **Chapter 8** summarises new developments and validation results. It presents open issues and suggestions for further developments.

Chapter 2

Nuclear Analyses of Fusion Reactor Components

Since the neutrons created in the fusion reaction have no charge, they are not contained by the magnetic field. Therefore, they leave the plasma and interact with the surrounding reactor materials. Neutron transport simulations aim to quantify the spatial and energy distribution of the neutrons in the reactor geometry so that derived physical quantities important for the reactor design such as TBR, material degradation, activation, and heat deposition can be calculated.

Particle transport codes for nuclear analyses of fusion reactors primarily track neutrons and photons as required for nuclear heating calculations. Other particles such as electrons, positrons, etc. play a minor role.

2.1 Neutron Interactions with Matter

This section is based on Ellis and Singer (2008). First, important physical quantities are defined.

The neutron flux density Φ denotes the number of particles crossing an area of 1cm^2 per second (unit: $1/(\mathrm{cm}^2\mathrm{s})$). It can be described by the number density of neutrons n (unit: $1/\mathrm{cm}^3$) times their velocity v (unit: $\mathrm{cm/s}$):

$$\Phi = n \cdot v \quad . \tag{2.1}$$

When neutrons interact with a material i with the number density N_i, the reaction rate R (unit: $1/(\mathrm{cm}^3\mathrm{s})$ can be calculated like this:

$$R = \Phi \sigma_i N_i \quad . \tag{2.2}$$

Here, the proportionality constant σ_i is the microscopic nuclear cross-section of the material i. It describes the probability for an interaction between a neutron and a material nucleus to happen. This is an inherent property of the different nuclides and is also dependent on the energy of the incoming neutron. It has the unit of cm^2, which is often expressed in barn "b" (1b $= 10^{-24}$ cm^2).

The macroscopic cross-section Σ_i (unit: $1/\mathrm{cm}$) of the material i is related to the microscopic cross-section like this:

$$\Sigma_i = N_i \sigma_i \quad . \tag{2.3}$$

It shows the number of reactions taking place per distance travelled. Its reciprocal is the mean free path between interactions.

When a neutron travels through material, different types of interactions can occur between the neutron and the nuclei of the material. The total cross-section σ is actually the sum of the cross-sections of the different possible reactions.

In one part of the so-called elastic scattering interaction type, which can happen with neutrons of any initial energy, the neutron can scatter off the potential of a nucleus. In this case, the interaction can be regarded similar to a classical mechanic elastic collision. The neutron passes some of its kinetic energy to the nucleus, and continues on with less velocity. The removed energy depends on the scattering angle with scattering at 180° (back in the direction the neutron came from) transferring the maximum amount of kinetic energy and near 0° transferring nearly no energy.

The total kinetic energy and momentum of the system are conserved. Therefore, the maximum transferable energy depends on the mass of the nucleus. In a simplified way, this can be described by neglecting the difference between proton and neutron mass, and the binding energy. Using the atomic mass number A, the ratio between the neutron energy after the event E_1 and the initial neutron energy E_0 can be calculated like this (D'Auria, 2019):

$$\frac{E_1}{E_0} \approx \left(\frac{A-1}{A+1}\right)^2 \quad , \tag{2.4}$$

and the maximum transferable energy ratio E_t/E_0 in one scattering event can be calculated like this (D'Auria, 2019):

$$\frac{E_t}{E_0} = 1 - \frac{E_1}{E_0} \approx 1 - \left(\frac{A-1}{A+1}\right)^2 \tag{2.5}$$

This means in a collision with H-1 ($A = 1$), the entirety of the neutron's kinetic energy can be transferred in a head-on collision.

In can also happen that the neutron is absorbed into a compound nucleus. In this process both the kinetic energy of the velocity of the neutron relative to the nucleus and the released binding energy due to the absorbed neutron are converted into excitation energy of the compound nucleus. If this excitation energy is close to one of the discrete excited energy levels of the compound nucleus, this interaction is much more likely to happen, resulting in resonance peaks in the corresponding nuclear cross-section. This happens in the energy range between 1 eV and 1 MeV (Wu, 2017).

If the excited compound nucleus decays back to the ground state by emitting a neutron, this is also part of elastic scattering, since the total kinetic energy and momentum of the system is conserved.

If the excited compound nucleus decays by emitting a neutron, but remains in an excited state, this is called inelastic scattering, because the kinetic energy of the system is no longer conserved. The excited nucleus returns to the ground state through the emission of one or more characteristic gamma rays. Inelastic scattering can only happen with an incident neutron energy above a threshold specific to the nuclide. Due to the energy required for the excitation of the nucleus, the energy of the emitted neutron can be considerable lower than the incident neutron energy.

The excited compound nucleus can also decay without emitting any neutrons, instead only emitting gammas. This is called radiative capture. The cross-section for this is usually much larger at low energies and also has resonances in the energy range between 1 eV and 1 MeV.

In addition to potential scattering and compound formation, it can also happen that a neutron knocks nucleons out of the nucleus. This type of interaction only happens above comparatively high threshold energies. The neutron can be retained by the nucleus, which is excited by absorbing the kinetic energy of the neutron and later releases it in the form of gamma emission (Wu, 2017).

The notation for describing nuclear interactions is:

$$\text{(incoming particle type,outgoing particle type)} \quad , \tag{2.6}$$

so for example (n,p) means that a neutron is absorbed by a nucleus, causing it to emit a proton. Other emitted particles include gammas (n,γ) for radiative capture, deuteron (d), triton (t), He-3, and He-4 (α). It is also possible to emit more than one particle and a combination of two types of particles. Elastic scattering is described by (n,n) and inelastic scattering is denoted by (n,n').

Of particular relevance for nuclear fusion is the (n,2n) reaction. An incoming neutron with energy above a threshold value can cause the emission of two neutrons with significantly lower energies. This reaction makes it possible to increase the number of neutrons in the material, which is beneficial for the TBR. Materials such as beryllium and lead, which have a strong (n,2n) cross-section, are used as so-called neutron-multipliers.

2.2 Neutron Induced Gamma Production

For some applications such as shielding, the production of gamma radiation as a result of some types of neutron interactions and the transport and attenuation of this radiation is relevant.

Material nuclei are excited through interactions with a neutron. In the deexcitation process, they emit gamma photons with energies characteristic for the type of nuclide. Above high energy thresholds, secondary particles such as n, p, α, etc. are emitted along with the gamma, while the (n,γ) reaction is strongest at very low neutron energies (Ellis and Singer, 2008).

The following description of gamma interactions with material is based on Krieger (2019). When passing through material, gammas undergo different types of interactions with both the nucleus and the electron shell of atoms. The most important interaction types are photoelectric effect, Compton effect, and pair production. The probability for any of these effects depends on the energy of the gamma and the atomic number Z of the material. This is depicted in figure 2.1.

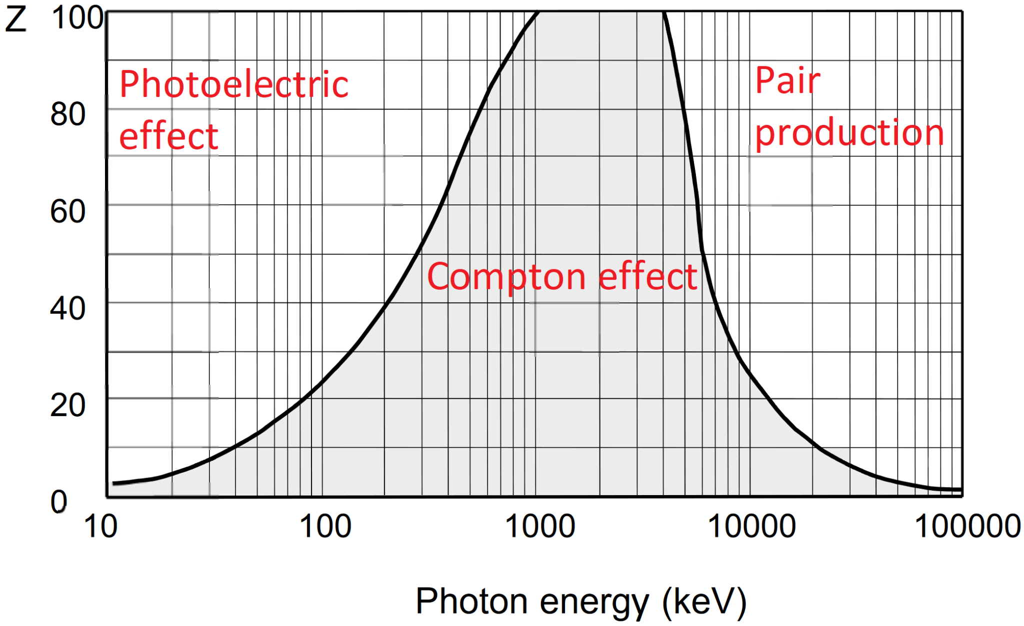

Figure 2.1: Area diagram of the most important relative parts of the photon interaction probability depending on photon energy and atomic number Z of the interaction material. The lines mark where the adjacent effects (photoelectric and Compton or Compton and pair production) have the same probability (modified from Krieger (2019)).

In the *photoelectric effect*, the gamma passes its energy on to an electron bound in a low shell in an atom and disappears. The probability τ for this effect to happen is proportional to the atomic number Z, the mass number A, the density ρ of the material and the energy of the gamma E_γ in two different ranges like this:

$$\tau \propto \rho \cdot \frac{Z^n}{A \cdot E_\gamma^3} \quad (E_\gamma < 511\,\mathrm{keV},\ n{=}4\text{–}4.5), \tag{2.7}$$

$$\tau \propto \rho \cdot \frac{Z^n}{A \cdot E_\gamma} \quad (E_\gamma > 511\,\mathrm{keV},\ n{=}4\text{–}4.5). \tag{2.8}$$

This means that gammas are attenuated more strongly by dense, heavier elements with large electron shells such as lead. The probability for the photoelectric effect goes down strongly above the binding energy of the electrons in the lowest shells in atoms.

At higher energies, the *Compton effect* becomes dominant. Here, the gamma scatters at an angle on an electron bound in an outer shell in an atom. It passes only part of its energy onto this electron and leaves with lowered energy. The probability σ_c for this effect to happen in the energy range 0.2 MeV till 10 MeV where it is dominant for most materials is

$$\sigma_c \propto \rho \cdot \frac{Z}{A \cdot E_\gamma^n} \quad (n{=}0.5 \text{ till } 1). \tag{2.9}$$

Since for most elements except hydrogen $Z/A \approx 1/2$, this means the probability for the Compton effect is independent of the mass number. The relation to E_γ means it decreases towards higher energies, but not as steeply as the photoelectric effect.

Pair production happens only above a threshold energy of 1.022 MeV. The gamma interacts with the electric field of a nucleus and is replaced by an electron-positron pair. The positron is subsequently annihilated, which causes the emission of two gammas with energy of 0.511 keV each in opposite directions. The probability κ of this process is

$$\kappa \propto \rho \cdot Z \cdot log(E_\gamma) \quad \text{for } E_\gamma > 1022\,\mathrm{keV}. \tag{2.10}$$

This means the probability for this rises with both Z and the gamma energy, which causes it to eventually outstrip the Compton effect in these directions.

In rare cases and at gamma energies above 2.044 MeV, pair production can happen in the electric field of a shell electron instead of a nucleus. This electron is ejected out of the atom so that two electrons and one positron are then travelling through the material. This is called *triplet production*.

Another possibility is *coherent scattering*. In this process, the gamma interacts with a shell electron of an atom without losing energy and without changing the electron shell. Instead, only the travel direction of the gamma is changed. The probability σ_{kl} is

$$\sigma_{kl} \propto \rho \cdot \frac{Z^{2.5}}{A \cdot E_\gamma^2} \approx \rho \cdot \frac{Z^{1.5}}{2 \cdot E_\gamma^2} \quad . \tag{2.11}$$

It is only relevant for low energies and the probability is generally lower than for the photoeffect.

In a *photonuclear reaction*, the gamma is absorbed by a nucleus, which is excited and de-excites by emitting a nucleon such as n or p. The threshold for this effect is between 6 MeV and 20 MeV for most nuclides. There is no clear dependence of the probability for this reaction to happen on Z. The probability is generally much lower than for the other gamma material interactions and can therefore be neglected.

Combining the interaction coefficients for the individual interactions while neglecting the less relevant triplett effect and photonuclear reaction results in a total attenuation coefficient μ:

$$\mu = \tau + \sigma_c + \sigma_{kl} + \kappa \quad . \tag{2.12}$$

With it, the exponential decline of gamma radiation penetrating a distance d into a material can be calculated:

$$I(d) = I_0 \cdot exp(-\mu \cdot d) \quad . \tag{2.13}$$

with initial intensity I_0 and intensity $I(d)$ at penetration depth d.

Since all individual coefficients are proportional to the density, the attenuation coefficients are often normalised to density: μ/ρ. This is called the mass attenuation coefficient. As an example, the μ/ρ for copper is displayed in figure 2.2. It can be seen that the attenuation coefficient goes down towards higher energies most strongly in the range of the photoelectric effect. It goes down less steeply for the Compton effect and starts to reverse direction for pair production. This means that higher energy photons penetrate more deeply and are less prone to losing part of their energy in Compton scattering.

2.3 Evaluated Nuclear Data Libraries

The nuclear cross-section data of the different types of interactions between different nuclides and incoming particles such as neutrons are compiled in nuclear data libraries. This section is based on Wu (2017) except where indicated otherwise.

In neutronics simulations for fusion systems the incident neutron energies cover the large energy range from 10^{-11} MeV to 20 MeV and data is needed for thousands of nuclides. Furthermore, the cross-sections can usually only be measured indirectly. Therefore experimental data does not fulfil the demand. This makes it necessary to use theoretical models, which describe the nuclear reaction physics, and fitting to interpolate between experimental data points to get cross-sections with sufficient spectral details. The resulting evaluated data for different nuclides is compiled into a library package, which is tested against the results of benchmark experiments.

Multiple international organisations publish and regularly update evaluated nuclear data libraries such as the ENDF/B library by the National Nuclear Data Center in the US, and the JEFF library by OECD/NEA (Organization for Economic Cooperation and Development / Nuclear Energy Agency). In this work, mainly ENDF/B-VII.0 (Chadwick et al., 2006), JEFF-3.1 (Koning et al., 2006), and JEFF-3.3 (Plompen et al., 2020) are used.

The differences between libraries can cause differences in results, which makes it useful to compare the simulation results of different libraries. Furthermore, sensitivity and uncertainty analyses are performed to quantify the impact of the nuclear data on the uncertainty of the simulation results.

Evaluated nuclear data libraries are published in the ENDF-6 format (Herman et al., 2021), which contains a descriptive part with information for the user, resonance parameters, tabulated cross-sections, distributions for secondary particles and photons, and covariance data. Resonance parameters are used to describe the strong fluctuations in the resonance region in an storage-space conserving way. The ENDF-6 formatted data has to be processed into a format the chosen transport code can interpret.

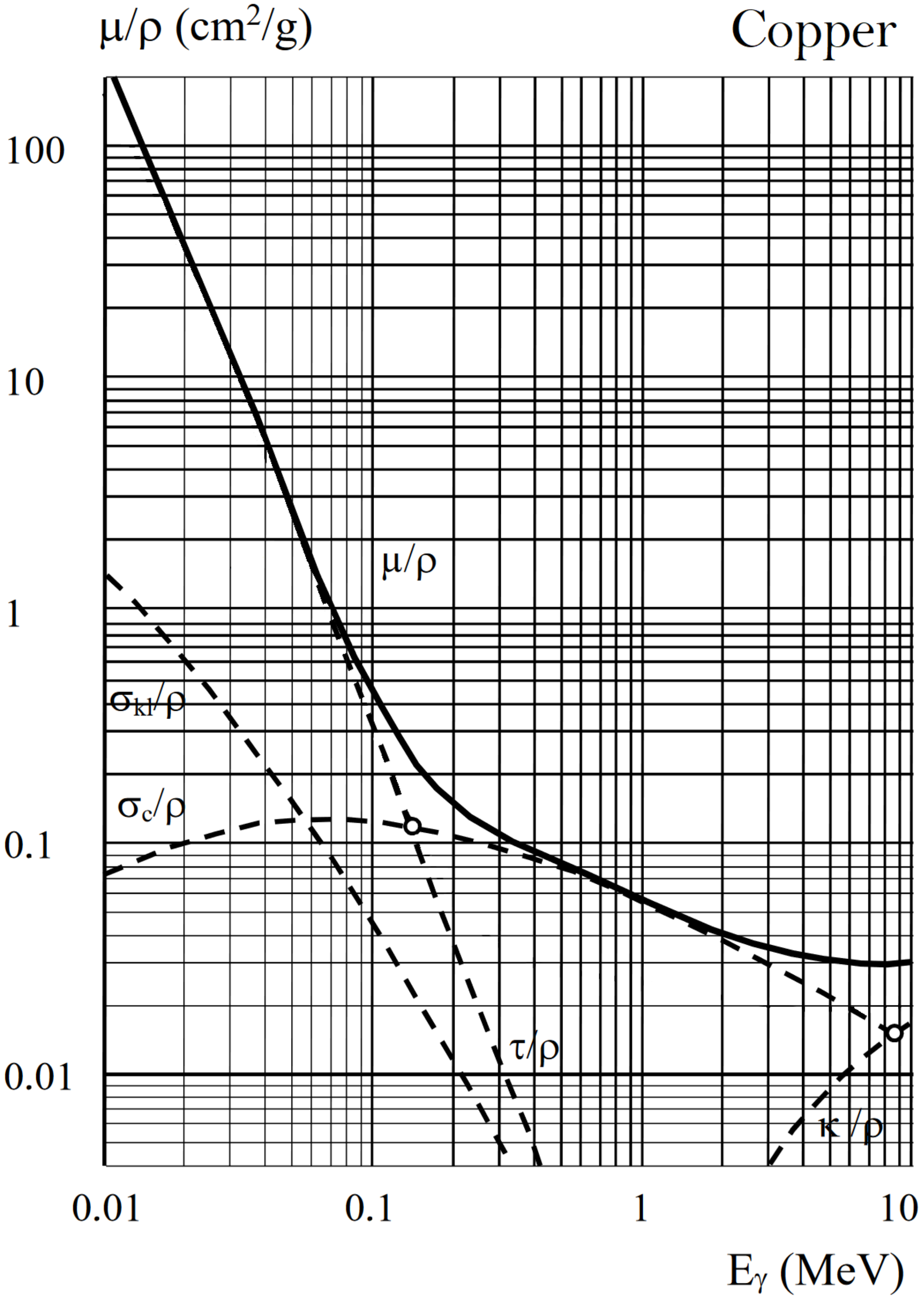

Figure 2.2: The total mass attenuation coefficient μ/ρ of copper plotted against the gamma energy E_γ and its constituents σ_{kl}/ρ for coherent scattering, σ_c/ρ for Compton effect, τ/ρ for photoelectric effect, and κ/ρ for pair production. Circles mark the points where the mass attenuation coefficients for photoelectric effect and Compton effect or Compton effect and pair production are identical (Krieger, 2019).

Geant4 offers a standard nuclear cross-section library called G4NDL4.5. The data in this library has been converted mostly from ENDF/B-VII and additional data has come from JENDL. Other converted libraries are available. The conversions are performed by a group at CIEMAT (Centro de Investigaciones Energéticas, Medioambientales y Tecnológicas), Spain. They published about it in Mendoza et al. (2012), Mendoza et al. (2014), and Mendoza and Cano-Ott (2018a). The user can download these additional libraries from the Nuclear Data Services (NDS) website of the International Atomic Energy Agency (IAEA) (`https://www-nds.iaea.org/geant4/`) (Mendoza and Cano-Ott, 2018b) and use UNIX environment variables to switch between libraries. This method is less flexible than in MCNP where the user can choose a mix of different libraries on the isotope level.

The resonance region in a cross-section can be divided into two ranges: the resolved resonance region at lower energies, where the peaks can be clearly distinguished, and the unresolved resonance region at higher energies, where the peaks overlap. To conserve storage space, evaluated nuclear data libraries in ENDF-6 format use resonance parameters to describe resonance cross-sections. For use in particle transport codes, the data has to be processed to create continuous energy cross-sections. This process is called resonance reconstruction (Wu, 2017).

MCNP takes continuous energy cross-sections in the ACE (A Compact ENDF) format (Conlin and Romano, 2019), which can be converted from ENDF-6 format. The neutron interaction data distributed with MCNP is linear-linear interpolable. The tolerance has been tightened along with increasing computer memory and currently is $1\,\%$ or less, with some recent tables at $0.1\,\%$, resulting in energy grids with up to about 100000 points (Brown et al., 2003).

For Geant4 the data also has to be in linear-linear interpolable format. The ENDF-6 format describes the cross-section with a combination of resonance parameters and cross-section data points. Since the data point part uses log-log or linear-log interpolation, both the data points and the resonance parameters have to be transformed. For the cross-section data points Mendoza and Cano-Ott (2018a) set the allowable interpolation error to $0.1\,\%$ and for the resonance parameter part, they had to set the error to $1\,\%$, because otherwise the number of data points grew too large (> 500000). This part of the processing has been done with the widely available PREPRO software package (Cullen, 2017). In the next step, they have used a self-developed code for converting the data into the Geant4 G4NDL format.

In the unresolved resonance region, the continuous energy cross-sections appear like smooth functions of energy, because the resonances are too close together to be resolved. Additionally, resonance self-shielding effects are neglected. The MCNP code has a function to accurately handle these self-shielding effects in the unresolved resonance region. It uses pre-produced probability tables from which the cross-section is sampled during the MCNP run. This function is used as default, but can be turned off so that the smooth cross-section is used instead (Brown et al., 2003). Geant4 does not have an equivalent function, but the function is turned on in MCNP for all calculations in this work, because it represents the physics more accurately and Geant4 should be compared with MCNP as it is widely used.

Another effect which has to be considered for the nuclear data used in particle transport codes is the Doppler broadening. The thermal motion of the target nucleus leads to temperature dependent changes in the relative velocity of the incident neutron. The resulting Doppler effect causes the resonance peaks in the cross-section to become broader and lower. Therefore, the data has to be adjusted for the temperature of the material in which it is used (Wu, 2017).

For MCNP, this is done as part of the pre-processing of the nuclear data library. For example the JEFF-3.3 library releases ACE-formatted data processed for multiple temperatures along with the ENDF-6 formatted file.

Geant4 performs the Doppler broadening on the fly (Mendoza et al., 2014). This allows for more flexibility in the material temperatures, but is slowing down the code.

Another physics aspect is the fact that at neutron energies below 5 eV, the chemical binding of the target nucleus in a molecule or crystal lattice to its surrounding atoms and their thermal motion has an effect on the elastic and inelastic scattering cross-sections (Herman et al., 2021). To account for this, a separate thermal scattering law (TSL) dataset is available for a limited number of nuclides in different chemical situations at specific temperatures. The JEFF-3.3 library (Plompen et al., 2020) for example includes data for hydrogen in water, ice and polyethylene. In this work, the JEFF-3.3 data is used in MCNP. In Geant4, only the standard G4NDL4.5 TSL data based on the ENDF/B-VII library is available.

Additionally to the probability for interactions to happen, the nuclear data files also describe the angular and energy distributions of secondary particles, which are defined as a function of the incident neutron energies. For some reactions, this is done for points in the incident neutron energy, making it necessary to interpolate the probability distribution in-between. Mendoza et al. (2014) describe another difference between Geant4 and MCNPX: Geant4 implements the sampling according to the ENDF-6 format rules, MCNPX has its own procedure, which allows it to preserve thresholds.

2.4 Particle Transport Simulation with the Monte Carlo Method

The neutron (and other particle) transport through the reactor is described by the Boltzmann equation. There are two basic approaches of numerically solving this transport problem. Barros (1997) summarises them as: "the probabilistic school, such as the Monte Carlo methods, whose basic philosophy is to solve approximately the exact problem, and the deterministic school, such as the discrete ordinates methods, whose basic philosophy is to solve exactly an approximate problem".

For a deterministic method like the discrete ordinate method, the phase-space has to be discretised into many small boxes, on which the solution is obtained. This introduces averaging approximations in space, energy, and time. Due to this, the Monte Carlo method is better suited to solving time-dependent problems with complex, three-dimensional geometry (Brown et al., 2003). Fusion neutronics calculations are usually steady-state and time-invariant so the time part is less relevant, but the complexity of the geometry makes Monte Carlo methods advantageous.

For the Monte Carlo method it is not necessary to solve the Boltzmann transport equation. Instead the statistical process of nuclear particles interacting with material is simulated. This is done by sequentially simulating the random walk of individual particles, so-called particle histories.

A schematic describing the working principle of the Monte Carlo method is displayed in figure 2.3. The required data can be separated into particle source, geometry and physics. The particle source data contains the probability distributions of the initial energy, position and momentum direction. The geometry data describes the dimensions of individual volumes and their material composition, which includes the mass density and the isotopic composition. The physics data consists of nuclear cross-section data collected in nuclear data libraries and in some cases additional models.

During the transport process, pseudo-random number generators are used to sample known probability distributions. A new particle history is started by sampling its initial conditions from the source data. The distance to the next collision is determined from the macroscopic cross-section of the material in the current volume. This is compared to the distance until the particle's trajectory meets the boundary of the current volume to determine if the transport continues in the next volume or if a collision happens in the current one. Other cut-offs due to time, energy, or weight are considered. If a collision happens, the nuclide involved in the collision is sampled according to the material composition of the volume, and the applicable physical process is used to determine the energies and directions of any particles exiting the collision according to the nuclear cross-section data. The processes of crossing boundaries and collisions are repeated until the particle and all its secondaries are killed either in a physical capture process or due to escaping the simulated geometry or due to variance reduction. Next, another particle history is started from the source until the desired number of particle histories are completed. With each new history, the particle distributions in the geometry become better known.

In contrast to deterministic methods, which return information on physical quantities throughout the phase-space of the problem, for Monte Carlo methods, the user has to specify which information to collect. For this, the user has to pick a location like a geometry volume or a surface, and a physical quantity such as the flux. Further options like energy bins or which particle type to consider can be chosen. This is called a tally in MCNP and a scorer or detector in Geant4. If the geometrical distribution of the physical quantity is of interest, a mesh can be defined on which the specified result is collected.

According to Brown et al. (2003), the Monte Carlo method is implicitly sampling the unknown probability density function $f(x)$ for scoring x. The true result is the expected value $E(x)$ or true mean:

$$E(x) = \int x\, f(x) \mathrm{d}x \quad . \tag{2.14}$$

For a total number of particle histories N, the true mean $E(x)$ is estimated by the sampled mean $\bar{x}$ from the contribution x_i of each individual particle history i like this:

$$\bar{x} = \frac{1}{N} \sum_{i=1}^{N} x_i \quad . \tag{2.15}$$

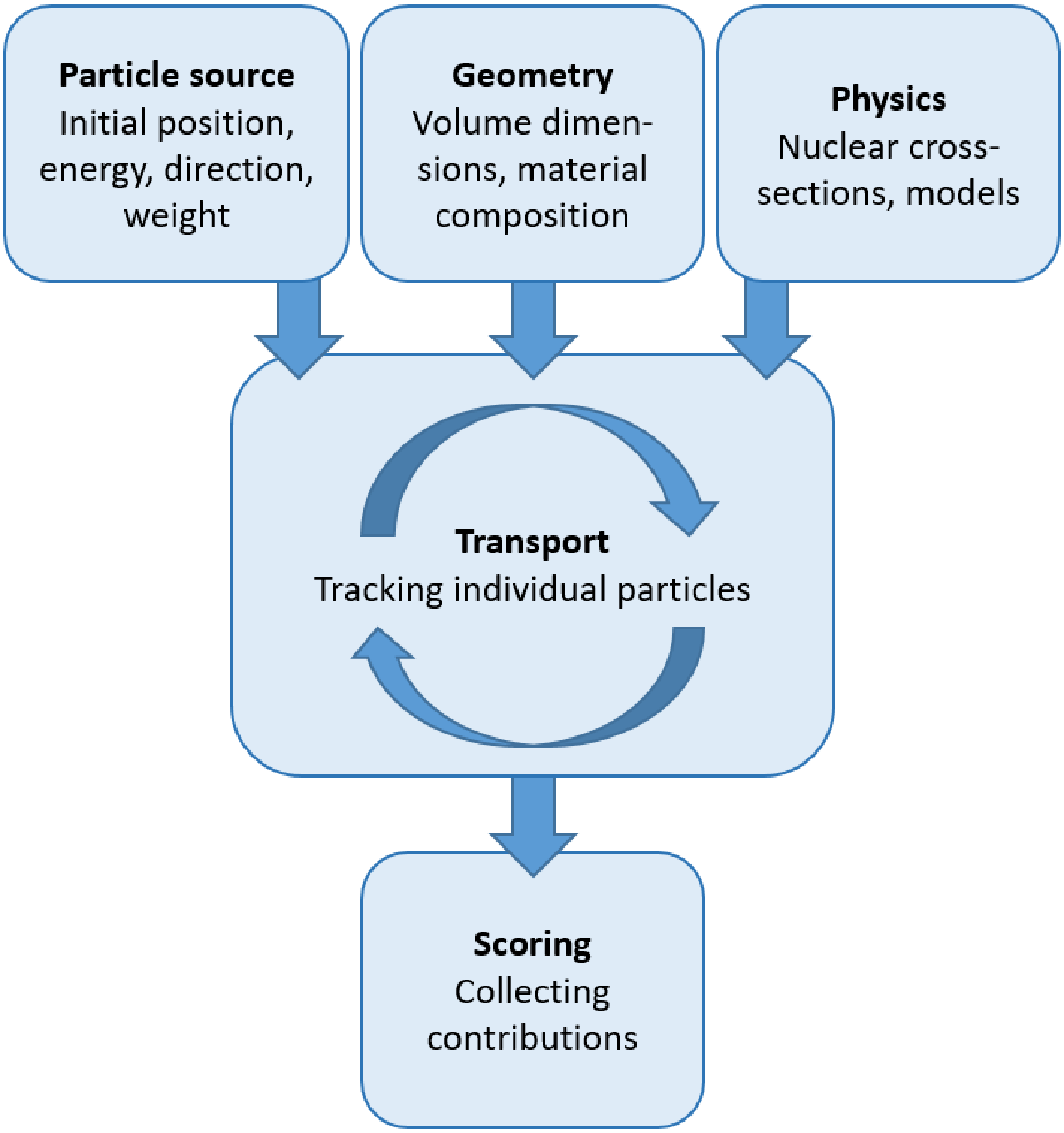

Figure 2.3: Schematic of the working principle of the Monte Carlo method.

According to the Strong Law of Large Numbers in the case of finite $E(x)$:

$$\lim_{N\to\infty} \bar{x} = E(x) \quad . \tag{2.16}$$

In summary, the Monte Carlo method estimates the true result by averaging the contribution of individual particle histories. For a large enough number of histories this estimate approaches the true result.

2.4.1 Precision and Accuracy of Monte Carlo Result

According to Brown et al. (2003), the accuracy describes how close the result calculated in the Monte Carlo simulation comes to the true physical result. The difference between the two is the systematic error. The accuracy is affected on the code level by factors such as the mathematical models, uncertainties in the reaction cross-sections, and coding errors. On the problem modelling level, accuracy depends on well-represented source distribution, geometry, and material descriptions. Furthermore, the user can hamper the accuracy by wrongly used variance reduction methods.

The uncertainty caused by the statistical fluctuations of the recorded x_i values around the mean value is called precision. It decreases proportionally to $\frac{1}{\sqrt{N}}$ and variance reduction methods seek to improve it (Brown et al., 2003).

Looking at just the Monte Carlo simulation, the accuracy is unknown. A precise result can be inaccurate due to the discussed error sources. Uncertainty estimates of Monte Carlo simulations only refer to precision and not accuracy (Brown et al., 2003). It is possible to gauge the uncertainty due to the uncertainty of nuclear cross-sections by additional sensitivity analyses. Additionally, benchmark experiments are performed to compare the results of Monte Carlo simulations to measured data and estimate the accuracy this way.

The statistical precision is quantified by MCNP according to Brown et al. (2003) using the estimated relative error R. It is calculated from the sampled mean $\bar{x}$ and its estimated variance $S_{\bar{x}}^2$:

$$R = \frac{S_{\bar{x}}}{\bar{x}} = \frac{\sqrt{\frac{1}{N}(\overline{x^2} - \bar{x}^2)}}{\bar{x}} \quad , \tag{2.17}$$

where

$$\overline{x^2} = \frac{1}{N}\sum_{i=1}^{N} x_i^2 \quad . \tag{2.18}$$

Only results with statistical error < 0.1 for standard tallies can be deemed statistically trustworthy. For a special tally called the point detector, the statistical error needs to be < 0.05. Here, a deterministic calculation is performed for every source and particle interaction during the run to estimate the probability of hitting a specific point defined as detector. The tally takes into account the probability of the particle being scattered into the right solid angle and the probability of it being scattered away on the way to the defined point. The contributions of all events are added up to form the final result (Brown et al., 2003).

2.4.2 Convergence Criteria

It can happen that despite a small statistical error, the problem is not yet sampled well enough for a certain number of histories, for example because it is still missing important paths with strong effects on the final result. Due to this, further criteria need to be considered to ensure a fully converged result with reliable confidence intervals. In the following, the criteria employed by MCNP are described based on Brown et al. (2003).

The figure of merit (FOM) is defined as follows:

$$FOM = \frac{1}{R^2 T} \quad . \tag{2.19}$$

with R the relative error R and T the computing time. Since R^2 is proportional to $1/N$ and T is proportional to N, the FOM is approximately constant during the Monte Carlo run except for potential statistical fluctuations early in the run.

The relative variance of the estimated R, which is called relative variance of the variance (VOV), can also be used to ascertain the quality of convergence. The VOV involves the third and fourth order moments of the history probability density function $f(x)$. Due to this, it is more sensitive than R to large history score fluctuations. The expanded equation for it is

$$VOV = \frac{\sum x_i^4 - \frac{4}{N}\sum x_i \sum x_i^3 + \frac{8}{N^2}\sum x_i^2 (\sum x_i)^2 - \frac{4}{N^3}(\sum x_i)^4 - \frac{1}{N}(\sum x_i^2)^2}{(\sum x_i^2 - \frac{1}{N}(\sum x_i)^2)^2} \quad . \tag{2.20}$$

The criterion for the VOV is to be < 0.1 and to decrease proportional to $1/N$.

While running a Monte Carlo problem there can be individual histories which have a particularly large contribution to the end result, but are unlikely to be sampled. This may be detected by abrupt decreases in the FOM and the R, but can also be missed. In this case, a result would be achieved that fulfils the previous criteria, but actually underestimates the correct result. To detect a situation like this, the 201 largest history scores x are saved and continually updated during the run. The convergence criterion is that these largest history scores have to decrease faster than $1/x^3$. To check for this, a generalized Pareto function

$$\text{Pareto} \;\; f(x) = a^{-1}(1 + kx/a)^{-(1/k)-1} \tag{2.21}$$

is used for fitting. This function can fit different kinds of value distributions including $1/x^n$, exponential ($k = 0$), and constant ($k = -1$). The $SLOPE$ n is calculated from the fitting variable k:

$$SLOPE = (1/k) + 1 \quad . \tag{2.22}$$

In the case of the $SLOPE$ exceeding 10, it is set to 10. The criterion is considered fulfilled if $SLOPE > 3$.

The standard code MCNP is using the following list of criteria based on the previously explained quantities:

1. Non-monotonic behaviour (no up or down trend) of the estimated mean $\bar{x}$ as a function of histories N for the last half of the problem.
2. Estimated relative error $R < 0.1$ (or $R < 0.05$ for point detector tally).
3. R monotonically decreasing for the last half of the problem.
4. R decreasing proportional to $\frac{1}{\sqrt{N}}$ for the last half of the problem.
5. Estimated variance of variance $VOV < 0.1$.
6. VOV monotonically decreasing for the last half of the problem.
7. VOV decreasing proportional to $\frac{1}{N}$ for the last half of the problem.
8. Figure of merit FOM statistically constant for the last half of the problem.
9. Nonmonotonic behaviour of FOM for the last half of the problem.
10. $SLOPE > 3$.

These are called the 10 statistical checks, which help the user assess the quality of convergence. If they are not fulfilled, it indicates that the user has to increase the number of histories or introduce variance reduction methods.

2.4.3 Variance Reduction

In the case of deep penetration problems which include thick shielding, large geometries, or tally areas which are small or far away from the sources, or combinations thereof, it can happen that the computational effort to achieve statistically reliable results becomes prohibitive. Variance reduction aims to guide more particle histories into the region of interest to improve the statistics of tally results without breaking the physics representation.

MCNP offers many different approaches to variance reduction. The one which is used in this thesis is called "geometry splitting with Russian roulette". The equivalent is called "importance biasing" in Geant4.

Brown et al. (2003) describe the method this way: importance values I_i are assigned to the cells of the geometry. The user assigns regions of interest higher importance values. Usually the values are rising from the area where particles are being produced towards the region of interest. Unimportant regions receive low importance values.

Particles are assigned weight values from the start. The contribution a tally makes to a tally is multiplied with its current weight value. When a particle with weight w crosses from cell 1 into cell 2, the ratio of the importance values I_2/I_1 determines what will happen with the particle.

If $I_2/I_1 < 1$, the particle is travelling into a less important region and Russian roulette is applied. This means, particles are killed with the probability $1 - I_2/I_1$ and any surviving particles have their weight adjusted by a factor of I_1/I_2. This way, less particles have to be tracked in the less important regions, but the physics are being balanced by the adjusted weight of the surviving particles.

If $I_2/I_1 > 1$, the particle is travelling into a more important region and splitting is applied. If I_2/I_1 is an integer $n \geq 2$, the particle is split into n identical particles, each with the weight w/n. I_2/I_1 is not an integer, splitting is done probabilistically. Defining n as the largest integer in I_2/I_1, the probability for creating $n+1$ particles is given by $p = I_2/I_1 - n$ and the probability for creating n particles is given by $1 - p$. The weight given to each particle is $w \cdot I_2/I_1$. The newly created particles are tracked individually from their creation onwards. This way, more particles can be tracked in the regions of interest, while the lowered weight ensures correct results.

2.4.4 Geometry Representation

A Monte Carlo method does not require discretisation in the geometry description and allows instead for the geometry to be described down to the computational precision limit. When representing a physical object in a Monte Carlo code, the object is split into regions depending on material composition and variance reduction concerns. In the following, the different approaches of MCNP and Geant4 in representing geometry are described.

According to Brown et al. (2003), the MCNP geometry description is based on Boolean operations on half-spaces which can be defined by first and second degree surfaces such as planes, cylinders, spheres, cones, ellipsoids, and others. Surfaces are represented as $f(x, y, z) = 0$, for example a sphere of radius R centred at the origin is represented as $f(x, y, z) = x^2 + y^2 + z^2 - R^2 = 0$. A positive/negative-notation is used to define the space above/below or inside/outside a surface: any point with $f(x, y, z) > 0$ is located on the positive side of the surface. In the example of the sphere, this makes the inside of the sphere negative. The user has to set a defined number of variables to define a surface. In the case of a sphere on the origin, the user only has to set the value of the radius R while for a general sphere the values for x, y, and z coordinates have to be given before the radius R.

The volume regions are called "cells" and are constructed by intersections, unions, and complements of the positive/negative spaces defined by the surfaces, i.e Boolean operations on the specified surfaces. The material of the cell and its density is assigned as well.

In Geant4, the basic building block of a geometry description is the "solid". According to Geant4 Collaboration (2019a), a solid is a geometrical object that has a shape and specific values for each of that shape's dimensions. This means, unlike MCNP, the geometry description is based on three-dimensional objects. There are no stand-alone surfaces like the plane type of MCNP. The available standard solids include boxes, tubes, cones, spheres, wedges and tori. Segments and shells can be described by giving starting and ending angle or inner and outer radius in the dimensions. Two solids can be combined into a boolean solid by the operations union, intersection, or subtraction, however, this feature may slow down the particle tracking.

The next level of the Geant4 geometry description is the logical volume. A logical volume is defined by a solid and a material type. The same solid can be assigned to multiple logical volumes.

Finally, physical volumes are created from logical volumes and placement coordinates. The same logical volume can be placed multiple times. The placement of volumes is hierarchical: all new volumes need to be placed inside a parent volume. The first volume, which has to contain all other volumes, is called World volume. The rotation and translation of a newly placed volume is defined with respect to its parent volume. This means, a physical volume which contains an inner structure of child volumes placed inside, can be placed multiple times, translated, or rotated, while keeping its internal structure intact.

Child volumes are not supposed to extend beyond their parent volumes, or overlap with other child volumes, because this can confuse the local material definition during particle transport. The user has to make sure the geometry description avoids such conflicts.

In addition to this standard geometry structure, Geant4 provides some other geometry approaches like the tesselated solids, and allows users to define new solid types. The newly defined solid type has to implement methods to decide whether a particle is inside or outside the volume and to calculate the distance to the volume boundaries. These methods are required for the particle tracking.

2.4.5 Material Representation

Material descriptions are assigned to the geometry volumes so that during the particle transport, material interaction partners can be picked. Both the MCNP and the Geant4 standard is described in the following according to Brown et al. (2003) and Geant4 Collaboration (2019a).

MCNP defines materials in the material card of the input file. Each material has a list of contained isotopes with nuclear data library identifications and the nuclide fraction of each isotope. Nuclide fractions can be given as weight or atomic fractions. These nuclide fractions do not have to be normalised. Temperatures are set by picking a nuclear data library processed for the required temperature.

The density of material is not specified on the material card. Instead it is given when assigning a material to a geometry volume on the cell card. This system makes it possible to have the same material appear with different densities in different parts of the geometry.

Geant4 material types are not built directly out of isotope types, but instead use intermediary element types or already defined material types for this. Isotope types are defined by proton number, and number of nucleons. Element types can be built up out of isotope types for user-specified isotopic compositions, or just defined with proton number and molar mass to get the natural isotopic composition.

For a new material type, its name, mass density, physical state, temperature, and pressure need to be defined (unless standard conditions are desired). This means, unlike for MCNP a multiple material types have to be defined if the same composition appears with multiple densities. The other difference is that the temperature of the material is defined here instead of by choosing a library pre-processed for the desired temperature. The reason for this is that Geant4 does the temperature processing during the run.

Geant4 also offers a database of materials and elements out of which the user can pick a definition.

When converting material descriptions from MCNP to Geant4 format, some mathematical operations have to be performed such as converting atom density to mass density, normalising mass fractions, and converting atomic fractions < 1 to corresponding integer numbers. The atomic weights and isotopic composition data for this are taken from the database of the National Institute of Standards and Technology (Coursey et al., 2015).

Chapter 3

Presentation of the Verification and Validation Strategy and Implementation

Geant4's suitability for fusion neutronics application is supposed to be investigated. The verification and validation strategy consists of three parts. In the first part, Geant4's basic functioning is verified and validated with code-to-code benchmarks in comparison with the standard code MCNP on the basis of very simple geometries. The second part employs benchmark experiments taken from the Shielding Integral Benchmark Archive and Database (SINBAD). Geant4 results are compared with experimental and MCNP results. In the final part, Geant4's suitability is tested by applying it to a DEMO neutronics calculation.

In the following, the geometry and representation in both MC codes of the chosen benchmarks are described. Both for the realisation of the verification and validation (V&V) strategy within this work and for any future use of Geant4 for fusion neutronics analyses, it is necessary to extend the available Geant4 code with some missing functionalities. The flexible toolkit structure of Geant4 makes it possible to implement and integrate these functionalities. When code extensions are necessary to perform these benchmarks, they are introduced as well.

The conversion and validation of the neutron source functionalities, which are used to set the initial parameters of the particle histories, are discussed separately in chapter 4.

3.1 The Code-to-Code Benchmark Strategy

For the code-to-code benchmarks, simple geometry and neutron source descriptions, which can be set up identically for Geant4 and MCNP, are used. The geometry is filled with only one single isotope at a time. To conserve computation time, eleven most fusion relevant isotopes have been chosen: isotopes of the breeder ceramic and neutron multiplier (Li-6, Li-7, Be-9, O-16, Si-28, and Pb-208), and isotopes of the structural materials and shielding (H-1, C-nat, Cr-52, Fe-56, and W-184).

3.1.1 Single Interaction Code-to-Code Benchmark

Geant4 does not provide a standard application. Instead the user has to build their own application using parts of the toolkit and own programming. When setting up a new application, a good starting point is the suite of examples provided by the toolkit. The application used in this work is developed mainly based on the Hadr04 example, which includes the physics representation to deal with the converted evaluated nuclear cross-section libraries. This is combined with parts from other examples to implement the collection of data during the run and the output.

Potential mistakes in the implementation of this application have to be ruled out. Therefore, a code-to-code benchmark previously performed by Mendoza et al. (2014) to test the converted ENDF/B-VII.0 library is used to verify that the results calculated by the application developed for this thesis are consistent with the results obtained by Mendoza et al. (2014).

A schematic of the geometry of the single-interaction code-to-code benchmark can be seen in figure 3.1. The geometry consists of a cylinder volume with length of 2 m and a radius of only 1 μm. This volume is filled with material consisting exclusively of one of the previously mentioned isotopes at the natural density of the element. A neutron beam with isolethargic energy spectrum is shot at the centre of the cylinder along its symmetry axis, which is aligned along the z-axis. The isolethargic energy spectrum is created by first creating N energy points E_i which are equidistant in log(E). To do this, a step size constant b needs to be calculated like this:

$$
\begin{aligned}
E_1 &= E_0\,10^{b} \quad , && (3.1)\\
E_i &= E_0\,10^{i\cdot b} \quad , && (3.2)\\
\Leftrightarrow for\ i = N: \quad b &= \tfrac{1}{N} log\left(\tfrac{E_N}{E_0}\right) \quad . && (3.3)
\end{aligned}
$$

Then the probability density $p(E_i)$ is defined as

$$p(E_i) = \frac{1}{E_i} \quad . \tag{3.4}$$

The energy spectrum ranges from $E_0 = 10^{-10}$ MeV till $E_N = 20$ MeV and $N = 1000$ steps are used.

Due to the small radius, nearly all neutrons undergo just a single material interaction before leaving the volume. The neutron current consisting of scattered or secondary neutrons is recorded on the side surface of the cylinder.

The JEFF-3.1 and ENDF/B-VII.0 nuclear data libraries are used in the simulations. To achieve sufficiently low statistical errors, 10^8–10^9 histories were simulated. Results calculated with the G4PSCylinderSurfaceCurrent primitive scorer of Geant4.10.03 are compared to results calculated with the surface current of MCNP5-1.6. Isolethargic energy bins from 10^{-10} MeV to 20 MeV calculated in the same way as the energy spectrum are used.

To correctly calculate the neutron interactions at low energies below 1 eV, the thermal scattering law (TSL) treatment has to be used. However, data for this is only available for a limited amount of elements in specific molecules. For the single-isotope materials used in this benchmark, which do not occur naturally, it is not possible to find TSL data. Due to this, the TSL treatment is deactivated and results below 1 eV are disregarded.

MCNP functions which are missing in Geant4 such as the unresolved resonance range probability table treatment are not turned off, since the aim is to test how well Geant4 compares to MCNP as it is routinely used.

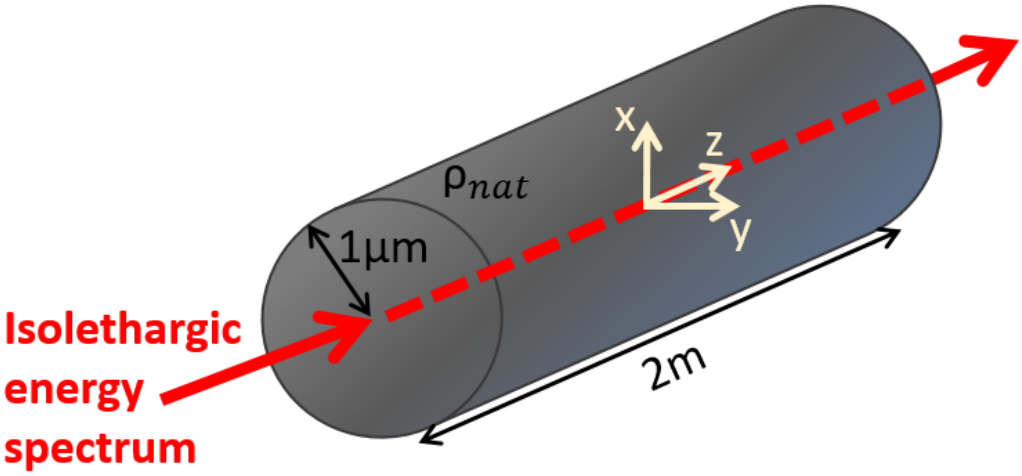

Figure 3.1: Schematic of the single-interaction code-to-code benchmark.

3.1.2 Multiple Interaction Code-to-Code Benchmark

The second benchmark had been previously performed by Pampin et al. (2012) (also published with more details in Davis (2012)) when assessing other alternative codes to MCNP. Repeating it to validate Geant4 allows the comparison with these codes.

In this benchmark, neutrons are passing through thick material, causing them to have multiple interactions before being detected. Due to this, minor deviations can add up and are made more visible than in the first benchmark. Pampin et al. (2012) only detected and compared neutron flux. In this work, this benchmark is additionally used to investigate the agreement between Geant4 and MCNP for the total gamma flux and the energy deposition.

A schematic of the geometry set-up used for the multiple-interaction code-to-code benchmark is illustrated in figure 3.2. It consists of a sphere with radius 30 cm with an isotropic, monoenergetic 14.1 MeV neutron source at the centre. The sphere is filled with one of the selected isotopes (H-1, Li-6, Li-7, Be-9, C-nat, O-16, Si-28, Cr-52, Fe-56, W-184, and Pb-208) at a time at a uniform density of $1\,\mathrm{g/cm^3}$.

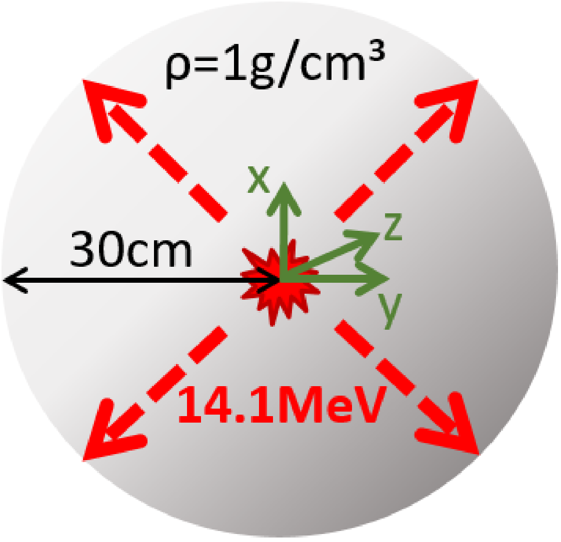

Figure 3.2: Schematic of the multi-interaction code-to-code benchmark.

Same as for the single-interaction benchmark, the thermal scattering law neutron treatment is deactivated. Therefore, results below 1 eV have to be disregarded.

Again, the MCNP unresolved resonance range probability table treatment is not turned off.

The average neutron flux in the sphere is recorded with the track length estimator of cell flux tally in MCNP and the G4PSCellFlux primitive scorer in Geant4 in combination with a particle filter which lets in only neutrons.

For the neutron flux spectra, Pampin et al. (2012) binned the results in the TART-616 energy group format. This energy group structure consists of 616 energy bins which are equally spaced in the natural logarithm of the energy, with 50 bins per energy decade, between 10^{-11} MeV and 20 MeV. The energy value E_i of the i-th bin of this group structure is calculated as

$$E_i = E_0 e^{i\,b} \quad , \tag{3.5}$$

out of the start energy E_0. This can be restructured to calculate the constant b:

$$b = \frac{1}{i} ln(\frac{E_i}{E_0}) \quad . \tag{3.6}$$

Inserting $i = 600$, $E_0 = 10^{-11}$ MeV, and $E_i = 20$ MeV, b can be calculated and used in turn to calculate all energy bins between 10^{-11} MeV and 20 MeV.

For isotopes, which already achieved a statistical error $< 1\%$ in the energy range 10^{-6} MeV–20 MeV, 10^8 particle histories have been used. For the other cases, the particle histories have been increased to $5 \cdot 10^8$ or 10^9.

For the calculation of gamma flux and energy deposition, another physics package, which simulates the transport of photons and charged particles called G4EmStandardPhysics, is required in Geant4 in addition to the NeutronHP package, which simulates neutron transport on the basis of evaluated nuclear cross-section data libraries.

The gamma flux is detected with the track length estimator of cell flux tally in MCNP and with G4PSCellFlux primitive scorer in combination with a particle filter, which only counts gammas in Geant4.

The energy deposition is detected with the MCNP track length estimate of energy deposition tally. In standard Geant4, it is impossible to separate neutron and gamma heating. The G4PSDoseDeposit primitive scorer collects all heating data from any secondary particles. However, when combining it with a particle filter to count only the neutron contribution, the result is zero.

3.2 The Experimental Benchmark Strategy

The code-to-code benchmarks are intended to verify and validate Geant4's basic neutron transport capabilities. Next, Geant4 is validated against experimental data from several benchmark experiments collected in the Shielding Integral Benchmark Archive and Database (SINBAD) (Kodeli et al., 2014). These allow to test Geant4's performance with realistic materials in technical geometries.

3.2.1 Transmission Through Iron Spheres Experiment

The first experimental benchmark is on the neutron transmission through iron shells. Since iron is the most important structural material, it is necessary to investigate Geant4's performance in this material under realistic conditions.

The experiment has been performed by Simakov et al. (2000) at Institute of Physics and Power Engineering (IPPE), Obninsk, Russia. The KG-0.3 generator has used a pulsed deuteron beam (2 ns bursts) with energy 280 keV hitting a titanium-tritium target to create 14.1 MeV neutrons through the T(d,n)He-4 reaction. The α-particles have been detected at the angle of 173° by a silicon surface barrier detector to determine the 14.1 MeV neutron yield.

The neutron source has been placed through a radial hole at the centre of five iron spheres with different thicknesses to test neutron transmission. The schematics of these spheres can be seen in figure 3.3, and further characteristics are shown in table 3.1. The wall thicknesses of 2.5–28 cm cover 0.5–6.1 neutron mean free paths in iron. In the smallest sphere, the ratio between the volume of the hole V_h and the total volume V is 10.6 %. This ratio decreases for the larger spheres down to 0.6 % for the largest sphere.

Table 3.1: The characteristics of the five iron shells of the SINBAD IPPE benchmark.

No	Wall Thickness $R - r$, cm	fraction of iron mean free path	Nucl. dens $10^{22}/\text{cm}^3$	V_h/V %
1	2.5	0.5	8.385	10.6
2	7.5	1.6	8.206	3.3
3	10.0	2.2	8.210	3.7
4	18.1	3.9	8.329	0.9
5	28.0	6.1	8.329	0.6

A schematic of the experimental set-up can be seen in figure 3.4. Leakage neutron spectra have been detected with the time of flight (TOF) method by a fast scintillator detector (p-terfenil + FEU-143) at an angle of 8° to the deuteron beam direction in a distance of 6.8 m. The neutron detector has been placed inside a lead enclosure behind a concrete wall with an opening. For background measurements, a 1 m long iron shadow bar has been placed between the test sphere and the detector.

The neutron detector has a time resolution of 3 ns and background γ-ray suppression. Its efficiency has been determined using a Cf-252 fission chamber and the bare neutron source.

The SINBAD data for this benchmark experiment contains MCNP input files created for the original evaluation, which describe the geometry, material, and neutron source. Since the geometry is fairly simple, it is hard-coded into the Geant4 geometry description subroutine.

The iron spheres have some slight impurities, which are modelled in the MCNP material description. In table 3.2, the material composition of the spheres is displayed. Same as for the geometry, the material description is converted and hard-coded into the Geant4 geometry description subroutine.

Simakov et al. (2000) have also found a discrepancy between a standard MCNP calculation of the energy spectra ("time-independent") and a MCNP calculation which properly simulates the time-of-flight method by tracking the travelling time of the neutrons and then converting from travel-time to energy ("time-dependent"). They have hypothesised that the non-negligible size of the test sphere in comparison with the distance between test sphere and detector, in particular when scattering in the test sphere causes time-delays, is the reason for this discrepancy.

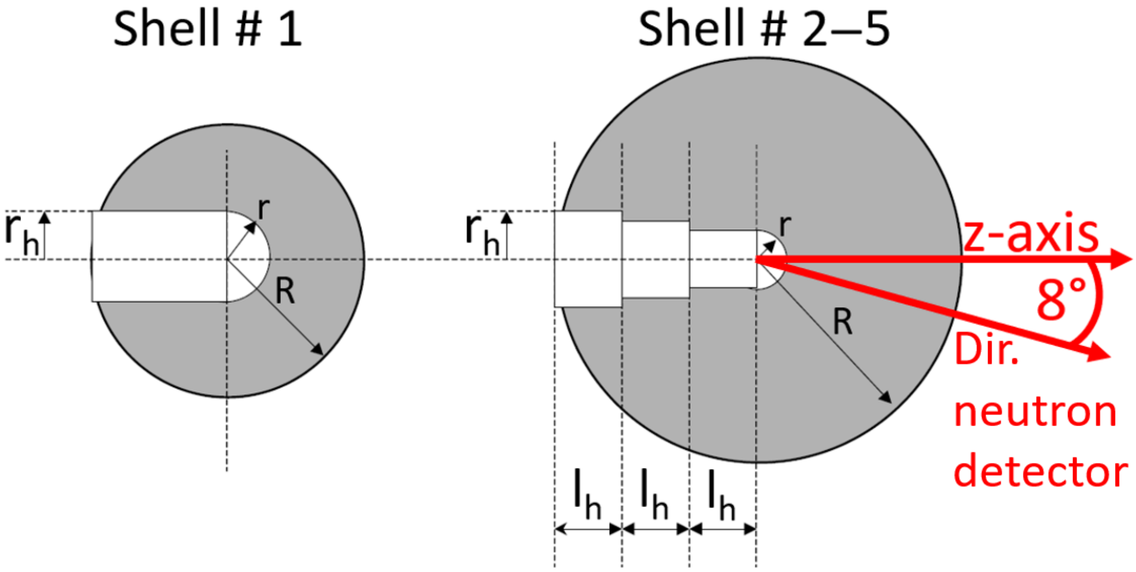

No	Shell Radii		Hole Configuration
	R, cm	r, cm	$r_h(l_h)$, cm
1	4.5	2.0	2.0(2.5)
2	12.0	4.5	3.2(4), 3.0(3.5)
3	12.0	2.0	3.2(4), 3.0(3.5), 2.0(2.5)
4	20.0	1.9	2.5(10.3), 1.9(7.8)
5	30.0	2.0	4(7), 2.5(7.8), 2.0(13.2)

Figure 3.3: A schematic of the five sphere configurations used in the SINBAD IPPE benchmark (edited from Simakov et al. (2000)). The sizes are listed in the table below.

A correction function $C_t(E)$ has been calculated out of the leakage spectra obtained with the time-independent $L(E)$ and the time-dependent $L(E(t))$ MCNP technique:

$$C_t(E) = \frac{L(E)}{L(E(t))} \quad , \tag{3.7}$$

and has been applied to the experimental results, so that a time-independent result for the use in comparisons is available.

The neutron detection is implemented in the MCNP representation using the point-detector tally. For a point detector tally, a deterministic calculation is performed for every source and particle interaction during the run to estimate the probability of hitting a defined point in the geometry in the next step. It takes into account the probability of being scattered into the right solid angle and the probability of being scattered away on the way to the defined point. The contributions of all events are added up to form the final result (Brown et al., 2003).

In a geometry such as the SINBAD IPPE benchmark where the detector area is small and positioned far away from the source, the point detector tally makes it possible to arrive at a viable solution with less particle histories. A variation of the point detector tally is the ring detector tally. In this case, the probable contribution is calculated for a sampled point on a predefined ring around one of the x, y, or z coordinate axes. This method is used in the MCNP input files provided by SINBAD.

A ring with radius R_{Ring} denoted by an 8°-angle off the z-axis at the distance D_z is used to make use of the rotational symmetry. As the distance $D = 679\,\mathrm{cm}$ between source at (0,0,0) and detector is the hypotenuse of the right-angled triangle further consisting of the ring radius R_{Ring}, and the distance along the coordinate axis D_z, the values for defining the ring detector can be calculated like this:

$$R_{Ring} = D \cdot \sin(8^\circ) \quad , \tag{3.8}$$

$$D_z = D \cdot \cos(8^\circ) \quad . \tag{3.9}$$

The point detector functionality is not available in baseline Geant4. Instead, higher numbers of particle histories are used to produce sufficiently low statistical errors.

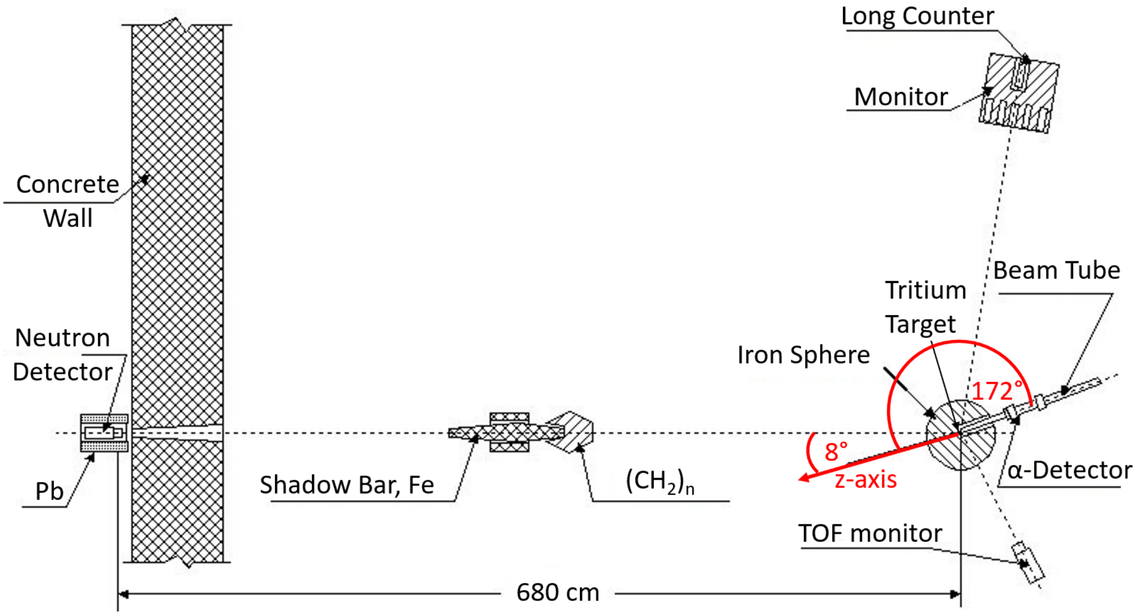

Figure 3.4: Schematic of the experimental set-up of the SINBAD IPPE benchmark (edited from Simakov et al. (2000)). The shadow bar has only been used for the background measurement.

Table 3.2: The material composition of the spheres of the SINBAD IPPE benchmark.

	Atomic Fraction		
Isotope	Sphere 1	Sphere 2 & 3	Sphere 4 & 5
Fe-54	0.0589	0.0585	0.0584
Fe-56	0.9152	0.9089	0.9083
Fe-57	0.0209	0.0208	0.0208
Fe-58	0.0028	0.0028	0.0028
Cnat	0.0022	0.0015	0.002
Cr-52		0.0030	
Mn-55		0.0045	0.005
Si-28			0.00249
Si-29			0.00013
Si-30			0.00008

The Geant4 detector volume is described by a tube placed along the deuteron beam direction at the previously calculated distance D_z, with inner radius R_{inner}, outer radius R_{outer} and height h. The values for these are:

$$\begin{aligned} R_{inner} &= D \cdot \sin(8^\circ) - R_O \quad , & (3.10)\\ R_{outer} &= D \cdot \sin(8^\circ) + R_O \quad , & (3.11)\\ h &= 0.1\,\mathrm{cm} \quad . & (3.12) \end{aligned}$$

As Geant4 does not allow stand-alone surfaces, the volume needs to have a height h and it is set like this to be negligible compared to the source-detector distance. The standard G4PSPassageCellCurrent scorer is used to detect the particles passing through this volume.

Leakage spectra $L(E)$ are calculated by integrating the scored neutron energy spectra $N(E)$ over the full sphere (4π) and normalising to one source neutron, using the detector solid angle $\mathrm{d}\Omega$ and the number of histories N_n:

$$L(E) = \frac{4\pi\, N(E)}{\mathrm{d}\Omega\, N_n} \quad , \tag{3.13}$$

with

$$\mathrm{d}\Omega = \frac{A}{D^2} \quad , \tag{3.14}$$

where A is the detector surface area, this yields

$$L(E) = \frac{4\pi\, N(E)\, D^2}{A\, N_n} \quad . \tag{3.15}$$

MCNP automatically normalizes for surface area A and number of histories N_n. For Geant4 these normalisations are performed as part of the post-processing. The detector surface area A is calculated like this:

$$A = \pi(R_{outer}^2 - R_{inner}^2) \quad . \tag{3.16}$$

The next post-processing step is to fold the previously calculated leakage spectra with the detector response function. Simakov et al. (2000) determined this detector response function, which accounts for the detector time resolution and the interactions of the neutrons with the collimator in the detector shield, by comparing the experimental and MCNP-calculated energy spectra for the bare neutron source at the detector angle 8° (see figure 3.5). The 14.1 MeV peak and the broad 0.2–5 MeV range, which is caused by inelastic scattering on the target assembly, are well reproduced in the MCNP calculation, but in the 5–12 MeV energy interval there is a discrepancy, which is resolved by the detector response function.

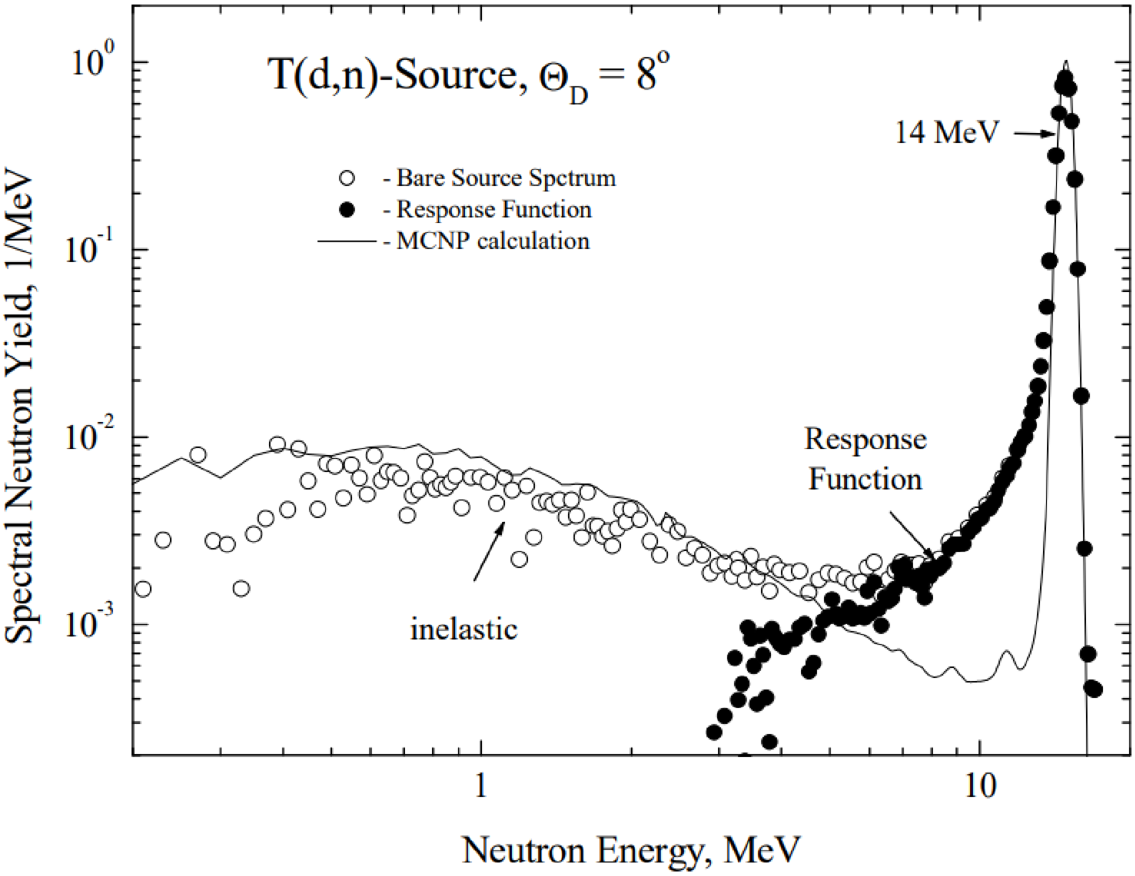

Figure 3.5: Comparison of the experimentally measured spectrum of the bare neutron source, and the MCNP calculation. The detector response function was used to correct the discrepancy (Simakov et al., 2000).

Finally, the spectra are integrated over larger energy steps and $Calculation/Experiment$ (C/E) ratios are calculated for these values.

3.2.2 Tritium Production in Test Blanket Module Experiment

Tritium self-sufficiency is an important requirement for a future fusion power plant. Therefore, reliable neutronics calculations of the tritium production efficiency for the considered breeder blanket concepts is mandatory. Due to this, the choice for the second validation benchmark is an irradiation experiment which has been performed at the Frascati Neutron Generator (FNG) by Batistoni et al. (2007) to measure the tritium production in a mock-up of the Helium Cooled Pebble Bed (HCPB) type Tritium Breeder Module (TBM). An MCNP representation of the experiment has been created and is available from SINBAD. This representation is translated for Geant4.

In figure 3.6, a schematic of the HCPB TBM mock-up is displayed. The mock up consists of a stainless steel box of external dimension 310 mm x 290 mm x 310 mm filled with horizontal layers of the neutron multiplier beryllium and the breeder material lithium carbonate separated by stainless steel plates. Metallic beryllium with major impurities O = 0.88 wt%, Fe = 0.16 wt%, and C = 0.075 wt% and powdered Li_2CO_3 of $> 99\,\%$ purity and natural Li-6 enrichment (7.5 % Li-6 and 92.5 % Li-7) are used. The rear breeder part is simulated by a second stainless steel box of dimension 310 mm x 148 mm x 310 mm which is also filled with lithium carbonate. These boxes rest on an aluminium table.

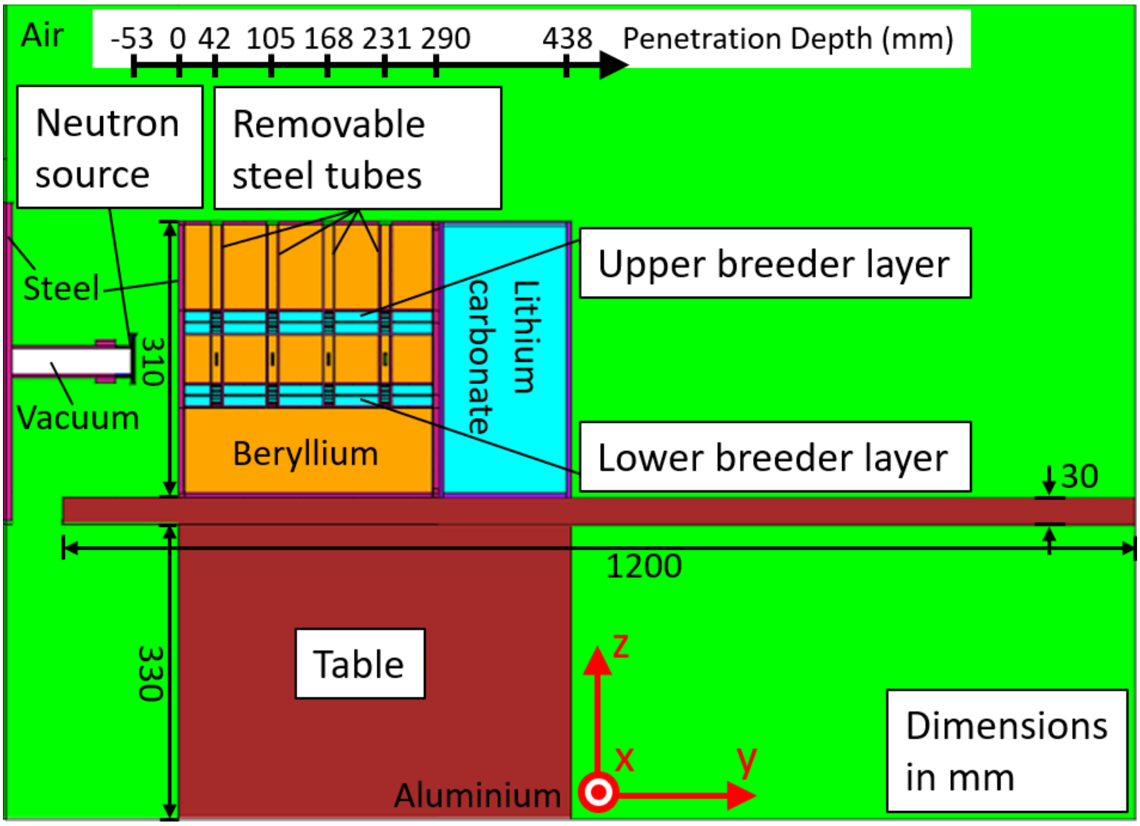

Figure 3.6: Schematic of the HCPB TBM mock-up, the FNG neutron source, and the aluminium table used in the experiment created from the MCNP geometry representation with the MCNP plotting tool.

The neutron generator is positioned at a distance of 53 mm from the centre of the front of the box. The total number of neutrons produced during the irradiation has been measured with an α-particle detector, a niobium foil located on the centre of the front surface of the breeder box, and two perpendicularly placed niobium wires in the same position. The wires have been used to check the source alignment by cutting them into segments and detecting the activation in each segment. This way, it has been detected that the breeder box is shifted 3 mm upwards with respect to the position of the neutron source. The result of $5.834 \cdot 10^{15}$ neutrons detected with the α-particle detector deviates only 1.02 % from the Nb foil result and only 0.98 % from the Nb wire result.

The neutrons produced by the source penetrate into the breeder box along the y-axis. At four different penetration depths, stacks of twelve breeder pellets are placed in the upper and the lower breeder layer using removable steel tubes. A schematic with close-ups of this part is displayed in figure 3.7. The pellets are numbered from 1 to 12 with 1 corresponding to closest to the central axis and 12 to furthest away. At the same penetration depths, activation foils consisting of niobium, gold, aluminium, and nickel are placed at the centre of the middle beryllium layer.

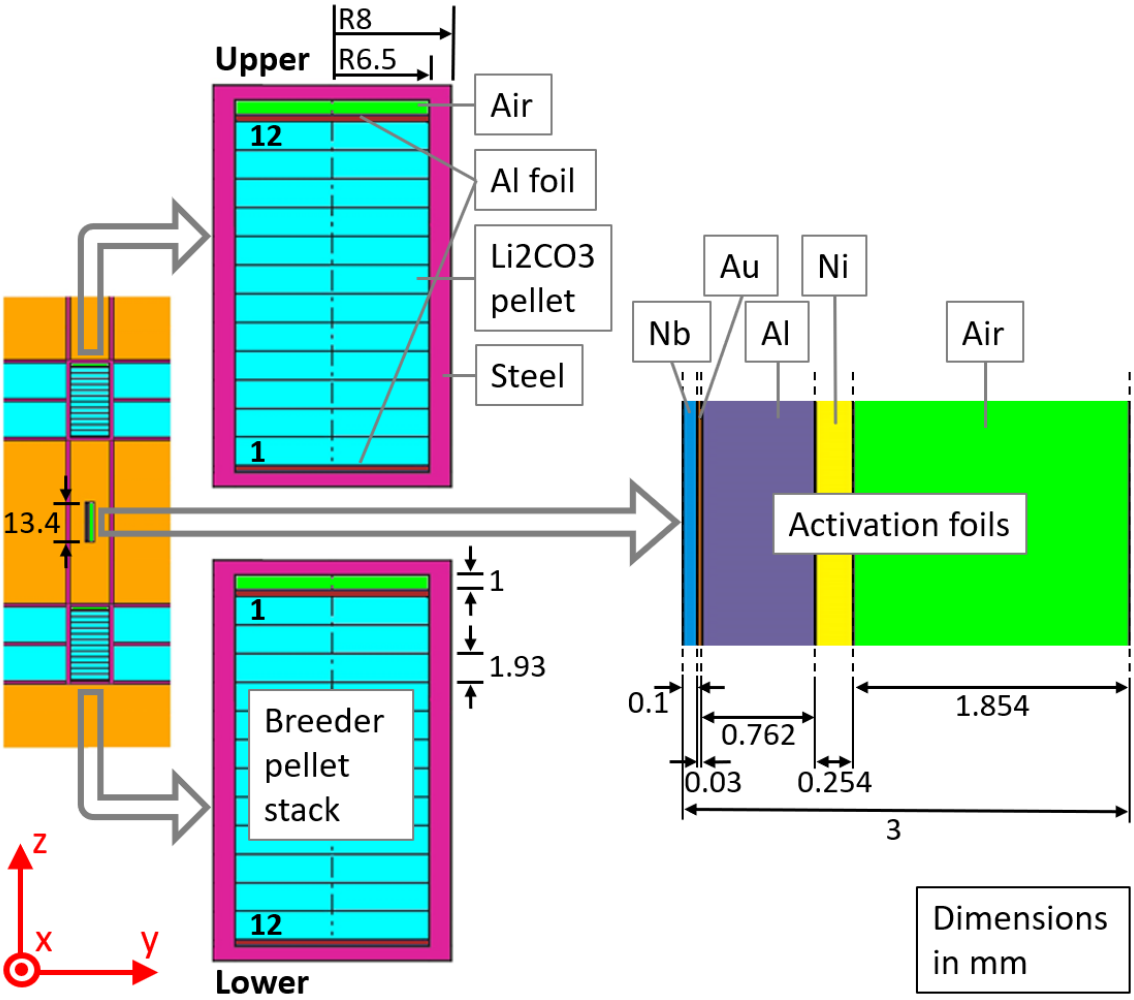

Figure 3.7: Schematic of the HCPB TBM mock-up breeder and beryllium layers with breeder pellet stacks and activation foils (modified from several schematics provided by SINBAD (Kodeli et al., 2014)).

The measurement of the reaction rates in the activation foils has been performed after the irradiation. Both the activation foils and the breeder pellets have been removed out of the mock-up. The activities of the foils have been measured in the FNG laboratory with HPGe detectors. The reaction rate value is given as the number of activated nuclei divided by both the total number of nuclei in the material and the total number of irradiation neutrons. The total relative experimental errors due to counting statistics, detector calibration, and FNG source calibration have been determined to be $\pm 4.1 - 4.7\,\%(1\sigma)$.

The activation foils have been chosen to monitor different energy ranges of the neutron flux. The (n,γ) reaction of Au-197 is strongest at low energies, while the other three cross-sections have an energy threshold. Due to this, Au-197 can be used to monitor low energy neutron flux, the (n,p) reaction of Ni-58 and the (n,α) reaction of Al-27 with thresholds at 0.4 MeV and 3.25 MeV can be used to monitor fast neutron flux, and the (n,2n) reaction of Nb-93 with a threshold at 8.93 MeV can be used to monitor the uncollided neutrons.

The measurement of the tritium activity in the breeder pellets has been divided among three groups: The upper layer breeder pellet stacks have been measured at Technical University Dresden (TUD), the lower layer breeder pellet stacks have been measured by ENEA (Italian National Agency for New Technologies, Energy and Sustainable Economic Development) and individual pellets of both layers have been measured by JAEA (Japan Atomic Energy Agency). The pellets have been dissolved

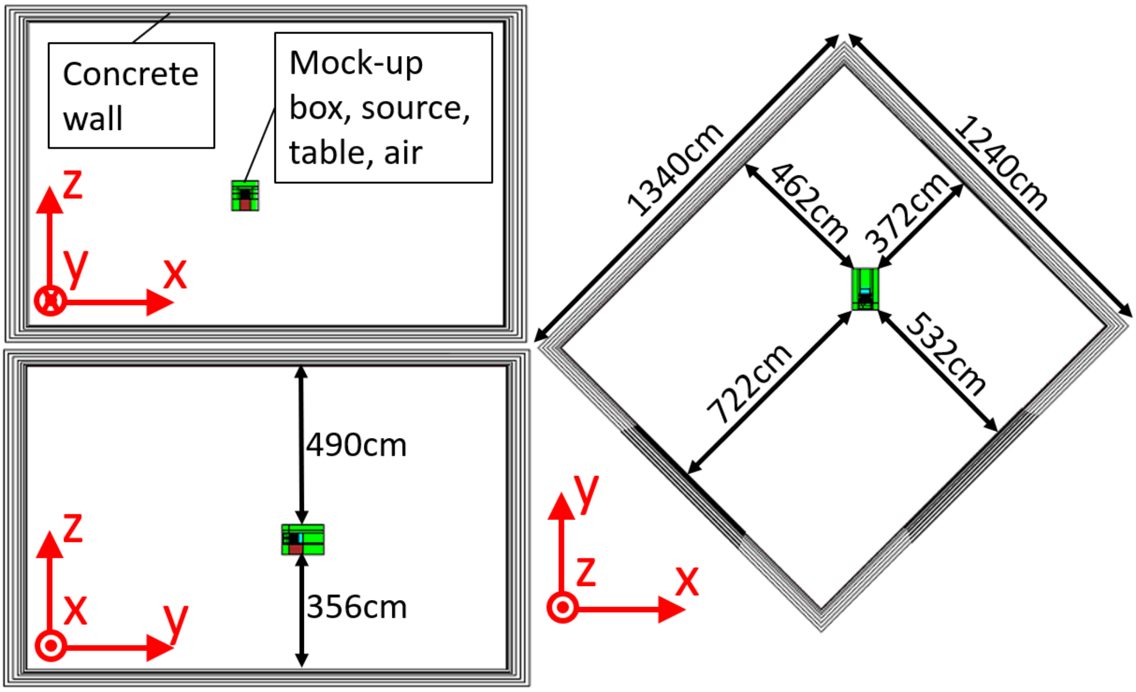

Figure 3.8: Schematic of the HCPB experimental chamber created from the MCNP geometry representation with the MCNP plotting tool.

in an acidic solution containing a scintillator and the tritium activity has been measured by β-counting. The detection efficiency has been determined by comparing the obtained results with those measured in a mixture of unirradiated Li_2CO_3 powder and distilled tritiated water of known activity. The combined total relative uncertainty of the experimental procedure has been given as 4.8 $\%(2\sigma)$ by ENEA, 5.4 $\%(2\sigma)$ by TUD, and 6.4 $\%(2\sigma)$ by JAEA. This represents the combination of factors such as the uncertainty of sample weight and the random error of β-counting.

The MCNP geometry representation and the conversion for Geant4 is described in the following.

The geometry of fusion reactors such as DEMO is developed in the CAD (Computer-Aided Design) format. During development, there is a cycle of design iterations and neutronics calculations. To perform calculations for a new design, it has to be converted into the internal geometry format of the neutronics code.

Regularly converting complex geometries consisting of a large number of often irregular shapes by hand is not feasible due to being time-consuming and holding the risk of introducing errors. Therefore, automatic geometry conversion programs such as McCad (Lu et al., 2017) or MCAM/SuperMC (Wu et al., 2015) have been developed to convert the design geometry from the CAD format into the internal format of Monte Carlo codes like MCNP.

As part of a previous PhD work by Qiu (2016), a new geometry format called the HalfSpaceSolid has been developed for Geant4, which imports the MCNP approach of defining volumes by the combination of the positive/negative half-space next to surfaces. Additionally, McCad has been expanded by Qiu et al. (2016) with the capability to convert from CAD to a HalfSpaceSolid-based or tesselated geometry description in the GDML (Geometry Description Markup Language) format, which can be read in by Geant4. GDML is an application independent geometry description format. The GDML scheme and the Geant4 GDML parser have been extended for the half-space solid type.

For the current benchmark, the geometry description in the MCNP input file has been created by Batistoni et al. (2007) and is available through SINBAD (Kodeli et al., 2014). In figure 3.6, the MCNP representation of the breeder mock-up box and its close surroundings including the aluminium support on which it rests, and the target geometry of the FNG source can be seen. The detected shift between the breeder box and the neutron source is included in this representation. Figure 3.8 shows how the concrete walls of the experimental chamber and the positioning of the mock-up is simulated. Only the air close to the mock-up is included in the simulation, further out it is replaced by vacuum, since it has little effect on the simulation results.

Since a CAD-formatted version of this geometry description is not available, the MCNP input file first has to be converted to CAD format using the SuperMC code (Wu et al., 2015). SuperMC also supports the conversion all the way into the GDML format, however, it does not manage to convert this geometry set-up in its entirety, leaving out several parts. Therefore the geometry conversion has to continue in another way.

The CAD geometry produced by SuperMC is loaded into the SpaceClaim program for inspection. Batistoni et al. (2007) have divided the mock-up and rear block of the geometry in concentric rings around the y-axis and layers in y-direction, probably for variance reduction purposes. Since this is not necessary for the current application, the geometry is simplified by adding up adjacent volumes of the same material. This makes the geometry more clear for inspection and also cuts down on computation time during the particle tracking. Then, the conversion into the GDML format for Geant4 is performed using McCad. A detailed description of the implementation of the GDML geometry representation in Geant4 can be found in appendix B.2.

The MCNP-formatted material description given in the SINBAD-provided MCNP input file is converted into a Geant4-formatted material representation and into GDML syntax. This is entered into the materials section of the GDML input file.

The recording of data in MCNP according to Brown et al. (2003) is using the track length estimate of cell flux tally. The current neutron energy E, the weight W, and the track length $TL(E)$ of all neutrons travelling through the cell are recorded in the simulation. The average flux $\bar{\Phi}_i$ for an energy bin i is estimated by summing up the contributions of all tracks in the cell volume V with energy within the lower energy threshold E_{il} and upper energy threshold E_{iu} like this:

$$\bar{\Phi}_i = \frac{1}{V} \sum_{E_{il}<E<E_{iu}} W \cdot TL(E) \quad . \tag{3.17}$$

MCNP also automatically normalises the final result to the number of calculated neutron histories N_{hist}, so that the final result is $\bar{\Phi}_i/N_{hist}$. In this case $W = 1$ for all particles, because neither variance reduction methods nor any source settings are affecting the weight.

This standard track length tally can be modified with the tally multiplier function of MCNP to calculate the reaction rates in the activation foils. This is done by multiplying the track length $TL(E)$ of all detected particles with the energy dependent reaction cross-section value $\sigma_{act}(E)$ of the relevant reaction of the respective activation foil to get the reaction rate R_i in the energy bin i:

$$R_i = \frac{1}{V \cdot N_{hist}} \sum_{E_{il}<E<E_{iu}} W \cdot TL(E) \cdot \sigma_{act}(E) \quad . \tag{3.18}$$

For the breeder pellets, the track length tally is further modified to calculate the number of tritons X^{Li-6} produced out of Li-6 per neutron history N_{hist} for the neutron energy bin i like this:

$$X_i^{Li-6} = \frac{n_{Li-6}}{N_{hist}} \sum_{E_{il}<E<E_{iu}} W \cdot TL(E) \cdot \sigma_{Li-6}(E) \quad . \tag{3.19}$$

It is using the number density n_{Li-6} of Li-6 in the breeder pellet material, and the nuclear cross-section $\sigma_{Li-6}(E)$ of the tritium producing reaction of Li-6. In contrast to the activation foil calculation, no volume normalisation is performed. The number of tritons X_i^{Li-7} produced out of Li-7 within the neutron energy bin i is calculated in an equivalent way.

In post-processing, the specific tritium activity A_i^T of energy bin i in a pellet is calculated like this:

$$A_i^T = \frac{N_{tot}\lambda_T(X_i^{Li-6} + X_i^{Li-7})}{m_{pellet}} \quad , \tag{3.20}$$

with the total number of emitted neutrons N_{tot}, the tritium decay constant λ_T, and the pellet mass m_{pellet}.

When converting the data recording for Geant4, several available approaches provided by Geant4 have to be considered. The standard data recording routines called Primitive Scorers map most closely onto the suite of tallies in MCNP and are used for the code-to-code benchmarks and the transmission through iron spheres benchmark.

The Primitive Scorer classes cannot be used for the current benchmark. On the one hand, the large number of over 100 detector volumes each of which with over 100 energy bins cause problems with the run-time memory when using Primitive Scorers for data collection. On the other hand, the tritium activity in the pellets and the reaction rate in the activation foils has to be calculated. MCNP is doing this with its track length tally in combination with the tally multiplier function, which multiplies the detected particle track length in a volume with an energy-dependent cross-section factor before performing the energy binning, as can be seen in equation 3.18 and 3.19. Since this function is not available in the Geant4 Primitive Scorer classes, other detector options have been investigated.

In addition to the Primitive Scorer classes, Geant4 offers a more flexible tallying functionality: the Sensitive Detector class. The user can set up their own Sensitive Detector type class according to the provided basic structure. They can define which physical quantities should be recorded when a particle track is passing through an associated geometry volume during particle transport.

Two Sensitive Detector classes are created: the first is for the detection of track length supporting the multiple energy bin structure available for MCNP tallies and alleviating the run-time memory issues. The second is based on the first and additionally implements the tally multiplier function. So far, no automatic processing of ENDF-formatted data is included. Instead, data is processed into files which are read in by the code during the run. For the Li-6 and Li-7 tritium producing reaction, data processed from JEFF-3.3 is used and for the activation foil reaction rates dosimetry data from IRDFF-v.1.05 (Zsolnay et al., 2012) is used. Details of the development of these two Sensitive Detector classes can be found in appendix B.3.

The GDML syntax provides the auxiliary information function to add keywords to volume definitions. This is used to mark the volumes for which data should be recorded during the run. Different keywords are used for breeder pellets and the different types of activation foils. The Geant4 application is edited to pick up these keywords and assign the associated type of Sensitive Detector to the volumes.

For Geant4, only the part within the sum of equation 3.18 and 3.19 is calculated during the simulation. The intermediate results are written out at the end of the run and the calculation is finalised in post-processing.

Statistical checks for convergence testing are important to check the quality of the result of a MC simulation. They are already available as part of the Geant4 toolkit and have been modified and expanded to be more comparable with the statistical checks provided by MCNP. The development is described in more detail in appendix B.4.

For this benchmark, nearly all Geant4 and MCNP results pass the statistical checks for 10^{10} particle histories. For the four individual Geant4 results which do not pass, $3.5 \cdot 10^{10}$ particle histories are used.

3.2.3 Shielding and Variance Reduction Experiment

Shielding configurations to attenuate the radiation coming from the fusion plasma are designed to protect sensitive parts of the reactor such as the magnetic coils. Their efficacy has to be verified by neutronics calculations. The low number of particles reaching deep into a shielding configuration pose difficulties for the statistics of Monte Carlo tallies. To alleviate this issue, variance reduction techniques are applied.

For testing both Geant4's variance reduction capabilities and coupled neutron-photon transport, the SINBAD ITER bulk shield benchmark (Batistoni et al., 1999) (Freiesleben et al., 1998) is chosen as third experimental benchmark. It is on a deep penetration shielding calculation using a mock-up of the ITER bulk shield.

A schematic and a picture of the set-up of the ITER bulk shield mock-up are displayed in figures 3.9 and 3.10. According to Batistoni et al. (1999), along the penetration depth from the source, the mock-up consists of:

- A 1 cm copper layer simulating the first wall.
- A shielding block made of stainless steel AISI 316 type (SS316) plates (100 cm x 100 cm, thickness 4.4 cm–5.0 cm) and Perspex plates (100 cm x 100 cm, thickness 2.06 cm). These represent shielding blanket and vacuum vessel. According to analysed made by Batistoni et al. (1999), the steel has a chemical composition by weight fraction of 68.1 % iron, 16.8 % chromium, 10.7 % nickel, 2.12 % molybdenum, 1.14 % manganese, and below 1 % of silicon, copper, cobalt, vanadium, carbon, sulphur, phosphorus, tin, lead and boron respectively. Perspex has the chemical

formula ($C_5O_2H_8$)$_n$ and the sample tested by Batistoni et al. (1999) has a high degree of purity (all trace elements < 5 appm).

- A block with alternating copper and stainless steel plates (47 cm x 47 cm, thickness 2.2 cm) representing the toroidal field coil.
- A rear shield made of polyethylene to protect against backscattered radiation from the bunker walls.
- In two SS316 plates, lateral penetration allows to insert detectors in positions A and B. The remaining space is closed with form bricks made of SS316.
  - Position A is located at a penetration depth of 41.5 cm from the front, directly behind a 6 cm thick Perspex layer and represents the back plate of the shielding blanket.
  - Position B is located at a penetration depth of 87.6 cm and represents a position close to the boundary between vacuum vessel and toroidal field coils.

As can be seen in figure 3.10, the mock-up is located at the centre of the FNG bunker, on a movable tower at 4 m from the floor, and at a distance of 5.3 cm from the neutron source.

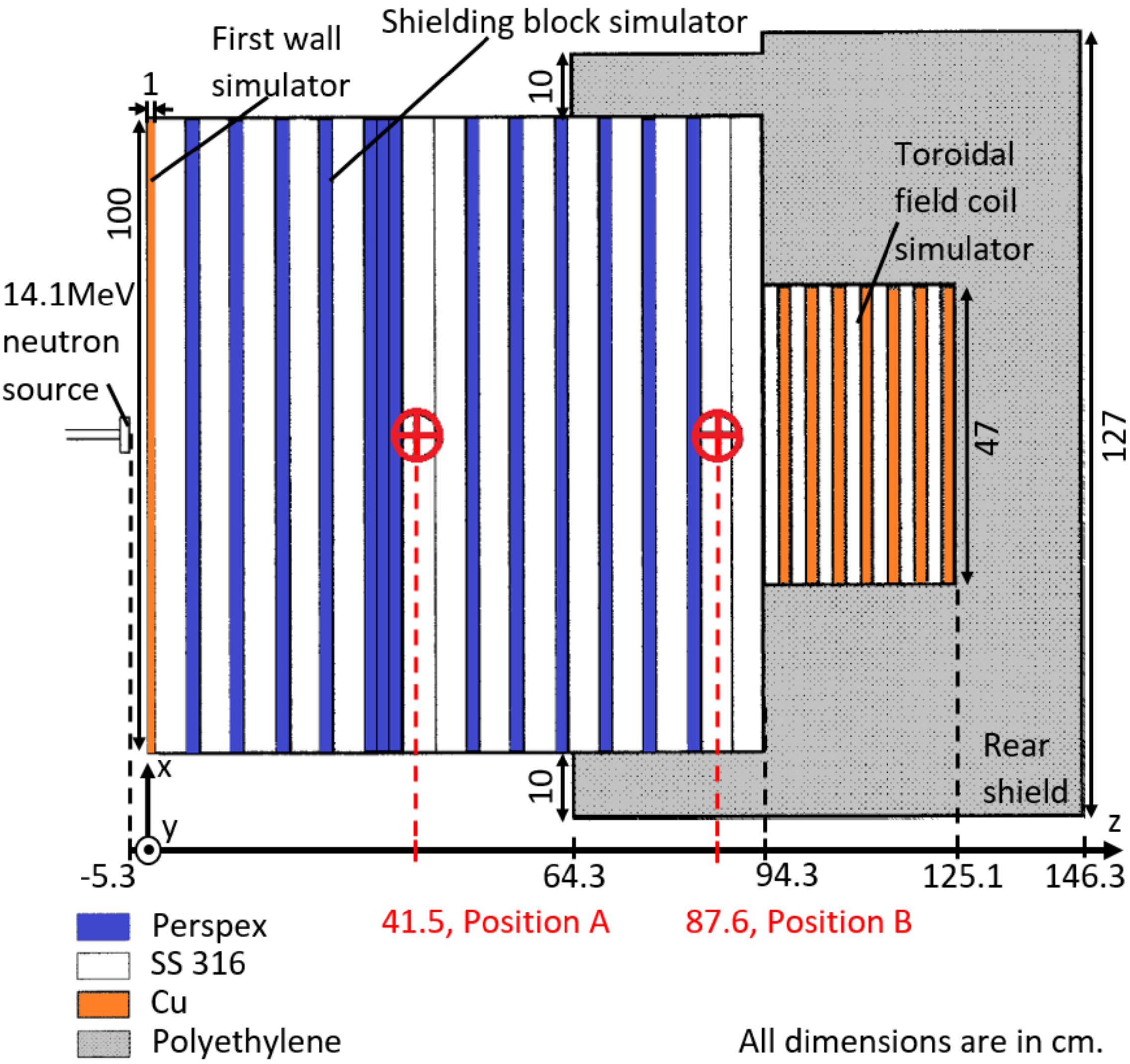

Figure 3.9: Schematic of the ITER bulk shield mock-up with positions A and B of gamma and neutron flux spectra measurements (adapted from Freiesleben et al. (1998)).

The FNG produces 10^{11} 14 MeV neutrons per second by accelerating deuterons onto a tritium target. The neutrons get most of their kinetic energy from the ensuing fusion reactions, which emit

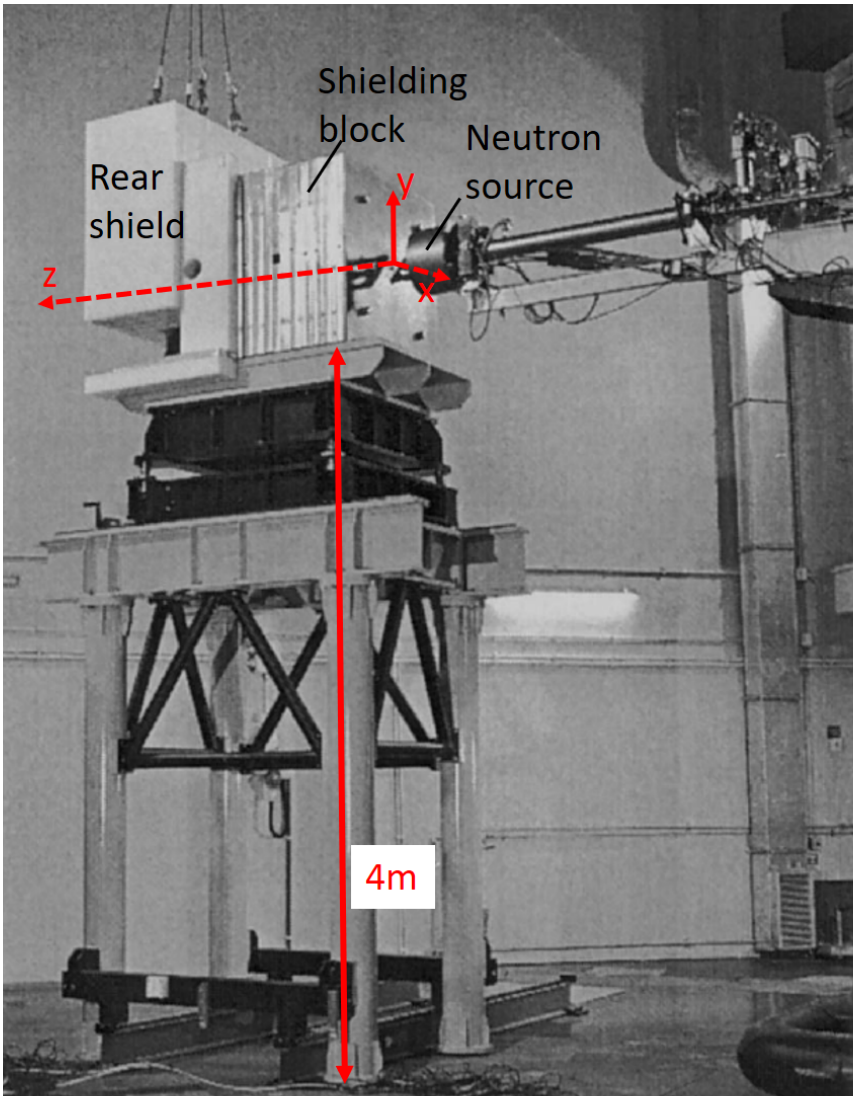

Figure 3.10: The ITER bulk shield mock-up experimental set-up at the FNG (adapted from Batistoni et al. (1999)).

neutrons isotropically. Therefore, the resulting neutron distribution is nearly isotropic. This has been measured through the associated α-particle flux with $\pm 2\,\%$ accuracy.

According to Freiesleben et al. (1998), a combination of multiple detectors has been used for the detection of the neutron and gamma flux spectra. This includes gas-filled proportional counters, a stilbene scintillation spectrometer, and a NE213 scintillation spectrometer. The obtained pulse height distributions have been unfolded to get the energy spectra of the fluxes, and have been normalised to one source neutron. Calculations with the MCNP-4A code and the FENDL-1 library have been performed to correct for different detector materials and geometries so that the results are for a 2 cm SS316 sphere at position A and B. In overlapping energy ranges, uncertainty-weighted averaging of different flux spectra has been performed.

The Monte Carlo Representation of the ITER Bulk Shield Experiment is available from SINBAD for MCNP and has been converted for Geant4. The representation of the FNG neutron source is described in section 4.2.3.

The data available from SINBAD contains a MCNP input file with a geometry description. To convert this for Geant4, first, the SuperMC code (Wu et al., 2015) has been used to convert the MCNP input file into CAD format and then McCad (Lu et al., 2017) has been used to convert it into HalfSpaceSolid-based GDML format. The conversion process is described in more detail in appendix B.2.

In the MCNP model, the detector positions are represented by spherical volumes inside of the steel slabs at the respective penetration depths. The resulting left-over slab volume with a spherical void in the middle causes issues for the Geant4 representation with HalfSpaceSolids. To work around this, the sphere volumes and the slab have been converted with reintegrated spheres separately. Then, a sphere cut-out has been edited into the slab volume using the GDML syntax in the GDML file.

Next, the material description in the MCNP input file has been converted for Geant4 according to the principles explained in section 2.4.5.

The JFFF-3.3 nuclear data library is used. TSL data for hydrogen in polyethylene and in light water is taken from JEFF-3.3 for MCNP, and from the standard G4NDL4.5 data, which is based on the ENDF/B-VII library, for Geant4.

For the tracking of the gammas in Geant4, the G4EmStandardPhysics physics list is used in addition to the NeutronHP package already used for the nuclear cross-section library based neutron transport.

The MCNP model has eight track length detector tallies: for each position "A" and "B" it has two neutron flux spectra, each with fine and with coarse ("integral") energy bins, and two gamma flux spectra, each also with fine and with coarse ("integral") energy bins. No tally multiplier is used. The neutron and gamma spectra have different energy bins, so 4 sets of energy bins exist in total.

For Geant4, the lists of energy bins are extracted and put into files to be read in by the code. Since no tally multiplication is required, one of the Sensitive Detector classes previously developed for the HCPB mock-up benchmark (see section 3.2.2) is used. The detector volumes are marked with aux type "SensDet" in the GDML file.

For the variance reduction, which is necessary for the shielding calculation, the MCNP input file contains a list of importance values associated with MCNP cells. These are transferred to the corresponding Geant4 volumes after the CAD and GDML conversion. The development of support for importance biasing for both neutrons and gammas, including a slight modification of the Sensitive Detector class is described in appendix B.5.

Implementations of importance biasing have been attempted based on two standard Geant4 implementation examples provided in the "/extended/biasing/" directory. The first is called "B01". However, it has become clear only neutron *or* gamma biasing is supported, not both at the same time. Since both are needed for the bulk shield benchmark, instead the general biasing "GB03" example has been adapted. For this, a problem has been found for combining the HalfSpaceSolid geometry representation with importance biasing. This problem could not be solved. Since it is the closest to a viable solution, the results for this implementation are presented. Suggestions for potential approaches to solve the remaining issues are made in appendix B.5.

3.3 Application to DEMO Nuclear Analysis

The final step of the evaluation of Geant4's suitability for nuclear design analyses of the DEMO reactor is the application of the code to a DEMO neutronics calculation. The successful application shows Geant4's ability to handle large, complex geometry descriptions automatically converted from CAD. To make this possible, additional functionalities have been added to Geant4 such as the reflective boundary function, which is also tested during this application. Furthermore, Geant4's support of flexible, programmable source descriptions is shown by the representation of the DEMO plasma neutron source.

The development process of the DEMO design and important integrated parts like the breeder blankets go through iteration steps. Neutronics calculations are to be performed in each step to assess whether the design fulfils the requirements. One key design requirement is tritium self-sufficiency, which is quantified by the TBR being sufficiently larger than unity. Several different breeding blanket concepts currently under development internationally and in Europe aim to achieve this goal. To compare the different European blanket types, a baseline EU DEMO model with an empty blanket area is produced in CAD format for new DEMO design iterations. The empty space can then be filled with different blanket types.

As a final confirmation of Geant4's usability and reliabilty for such a routine DEMO design application, a calculation previously performed with MCNP is reproduced and evaluated. For this, the EU DEMO with HCPB breeder blanket modules integrated into the baseline 10° sector model is used. The neutron flux spectrum in the blanket volumes and both the spectral contributions to the TBR and the total TBR result are calculated. This set-up has been previously developed for MCNP and has been analysed by Pereslavtsev et al. (2017). It is using the DEMO BL2015 design iteration as described by Hernández et al. (2020). In figure 3.11 the CAD model of this DEMO sector is displayed.

3.3.1 Geometry Representation of the DEMO Reactor

The rotational symmetry of fusion power plants can be used to reduce the calculation time of neutronics calculations by representing the full power plant by a sector. One can imagine this like representing a cake by a slice of it. The symmetry of the power plant dictates the minimum size of such a sector. For stellarator types, the sectors have to be fairly large due to the poloidal twist in the magnetic field and the resulting variation in the shape of the magnetic field coils. For tokamak types, the magnetic field is uniform, which allows smaller sectors. The minimum sector size depends on the toroidal field coil size and additional geometry structures like port placement. In the case of the DEMO model used in this thesis, the sector size is 10°.

The practice used in MCNP is to define the cut-layers of the sector model as reflective boundaries, so that particles cannot leave the geometry in a non-physical way. Since an equivalent standard method for Geant4 does not exist, this functionality has been developed and integrated into the Geant4 application. For this, a standard Geant4 subroutine has been used, which governs the reflection and transmission behaviour of optical photons at material boundaries called G4OpBoundaryProcess. It was modified to work on any type of particle and to perform a specular reflection at the surface of any volume with a trigger name. This new subroutine is called MyBoundaryProcess.

In the usual reactor case, there are two reflective boundary surfaces at the sides of the slice. The geometry description of the reactor has to be modified to include two box volumes placed so that their side surfaces are at the two planes where the reflection is required. The box volumes are named "Reflector1" and "Reflector2". These trigger names are picked up by the code. The normal vector of the boundary surfaces required for reflection is hard-coded into the subroutine. If other reactor configurations with a different placement of boundary surfaces are used in the future, these normal vectors have to be changed.

The correct behaviour of MyBoundaryProcess has been tested for different incidence angles in a simple geometry set-up using a point source and a reflecting box and also observed for a number of individual particles in the final DEMO reactor set-up. The final validation is the use in the DEMO analysis to obtain results consistent with MCNP.

Since the design and development process of the breeder blanket undergoes many iteration steps, a full CAD representation of the internal breeder structure is not produced. For MCNP, the repeated structure technique is used instead, which allows to fill geometry volumes with repeating patterns. This way, a representation is created which may not be fully correct from an engineering point of view, but is correct enough for neutronics calculations while cutting down significantly on development time. For

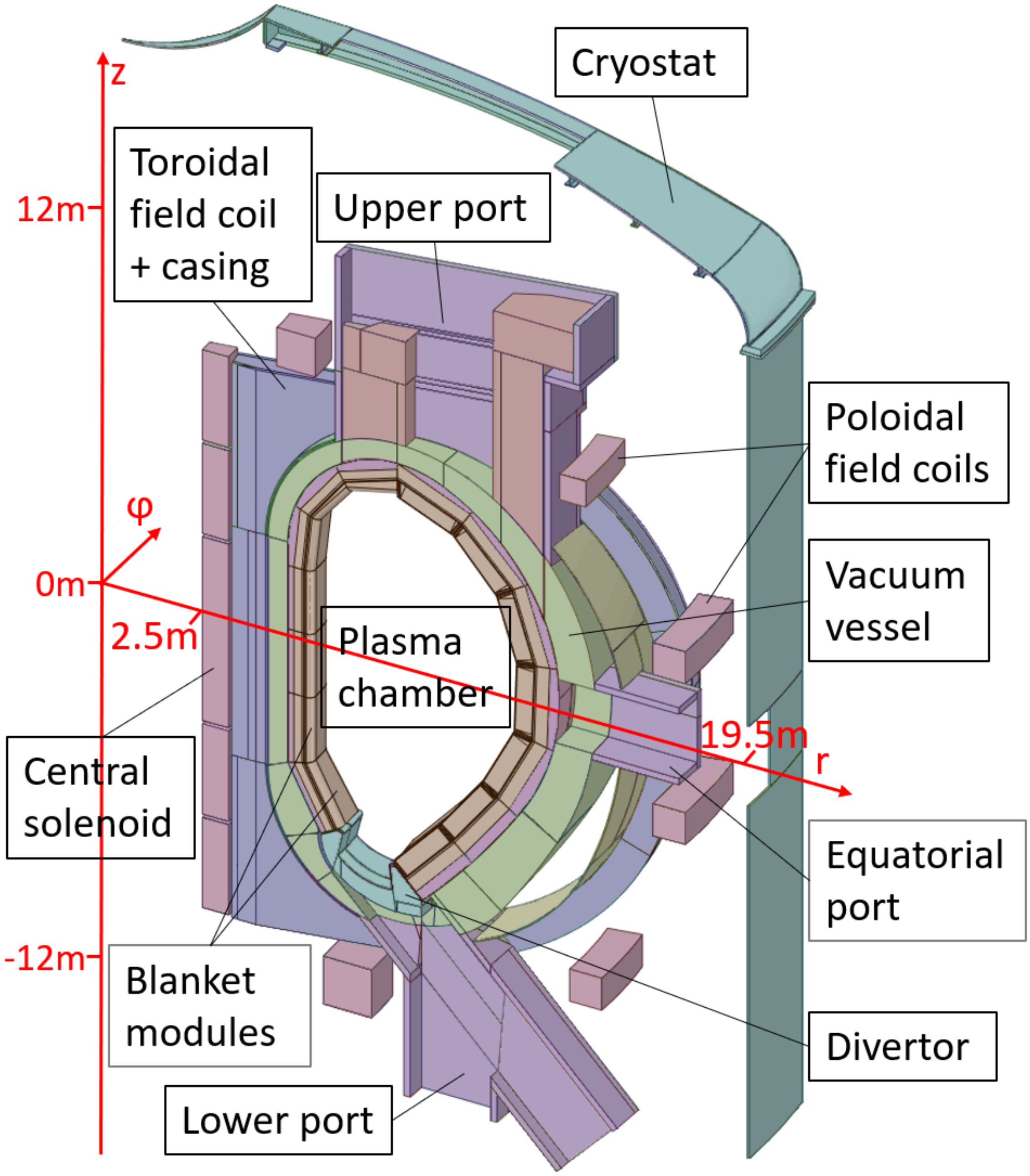

Figure 3.11: The CAD representation of the EU DEMO 10° sector model adapted by Pereslavtsev et al. (2017) to include the HCPB breeder blanket boxes.

this reason, a CAD representation exists only for an individual blanket module, which can be seen in figure 3.12.

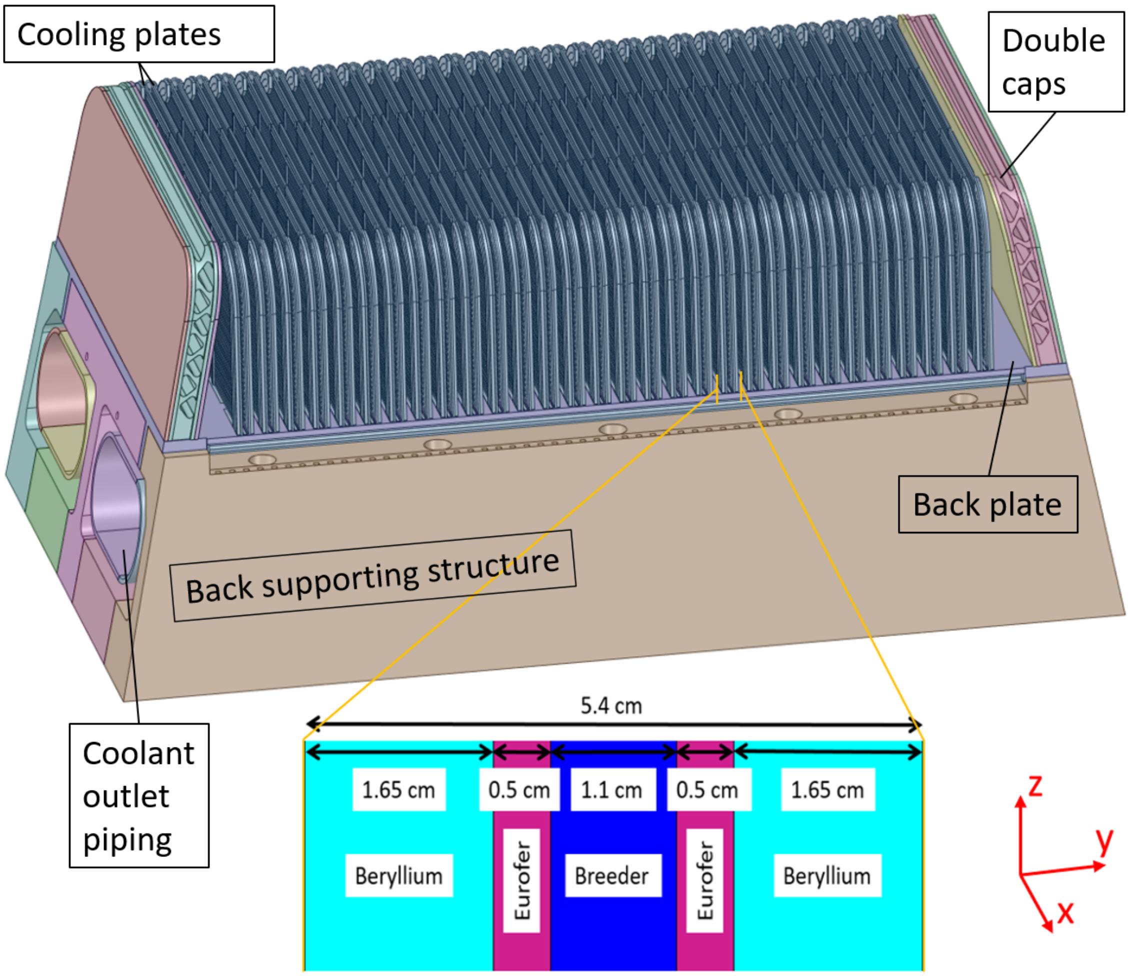

Figure 3.12: The CAD representation of a HCPB breeder blanket box. The front wall and tungsten armour is removed to expose the internal breeder structure. Descriptions of components are taken from Hernández et al. (2017). The MCNP representation of the breeding volume as repeating layers of beryllium neutron multiplier, eurofer steel cooling plates, and $LiSO_4$ breeder material is shown (Nunnenmann et al., 2020).

The basic CAD DEMO model only contains the outer bounds of the breeder area. This has been modified by Pereslavtsev et al. (2017) to contain the blanket boxes, including their back structure, front plates and parts at the ends which are filled with neutron multiplier. They have used the repeated structure method to represent the layers of breeder material and neutron multiplier separated by eurofer type steel plates at the front of the breeder.

For this thesis, most of the reactor geometry including the breeder blanket boxes are converted with the McCad conversion tool (Lu et al., 2017) from the CAD format into GDML format. The only problem encountered in the conversion process is the torus shape of the magnet shield layer, which causes issues in the HalfSpaceSolid representation. As this part is located further outwards from the plasma than the breeder blankets, it should not make a significant difference for the TBR calculation and is therefore left out of the geometry.

Two different modelling solutions are created for both codes: First, the part of the geometry which contains the repeated structure in the existing MCNP representation is filled with a *homogenised* version of the material in both the MCNP and the Geant4 representation. This is expected to return inaccurate TBR results, but allows a comparison between Geant4 and MCNP independent of the repeated structure issue.

Second, a repeated structure representation has been developed for Geant4 to create a *heterogeneous* model. The way MCNP describes geometry by boundary surfaces allows to extend and repeat the schematic shown in figure 3.12 until it meets a boundary. This way, a volume can be easily filled completely.

Geant4 has a hierarchical geometry representation, which means child volumes can be placed multiple times inside parent volumes. This makes it possible to repeat a geometry pattern. However, in contrast to MCNP, there is no automatic cut-off at the parent volume boundary layer and the user has to make sure child volumes do not protrude outside the parent volumes. Any protrusion can confuse the particle tracking during the run.

Geant4 provides the replicated volume method for repeating shapes in 1D, which works well with the breeder blanket plate layers. This is only available for the basic Geant4 shapes and the breeder blanket boxes created by Pereslavtsev et al. (2017) for the MCNP input have irregular shapes to best fill out the available blanket space. Consequently, the irregular shapes of the repeated structure part of all the breeder boxes have to be represented by basic Geant4 shapes which could then be filled with the repeating breeder layers.

In figure 3.13, the three steps are displayed. First, the breeder volume is converted with McCad into a GDML HalfSpaceSolid representation. Second, basic Geant4 shapes are chosen to fill this volume. The G4Tubs type is used to create partial cylinders to fit the round edges and one big and two smaller G4Box volumes are used to fill the leftover cuboid areas. Third, these basic Geant4 shapes are filled with the repeating breeder layers.

As Geant4's replicated volume function allows no partial repeats and also the parent volume has to be completely filled, the lengths can only take on values of integer multiples of the schema thickness. The resulting dimensions of the basic shapes fit to multiple breeder volumes and therefore can be placed multiple times. Due to the varied breeder volume shapes several different sizes are necessary.

All of this is done in the GDML file using the GDML syntax.

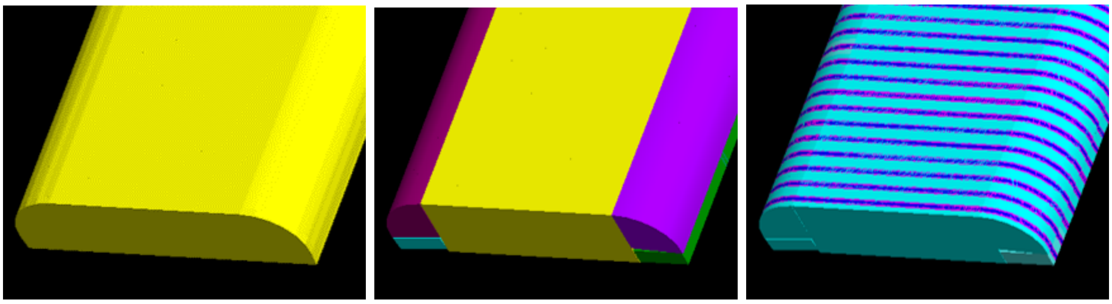

Figure 3.13: The converted HalfSpaceSolid representation of the breeder volume (left), the basic Geant4 shapes used to fill the breeder volume (middle), and the same shapes filled with the repeating breeder layer structure (right). Middle and right were previously published in Nunnenmann et al. (2020).

The most long-winded part of the process is the placement of the basic Geant4 shapes so that they fill the volume as fully as possible but still do not protrude. Usually, Geant4 basic shapes have an internal coordinate system and centre. When a child volume is placed inside, this happens automatically in reference to this coordinate system. This makes it simpler to place child volumes along the axes of symmetry. In the HalfSpaceSolid representation, the volumes can take on more irregular shapes, which makes axes of symmetry unfeasible. However, as a future development, it would be helpful to include a definition of a centre of mass in the syntax, which could automatically be calculated as part of the geometry conversion. With this, future geometry adaptations would be made somewhat simpler.

For the current geometry conversion, the general position and rotation of the individual breeder volumes is extracted from the CAD file in SpaceClaim and then more finely adjusted for the contained basic Geant4 shapes using the Geant4 OpenGL plotter for visual inspection.

The irregular shape of the breeder volumes cannot be fully filled with basic Geant4 shapes. It is theoretically possible to create a large number of small shapes to fill any remaining gaps, but in combination with the issues of placement without overlaps this has been considered too time-consuming. Instead, the leftover space is filled with homogenised material. The amount of leftover space varies between the different blanket volumes depending on the irregularity of their shape. In total, 91.6 % of the volume of all breeder volumes is filled with the repeating structure representation.

This time-consuming approach which did not fill 100 % of the volume with repeated structure is used in this thesis to make the exploration of Geant4's reliability in calculating the TBR possible. For future routine use, it would not be feasible, even with the centre of mass calculation included. This is an unsolved issue. A potential approach for a solution might be to develop a pre-processing program which creates repeated structure in the GDML HalfSpaceSolid syntax for individual volumes. The resulting pieces of syntax could then be copied into the McCad converted GDML file at the correct positions. This way, the ability of the HalfSpaceSolid representation to represent irregular shapes could be used. However, this approach would make the GDML file longer and increase the already high number of detector placements, because it would create an even larger number of independent breeder volumes into which a detector would have to be placed.

3.3.2 Detection of Neutron Flux and TBR in the DEMO Reactor

Both neutron flux spectrum averaged over the breeder volumes and the TBR are detected. The calculation of the neutron flux in the breeder volumes is performed in MCNP with the track length estimate of average cell flux tally, which calculates the average flux in a cell according to equation 3.17 by dividing the track length by the volume of the cell (Brown et al., 2003).

For the MCNP heterogeneous set-up, this volume only consists of the breeding zones, while for the homogenised set-up of both codes, the whole breeder volume is used. For the mostly heterogeneous set-up of Geant4, the average neutron flux results of the homogenised and the heterogeneous parts are individually divided by the associated volume and then added up to obtain the total result.

For the display of flux spectra, the results in individual energy bins are also divided by lethargy like this:

$$\bar{\Phi_i}^* = \frac{\bar{\Phi}_i}{ln(E_i/E_{i-1})} \quad , \tag{3.21}$$

using the upper and lower energy bin threshold E_i and E_{i-1}.

For further analysis, the ratio between the flux spectrum results in the heterogeneous and the homogenised set-up is calculated for both Geant4 and MCNP. Additionally, the ratio between the Geant4 and the MCNP flux spectrum result is computed.

The integral TBR equation (see 1.8) is estimated by the MC technique by summing up contributions of particle histories. In MCNP, the track length estimate of average cell flux tally is combined with the tally multiplier function, similar as for the calculation of tritium production in section 6.2. The tally multiplier function multiplies the detected track length $TL(E)$ with the energy-dependent cross-section value $\sigma(E)$ of the tritium producing reaction and the number density n of either of the lithium isotopes Li-6 and Li-7. The results are added up for both lithium isotopes and divided by the total number of calculated neutron histories N_{hist}:

$$TBR = \frac{1}{N_{hist}} \left(n_{\text{Li-6}} \sum_{i=1}^{N_{hist}} \sigma_{\text{Li-6}}(E) \cdot TL_i(E) + n_{\text{Li-7}} \sum_{i=1}^{N_{hist}} \sigma_{\text{Li-7}}(E) \cdot TL_i(E) \right) . \tag{3.22}$$

For the TBR, a spectral distribution is also produced by using the energy binning in MCNP and dividing by lethargy as in equation 3.21.

For the Geant4 representation, the newly developed Sensitive Detectors discussed for the HCPB experimental benchmark (see section 6.2) are used. Again, the auxiliary information function of the GDML syntax is used to add keywords to volume definitions to mark the volumes for which data should be recorded during the run. Both the average neutron flux spectrum and the Li-6 and Li-7 contribution to the TBR are detected. For the heterogeneous set-up, the heterogeneous and homogenised contributions to flux, Li-6 and Li-7 results are added up separately to enable comparative analysis. The summing up and multiplying with pre-factors to calculate the resulting TBR is performed in post-processing.

The statistical checks introduced in section HCPB are used to choose a high enough number of particle histories in the calculation, so that a satisfactory quality of the MC results is achieved.

Chapter 4

Neutron Source Representation and Conversion

For Monte Carlo simulations of neutron transport, every simulated neutron needs to have a set of defined starting conditions: the initial position in the geometry, the initial momentum direction, and the initial energy. For fusion applications, a code needs to be able to represent different types of neutron sources such as the plasma in a fusion power plant or the accelerator based neutron generators of irradiation experiments.

MCNP offers two ways of representing a neutron source: using an SDEF (source definition) card in the MCNP input file for inputting data sets and choosing between many different interpolation and sampling options, or programming a source subroutine which is compiled along with the code. Geant4 provides the same level of flexibility. There are standard sampling functions available, and it is also possible for the user to program their own source subroutine.

4.1 Creation of Simple Sources

The code-to-code benchmarks use simple neutron sources. In this case, only descriptions are available, so the sources are produced for both Geant4 and MCNP without any conversions.

4.1.1 Beam Neutron Source

For the Single Interaction Code-to-Code Benchmark (see section 3.1.1), the source is created using the GeneralParticleSource function in Geant4. Macro commands in the input file are used to create a neutron beam along the z-axis by setting the particle type to "neutron", putting a point source at (0,0,-100 cm), and setting the momentum direction to (0,0,1).

The probability distribution of the neutron energy is using the same structure which is used as bins for the results. In section 3.1.1, the way of calculating the 1000 isolethargic energy bins (see equations 3.2–3.3) and the probability distribution (see equation 3.4) is already described.

The values for the energy and corresponding probability points are calculated and written into a text file. Macro commands in the Geant4 input file are used to read in the data from the file and define the interpolation as linear.

The MCNP version has been created with a source definition (SDEF) card in the MCNP input file. Source position, momentum direction and particle type are set to the same constant values as for Geant4. For the energy probability distribution, the source information card is used to define the same energy points and the source probability card is used to define the same corresponding probability density points as used in Geant4.

4.1.2 Isotropic Neutron Source

For the Multiple Interaction Code-to-Code Benchmark (see section 3.1.2), the neutron source is created for Geant4 in the PrimaryGeneratorAction subroutine using the ParticleGun method. The ParticleGun functions provide an interface for passing on the value of particle type, position, momentum direction, and energy for every new particle. The user is free to write any sort of sampling routine to produce these values. The particle type is set to "neutron", the position is set to be at the centre of the sphere at the origin of the coordinate system, and the energy is set to 14.1 MeV.

The Hadr04 example of Geant4 includes a sampling routine for an isotropic momentum direction distribution, which has been used for this problem. For every new particle, the polar angle θ and azimuthal angle φ of a spherical coordinate system are calculated using two independent random numbers created by Geant4's random number generator. The random number generator creates random numbers in the range [0,1) which is translated into the range [-1,1) for $\cos(\theta)$, [0,1) for $\sin(\theta)$, and [0,2π) for φ according to:

$$\cos(\theta) = 2 \cdot random1 - 1 \quad , \tag{4.1}$$

$$\sin(\theta) = \sqrt{1-\cos^2(\theta)} \quad , \tag{4.2}$$

$$\varphi = 2\pi \cdot random2 \quad . \tag{4.3}$$

Then, the momentum direction in x, y, and z-direction is calculated as:

$$u_x = \sin(\theta) \cdot \cos(\varphi) \tag{4.4}$$

$$u_y = \sin(\theta) \cdot \sin(\varphi) \tag{4.5}$$

$$u_z = \cos(\theta) \quad . \tag{4.6}$$

The MCNP version is created with an SDEF input card. Position, energy and particle type were set the same as in Geant4. An isotropic momentum direction distribution is the default for this type of source.

4.2 Neutron Source Conversion for Experimental Benchmarks

All experimental benchmarks use the same type of neutron generator. Neutrons are created by accelerating deuterium nuclei onto a titanium-tritium target so that a fusion reaction happens between deuterium and tritium nuclei. A schematic of this is displayed in figure 4.1.

4.2.1 Transmission Through Iron Spheres Neutron Source

For the transmission through iron spheres benchmark experiment (see section 3.2.1) performed by Simakov et al. (2000) at Institute of Physics and Power Engineering (IPPE), Obninsk, Russia, the MCNP input files in the SINBAD package include a source description in the SDEF format. The source is identical for all five iron sphere shells used in the experiment.

The MCNP version has the geometry positioned so that the deuterons are coming in along the x-axis in positive x-direction. For simplicity's sake, this has been changed for Geant4 to the z-axis in positive z-direction (as shown in figure 4.1). This has been done, because in Geant4, geometric bodies which are not entirely rotationally symmetric like for example cylinders or cones are aligned along the z-axis by default. Furthermore, this coordinate transformation aligns the geometry with a standard spherical coordinate system which makes the source configuration easier to describe.

With the deuterons coming in along the z-axis in positive z-direction, the tritium target is positioned perpendicular to it in the x-y-plane at the origin. This is described by sampling the starting position of the source particles uniformly on the $z = 0$ surface within a circle of radius $R_c = 3$ mm around the origin, which represents the radius of the deuteron beam. For Geant4, this has been implemented by setting $z_{pos} = 0$, sampling x_{pos} and y_{pos} in the range $[-R_c, R_c]$ and rejecting any values where $x_{pos}^2 + y_{pos}^2 > R_c^2$.

Simakov et al. (2000) used the time of flight (TOF) method and an aluminium activation foil to measure the angular distribution along the polar angle θ of the mean energy of neutrons leaving the source, and the yield of uncollided neutrons and compared it with MCNP calculations. This is displayed in figure 4.2. This distribution is caused on the one hand by the target and target holder materials: the strongest attenuation of the yield happens at $\theta = 90°$ where the created neutrons have to travel the longest path through these materials. On the other hand, the momentum direction of the created neutrons has an anisotropy along the flight-direction of the deuterons (positive z-axis in the figure). There is a slightly higher probability for the created neutrons to be moving in the same direction as the deuterons. This causes the relative yield to be higher at $\theta = 0°$ and lower at $\theta = 180°$. The total (integrated over 4π) attenuation of the uncollided neutron yield is only $2.5\,\%$.

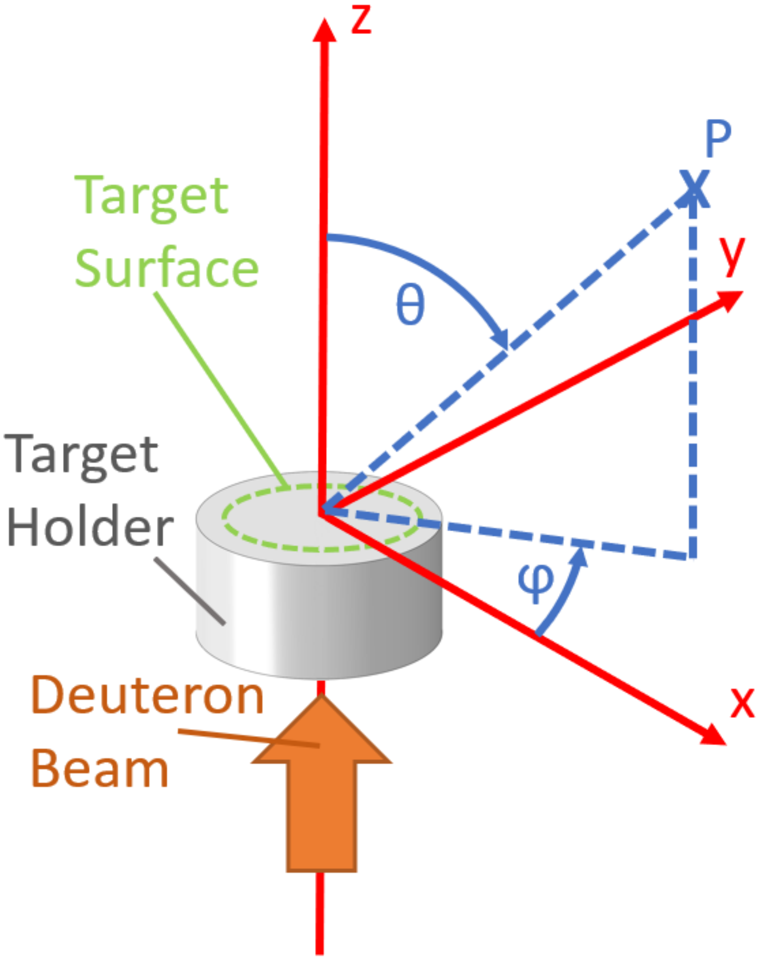

Figure 4.1: The geometry of the neutron source description of a neutron generator. The deuteron beam enters into the cup-shaped target holder and hits the titanium-tritium target surface which is located at the bottom of the cup. The polar angle θ and the azimuthal angle φ are used to describe the probability distribution of the neutron emission.

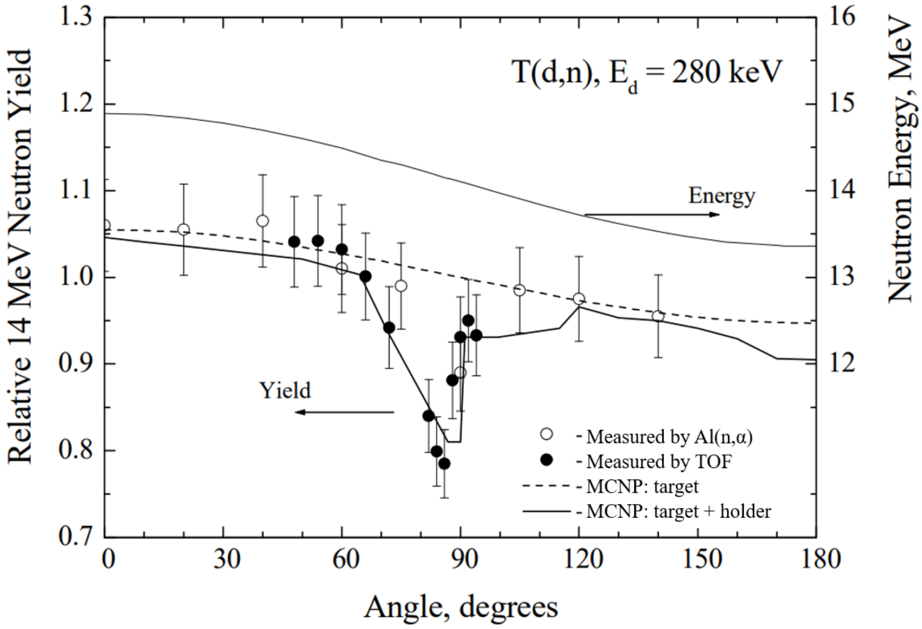

Figure 4.2: The 14 MeV neutron yield and mean energy versus polar angle θ measured in the IPPE experiment (modified from Simakov et al. (2000)).

As a result, the momentum direction distribution of the neutrons is anisotropic along the direction of the z-axis and isotropic perpendicular to it. Additionally, the initial energy of the neutrons is shifted a bit higher than the 14.1 MeV produced by the fusion reaction in direction of the positive z-axis and a bit lower in direction of the negative z-axis.

This is described in the MCNP SDEF card by a set of points of the cosine of the polar angle θ and corresponding probability density points with linear interpolation during sampling. Isotropic sampling is used for the azimuthal angle φ. Energy points corresponding to the polar angle cosine points are given in a dependent source distribution card. This means, that after sampling the linear interpolation factor for the polar angle cosine, the same interpolation factor is used to interpolate between the corresponding energy points.

For Geant4, the probability density values are normalised. The probability density and the energy are piece-wise linear functions of the cosine of the polar angle θ described by the values for probability density or energy at the interval edge points.

The linear interpolation between the interval edge points is calculated for probability density and energy, yielding an ordinate and a slope value for every interval i. These values are put into the PrimaryGeneratorAction subroutine of Geant4 along with the polar angle cosine points. For the sampling of the polar angle cosine the acceptance-rejection method as it is described in Rubinstein and Kroese (2016) has been chosen. This method is implemented in the Geant4 example /extended/eventgenerator/particleGun/2 from which it was modified to sample a value for the polar angle cosine and find the interval i into which it falls.

Then, the azimuthal angle is randomly sampled in the range [0,2π) and the values for x,y,z-direction set like previously described in equations 4.2, 4.4-4.6. The energy is calculated using the polar angle cosine and the energy y-intercept and slope of the same interval i.

4.2.2 Reliability of Tritium Breeding Estimation Neutron Source

For the Frascati Neutron Generator (FNG) used in the HCPB mock-up experiment (see section 3.2.2), a Fortran90 (F90) subroutine is available which describes the physical processes of the deuteron-target-interactions in much detail (Milocco and Trkov, 2008). This subroutine is complex and has more than 1500 lines of code which makes the conversion difficult. However, of interest is really the output of the subroutine: the particle position, energy, and momentum direction distributions. Recalculating these for every new run is unnecessarily consuming run-time. This means the effort of translating the source subroutine would not yield any significant benefits. Therefore, an alternative SDEF representation of the position, energy and momentum direction distributions is used instead. Čufar et al. (2016) had previously created an SDEF with 200 momentum direction steps and an energy distribution with 20 keV resolution for each step. To verify sufficient agreement between SDEF and F90 version, both MCNP versions have been subjected to the validation which is discussed in subsection 4.4.

The geometry of the HCPB mock-up is aligned so that the deuterons are coming in in positive y-direction. Therefore, the axes in the general schematic displayed in figure 4.1 have to be renamed: z becomes y, x becomes z, and y becomes x. The target is positioned in the x-z-plane and the deuterons are penetrating a little into it before the fusion reaction happens. This results in the initial position of the neutrons being sampled on a surface perpendicular to the y-direction in a circle with the radius of the deuteron beam (0.35 cm) around the position (0, 0.00005 cm, 0).

For Geant4, the position sampling routine described in section 4.2.1, has been slightly modified to sample x_{pos} and z_{pos} (instead of x_{pos} and y_{pos}) within a circle of defined $radius = 0.35$ cm. The y_{pos} is set to 0.00005 cm.

MCNP allows the user to enter a set of input parameters, which are then used in user-modified subroutines such as the F90 version of the source subroutine. The F90 subroutine is able to represent different configurations of a neutron generator such as different beam energies or whether the target has multiple layers or is very thin. The modelling can be modified to take relativistic kinematics into account or to track the resulting particles after fusion reactions such as α, He-3 or T. The input parameters which describe the FNG set-up used in this experiment are displayed in table 4.1.

Table 4.1: The input parameters for the F90 representation of the FNG.

parameter	value
beam energy	260 keV
position of beam central spot	(0,0,0)
beam width	0.35 cm
beam direction	(0,1,0)
number of target layers	1
relativistic kinematics	yes
track residual (α, He-3, T)	no
restricted emission angles	no
ultra thin target	no
D+ fraction	1.0
T+, D2+, T2+, TD+ fraction	0.0
activate T-T reactions	no

Regarding y as the zenith direction of a spherical coordinate system (as illustrated in figure 4.1), the representation of the momentum direction in the SDEF samples the cosine of the polar angle θ in the range [-1,1] according to a probability distribution, while the perpendicular directions are represented by the azimuthal angle φ which is sampled uniformly in the range [0,2π].

The SDEF representation of the FNG created by Čufar et al. (2016) is representing the probability distribution of the polar angle cosine in the SDEF in a different way than for the previous source in section 4.2.1. The polar angle cosine is divided into 200 bins with corresponding probabilities. First, a bin is sampled according to these probabilities and then the exact polar angle cosine is found by uniform sampling within the boundaries of the chosen bin.

To convert this for Geant4, the probability distribution has been processed in Excel. The total integral of the probability has been calculated by summing up the integrals of the individual bins. Then the probability in each bin has been normalised by dividing with the total integral. This data has been put into files, which are read into the PrimaryGeneratorAction subroutine of Geant4 during the run.

The current bin i is sampled using the acceptance-rejection method, which is described in section 4.2.1. Then, the current cosine of the polar angle $\cos\theta_i$ is sampled using another random number $random$ in the range [0,1], the lower bin boundary $\cos\theta_i^{lower}$, and the bin step $\Delta\cos\theta = 0.01$:

$$u_y = \cos\theta_i = \cos\theta_i^{lower} + random \cdot \Delta\cos\theta \quad . \tag{4.7}$$

This produces the momentum in y-direction. For the x and the z-direction, $\sin\theta$ is calculated using equation 4.2. The azimuthal angle φ is sampled in the range [0,2π] like in equation 4.3. Then, the momentum in x and z direction can be calculated:

$$u_x = \sin\theta \cdot \cos\varphi \quad , \tag{4.8}$$
$$u_z = \sin\theta \cdot \sin\varphi \quad . \tag{4.9}$$

The distribution of the initial energy of a source particle depends on the momentum direction of the outgoing neutrons. This is created in the SDEF by describing the energy with a dependent source distribution card. The energy is sampled from 115 equidistant bins in the range [13 MeV, 15.3 MeV] according to a different probability distribution for each of the 200 steps of the polar angle cosine. The sampling happens in the same way as for the momentum direction: First, a bin is sampled according to the probability distribution of the current momentum direction and then the energy is found by uniform sampling within the boundaries of the chosen bin.

To convert this for Geant4, all probability distributions have been again normalised in Excel, the resulting data has been written into files, and is then read into the PrimaryGeneratorAction subroutine of Geant4 during the run. For every probability distribution, the maximum probability is found and saved in an array. After the momentum direction step is found, the corresponding energy probability distribution is sampled with the acceptance-rejection-method to find the current bin, and then the energy is sampled within this bin similarly as described for the polar angle cosine in equation 4.7.

4.2.3 ITER Bulk Shield Neutron Source

Both the ITER bulk shield benchmark experiment (see section 3.2.3) and the HCPB mock-up benchmark experiment have been irradiated by the FNG. However, some parameter settings have changed between the two experiments: The beam energy for the ITER bulk shield is 230 keV instead of 260 keV for the HCPB mock-up and the deuteron beam width is 0.3 cm instead of 0.35 cm.

Čufar et al. (2016) kindly agreed to create another MCNP SDEF description based on these changed parameters. They used the same momentum direction steps, and finer energy steps of 10 keV width instead of 20 keV in the range of 13 MeV till 15.4 MeV. The data has been processed and the Geant4 source subroutine described in section 4.2.2 has been slightly modified to accommodate this new data.

4.3 DEMO Plasma Source Subroutine

For MCNP, there is a Fortran90 subroutine developed by Fausser et al. (2012) which describes the way neutrons are created by fusion reactions in the plasma of a DEMO reactor. The initial positions of the neutrons are distributed according to a density profile inside the plasma shape, the neutron emission is isotropic, and the initial energy is sampled from a Gaussian distribution around 14.1 MeV.

To calculate the spatial distribution of the neutron emission, the shape and density distribution of the plasma has to be defined. In magnetic confinement, there is a boundary surface called the last closed magnetic surface $LCMS$. Inside of it, the plasma is confined and the magnetic field lines are closed. Outside of it, the magnetic field lines connect to material surfaces so that plasma escapes. A cut along the r-z-plane of the plasma description is displayed in figure 4.3.

The density of the plasma is constant on magnetic surfaces MS, which are calculated using the following parameters: the major radius R_0 is the distance from the centre of the tokamak to the centre of the plasma. The minor radius A is the distance from the centre of the plasma to the outer edge of the $LCMS$. The height from the midplane of the plasma to the upper edge of the $LCMS$ is given by the elongation El multiplied with A. The distance by which the upper edges of the plasma are shifted inwards from the centre of the plasma is given by the triangularity δ multiplied with A.

In the table in figure 4.3, the paramter settings used in this thesis to define the plasma configuration are displayed. They can be entered through the MCNP input file. In addition to the parameters shown in the figure, it is possible to enter a vertical and horizontal shift. Furthermore, the plasma peaking factor has to be specified. It defines the shape of the density profile $\rho(A)$.

After the plasma shape is defined in radial and z-direction, the angular range $\Delta\varphi$ in toroidal direction has to be set to the extent of the used sector model or to 360° in the case of using a full tokamak model. During validation, the angular range is set to 11.25°, but for the simulation a 10°-sector model of DEMO is used, so this parameter is changed.

To make this source description available for Geant4, the Fortran90 version has been translated into C++. It is implemented into the standard source description subroutine of Geant4: PrimaryGenerator-Action. Since only this one version of a DEMO source is used for this thesis, the parameters have been

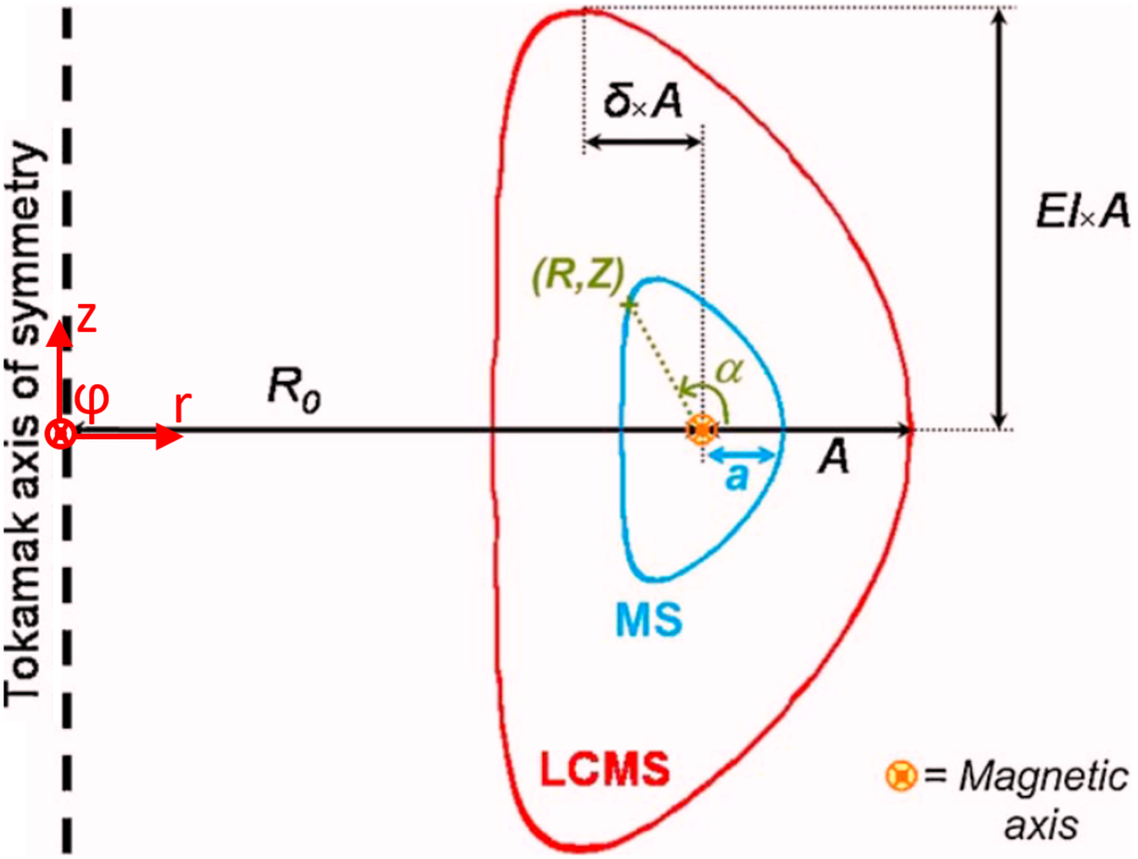

parameter	value
DD or DT	DT
temperature of plasma	15.4 keV
plasma major radius R_0	893.8 cm
plasma minor radius A	288.3 cm
elongation El	1.650
triangularity δ	0.333
plasma radial shift	0.0 cm
plasma peaking factor	1.508
plasma vertical shift	0.0 cm
starting angle φ_0	0°
angular range $\Delta\varphi$	10° (11.25° during validation)

Figure 4.3: A cut through the DEMO plasma in the r-z-plane (top) and a table of the parameters used in the Fortran90 representation of the plasma neutron source of the DEMO reactor (bottom). Shown is the last closed magnetic surface $LCMS$ which is characterised by the parameters major radius R_0, minor radius A, elongation El, and triangularity δ. Magnetic surfaces MS within the plasma are described by the reduced minor radius a and the poloidal angle α (Fausser et al., 2012).

hard-coded. If easily variable parameters become necessary for future uses, it poses no problem to add a messenger subroutine for reading in the parameters from an input file.

To illustrate the resulting neutron emission intensity distribution, the z-component of the distribution of the starting position is plotted against the radial component in figure 4.4. The gradient from the centre of the plasma towards the outer regions can be seen.

For the horizontal distribution, the coordinates are converted to $x = r \cdot \sin \varphi$ and $y = r \cdot \cos \varphi$. In figure 4.5, the y-component of the distribution of the starting position is plotted against the x-component, showing the sector of the torus for which the plasma neutron source is defined.

The general shape is similar between MCNP and Geant4 for both figures. Slight differences can be observed in individual bins. In the next section, analyses are performed to ensure these differences are merely statistical fluctuations.

4.4 Validation of the Converted Neutron Sources

In this section, the validation of the neutron sources converted for Geant4 from MCNP SDEF or MCNP source subroutine representations is described. The aim is to ensure the newly created Geant4 representation of the neutron sources are consistent with the original MCNP version. In the case of the SINBAD HCPB mock-up experiment described in section 4.2.2 and the SINBAD ITER bulk shield experiment described in section 4.2.3, there is both a F90 and an SDEF MCNP source version available. For the HCPB mock-up source description, both SDEF and F90 subroutine are routinely used, so the Geant4 results are compared with both. For the ITER bulk shield source description, the SDEF is only created as intermediary specifically for this thesis, so the comparison is done between the Geant4 result and the original F90 version. Furthermore, since the momentum direction is sampled isotropically in x- and z-direction and more complex in y-direction, the comparison was performed only for the y-direction.

The underlying principle for checking the agreement has previously been used by Häußler et al. (2016) for verifying the MCNP neutron source subroutine for stellarator-type fusion reactors. To investigate the agreement, the position, energy, and momentum direction of 10^8 to 10^9 source particles are recorded for the more complex newly created sources discussed in the previous sections. For MCNP, this is done with the PTRAC function and for Geant4 with a write to file command in the source subroutine.

A Fortran90 program is created which reads in the files with the source particle data, creates a binning structure and counts the hits per bin. The resulting histograms for MCNP and Geant4 are plotted against each other in OriginLab and a linear fit is performed to check the agreement. The acceptance criteria for a sufficiently consistent Geant4 version is that a linear fit with an ordinate of zero and a slope of 1 is achieved within the error range of the fit for reasonably fine bins.

As a first example, the resulting plots for the comparison of the energy distributions of the neutron source of the SINBAD HCPB benchmark are displayed in figure 4.6. The Geant4 version is compared with the MCNP SDEF version in the upper plot and the MCNP F90 version in the lower plot. It can be seen that the distributions are structured slightly differently, which is likely caused by the MCNP SDEF version and the Geant4 version based on it producing more discrete value ranges while the F90 version produces more continuous results. The overall agreement of the Geant4 version is good for both MCNP versions.

As a second example, the resulting plots for the comparison of the position and energy distributions of the DEMO plasma neutron source are displayed in figure 4.7. Here, both Geant4 and MCNP version are code based, so the resulting distributions are more continuous than the SDEF versions of the HCPB source energy distributions.

In table 4.2, the parameters of the fits are displayed for all sources. It can be seen that the criteria for consistency between Geant4 and MCNP results are achieved in all cases.

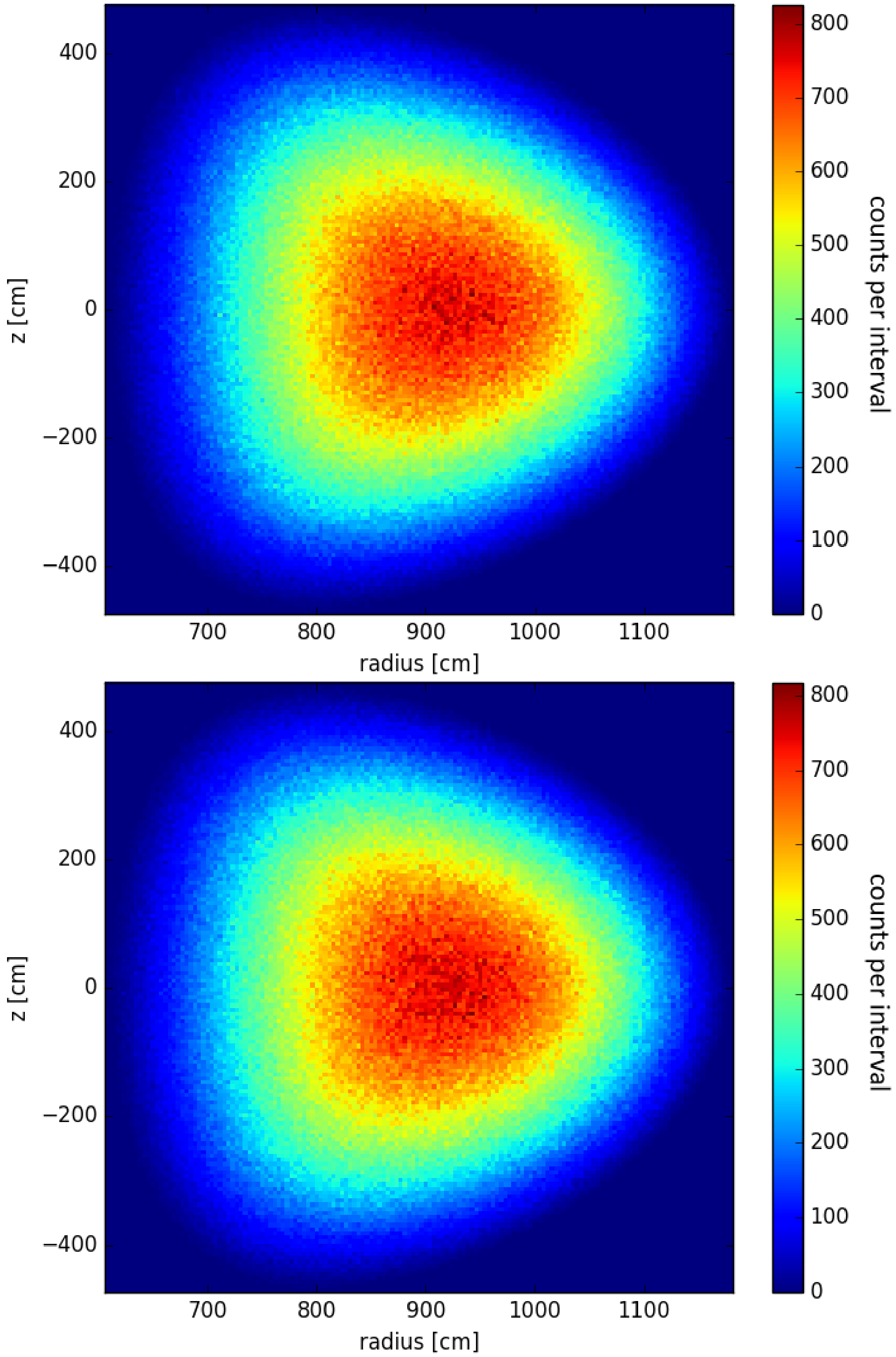

Figure 4.4: Distribution of the starting position of $5 \cdot 10^6$ source particles for the Geant4 (top) and MCNP (bottom) version of the DEMO reactor plasma neutron source subroutine. In each direction 150 intervals are used, leading to an increment of ≈ 3.8 cm in radial direction and ≈ 6.3 cm in z-direction.

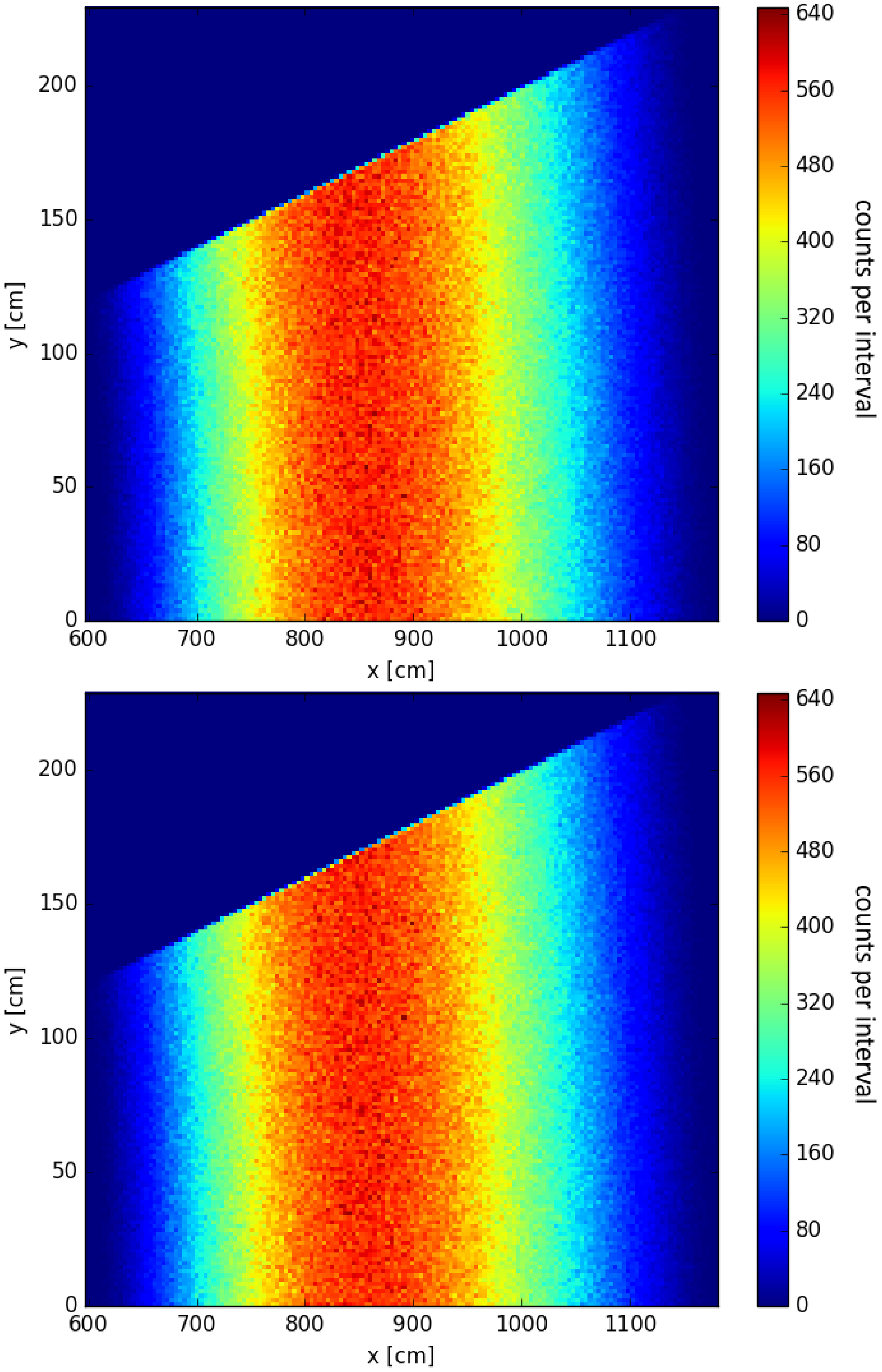

Figure 4.5: Distribution of the starting position of $5 \cdot 10^6$ source particles for the Geant4 (top) and MCNP (bottom) version of the DEMO reactor plasma neutron source subroutine. The coordinates are converted to $x = r \cdot \sin\varphi$ and $y = r \cdot \cos\varphi$. In each direction 150 intervals are used, leading to an increment of $\approx 3.8\,\mathrm{cm}$ in x-direction and $\approx 1.5\,\mathrm{cm}$ in y-direction.

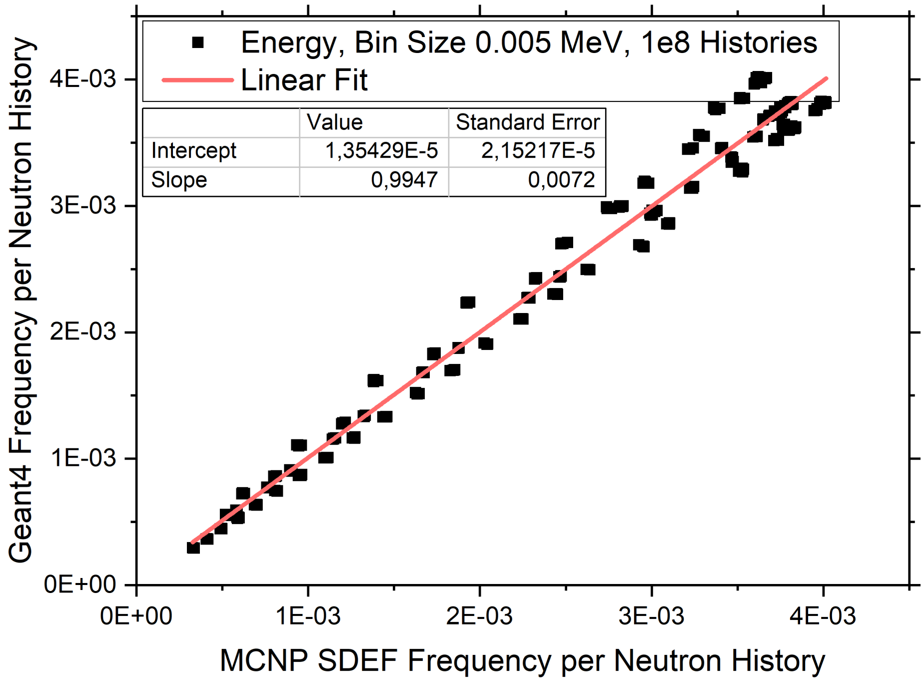

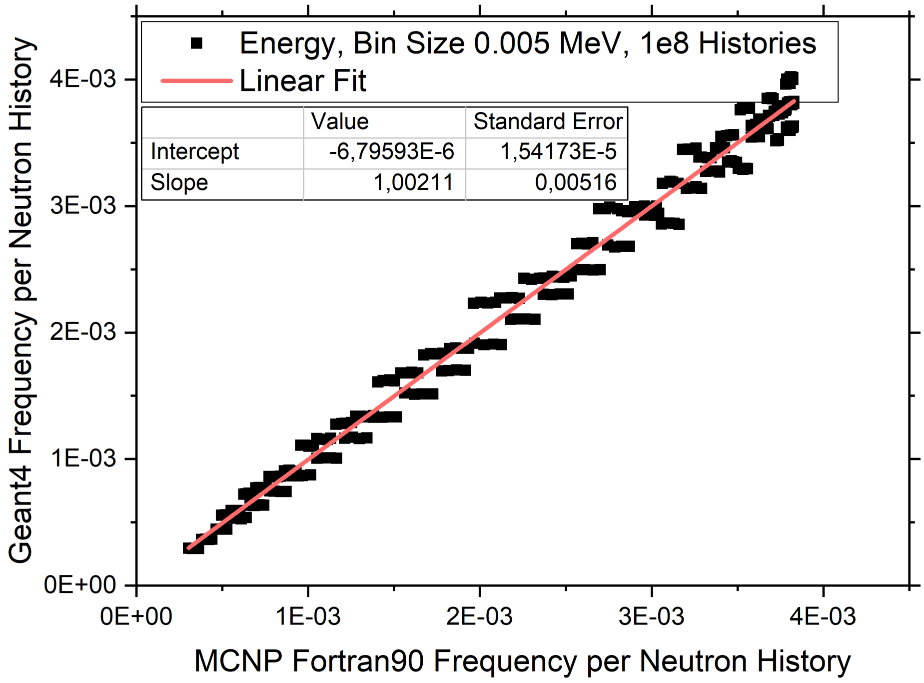

Figure 4.6: The neutron source conversion validation for the SINBAD HCPB benchmark experiment for the energy distribution of the Geant4 version compared with the MCNP SDEF version (upper plot) and the MCNP Fortran90 version (lower plot).

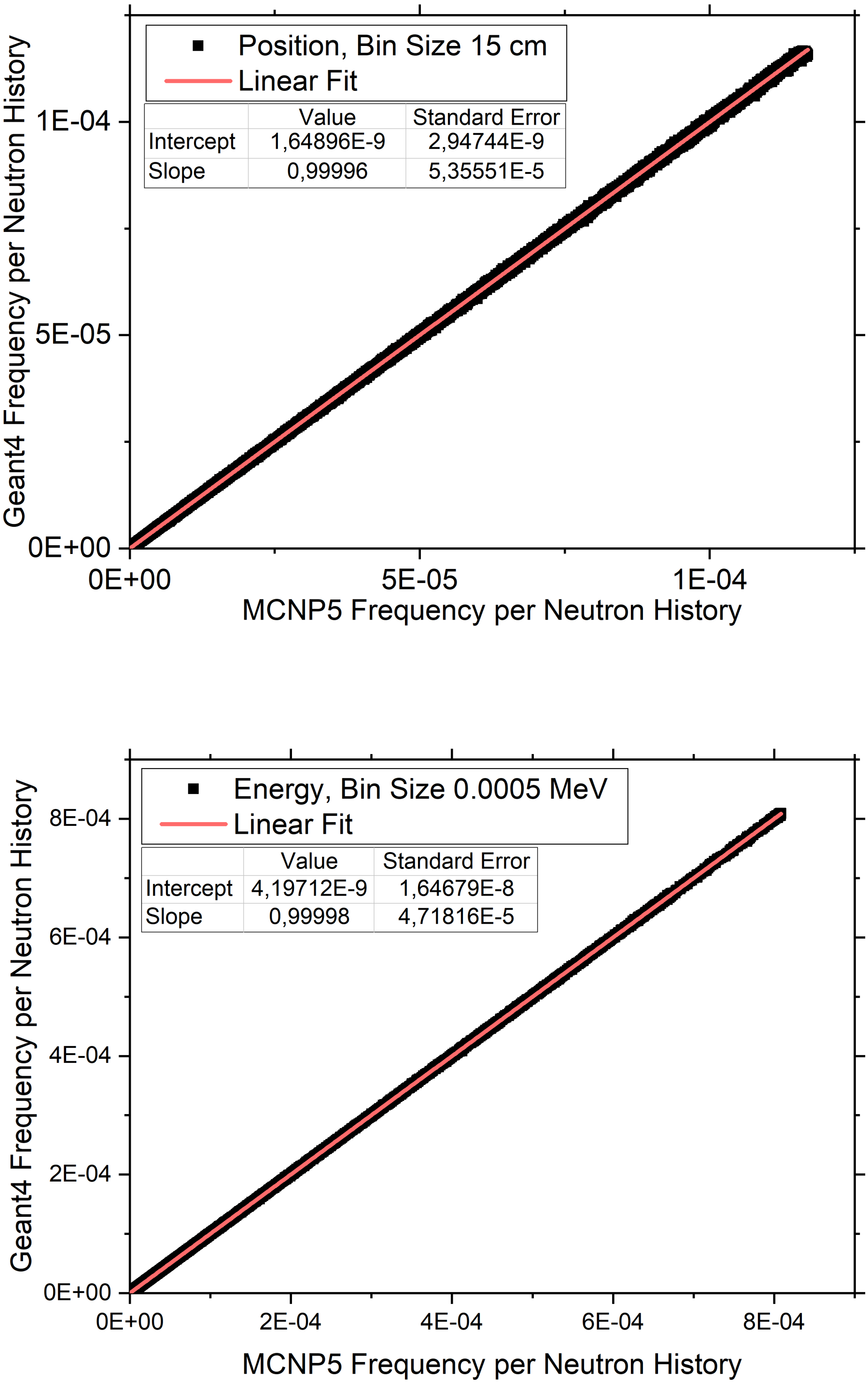

Figure 4.7: The neutron source conversion validation for the plasma neutron source of the DEMO reactor for the position distribution (upper plot) and the energy distribution (lower plot).

Table 4.2: Overview over the resulting parameters for the histogram fits of the Geant4 source subroutine against the respective MCNP source description. In all cases, 0 is within the error-range around the fitted intercept value and 1 is within the error-range around the fitted slope value.

	bin size	intercept	error	slope	error
IPPE					
position	0.05 mm	$3.1 \cdot 10^{-8}$	$3.6 \cdot 10^{-8}$	0.99965	0.00042
mom. dir.	0.05	$8 \cdot 10^{-9}$	$3.5 \cdot 10^{-8}$	0.99994	0.00022
energy	0.0001 MeV	$-6 \cdot 10^{-8}$	$2.5 \cdot 10^{-7}$	1.0001	0.00039
HCPB					
SDEF position	0.0 1cm	$2 \cdot 10^{-8}$	$1.0 \cdot 10^{-7}$	0.99988	$4.0 \cdot 10^{-4}$
F90 position	0.02 cm	$-3.8 \cdot 10^{-7}$	$5.2 \cdot 10^{-7}$	1.00039	$5.2 \cdot 10^{-4}$
SDEF mom. dir.	0.04	$6 \cdot 10^{-10}$	$1.0 \cdot 10^{-8}$	1	$1.0 \cdot 10^{-4}$
F90 mom. dir.	0.04	$6 \cdot 10^{-9}$	$1.0 \cdot 10^{-8}$	0.99994	$1.0 \cdot 10^{-4}$
SDEF energy	0.005 MeV	$1.4 \cdot 10^{-5}$	$2.2 \cdot 10^{-5}$	0.9947	0.0072
F90 energy	0.005 MeV	$-7 \cdot 10^{-6}$	$1.5 \cdot 10^{-5}$	1.0021	0.0052
ITER BS					
F90 position	0.1 mm	$3.7 \cdot 10^{-8}$	$6.4 \cdot 10^{-8}$	0.99987	$2.0 \cdot 10^{-4}$
F90 y mom. dir.	0.005	$1.8 \cdot 10^{-6}$	$3.8 \cdot 10^{-6}$	0.9993	0.0015
F90 energy	0.001 MeV	$-9 \cdot 10^{-7}$	$1.4 \cdot 10^{-6}$	1.0018	0.0023
DEMO					
position	15 cm	$1.6 \cdot 10^{-9}$	$2.9 \cdot 10^{-9}$	0.99996	0.000054
mom. dir.	0.025	$6 \cdot 10^{-10}$	$2.8 \cdot 10^{-9}$	0.99998	0.000070
energy	0.00005 MeV	$4 \cdot 10^{-9}$	$1.6 \cdot 10^{-8}$	0.99998	0.000047

Chapter 5

Verification and Validation of Geant4 with Code-to-Code Benchmarks

5.1 Analysis of Neutron Current Agreement in Single-Interaction Problem

In the first code-to-code benchmark calculations performed with Geant4.10.03 are compared to calculations performed with MCNP5-1.6. The benchmark uses a 2 m long cylinder with radius 1 μm (see figure 3.1). It is filled with a single fusion-relevant isotope at a time at the natural density of the corresponding element. Primary neutrons with energy in the range from 10^{-10} MeV till 20 MeV distributed in an isolethargic energy spectrum (see section 3.1.1, equation 3.2 till 3.4) travel along the central length axis of the cylinder. While passing through the cylinder, four basic options are possible:

1. An interaction happens, which removes the neutron, such as an (n,p), (n,d), (n,t), (n,α), (n,γ), or other reactions with more secondary particles which do not include any neutrons. No neutron is detected.

2. An interaction happens, which produces one secondary neutron in the case of elastic or inelastic scattering, or more than one secondary neutron in the case of (n,2n) or (n,3n) reactions. There are also a number of reactions, which produce one or more neutrons in addition to non-neutron secondary particles. The secondary neutron(s) travels in a direction away from the central length axis, which causes it to escape through the side surface of the cylinder and be detected.

3. Either no interaction happens, or a secondary neutron from option 2 travels close enough to the direction of the central length axis of the cylinder. Then the primary or secondary neutron leaves the cylinder volume through the back surface and no neutron is detected.

4. Multiple interactions happen, but this is very unlikely since the cylinder only has the radius of 1 μm.

The secondary neutrons passing through the side surface are detected as neutron current in the same isolethargic energy bins as for the primary neutrons, which is normalised to the number of neutron histories.

At different energy ranges, different interaction types are dominant. Most of the neutron removing reactions only happen above an energy threshold. The exceptions are the (n,γ) reaction for all considered nuclides, the (n,t) reaction for Li-6, and the (n,α) reaction for Pb-208, for which the cross-sections get stronger towards lower energy.

For the reactions which produce secondary neutrons there are also energy thresholds below which the reactions do not happen for inelastic scattering, (n,2n), (n,3n), and other reactions with multiple secondary particles, while the elastic scattering reaction can happen at any energy.

For this basic benchmark, the thermal scattering law (TSL) treatment of thermal neutrons is disregarded and the thermal energy range below 1 eV is excluded from the discussion. Outside of the thermal energy range, material interactions are not increasing the energy of the neutrons. Due to this, the energy of a secondary neutron cannot be larger than that of the associated primary neutron. The interaction type dictates the energy of the secondary neutron.

Elastic scattering has no energy threshold. The transferred energy per interaction depends both on the interaction angle and on the mass of the nuclide. The effect of the nuclide mass is illustrated by calculating the ratio between original energy E_0 and maximum transferable energy E_t according to equation 2.5. The result is displayed in table 5.1 along with the lowest energy E_{min} a neutron with primary energy 14.1 MeV can have after an interaction. It can be seen that for heavier nuclides only very little energy can be transferred, while a single interaction with H-1 can stop the neutron. Due to the dependence on the interaction angle, any amount of energy between 0 and E_t can be transferred per interaction.

Table 5.1: The maximum transferable energy ratio E_t/E_0 in a single elastic scattering interaction depending on the nuclide calculated with equation 2.5 and the lowest energy E_{min} a neutron with a primary energy of 14.1 MeV can have after a single elastic scattering interaction.

Isotope	E_t/E_0 (%)	$E_{min}(MeV)$
H-1	100.0	0.0
Li-6	49.0	7.2
Li-7	43.8	7.9
Be-9	36.0	9.0
Cnat	28.4	10.1
O-16	22.1	11.0
Si-28	13.3	12.2
Cr-52	7.4	13.1
Fe-56	6.9	13.1
W-184	2.2	13.8
Pb-208	1.9	13.8

Inelastic scattering only happens above a threshold. Since a part of the energy of the primary neutron is exciting the interaction nucleus, the secondary neutron has significantly less energy.

For (n,2n), (n,3n), and other reactions with one or more neutrons and other secondary particles, there are also high energy thresholds. Since the energy of the primary neutron is divided among more than one secondary particle, their individual energies are significantly lower than the primary neutron energy.

Additionally, the spectrum of the neutron current through the side surface is affected by local peaks and dips in the cross-section. Depending on whether a neutron-removing or secondary-neutron-creating interaction dominates the cross-section, a local peak either causes a dip or a peak in the neutron current spectrum.

Building on these underlying principles, the neutron current energy spectra are discussed for all nuclides. The spectra of the surface current and the corresponding $Geant4/MCNP$ ratios for **H-1** are displayed in figure 5.1. The statistical error of the calculations is shown as the 3σ-range in the ratio plot.

The nuclear cross-sections of H-1 for the libraries JEFF-3.3 and ENDF/B-VII.0 are displayed in figure 5.2. There are no visually apparent differences between the two libraries. Since the H-1 nuclide is just a single proton, only a very limited number of reactions are possible: elastic scattering and (n,γ). Elastic scattering is dominant throughout the spectrum; the cross-section of (n,γ) is 4.5 orders of magnitude lower at 20 MeV and gets stronger towards lower energies so that it is 2.5 orders of magnitude lower at 1 eV, which means that the impact on the neutron current is still low.

Due to the strong energy loss of the primary neutron in the elastic scattering interaction with the light H-1 nucleus, the neutron current is very low at the highest energies. The least energy loss happens for an interaction angle where the neutron travels straight forward or close to its original path, which causes it to pass through the end surface of the cylinder and to not be detected. Between the no loss case and the maximum loss case, there is a smooth continuum, which also translates to the neutron current spectrum.

There are no visually apparent differences between the shapes of the neutron current curves for ENDF/B-VII.0 and JEFF-3.1. The same is the case between neutron current curves produced by Geant4 and MCNP, so the $Geant4/MCNP$-ratio plot has to be consulted to tease the deviations out. Since the current is very low at the highest energies, the statistical error is large and there are strong statistical fluctuations, which remain mostly within the 3σ-range. Between 10^{-3} MeV and 1 MeV, there is a slight overestimation for both libraries which reaches slightly outside the 3σ-range. It is a bit more

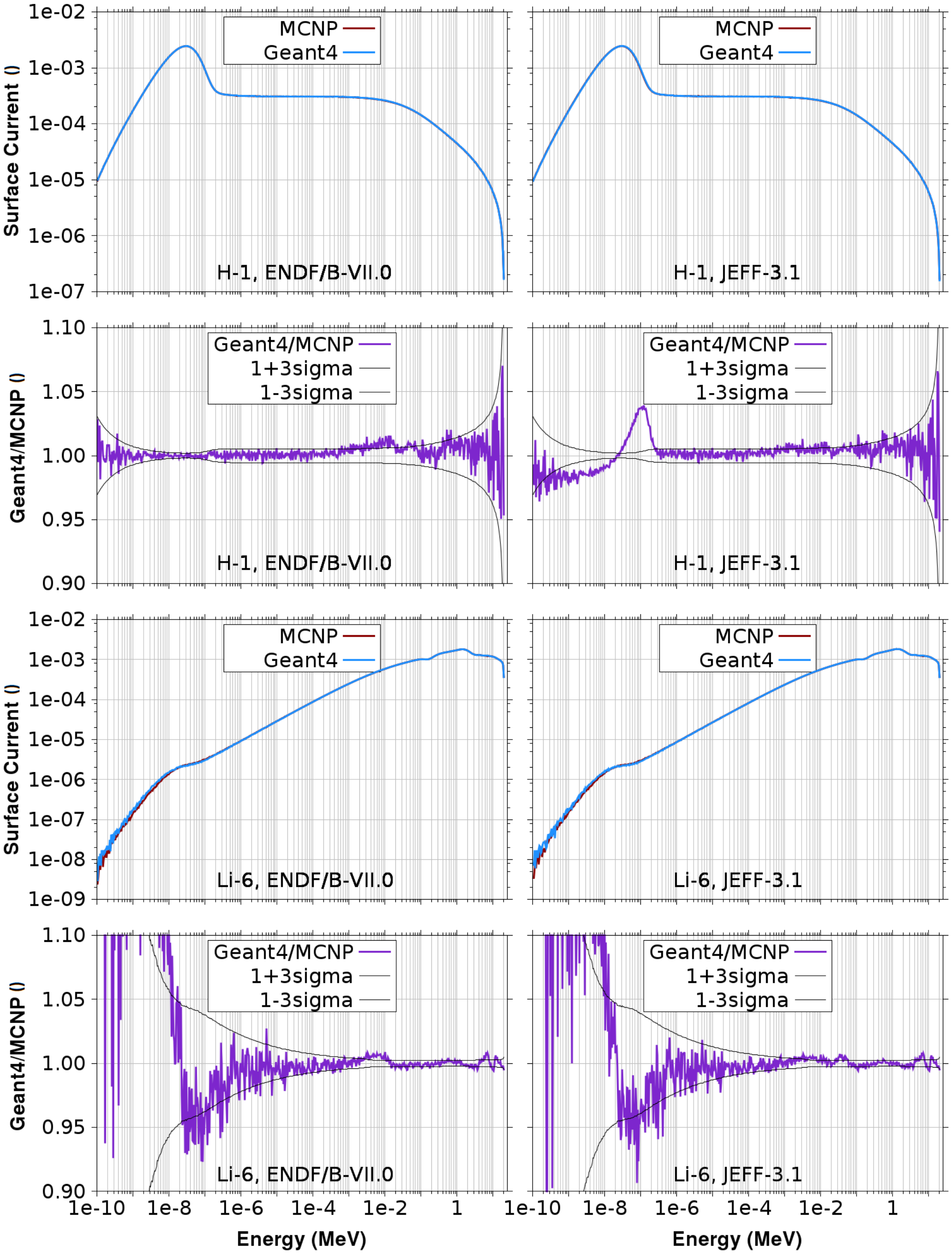

Figure 5.1: The Geant4 and MCNP result for the neutron current per source neutron through the side surface of a cylinder filled with H-1 (first row) and Li-6 (third row) plotted against the energy. The resulting ratio between Geant4 and MCNP surface current result plotted against the energy are shown in the second row for H-1 and the fourth row for Li-6. Plots in the left column present the results for the ENDF/B-VII.0 library and plots in the right column for the JEFF-3.1 library. The range below 1 eV should be disregarded due to the neglect of the TSL treatment.

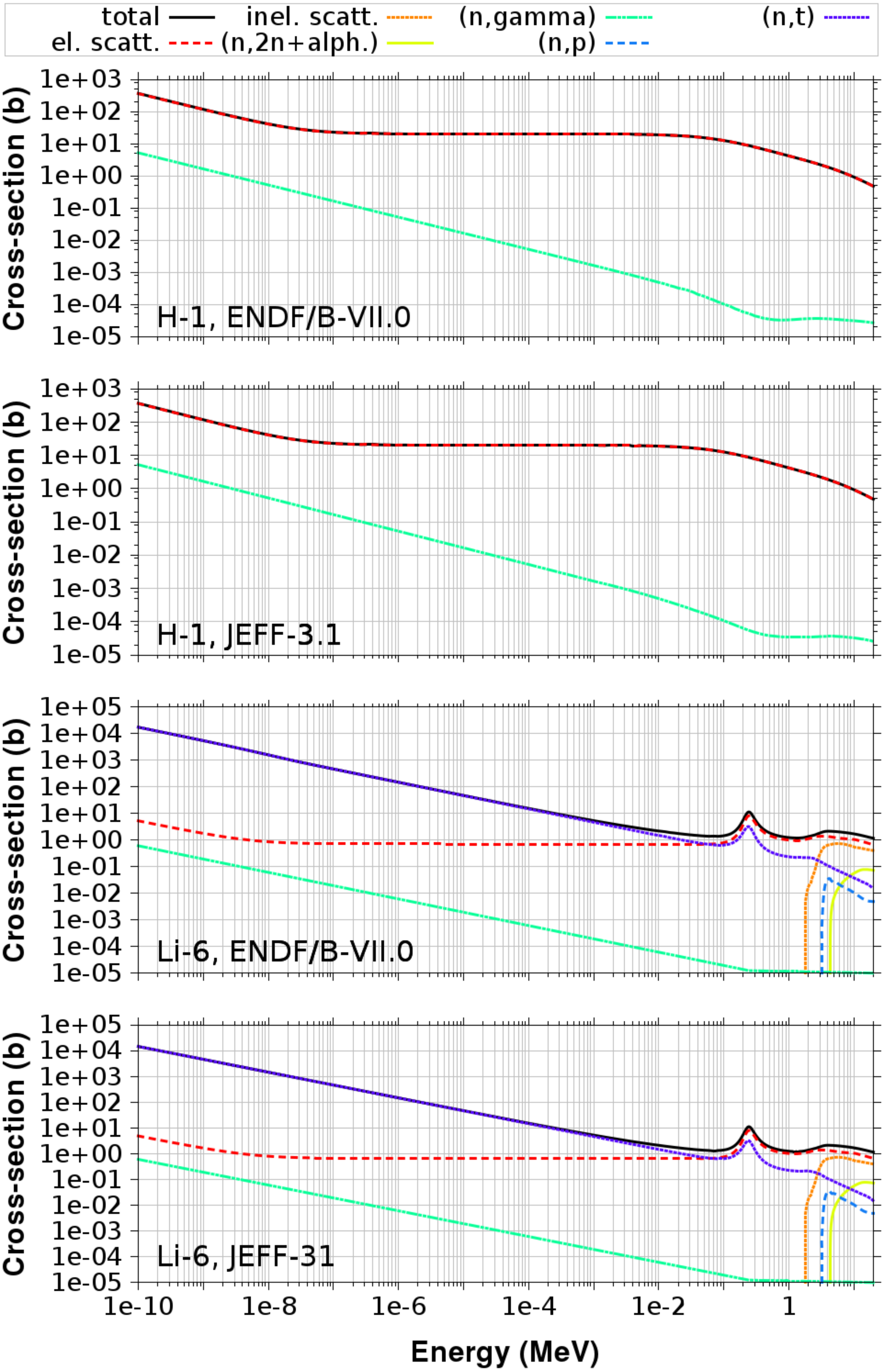

Figure 5.2: The nuclear cross-section of H-1 (top two plots) and Li-6 (bottom two plots) from the ENDF/B-VII.0 library (1st and 3rd plot) and the JEFF-3.1 library (2nd and 4th plot) plotted against the energy. The data is taken from the Soppera et al. (2014) online plotting tool and edited.

pronounced for ENDF/B-VII.0. On the whole, the deviations are either within the 3σ-range or below $5\,\%$, which constitutes good agreement.

The nuclear cross-sections of **Li-6** for the libraries JEFF-3.3 and ENDF/B-VII.0 are also displayed in figure 5.2. There are no visually apparent differences between the two libraries. At energies above 0.05 MeV elastic scattering is dominant. Despite being still a fairly light nuclide, the Li-6 nuclide is approximately a factor 6 heavier than a neutron, and therefore the maximum transferable energy ratio E_t/E_0 of $49\,\%$ (see table 5.1) is only half that of H-1. This means a single elastic scattering interaction with Li-6 can at most cut in half the primary neutron energy. This means the energy of a secondary neutrons is generally closer to that of the corresponding primary neutron and the neutron current at high energies is higher.

Secondary to elastic scattering, several threshold reactions are relevant at high energies: inelastic scattering above 1.8 MeV, (n,p) above 3.2 MeV, and (n,2n+α) above 4.35 MeV. The secondary neutrons from the inelastic scattering and the (n,2n+α) reaction have significantly lower energy and the (n,p) reaction is removing neutrons entirely. This causes the neutron current to go down towards higher energies than 1 MeV.

The (n,t) cross-section already becomes dominant below 0.05 MeV, which causes the neutron current displayed in figure 5.1 to go down towards lower energies. For Li-6, the (n,t) cross-section plays the role which the (n,γ) reaction plays for the other nuclides in that it gets stronger towards lower energies and removes neutrons. The (n,γ) reaction is more than 4 orders of magnitude lower than the total cross-section throughout the energy spectrum and therefore of little relevance.

The slight dip in the neutron current between 0.1 MeV and 0.2 MeV is likely related to the strong local peak of the elastic scattering and (n,t) cross-section just above this energy.

The statistical error becomes larger towards lower energies because the neutron current is declining there. Considering only the energy range above 1 eV, because TSL is disregarded, the $Geant4/MCNP$ ratio reaches outside of the 3σ-range in parts of the energy spectrum, but remains always smaller than $5\,\%$. This can be considered good agreement. The differences between the libraries are very slight.

The nuclear cross-sections of **Li-7** for the libraries JEFF-3.3 and ENDF/B-VII.0 are displayed in figure 5.3. To cut down on the total number of different cross-sections in the plot for clarity, some cross-sections are combined: cross-sections with one or more secondary neutrons and another secondary particle such as (n,2n+α), (n,3n+α), and (n,n+p) are combined into the (n,xn+X) cross-section, and cross-sections with no neutrons as secondary particles such as (n,d) are depicted as (n,X) cross-section. Since the tritium production is particularly relevant for fusion energy, the (n,t) cross-section is left separate. However, for Li-7, the tritium production does not have its own cross-section, but is instead part of the inelastic scattering cross-section.

No significant differences between the two libraries can be observed. Only the peak of the (n,d) cross-section is slightly higher for ENDF/B-VII.0, but since it is two orders of magnitude lower than the total cross-section, the effect of this should be small. For both libraries, elastic scattering is dominating this cross-section in all energy ranges. With one added neutron mass, the maximum transferable energy in an elastic scattering interaction with Li-7 becomes slightly lower than for Li-6 (see table 5.1). Therefore the energy of the secondary neutrons is on average less reduced than for Li-6 and a lot less than for H-1.

The resulting neutron current spectrum for the ENDF/B-VII.0 and the JEFF-3.3 library and the corresponding $Geant4/MCNP$ ratio for Li-7 is displayed in figure 5.4. At high energies, a number of threshold cross-sections are present: (n,n') above 0.5 MeV, (n,2n) above 8.5 MeV, (n,d) above 9 MeV, (n,2n+α) above 10 MeV, and (n,3n+α) above 12.9 MeV. The elastic scattering cross-section becomes less dominant compared to these reactions above 5 MeV. Inelastic scattering, (n,2n), (n,2n+α), and (n,3n+α) are removing neutrons to much lower energies, (n,d) is removing neutrons entirely. This causes the neutron current above the respective thresholds to be lower. Another influence is the shape of the dominant elastic scattering cross-section, which is strongest near 4 MeV, and going down towards both higher and lower energies. Since the elastic scattering cross-section produces secondary neutrons with energies slightly lower than the primary energy, this enhances the downward trend of the neutron current above slightly below 4 MeV.

The peak in the total cross-section near 0.25 MeV causes a peak in the neutron current just below near 0.2 MeV. Between the peak and 1 eV, the elastic scattering dominated total cross-section is nearly constant. This translates to nearly constant neutron current in this energy range.

The (n,γ) cross-section rises from more than five orders of magnitude lower than the total cross-section at 20 MeV to two orders of magnitude lower at 1 eV. Accordingly, it has no effect at high

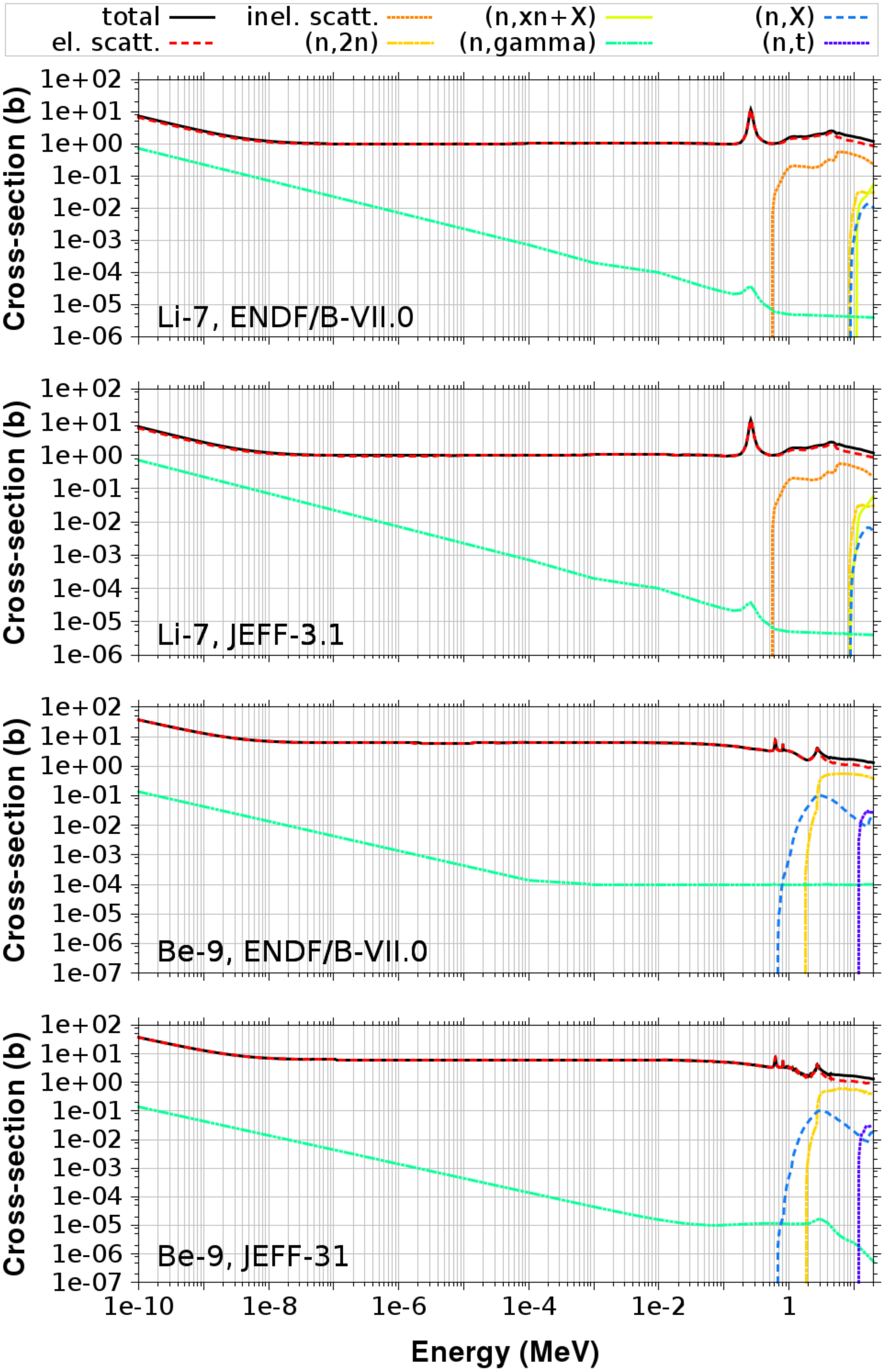

Figure 5.3: The nuclear cross-section of Li-7 (top two plots) and Be-9 (bottom two plots) from the ENDF/B-VII.0 library (1st and 3rd plot) and the JEFF-3.1 library (2nd and 4th plot) plotted against the energy. The data is taken from the Soppera et al. (2014) online plotting tool and edited. For clarity, some cross-sections are combined (for Li-7: (n,xn+X) = (n,2n+α)+(n,3n+α)+(n,n+p); (n,X) = (n,d); for Be-9: (n,X) = (n,p)+(n,d)+(n,α)).

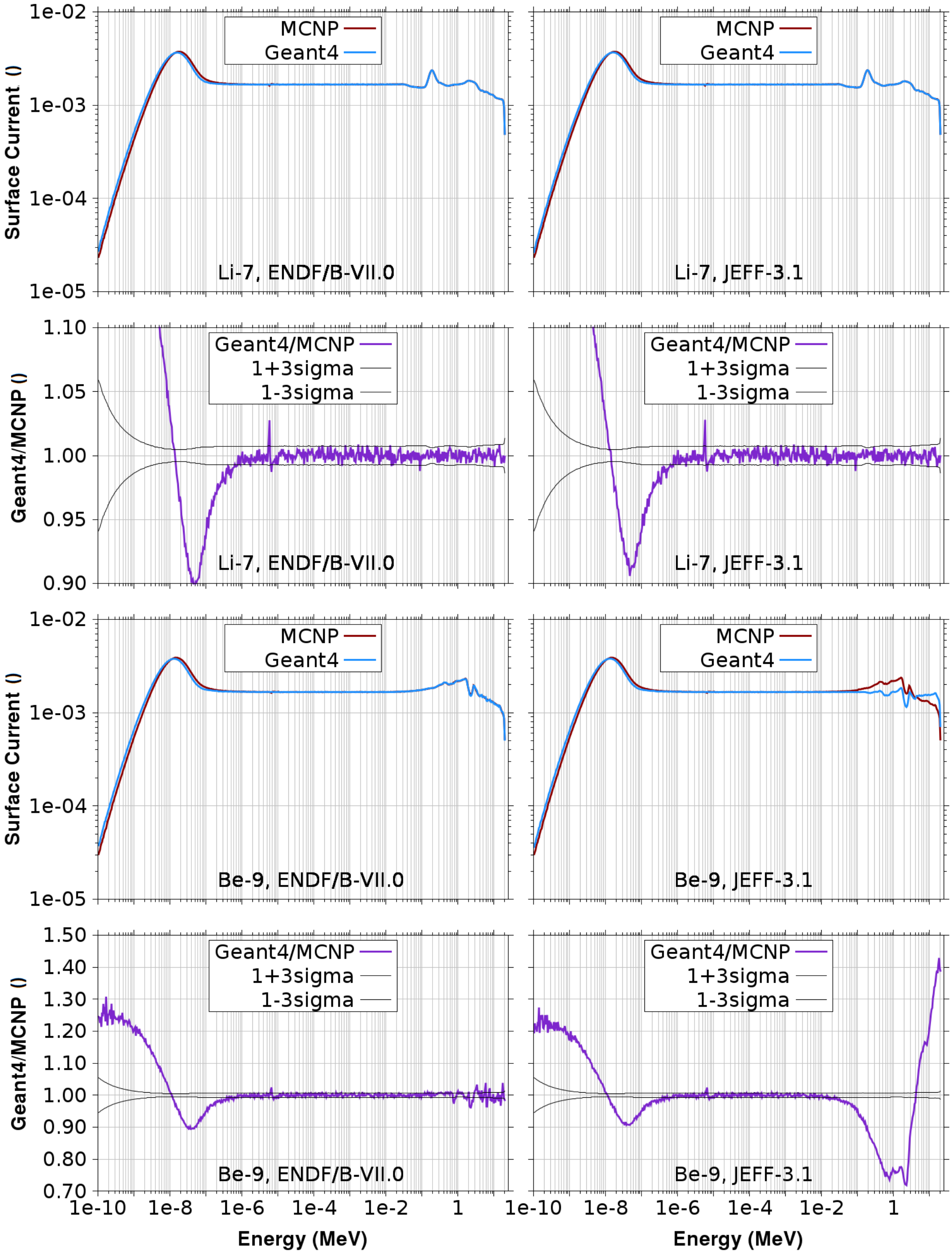

Figure 5.4: The Geant4 and MCNP result for the neutron current per source neutron through the side surface of a cylinder filled with Li-7 (first row) and Be-9 (third row) plotted against the energy. The resulting ratio between Geant4 and MCNP surface current result plotted against the energy are shown in the second row for Li-7 and the fourth row for Be-9. Plots in the left column present the results for the ENDF/B-VII.0 library and plots in the right column for the JEFF-3.1 library. The range below 1 eV should be disregarded due to the neglect of the TSL treatment.

energies and still little effect at low energies, so that no change to the nearly constant neutron flux between 1 eV and the local peak is effected.

The $Geant4/MCNP$ ratio is nearly always within a 3σ range except for one narrow peak near 6 eV which both libraries share. This is due to a small local dip in the otherwise smooth neutron current curve calculated by MCNP, which cannot be explained looking at the cross-sections.

The nuclear cross-sections of **Be-9** for the libraries JEFF-3.3 and ENDF/B-VII.0 are displayed in figure 5.3. For clarity, the (n,p), (n,d), and (n,α) cross-sections are combined into the (n,X) cross-section. There is no inelastic scattering reaction. The only visually apparent difference between the libraries is that the ENDF/B-VII.0 (n,γ) cross-section is constant at energies above 10^{-4} MeV, while the JEFF-3.1 (n,γ) cross-section goes down further. Both are several orders of magnitude below the total cross-section so this should not have much effect.

The neutron current spectrum for the ENDF/B-VII.0 and the JEFF-3.3 library and the corresponding $Geant4/MCNP$ ratio for Be-9 is displayed in figure 5.4. It can be seen that there is a strong deviation between the Geant4 and the MCNP calculation of the neutron current for the JEFF-3.1 library at energies above 0.01 MeV with an underestimation of close to 30 % near 2 MeV and an overestimation of up to nearly 45 % near 20 MeV. The cause for this is that the cross-section of the (n,2n) reaction is presented in a special format in the JEFF library publications from JEFF-3.1 onwards. It considers the different excitation levels of the residual individually as partial reactions. Since Geant4 cannot handle these partial cross-sections, in the later release of JEFF-3.2 and JEFF-3.3, Mendoza and Cano-Ott (2018a) replaced the Be-9 (n,2n) reaction with data from JEFF-3.0, where the total (n,2n) reaction is used.

Accordingly, the Geant4 JEFF-3.1 neutron current spectrum is showing the result of a neutron interaction with Be-9 which neglects the (n,2n) reaction. In comparison with the MCNP result, the effect of the (n,2n) reaction can be investigated. The (n,2n) cross-section has a threshold at 1.8 MeV and rises with rising energy until it reaches a nearly constant plateau near 3 MeV. In the plateau region, it is lower than the elastic scattering cross-section, but the difference is small enough for the (n,2n) reaction to have a significant effect.

The (n,2n) reaction removes primary neutrons, which otherwise could have undergone elastic scattering and lost only little energy before detection. This reduces the neutron current at energies above its threshold. It creates two secondary neutrons with significantly reduced energies, which raise the neutron current in their energy range. It can be seen that the MCNP spectrum is lower at energies above 4 MeV and higher between 0.01 MeV and 4 MeV. This indicates that the energy range of the secondary neutrons is above 0.01 MeV and overlapping the start of the plateau at 3 MeV.

The elastic scattering cross-section has small narrow local peaks near 0.6 MeV and 0.8 MeV, a broad dip near 2 MeV, and a stronger peak near 2.75 MeV. They translate to a series of peaks and dips in the neutron current, though the shapes are different.

There are several reactions which only happen above thresholds: 0.7 MeV for (n,α), 12 MeV for (n,t), 14.5 MeV for (n,p), and 16.5 MeV for (n,d). These reactions reduce the number of available neutrons at the energy range above their threshold. Their effect is limited, since their combined cross-section is more than 1.5 order of magnitudes lower than the elastic scattering cross-section. They have a small additional effect of lowering the neutron current at energies above their thresholds.

Below 0.01 MeV and down to 1 eV, the $Geant4/MCNP$ ratio remains within the 3σ range for both libraries, except for a small peak near 7 eV, which is caused by a small dip in the MCNP-calculated neutron current. This dip is also observed for the Li-7 $Geant4/MCNP$ ratio and again there is no apparent physical reason, since the cross-section is smooth in the adjacent energy range.

For ENDF/B-VII.0, the range of agreement within the 3σ range extends further up until 0.7 MeV. At higher energies, there are fluctuating deviations, which reach outside 3σ range, but remain below 5 %. The deviations are due to the Geant4 neutron current spectrum following the peaks and dips of the MCNP spectrum not quite exactly. A potential reason for this could be interpolation imprecision in the cross-section translation. This still constitutes good agreement for the ENDF/B-VII.0 result, while the large deviations due to the missing (n,2n) reaction cause the Geant4 calculation for the JEFF-3.1 library to have very bad agreement with MCNP.

The nuclear cross-sections of **Cnat** for the libraries JEFF-3.3 and ENDF/B-VII.0 are displayed in figure 5.5. For clarity, the (n,n+p) cross-section is depicted as (n,xn+X), and (n,p), (n,d), and (n,α) are combined into the (n,X) cross-section. There are no visually apparent differences between the two libraries.

The (n,γ) cross-section is more than 3.5 orders of magnitude lower than total cross-section at 1 eV and 20 MeV and even lower in-between. Therefore it has little effect on the neutron current calculation.

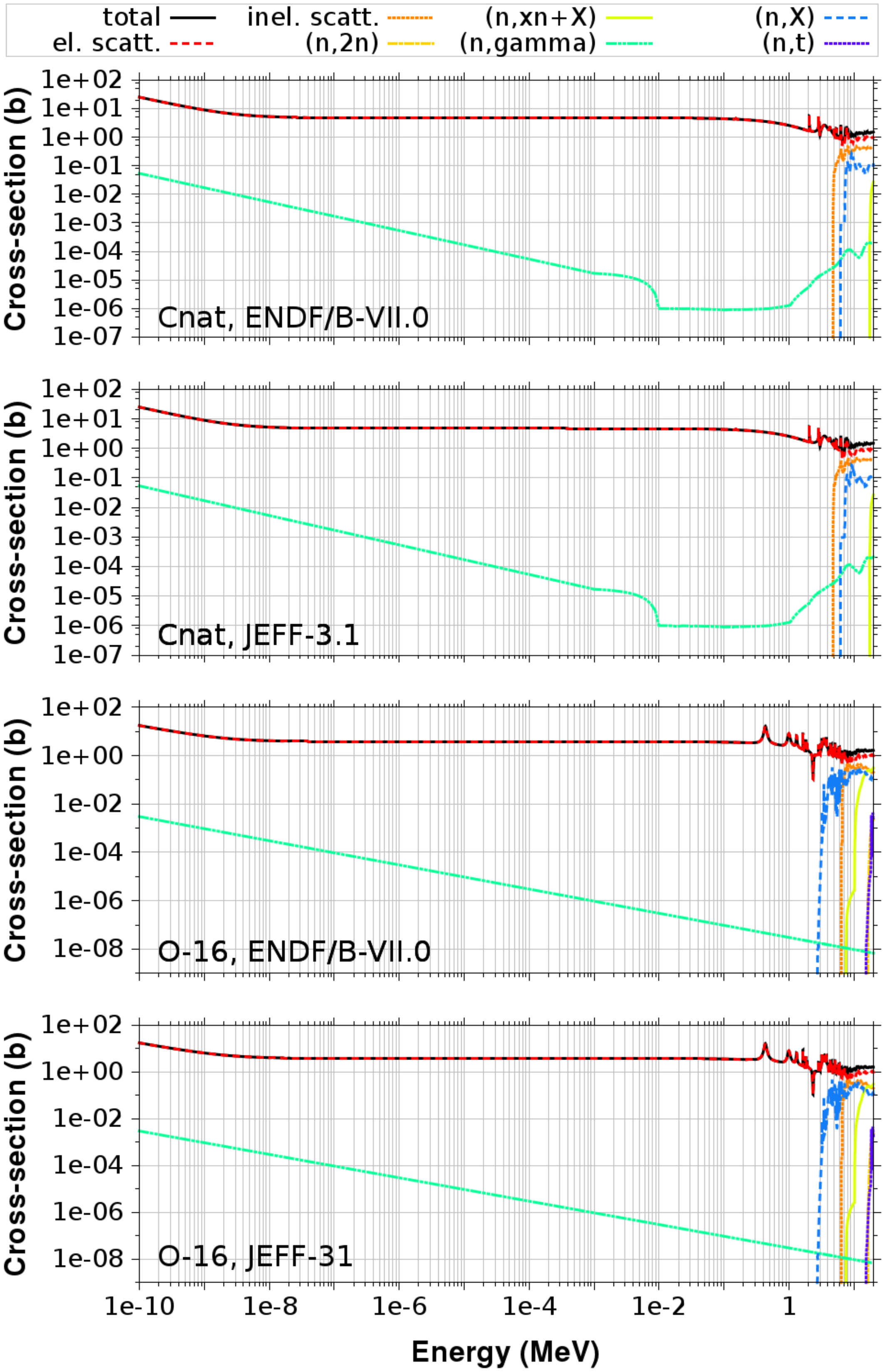

Figure 5.5: The nuclear cross-section of Cnat (top two plots) and O-16 (bottom two plots) from the ENDF/B-VII.0 library (1st and 3rd plot) and the JEFF-3.1 library (2nd and 4th plot) plotted against the energy. The data is taken from the Soppera et al. (2014) online plotting tool and edited. For clarity, some cross-sections are combined (for Cnat: (n,xn+X) = (n,n+p); (n,X) = (n,p)+(n,d)+(n,α); for O-16: (n,xn+X) = (n,n+α)+(n,n+3α)+(n,n+p); (n,X) = (n,p)+(n,d)+(n,α)+(n,2α)).

The neutron current spectrum for the ENDF/B-VII.0 and the JEFF-3.3 library and the corresponding $Geant4/MCNP$ ratio for Cnat is displayed in figure 5.6. Elastic scattering is dominant throughout. At energies above 0.1 MeV, the elastic scattering cross-section has a series of narrow and broader peaks and dips, which translates into similar features in the neutron current.

Above its threshold of 4.8 MeV, the inelastic scattering cross-section comes close to the elastic scattering cross-section. Also the combined (n,X) cross-section with the individual thresholds 14.5 MeV for (n,p), 15.3 MeV for (n,d), and 6.2 Mev for (n,α), is only one order of magnitude lower. The inelastic scattering reaction is removing neutrons to significantly lower energies and the (n,X) reactions are removing neutrons entirely. This causes the neutron current in the energy range above their thresholds to decline. At energies above 17.3 MeV, the (n,n+p) reaction exerts a weak similar effect. Since these reactions also have a series of peaks and dips, they cause additional fluctuations in the neutron current spectrum.

The fact that the neutron current goes slightly up between 0.1 MeV and 1 MeV despite the elastic scattering dominated cross-section going down in this range, is likely caused by the secondary neutrons of the inelastic scattering and to a much lesser extent the (n,n+p) reaction ending up in this energy range.

Below 0.1 MeV and down to 1 eV, elastic scattering is the only reaction of significance and its cross-section is close to constant, causing the neutron current also to be nearly constant in this energy range.

For both libraries, the $Geant4/MCNP$ ratio remains within the 3σ range throughout the energy range, except for a few individual bins for with slightly larger deviations, which still remain below 5 %. Among them, there is a small peak near 7 eV due to a small dip in the MCNP-calculated neutron current, which is also observed for Be-9 and Li-7. For this dip there is again no apparent physical reason, since the cross-section is smooth in the adjacent energy range. The Geant4 result is following the MCNP result very closely despite the fluctuations of the neutron current at high energies. This constitutes very good agreement.

The nuclear cross-sections of **O-16** for the libraries JEFF-3.3 and ENDF/B-VII.0 are displayed in figure 5.5. For clarity, (n,n+α), (n,n+3α), and (n,n+p) are combined into the (n,xn+X) cross-section, and (n,p), (n,d), (n,α), and (n,2α) are combined into the (n,X) cross-section. There are no visually apparent differences between the two libraries.

The neutron current spectrum for the ENDF/B-VII.0 and the JEFF-3.3 library and the corresponding $Geant4/MCNP$ ratio for O-16 is displayed in figure 5.6. Elastic scattering is dominant throughout. At energies above 0.2 MeV, a series of peaks and dips happens. These features in the cross-section are shifted slightly towards lower energies in the neutron current. There is a general downward trend towards higher energies in the cross-section, which translates into a downward trend also in the neutron current.

At high energies, a number of threshold reactions come in, some of which remove neutrons entirely such as (n,t) at 15.4 MeV, and the reactions combined into the (n,X) cross-section: (n,p) at 10.2 MeV, (n,d) at 10.5 MeV, (n,α) at 2.4 MeV, and (n,2α) at 13.7 MeV. Other threshold reactions produce secondary neutrons with significantly lower energies, because part of the energy is exciting the O-16 nucleus such as for inelastic scattering at 6.4 MeV or the energy is distributed between multiple particles such as for (n,2n) at 16.7 MeV, and the reactions combined in the (xn+X) cross-section: (n,n+α) at 7.6 MeV, (n,n+3α) at 16.5 MeV, and (n,n+p) at 12.9 MeV. Since both the (n,t) and (n,2n) cross-section have very high thresholds and are 2.5 orders of magnitude lower than the total cross-section at their highest point, their impact is limited. In contrast to this, the (xn+X), inelastic, and (n,X) cross-section take turns being the second strongest cross-section from high to lower energy and are less than one order of magnitude lower than elastic scattering, which means their impact is significant.

These reactions lower the neutron current above their respective thresholds, which causes the downward trend at high energies. The (xn+X) and inelastic reactions also increase the neutron flux at lower energies, but there is no clear secondary neutron peak apparent.

Below 0.2 MeV and down to 1 eV, elastic scattering is the only relevant reaction and its cross-section is close to constant, causing the neutron current also to be nearly constant in this energy range.

For both libraries, the $Geant4/MCNP$ ratio remains within the 3σ range throughout most of the energy range, except for a small peak near 7 eV due to a small dip in the MCNP-calculated neutron current, which is also observed for Li-7, Be-9, and Cnat. For this dip there is again no apparent physical reason, since the cross-section is smooth in the adjacent energy range. The statistical error is larger in the highest energy range, because the neutron current is lower there.

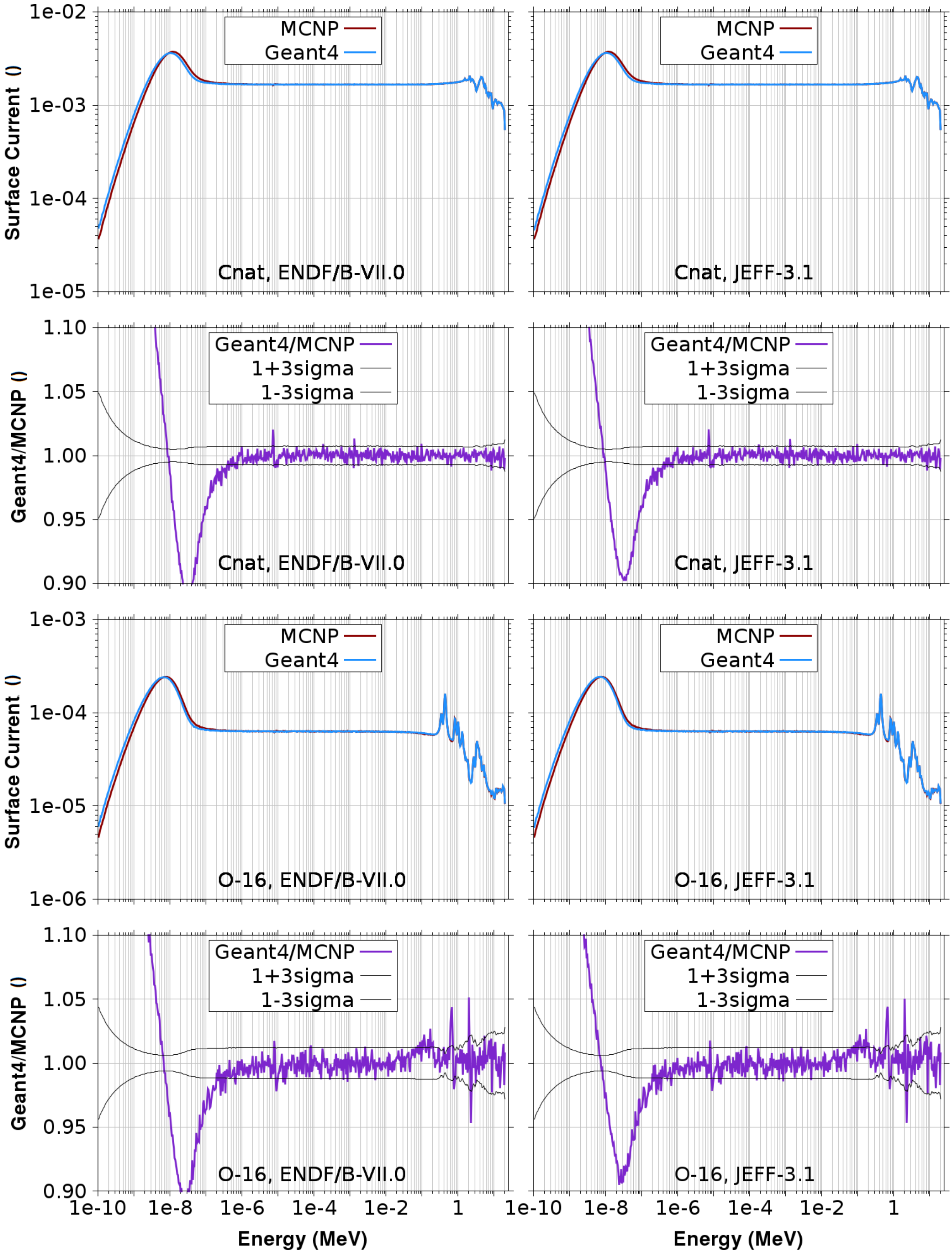

Figure 5.6: The Geant4 and MCNP result for the neutron current per source neutron through the side surface of a cylinder filled with Cnat (first row) and O-16 (third row) plotted against the energy. The resulting ratio between Geant4 and MCNP surface current result plotted against the energy are shown in the second row for Cnat and the fourth row for O-16. Plots in the left column present the results for the ENDF/B-VII.0 library and plots in the right column for the JEFF-3.1 library. The range below 1 eV should be disregarded due to the neglect of the TSL treatment.

There is a slight overestimation outside of the 3σ range towards the upper end of the constant cross-section range between 0.1 MeV and 0.2 MeV. This is likely caused either by imperfect representation of the elastic scattering cross-section, or by overestimation of the number of secondary neutrons produced by threshold reactions, which end up in this energy range.

There are two strong fluctuations in the $Geant4/MCNP$ ratio which reach outside the 3σ range. The first is caused by Geant4 calculating the neutron current dip at 0.6 MeV not quite as low and the peak at 0.8 MeV not quite as high as the MCNP result. The second is caused by Geant4 not quite exactly reproducing the dip at 2 MeV. These deviations are likely caused by imprecise interpolation of the features of the elastic scattering cross-section.

In general, the $Geant4/MCNP$ ratio remains within the 3σ range throughout the most part of the energy range for both libraries, and below 5 % everywhere. This constitutes good agreement.

The nuclear cross-sections of **Si-28** for the libraries JEFF-3.3 and ENDF/B-VII.0 are displayed in figure 5.7. For clarity, (n,n+α) and (n,n+p) are combined into the (n,xn+X) cross-section, and (n,p), (n,d), and (n,α) are combined into the (n,X) cross-section. The resulting neutron current spectrum for the ENDF/B-VII.0 and the JEFF-3.3 library and the corresponding $Geant4/MCNP$ ratio for Si-28 is displayed in figure 5.8.

The Si-28 cross-section can be divided into three regions: the threshold region above 1.8 MeV, the resonance region between $3 \cdot 10^{-2}$ MeV and 1.8 MeV, and the low energy region below $3 \cdot 10^{-2}$ MeV. Elastic scattering is dominant throughout the energy range.

In the threshold region, the elastic scattering cross-section has small fluctuations which overlay a general trend of going down towards higher energies until 10 MeV and going up till 20 MeV. This is one part of the cause for the similar trend in the neutron current in this energy range.

There are a number of threshold cross-sections, which come close to the elastic scattering cross-section. These include inelastic scattering above 1.8 MeV, (n,X) consisting of (n,p) above 4 MeV, (n,d) above 10.5 MeV, and (n,α) above 2.7 MeV, and (n,n+X) consisting of (n,n+α) above 10.4 MeV and (n,n+p) above 12 MeV. Less relevant is the (n,2n) reaction, which has a very high threshold of 17.8 MeV and is more than 2 orders of magnitude lower than the total cross-section. The (n,X) reaction is removing neutrons and therefore lowering the neutron current above its threshold. The other threshold reactions also lower the neutron current above their threshold by removing neutrons to lower energies. Additionally, they create secondary neutrons, which raise the neutron current at lower energies. This effect in combination with the shape of the elastic scattering cross-section causes a broad peak centred near 2 MeV.

The JEFF-3.1 library includes a cross-section for the (n,t) reaction with a threshold of 12 MeV, which is absent for ENDF/B-VII.0. Since this cross-section is always 3 or more orders of magnitude lower than the total cross-section, this has likely no significant effect.

For ENDF/B-VII.0, at the highest energies the inelastic scattering cross-section is higher, the (n,X) combined cross-section is lower, and the elastic scattering cross-section is slightly higher. The resulting total cross-section appears to be identical. In combination this difference causes the ENDF/B-VII.0 result to lack the small local peak near 20 MeV in the neutron current, which is present for JEFF-3.3.

The (n,γ) cross-section is more than 3.5 orders of magnitude lower than the total cross-section at energies above 1.8 MeV. In this energy range, the shape of the curve is slightly different between the libraries, but the effect is likely negligible.

In the resonance region, the elastic scattering cross-section has several strong features and smaller fluctuations. Despite the cross-section features being a combination of dip and peak, the resulting features in the neutron current are just dips such as the small dip near 0.05 MeV, the dip near 0.15 MeV, and the dip near 0.55 MeV. For the dip near 0.75 MeV, the elastic scattering cross-section alone does not suffice as explanation. At higher energies, the fluctuations of the elastic scattering cross-section become smaller and the general trend is declining slightly.

The (n,γ) resonance region is characterised by strong narrow fluctuations, which sometimes reach close to the elastic scattering cross-section. Since this reaction removes neutrons, it lowers the neutron current. This way, slight additional fluctuations are introduced into the neutron current spectrum. It is likely that the dip near 0.75 MeV is caused by some closely packed resonance peaks.

In the energy range below the resonance region down to 1 eV, the elastic scattering cross-section is nearly constant. The (n,γ) cross-section rises until it is only less than two orders of magnitude lower than the total cross-section at 1 eV. The effect of the (n,γ) cross-section is not strong enough to make the neutron current visibly go down towards lower energies, instead the constant elastic scattering cross-section is causing it to be nearly constant.

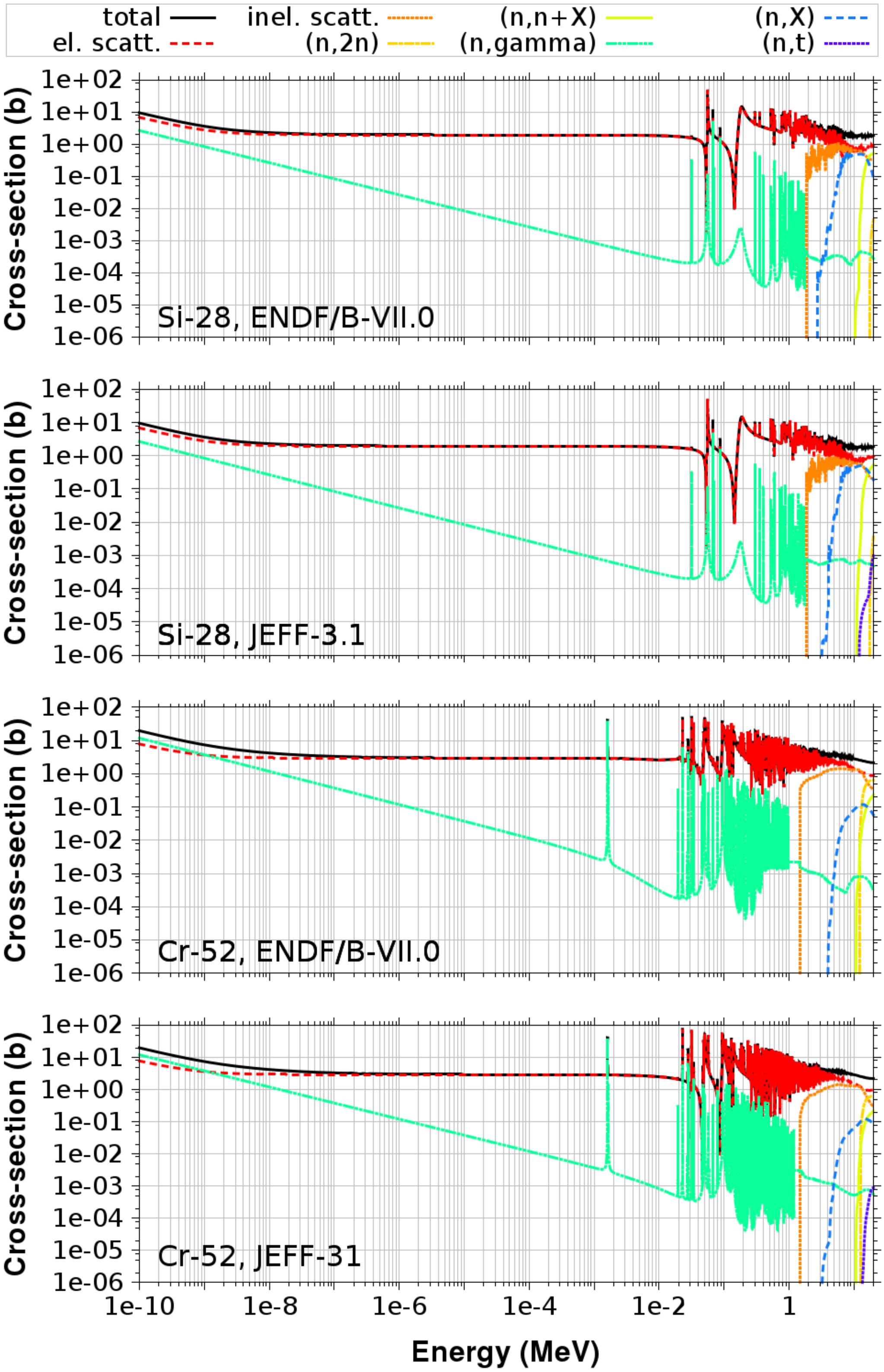

Figure 5.7: The nuclear cross-section of Si-28 (top two plots) and Cr-52 (bottom two plots) from the ENDF/B-VII.0 library (1st and 3rd plot) and the JEFF-3.1 library (2nd and 4th plot) plotted against the energy. The data is taken from the Soppera et al. (2014) online plotting tool and edited. For clarity, some cross-sections are combined (for Si-28: (n,xn+X) = (n,n+α)+(n,n+p); (n,X) = (n,p)+(n,d)+(n,α); for Cr-52: (n,xn+X) = (n,n+α)+(n,n+p); (n,X) = (n,p)+(n,α)).

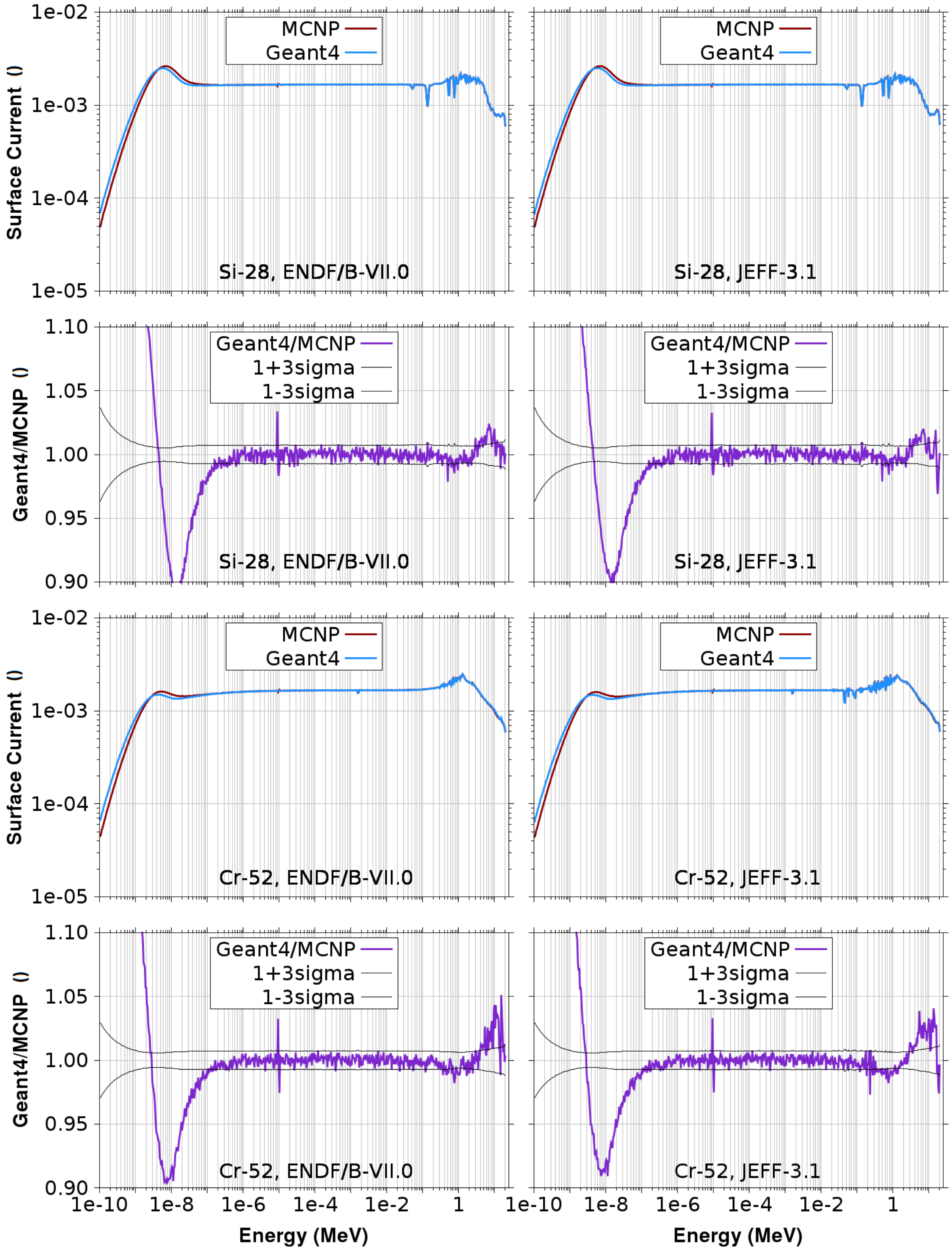

Figure 5.8: The Geant4 and MCNP result for the neutron current per source neutron through the side surface of a cylinder filled with Si-28 (first row) and Cr-52 (third row) plotted against the energy. The resulting ratio between Geant4 and MCNP surface current result plotted against the energy are shown in the second row for Si-28 and the fourth row for Cr-52. Plots in the left column present the results for the ENDF/B-VII.0 library and plots in the right column for the JEFF-3.1 library. The range below 1 eV should be disregarded due to the neglect of the TSL treatment.

For both libraries, the $Geant4/MCNP$ ratio remains within the 3σ range throughout most of the energy range. A larger pattern of deviation happens for both libraries in the energy range of the broad secondary neutron peak between 0.3 MeV and 10 MeV. Geant4 produces an overestimation of the neutron current at the higher energy end of the peak and an underestimation at the lower energy end of peak. The cause for this could be on the one hand that at high energies the neutron removal by reactions which produce lower-energy secondary neutrons is underestimated and as a result, there are fewer secondary neutrons at lower energies, leading to an underestimation of the neutron current at the lower energy end of the peak. On the other hand, the calculation of the energies of secondary neutrons could be slightly skewed.

Overlaid on this are additional minor dips in the $Geant4/MCNP$ ratio near 0.5 MeV and 0.75 MeV. These align with dips in the neutron current. Geant4 appears to be overestimating the depth of these dips slightly.

For the JEFF-3.1 library, the small local peak in the neutron current just below 20 MeV is not perfectly reproduced. This causes a local fluctuation between overestimation and underestimation.

Similarly as for Li-7, Be-9, and Cnat, there is a localised deviation at low energies due to a fluctuation in the MCNP-calculated neutron current. It is shifted to slightly higher energy compared to the other nuclides and happens near 10 eV. For this fluctuation there is again no apparent physical reason, since the cross-section is smooth in the adjacent energy range.

In general, all deviations are either within the 3σ range or below 5 $\%$, so the agreement is good.

The nuclear cross-sections of **Cr-52** for the libraries JEFF-3.3 and ENDF/B-VII.0 are displayed in figure 5.7. For clarity, (n,n+α) and (n,n+p) are combined into the (n,xn+X) cross-section, and (n,p) and (n,α) are combined into the (n,X) cross-section. The resulting neutron current spectrum for the ENDF/B-VII.0 and the JEFF-3.3 library and the corresponding $Geant4/MCNP$ ratio for Cr-52 is displayed in figure 5.6.

The Cr-52 cross-section can be divided into three regions: the threshold region above 1.5 MeV, the resonance region between $1.6 \cdot 10^{-3}$ MeV and slightly overlapping the threshold region up to 2 MeV, and the lower energy region below $1.6 \cdot 10^{-3}$ MeV. Elastic scattering is nearly always dominant.

In the threshold region, the elastic scattering cross-section has a general downwards trend towards higher energies and fluctuations decreasing in size, while being more pronounced for the JEFF-3.1 cross-section. In this range, several threshold reactions come in: reactions which produce secondary neutrons with significantly lower energy such as inelastic scattering above 1.5 MeV, (n,2n) above 12.5 MeV, (n,n+α) above 1.2 MeV, and (n,n+p) above 3.3 MeV, and reactions which remove neutrons entirely such as (n,p) above 9.5 MeV and (n,α) above 11 MeV. Just like for Si-28, the (n,t) cross-section is missing for ENDF/B-VII.0. For JEFF-3.1, it comes in above 13.5 MeV.

The inelastic scattering and the (n,2n) cross-section both come close to the elastic scattering cross-section and have a strong impact on the neutron current, while the other threshold reactions except (n,t) have a minor impact. For (n,t) and (n,γ), the cross-sections are more than 3 orders of magnitude lower and therefore the impact is low. Therefore differences, such as the lack of the (n,t) cross-section for ENDF/B-VII.0 or between the shapes of the (n,γ) curve, have little impact on the neutron current.

The diminishing elastic scattering cross-section in combination with the threshold reactions cause the neutron current to go down towards higher energies. Since the dominant threshold reactions produce secondary neutrons, and in the case of (n,2n) even two of them, the neutron current is raised at lower energies. The primary neutrons from the broad energy range above the lowest threshold of 1.5 MeV are converted into secondary neutrons, which also populate a broad energy range. It can be seen in the neutron current plot that this causes a broad secondary neutron peak centred around 1.5 MeV. Just above, the inelastic scattering cross-section is rising up strongly and curving to a slower decrease. This shape can be seen reproduced next to the peak in the neutron current.

At the highest energies, there is another slight library difference: For JEFF-3.1, the elastic scattering cross-section is constant above 15 MeV, while for ENDF/B-VII.0 the cross-section goes down continuously towards higher energies. As a result, the neutron current is going down more smoothly for ENDF/B-VII.0 towards high energy while there is a small step for JEFF-3.1.

The resonance region has a range above $2 \cdot 10^{-2}$ MeV where there are closely stacked resonance peaks for both elastic scattering and (n,γ) in the cross-section. Differences between the two libraries can be observed. For ENDF/B-VII.0, the resonance peaks of the (n,γ) cross-section stop at 1 MeV, while for JEFF-3.1 they continue to slightly higher energies.

For JEFF-3.1, the fluctuation peaks in the elastic scattering cross-section reach higher and lower than for ENDF/B-VII.0. There are strong dips in the cross-section near $4.5 \cdot 10^{-2}$ MeV and $9 \cdot 10^{-2}$ MeV, which end at 0.5 b for ENDF/B-VII.0, while they go as low as 0.005 b for JEFF-3.1 and as a consequence are also wider at 0.5 b.

For JEFF-3.1, some of the (n,γ) resonance peaks are shifted to higher values. In combination with the lower dips of the elastic scattering cross-section, this causes more overlap between the two cross-sections than for ENDF/B-VII.0. Additionally, between $2 \cdot 10^{-2}$ MeV and $4 \cdot 10^{-2}$ MeV the base curve on which the (n,γ) resonance peaks sit is higher for JEFF-3.1 and between $4 \cdot 10^{-1}$ MeV and 1 MeV, the height of the resonances from top to bottom is larger for JEFF-3.1 and they are shifted towards lower values.

The more pronounced features in the elastic scattering cross-section and to a lesser extent the increased impact of the (n,γ) cross-section causes the neutron current calculated with JEFF-3.1 to have stronger fluctuations beginning at the lower energy end of the resonance region, while the fluctuations only start above 0.3 MeV for ENDF/B-VII.0 and are less pronounced.

In the region below $2 \cdot 10^{-2}$ MeV there is only one strong narrow peak at $1.6 \cdot 10^{-3}$ MeV interrupting the constant elastic scattering cross-section and the monotonic increase towards lower energy for the (n,γ) cross-section. The (n,γ) peak is so strong, it even reaches above the elastic scattering cross-section. This causes a slight dip in the neutron current near this energy.

Below $1.6 \cdot 10^{-3}$ MeV, the dominant elastic cross-section for both libraries continues being nearly constant, which translates to the neutron current. The neutron removing (n,γ) cross-section rises towards lower energies and is ≈ 1.5 orders of magnitude lower than the total cross-section at 1 eV. This causes a very slight downward trend in the neutron current towards low energies.

For both libraries, the $Geant4/MCNP$ ratio remains within the 3σ range throughout most of the energy range. Just as for Si-28, a larger pattern of overestimation in the primary neutron dip and underestimation in the secondary neutron peak can be observed. Again, the cause for this is either an underestimation of the removal of neutrons at higher energies and a resulting underestimation of the amount of secondary neutrons at lower energies, or a skewed calculation of secondary neutron energies. However, the deviation for the overestimation exceeds the deviation for the underestimation. This indicates neutron removal at high energies without secondaries is also underestimated.

Close to 0,2 MeV, there are fluctuations in the JEFF-3.1 $Geant4/MCNP$ ratio, which reach outside of the 3σ range. Likely the stronger fluctuations in the cross-section of JEFF-3.1 are more prone to interpolation imprecision.

Similarly as for Li-7, Be-9, Cnat, and Si-28, there is a localised deviation at low energies due to a fluctuation in the MCNP-calculated neutron current. Similarly as for Si-28, it happens near 10 eV. For this fluctuation there is again no apparent physical reason, since the cross-section is smooth in the adjacent energy range.

In general, all deviations are either within the 3σ range or below 5 %, so the agreement is good.

The nuclear cross-sections of **Fe-56** for the libraries JEFF-3.3 and ENDF/B-VII.0 are displayed in figure 5.9. For clarity, (n,n+α) and (n,n+p) are combined into the (n,xn+X) cross-section, and (n,p), (n,d), (n,He-3), and (n,α) are combined into the (n,X) cross-section. The resulting neutron current spectrum for the ENDF/B-VII.0 and the JEFF-3.3 library and the corresponding $Geant4/MCNP$ ratio for Fe-56 is displayed in figure 5.10.

The Fe-56 cross-section can be divided into three regions: the threshold region above 0.86 MeV, the resonance region between 10^{-3} MeV and slightly overlapping the threshold region up to 1.3 MeV, and the lower energy region below 10^{-3} MeV. Elastic scattering is nearly always dominant.

In the threshold region, the elastic scattering cross-section has a slight downward trend towards higher energies, which is partially responsible for the neutron current also going down. The (n,γ) cross-section is more than 3 orders of magnitude lower and therefore of low relevance.

A number of threshold reactions come in such as reactions which produce secondary neutrons with significantly lower energies (inelastic scattering above 0.86 MeV, (n,2n) above 11.5 MeV, (n,n+α) above 7.8 MeV, and (n,n+p) above 10.4 MeV) and reactions which remove neutrons ((n,p) above 3.0 MeV, (n,d) above 8.2 MeV, (n,He-3) above 10.8 MeV, (n,α) above 0.9 MeV, and (n,t) above 12.2 MeV). These reactions lower the neutron current above their thresholds and in the case of the secondary neutron producing reactions, they raise the neutron current at lower energies. A broad peak centred at 1 MeV is the result.

The shape of the elastic scattering reaction is slightly different between the libraries. For JEFF-3.1, the small fluctuations continue to higher energies and also the inelastic scattering cross-section has stronger fluctuations, which reach up higher. As a result, the secondary neutron peak has a slightly different shape.

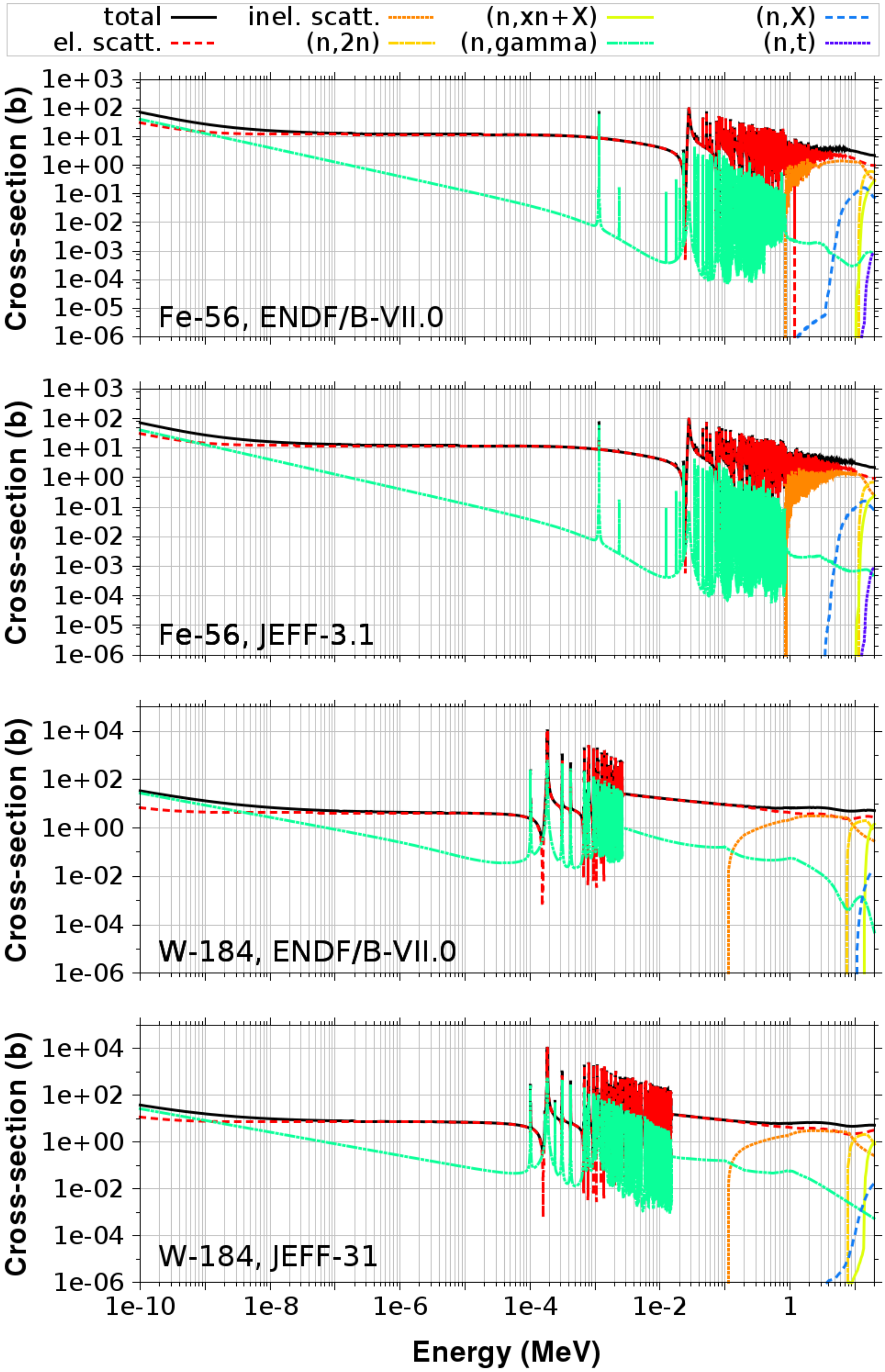

Figure 5.9: The nuclear cross-section of Fe-56 (top two plots) and W-184 (bottom two plots) from the ENDF/B-VII.0 library (1st and 3rd plot) and the JEFF-3.1 library (2nd and 4th plot) plotted against the energy. The data is taken from the Soppera et al. (2014) online plotting tool and edited. For clarity, some cross-sections are combined (for Fe-56: (n,xn+X) = (n,n+α)+(n,n+p); (n,X) = (n,p)+(n,d)+(n,He-3)+(n,α); for W-184: (n,xn+X) = (n,3n); (n,X) = (n,p)+(n,α)).

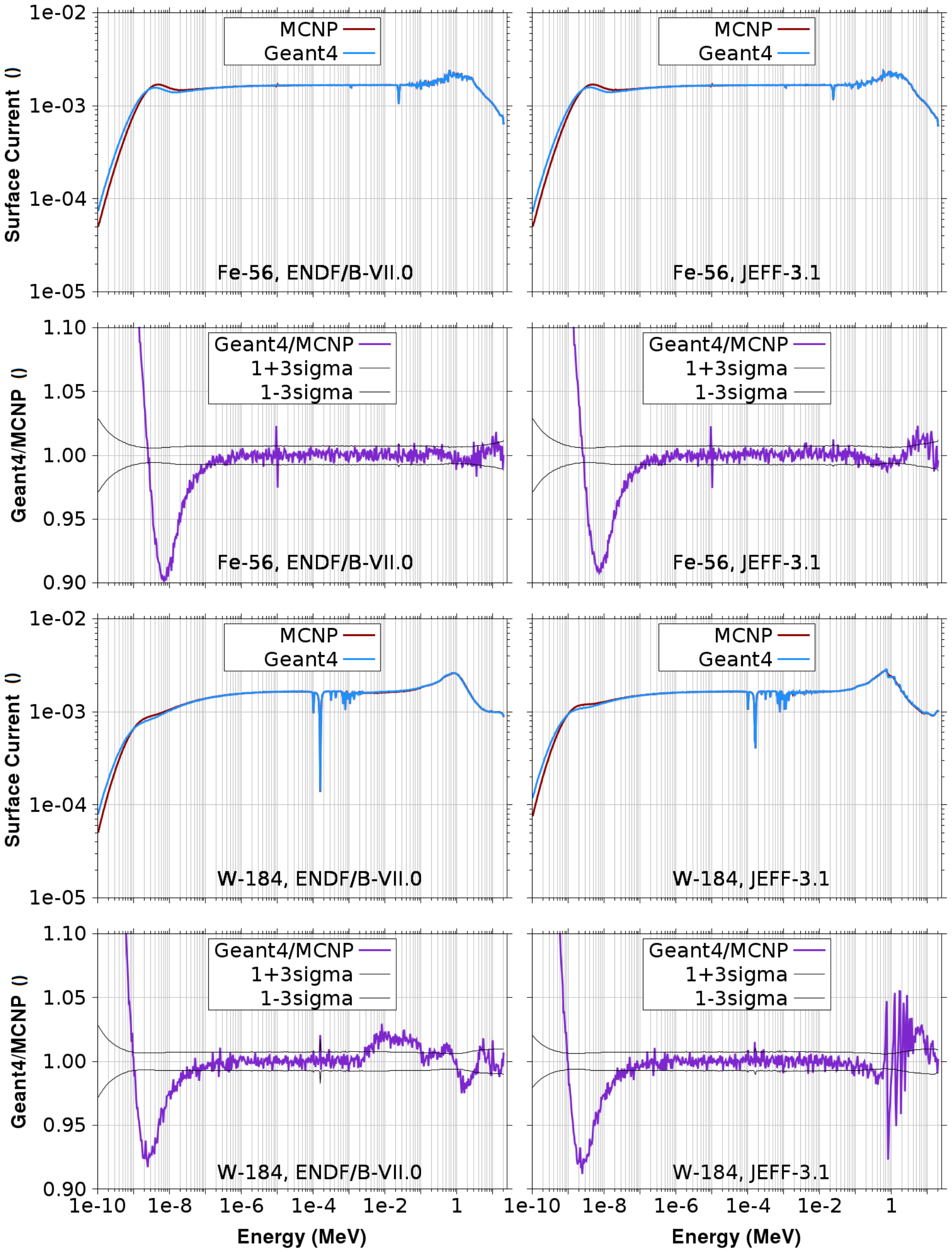

Figure 5.10: The Geant4 and MCNP result for the neutron current per source neutron through the side surface of a cylinder filled with Fe-56 (first row) and W-184 (third row) plotted against the energy. The resulting ratio between Geant4 and MCNP surface current result plotted against the energy are shown in the second row for Fe-56 and the fourth row for W-184. Plots in the left column present the results for the ENDF/B-VII.0 library and plots in the right column for the JEFF-3.1 library. The range below 1 eV should be disregarded due to the neglect of the TSL treatment.

In the higher energy part of the resonance region, both elastic and (n,γ) cross-sections have tightly packed resonance peaks. The elastic scattering cross-sections are fairly similar between the two libraries. Their fluctuations cause minor fluctuations in the neutron current in this range. Similarly as for Cr-52, above 0.4 MeV, the (n,γ) cross-section of ENDF/B-VII.0 does not reach as low as for JEFF-3.1. The effect of this is likely limited, since the lower end of the resonances are more than 3 orders of magnitude lower than the total cross-section. There are some minor differences at the upper end of the (n,γ) resonance peaks, which likely account for the slight differences in the fluctuation pattern of the neutron current between the two libraries.

Near $2.5 \cdot 10^{-2}$ MeV, there is a strong dip in the elastic scattering cross-section. At slightly higher energy, there is a peak. In the (n,γ) cross-section, there is also a broader peak in this position, which slightly overlaps with the dip. The difference between libraries for the elastic scattering and (n,γ) cross-section in this energy range is limited: the elastic scattering dip is slightly lower for ENDF/B-VII.0 and the broader (n,γ) peak is slightly higher for JEFF-3.1. As a result, there is a strong dip in the neutron current near this energy, which is deeper for ENDF/B-VII.0.

Below the dip, the elastic scattering cross-section does not have anymore resonance peaks and instead only rises up slowly, but the neutron current is constant until very close to the dip. The (n,γ) cross-section has a few resonance peaks, but they are not strong enough to have an impact on the neutron current, except for near 10^{-3} MeV where a (n,γ) resonance peak is stronger than the elastic scattering peak. This causes a slight dip in the neutron current close to this energy.

Similar to Cr-52, the elastic scattering cross-section is nearly constant between 1 eV and 10^{-3} MeV producing a nearly constant neutron current in this energy range. The (n,γ) cross-section rises towards lower energies and is 1.5 orders of magnitude lower at 1 eV, causing a very slight downward trend.

For both libraries, the $Geant4/MCNP$ ratio remains within the 3σ range throughout most of the energy range. Just as for Si-28 and Cr-52, a larger pattern of overestimation in the primary neutron dip and underestimation in the secondary neutron peak can be observed. For ENDF/B-VII.0, this effect is so weak that the $Geant4/MCNP$ ratio reaches outside the 3σ range only for few energy bins. The centre of the underestimation dip is positioned at higher energies than for JEFF-3.1.

Similarly as for Li-7, Be-9, Cnat, Si-28, and Cr-52 there is a localised deviation at low energies due to a fluctuation in the MCNP-calculated neutron current. Similarly as for Si-28 and Cr-52, it happens near 10 eV. For this fluctuation there is again no apparent physical reason, since the cross-section is smooth in the adjacent energy range.

In general, all deviations are either within the 3σ range or below 5 %, so the agreement is good.

The nuclear cross-sections of **W-184** for the libraries JEFF-3.3 and ENDF/B-VII.0 are displayed in figure 5.9. For clarity, (n,3n) is depicted as (n,xn+X) cross-section, and (n,p) and (n,α) are combined into the (n,X) cross-section. The resulting neutron current spectrum for the ENDF/B-VII.0 and the JEFF-3.3 library and the corresponding $Geant4/MCNP$ ratio for W-184 is displayed in figure 5.10.

The W-184 cross-section can be divided into four regions. The threshold reaction region starts above 0.1 MeV, which is unusually low compared to the other nuclides. Below, there is an intermediate range down until the start of the resonance region. The resonance region is also positioned at lower energies than for other nuclides and ranges from $3 \cdot 10^{-3}$ MeV for ENDF/B-VII.0 and $1.5 \cdot 10^{-2}$ MeV for JEFF-3.1 down to 10^{-4} MeV for both libraries. From 10^{-4} MeV down to 1 eV is the lower energy region. Elastic scattering is dominant throughout most of the spectrum.

In the threshold reaction region, the elastic scattering cross-section has a slight downward trend towards higher energies. The (n,γ) cross-section has also a downward trend, starting at more than 1.5 orders of magnitude lower than the total cross-section and increasing to 4 orders of magnitude lower at 20 MeV. Therefore its impact is low in the energy range and the difference in shape between the libraries of little effect.

The threshold reaction region starts with inelastic scattering above 0.1 MeV. Its cross-section rises to the same level as elastic scattering near 1.5 MeV and stays on this level up until 9 MeV. At higher energies it drops of to a bit more than 1 order of magnitude below the total cross-section, which still exerts a minor effect.

The other secondary neutron producing reactions (n,2n) and (n,3n) come in above 7.5 MeV and above 14 MeV. They are the second strongest reaction behind elastic scattering in the range above 9 MeV and close to 20 MeV respectively. Their cross-sections do not come as close to elastic scattering as inelastic scattering. For JEFF-3.3, the (n,2n) cross-section reaches closer to the elastic scattering cross-section and the (n,3n) cross-section maximum is slightly lower than for ENDF/B-VII.0.

The neutron removing reactions (n,p) and (n,α) come in above 10.75 MeV and above 11.25 MeV. Their maximum value is more than 2.5 orders of magnitude lower than the total cross-section, so their effect is low.

The effect on the neutron current is that it is low above 7 MeV due to (n,2n), (n,3n) and to a lesser extent inelastic scattering creating secondary neutrons with significantly lower energies. The shape of the neutron current curve in this range is different between JEFF-3.3 and ENDF/B-VII.0 due to the slight differences in the elastic scattering cross-section curves and the relative strength of the (n,2n) and (n,3n) cross-sections.

Below 7 MeV, the neutron current rises towards lower energies up to a peak which is centred around 0.8 MeV. In this range, inelastic scattering is still moving neutrons to lower energies, but less effectively than the (n,2n) and (n,3n) reactions. Simultaneously, an increasing number of secondary neutrons, which are created from higher energy primary neutrons by (n,2n), (n,3n) and inelastic scattering, are coming in.

Below the peak, the neutron current goes down slowly towards lower energies. In this region, the energy loss of neutrons by inelastic scattering is going down until it stops at the threshold near 0.1 MeV. Combined with the lowering number of secondary neutrons due to (n,2n) and (n,3n) reactions at higher primary neutron energies, the inelastic secondary neutrons create a slowly decreasing tail to the peak, which reaches into the intermediary range. In this range, only elastic scattering and (n,γ) reaction are present. Both cross-sections increase slightly towards lower energies and at their lowest point, there is only 1.5 orders of magnitude difference between them. The resulting neutron current is nearly constant.

In the resonance region, there are strong fluctuations in both the elastic scattering and the (n,γ) cross-section. The resonance peaks of the (n,γ) cross-section reach above the baseline of the elastic scattering cross-section. Due to this there is a double effect of lowered neutron current due to the neutron removal of the (n,γ) reaction and due to the dips in the elastic scattering cross-section.

The cross-section fluctuations of the resonance region cause local dips in the neutron current. In the unresolved resonance region, the peaks are so close together that they almost cancel each other out which leads to only small fluctuations in the neutron current. Since this region extends to higher energies in the JEFF-3.1 cross-section, the fluctuations in the neutron current also extend to there. Additionally, there are differences in the resonance peaks, for example JEFF-3.1 has one for (n,γ) near $2.5 \cdot 10^{-4}$ MeV which does not exist for ENDF/B-VII.0. This is transferred to a minor dip in the neutron current spectrum near this energy, which only exists in the JEFF-3.1 spectrum.

For ENDF/B-VII.0, the neutron current has a deeper dip near $1.5 \cdot 10^{-4}$ MeV. The causative dip in the elastic scattering reaction has a similar depth for both libraries, but it is a bit broader for ENDF/B-VII.0.

The elastic scattering cross-section is nearly constant between 1 eV and 10^{-4} MeV and the (n,γ) cross-section rises towards lower energies and is 1 orders of magnitude lower at 1 eV, causing a very slight downward trend towards lower energies.

For JEFF-3.1, the $Geant4/MCNP$ ratio in the energy range above 0.1 MeV has a larger pattern of overestimation in the primary neutron dip and underestimation in the secondary neutron peak just as Si-28, Cr-52, and Fe-56. This likely happens, because at high energies the reactions, which produce significantly lower-energy secondary neutrons, are underestimated in favour of elastic scattering, which produces secondary neutrons closer in energy to the primary neutron.

In this case, there is a strong additional effect happening: on the high energy side of the broad secondary neutron peak, the neutron current curve produced by Geant4 is shaped like a staircase. The general trend is still following the smooth MCNP curve, causing the $Geant4/MCNP$ ratio to strongly fluctuate and the tips of the fluctuation to reach beyond 5 % deviation. The staircase-like shape of the curve does not seem realistic. It is likely an artefact due to too large bins in the energy distribution data of the secondary neutrons for one or more of the relevant reactions (elastic and inelastic scattering, (n,2n), and (n,3n)).

For ENDF/B-VII.0, there is no fluctuation at the higher energy side of the secondary neutron peak. The larger pattern of overestimation in the primary neutron dip and underestimation in the secondary neutron peak is shifted towards lower energies. The underestimation by Geant4 now happens at the higher energy side of the secondary neutron peak and the overestimation is spread out along the lower energy tail of the peak down until the resonance region. This could be caused either by the effect of the inelastic scattering reaction being overestimated, or by the energy of the secondary neutrons produced by the (n,2n) and/or (n,3n) reaction being underestimated. The deviations reach outside the 3σ range but not outside 5 %.

At the high energy side of the primary neutron dip, there are also some fluctuations, because Geant4 does not quite reproduce the shape of the MCNP curve. They also reach slightly outside the 3σ range but not outside 5 %.

Below 0.1 MeV, both libraries have a $Geant4/MCNP$ ratio which remains within the 3σ range except for near the largest dip of the neutron current in the resonance region. Here the statistical error is larger due to the lowered neutron current in the dip. For both libraries, Geant4 slightly underestimates the depth of the dip causing a $Geant4/MCNP$ ratio which extends slightly outside the 3σ range, but remains within 5 % deviation.

In conclusion, the agreement is only mediocre for JEFF-3.3, because the deviation extends beyond 5 % and the shape of the curve does not appear to be in accordance with plausible physics. For ENDF/B-VII.0, the deviation remains within 5 %, so the agreement can still be called good, however, the deviation is outside the 3σ range throughout a larger part of the energy range than for the other nuclides.

The nuclear cross-sections of **Pb-208** for the libraries JEFF-3.3 and ENDF/B-VII.0 are displayed in figure 5.11. For clarity, (n,3n), (n,n+α), (n,n+2α), (n,n+p), (n,n+d), and (n,n+t) are combined into the (n,xn+X) cross-section, and (n,p), (n,d), and (n,α) are combined into the (n,X) cross-section. The resulting neutron current spectrum for the ENDF/B-VII.0 and the JEFF-3.3 library and the corresponding $Geant4/MCNP$ ratio for Fe-56 is displayed in figure 5.12.

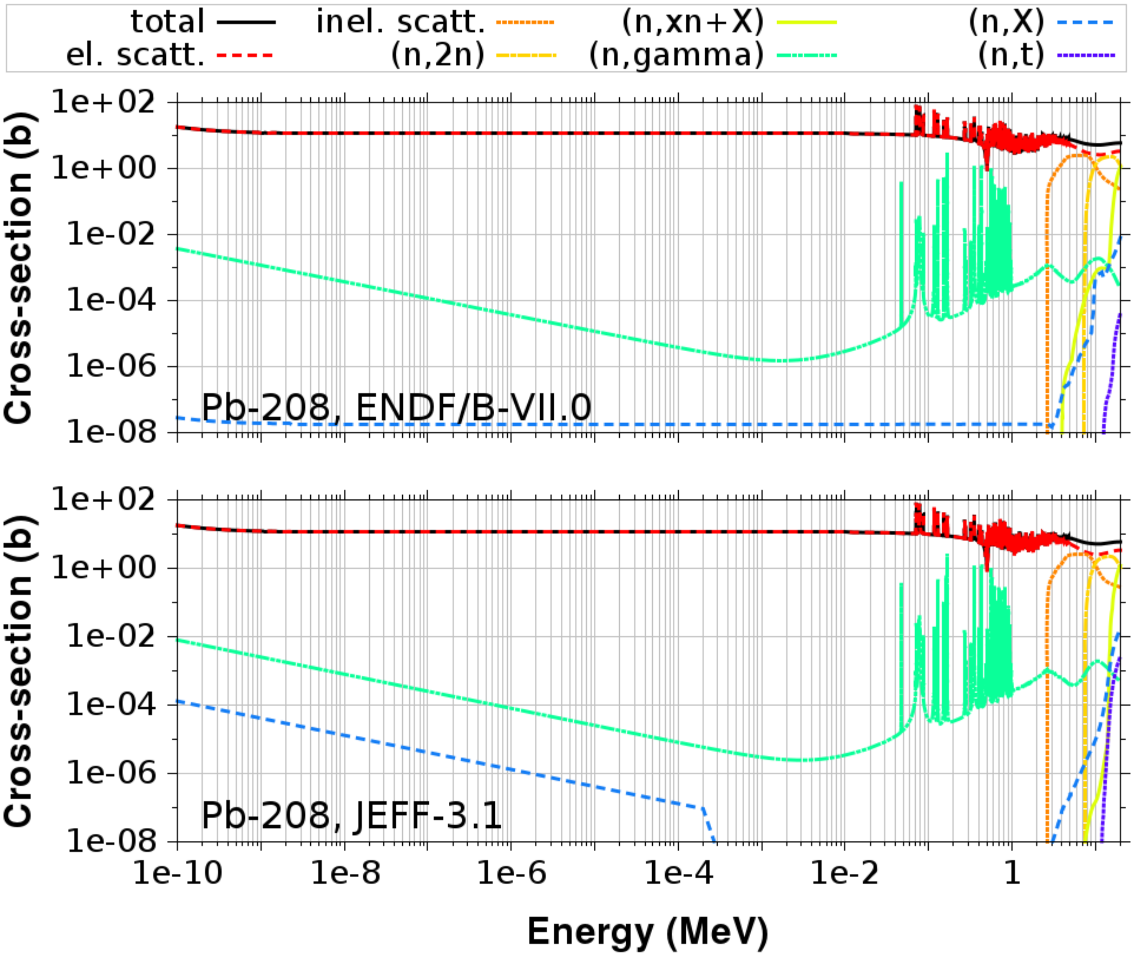

Figure 5.11: The nuclear cross-section of Pb-208 from the ENDF/B-VII.0 library (top plot) and the JEFF-3.1 library (bottom plot) plotted against the energy. The data is taken from the Soppera et al. (2014) online plotting tool and edited. For clarity, some cross-sections are combined ((n,xn+X) = (n,3n)+(n,n+α)+(n,n+2α)+(n,n+p)+(n,n+d)+(n,n+t); (n,X) = (n,p)+(n,d)+(n,α).

The Pb-208 cross-section can be divided into four regions. The threshold reaction region starts above 2.6 MeV. Below, there is a small intermediate range down until the start of the resonance region. The resonance region ranges from $4 \cdot 10^{-2}$ MeV till 1 MeV. Below $4 \cdot 10^{-2}$ MeV is the lower energy region. Elastic scattering is dominant throughout the spectrum.

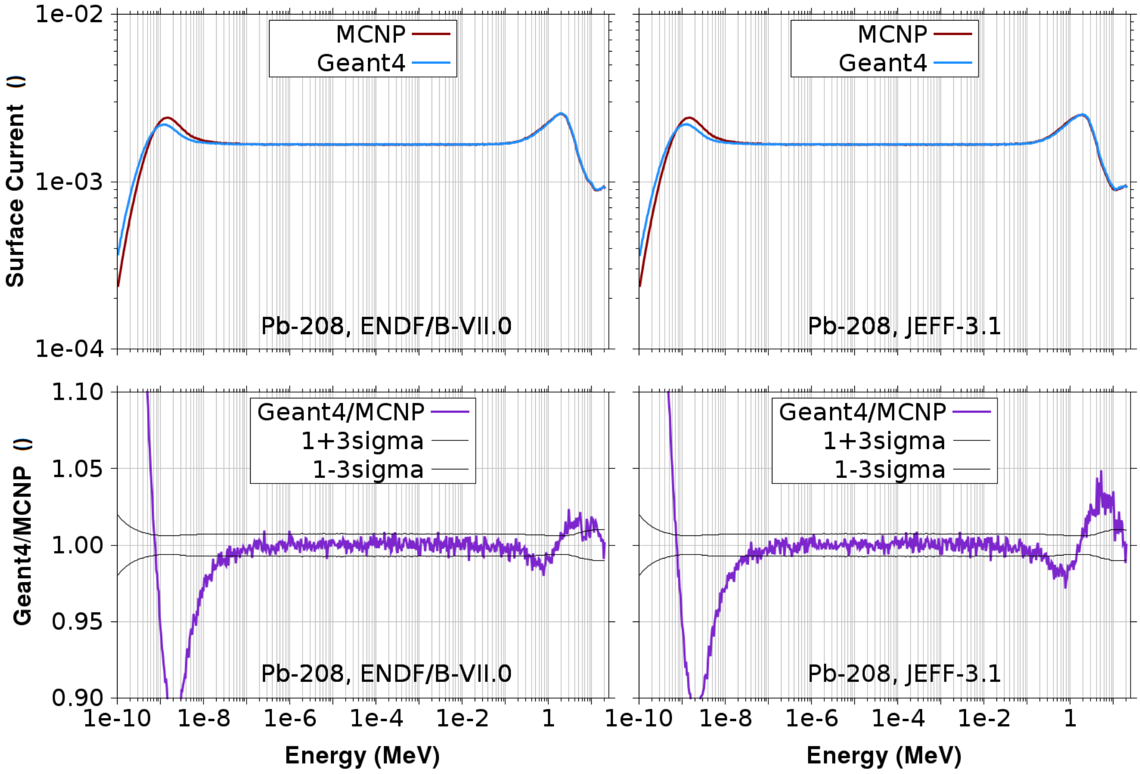

Figure 5.12: The Geant4 and MCNP result for the neutron current per source neutron through the side surface of a cylinder filled with Pb-208 (first row) plotted against the energy. The resulting ratio between Geant4 and MCNP surface current result plotted against the energy are shown in the second row. Plots in the left column present the results for the ENDF/B-VII.0 library and plots in the right column for the JEFF-3.1 library. The range below 1 eV should be disregarded due to the neglect of the TSL treatment.

In the energy range above the resonance region, the elastic scattering cross-section continues to be dominant. It goes up slightly to a its highest point near 3 MeV, then slightly down to a lowest point near 10 MeV and then up again slightly until 20 MeV.

The following threshold reactions are present: inelastic scattering above 2.6 MeV, a large number of reactions with one or more neutrons and one or more other secondary particles such as (n,2n) above 7.4 MeV, (n,3n) above 14.5 MeV, (n,n+α) which starts at low energies at very low level and is above 10^{-8} b above 4.0 MeV, (n,n+2α) above 7.0 MeV, (n,n+p) above 8.0 MeV, (n,n+d) above 12.9 MeV, and (n,n+t) above 13.0 MeV, and reactions with non-neutron secondary particles such as (n,p) above 4.2 MeV, (n,d) above 5.9 MeV, and (n,t) above 6.5 MeV. Inelastic scattering is the second strongest reaction between 2.6 MeV and 9.5 MeV; at higher energies (n,2n) is the second strongest, until the combined (xn+X) cross-section dominated by (n,3n) reaches approximately the same level near 20 MeV. The (n,γ) , (n,t), and other (n,X) reactions are of little relevance with their cross-sections being 2 or many more orders of magnitude lower in this energy range.

As described for other nuclides, reactions like inelastic scattering, (n,2n), and (n,3n) produce secondary neutrons with significantly lower energies. This lowers the neutron current above their threshold, and raises it at lower energies, in particular when more than one secondary neutron is produced. This causes the neutron current dip down to 10 MeV and the broad peak centred near 2 MeV and extending down until 0.1 MeV.

Slight differences in the four relevant cross-sections elastic, inelastic, (n,2n), and (n,3n) and their relative strengths are barely perceptible in the cross-section plot, but cause minor differences in the shape of the neutron current curve, such as the position of the deepest point of the primary neutron dip, which is shifted slightly towards lower energies for JEFF-3.1.

In addition to the elastic scattering and the (n,γ) cross-section, also the (n,α) cross-section extends to low energies, but its level is very low everywhere so that its effect on the neutron current result is negligible.

In the resonance region, the elastic scattering cross-section has a downward trend towards higher energies in the baseline with a number of smaller peaks added on top and a dip near 0.5 MeV. The (n,γ) cross-section baseline is more than 4 orders of magnitude lower, but a few of the narrow peaks reach up to less than one order of magnitude lower than the elastic scattering cross-section. All these features do not cause visible effects on the neutron current spectrum. For other nuclides, it can also be seen that in contrast to dips, peaks on the elastic scattering cross-section appear to have no appreciable effect on the neutron current. Another factor is that the resonance region is at least partially covered by the secondary neutron peak, which is caused by high-energy threshold reactions such as (n,2n).

In the energy range below $4 \cdot 10^{-2}$ MeV, both the (n,γ) and the (n,α) cross-section are more than 5 orders of magnitude lower than the elastic scattering cross-section and therefore have negligible impact on the neutron current spectrum. The elastic scattering cross-section is nearly constant in this range which translates to also nearly constant neutron current.

For both libraries, the $Geant4/MCNP$ ratio remains within the 3σ range throughout most of the energy range. Just as for Si-28, Cr-52, and Fe-56, a larger pattern of overestimation in the primary neutron dip and underestimation in the secondary neutron peak can be observed above 0.1 MeV. Here, the overestimation also extends to the high energy side of the peak and the underestimation is happening at the low energy side of the peak. As a result of the over- and underestimation, the $Geant4/MCNP$ ratio reaches outside the 3σ range. Over- and underestimation are more pronounced for JEFF-3.1 but still within $5\,\%$ deviation. Similar as for other nuclides, the overestimation is stronger than the underestimation, indicating that other effects such as neutron removal due to (n,γ) and (n,X) reactions may also be slightly underestimated in the primary neutron dip.

Due to the good agreement throughout most of the energy range and the deviation remaining below $5\,\%$ everywhere else, the agreement with MCNP can be considered good for Pb-208.

The general conclusions are that good agreement, which is defined as a $Geant4/MCNP$ ratio within the 3σ range or a deviation below $5\,\%$, is observed for most nuclides and libraries. The exceptions include Be-9 for the JEFF-3.1 library. Here, an underestimation of close to $30\,\%$ and an overestimation of more than $40\,\%$ is observed. The cause for this is a library translation issue due to the special format of the (n,2n) cross-section in some JEFF library releases, which causes the (n,2n) cross-section to be missing from the Geant4 calculation. This has been rectified in later JEFF conversion releases by Mendoza and Cano-Ott (2018a) by using the (n,2n) cross-section of JEFF-3.0, which is using a compatible format.

The other exception is W-184, which only has mediocre agreement for JEFF-3.1. There is unrealistic behaviour at high energies, which indicates too large bins in the energy distribution data of the secondary neutrons for one or more of the relevant reactions (elastic and inelastic scattering, (n,2n), and (n,3n)). This causes deviations which are larger than $5\,\%$ in some places.

The nuclides for which reactions which produce one or more secondary neutrons with significantly lower energies, are relevant (including Si-28 and heavier) show a common pattern in the deviations: Their spectra all show a dip in the neutron current at high energies above the thresholds of the relevant reactions, and a broad peak at somewhat lower energies (near 1 till 2 MeV) due to the secondary neutrons created by these reactions. The common deviation is an overestimation of the neutron current in the dip, and an underestimation in the secondary neutron peak. The overestimation is stronger than the underestimation, indicating that other effects such as neutron removal due to (n,γ) and (n,X) reactions may also be slightly underestimated in the neutron current dip.

Of minor importance, but without explanation, is a small fluctuation in the energy range between 6 eV and 10 eV for the nuclides Li-7, Be-9, Cnat, O-16, Si-28, Cr-52, and Fe-56 and both libraries in the MCNP neutron current causing a local deviation, which reaches beyond the 3σ range but remains below $5\,\%$.

To quantify the deviation between Geant4 and MCNP, Mendoza et al. (2014) have used the average relative deviation d. It is calculated from the neutron current result Φ_i in the i-th energy bin:

$$d = \frac{1}{N} \sum_{i=1}^{N} \frac{\left|\Phi_i^{\mathrm{Geant4}} - \Phi_i^{\mathrm{MCNP}}\right|}{\Phi_i^{\mathrm{MCNP}}} \quad , \tag{5.1}$$

with N being the total number of energy bins. Only energy bins in the range > 1 eV are considered due to the neglect of the TSL treatment relevant at lower energies.

They have used this to measure the improvements made to older versions of the Geant4 code. In the final version Geant4.9.6 considered in their paper, they have found $d < 1\,\%$ for 313 isotopes, $1\,\% < d < 5\,\%$ for 65 isotopes, and $d > 5\,\%$ for 6 isotopes.

The d results calculated for the most fusion-relevant isotopes and the two libraries JEFF-3.1 and ENDF/B-VII.0 can be seen in table 5.2. With the exception of the previously explained Be-9 with JEFF-3.1 library, the deviation is less than $1\,\%$ in all cases. The result for W-184, for which the spectrum revealed less good agreement, is on the larger side compared with the other nuclides but still well below $1\,\%$. Consequently, a similar agreement as by Mendoza et al. (2014) is achieved, which shows the Geant4 application developed for this dissertation performs on the level Geant4 usually does, which is in good agreement with MCNP for this single-interaction benchmark.

Table 5.2: The average relative deviation between Geant4 and MCNP calculated for the energy bins $> 1\,$eV.

Isotope	ENDF/B-VII.0 (%)	JEFF-3.1 (%)
H-1	0.65	0.61
Li-6	0.40	0.39
Li-7	0.31	0.31
Be-9	0.54	6.41
Cnat	0.29	0.29
O-16	0.68	0.68
Si-28	0.41	0.42
Cr-52	0.51	0.57
Fe-56	0.34	0.42
W-184	0.71	0.71
Pb-208	0.45	0.65

5.2 Analysis of Neutron Flux, Gamma Flux, and Energy Deposition Agreement in Multiple-Interaction Problem

The second code-to-code benchmark uses a spherical volume with an isotropic 14.1 MeV neutron source at the centre (see figure 3.2). It is filled with material of density $1\,\mathrm{g/cm^3}$ containing a single fusion-relevant isotope at a time. In contrast to the single-interaction benchmark, the neutrons undergo multiple interactions before leaving the geometry or being absorbed, allowing minor discrepancies to add up and become more visible.

5.2.1 Analysis of the Neutron Flux Agreement

The average neutron flux in the sphere volume is detected. Results obtained with the newer version Geant4.10.05.p01 and the older version Geant4.10.03 used in the previous benchmark are compared with results obtained with MCNP5-1.6. The JEFF-3.3 nuclear data library is used.

There are issues in the MCNP run of the sphere filled with O-16 for the JEFF-3.3 library. Due to this, MCNP results for O-16 are calculated with the JEFF-3.1 nuclear data library.

Two characteristic deviation values are calculated to quantify the agreement between the Geant4 versions and MCNP. The integral deviation d_{int} has been introduced by Pampin et al. (2012) who have originally created this benchmark to compare other alternative codes to MCNP. They compare the integral flux results of the tested codes. The integral flux is the sum over all N energy bins of the flux Φ_i in the individual energy bins. Accordingly, the integral deviation is calculated like this:

$$d_{int} = \frac{1}{N} \frac{\sum_{i=1}^{N} \Phi_i^{\mathrm{Geant4}} - \sum_{i=1}^{N} \Phi_i^{\mathrm{MCNP}}}{\sum_{i=1}^{N} \Phi_i^{\mathrm{MCNP}}} \quad . \tag{5.2}$$

Secondly, the average relative deviation d also used in the single-interaction benchmark is calculated with equation 5.1.

Since the thermal scattering law (TSL) treatment is disregarded in this benchmark, only energy bins > 1 eV are considered for the calculation of d and d_{int}. Despite large numbers of particle histories, the statistical errors remain too large for some of the energy bins of some isotopes. Except for Pb-208, which has a flux discontinuity and larger errors around 13 MeV, this is the case only for low energy bins. The results in these energy bins are also disregarded for the calculation of the integral and the average relative deviation.

The results for the integral deviation are displayed in table 5.3. All codes tested by Pampin et al. (2012) have an integral flux agreement of within $1\,\%$ with MCNP. It can be seen that Geant4 also produces this level of agreement, with the exception of H-1 where the deviation is only slightly larger. There are some slight but not significant changes between the two Geant4 versions.

Table 5.3: The deviation d_{int} between MCNP and Geant4 of the integral flux result calculated for the energy bins > 1 eV with relative error < 0.01.
(*) For O-16, the Geant4 JEFF-3.3 result was compared with the MCNP JEFF-3.1 result.

Isotope	Geant4.10.03 (%)	Geant4.10.05.p01 (%)
H-1	-1.18	-1.18
Li-6	-0.07	-0.07
Li-7	-0.01	-0.01
Be-9	-0.08	-0.07
Cnat	0.20	0.22
O-16	0.14*	0.58*
Si-28	-0.31	0.03
Cr-52	0.11	0.14
Fe-56	-0.22	-0.10
W-184	-0.04	0.09
Pb-208	-0.04	-0.05

The results for the average relative deviation d calculated according to equation 5.1 are displayed in table 5.4. It can be seen that in contrast to the single-interaction benchmark (see table 5.2), the deviation is now $> 1\,\%$ in many cases.

For Cnat and lighter nuclides, the agreement is comparatively good with deviations below $5\,\%$, which remain approximately unchanged between the different Geant4 versions. The nuclides O-16, Si-28, Cr-52, Fe-56, and Pb-208 show slight or strong improvements for the newer Geant4 version. Consequently, the O-16 and the Cr-52 deviation is $< 5\,\%$ and the Si-28 deviation is even $< 1\,\%$ for Geant4.10.05.p01. Only Fe-56, W-184, and Pb-208 have deviations larger than $5\,\%$ for Geant4.10.05.p01, and only for W-184 the agreement gets worse for the newer Geant4 version.

Table 5.4: The average relative deviation d between Geant4 and MCNP calculated for the energy bins $> 1\,$eV with relative error < 0.01.
(*) For O-16, the Geant4 JEFF-3.3 result was compared with the MCNP JEFF-3.1 result.

Isotope	Geant4.10.03 $(\%)$	Geant4.10.05.p01 $(\%)$
H-1	0.48	0.48
Li-6	1.36	1.36
Li-7	0.72	0.75
Be-9	1.43	1.43
Cnat	1.28	1.37
O-16	7.11*	3.75*
Si-28	11.67	0.57
Cr-52	14.59	3.82
Fe-56	108.24	15.95
W-184	46.70	58.75
Pb-208	11.65	9.67

Next, the average flux and the $Geant4/MCNP$ ratios plotted against the individual energy bins are discussed. Again, the energy range lower than $1\,$eV should be disregarded due to the neglected TSL treatment. The relative error σ of the MCNP calculation is multiplied by three, added or subtracted from one and included in the $Geant4/MCNP$ ratio plot to give an indication of the statistical error range. Figure 5.13 contains results for spheres filled with H-1, Li-6, Li-7, and Be-9, figure 5.14 contains results for spheres filled with Cnat, O-16, and Si-28, figure 5.15 contains results for spheres filled with Cr-52 and Fe-56, and figure 5.16 contains results for spheres filled with W-184 and Pb-208. The cross-sections for the discussed nuclides can be referenced in figure 5.2, 5.3, 5.5, 5.7, 5.9, and 5.11, for the libraries JEFF-3.1 and ENDF/B-VII-0. The differences towards the JEFF-3.3 library used here should only be minor.

The neutrons are created with an energy of 14.1 MeV and lose energy through repeated interactions with the material in the sphere volume, populating the lower energy ranges, until eventually being removed by absorption or escape from the volume. The probability for the different interactions to happen is described by the nuclear cross-section of the respective isotope. At different energy ranges, different interaction types dominate this cross-section. Outside of the thermal energy range, which is excluded from this discussion, material interactions are not increasing the energy of the neutrons. Due to this, the average flux plots are discussed from high energy to low energy.

At the highest energy, the peak of uncollided neutrons can be seen at 14.1 MeV. The height of this peak correlates with the mass number: the lower the mass number, the lower the peak. This is likely caused by setting the density for all isotopes to the same value of $1\,\mathrm{g/cm^3}$. Isotopes with lower mass numbers end up with a higher number density of nuclei in the material and accordingly a higher interaction probability denoted by the macroscopic cross-section. H-1 has the lowest peak, because its low weight causes the number density to be very high (6 times that of Li-6, 208 times that of Pb-208). This outweighs the effect of the total microscopic cross-section, which is higher for example for Li-6 and Li-7.

Below the peak, the average flux result in an energy bin depends on the one hand on the number of neutrons which are added from higher energies due to interactions with one or more secondary neutrons at those energies and on the other hand on the number of neutrons which are removed either to lower energies or entirely due to interactions at this energy. Local dips and peaks in the average flux can be observed due to strong local features of the cross-section. The cause for this is that at energies where the cross-section has an intermediate peak, the removal of neutrons is heightened, leading to a lower average flux, and inversely at intermediate dips in the cross-section, the removal of neutrons is reduced, causing an increased average flux. These features in the average flux spectrum include the dip near 0.02 MeV for Li-6, the dip near 0.25 MeV for Li-7, the small dip near 0.7 MeV for Be-9, a series of dips and one peak between 0.3 MeV and 5 MeV for O-16, a combination of peak and dip near 0.05 MeV and

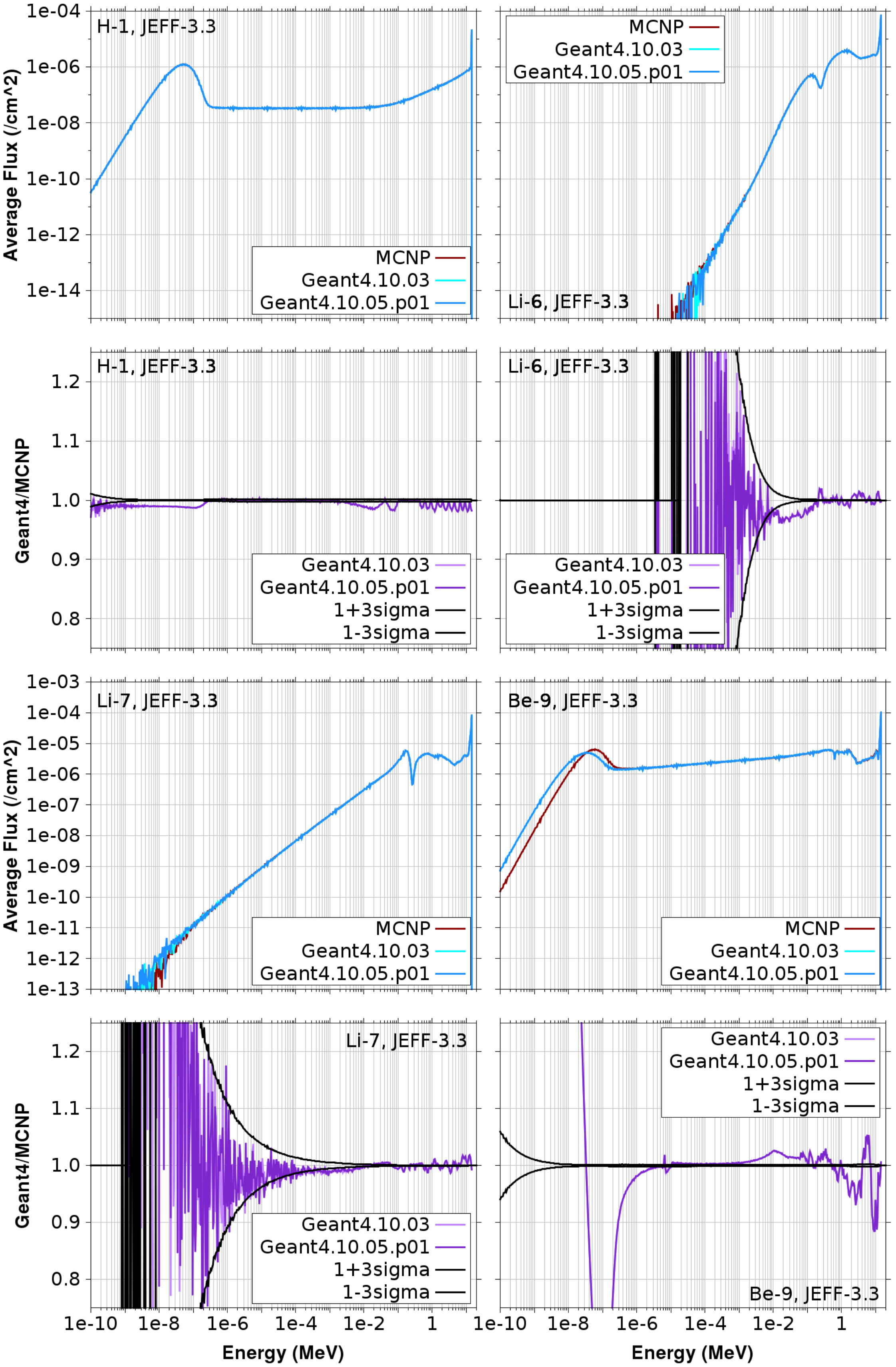

Figure 5.13: The Geant4 and MCNP result for the average neutron flux and the ratio between Geant4 and MCNP result plotted against the energy in a 30 cm sphere filled with H-1 (two upper left plots), Li-6 (two upper right plots), Li-7 (two lower left plots), and Be-9 (two lower right plots). The JEFF-3.3 nuclear data library is used.

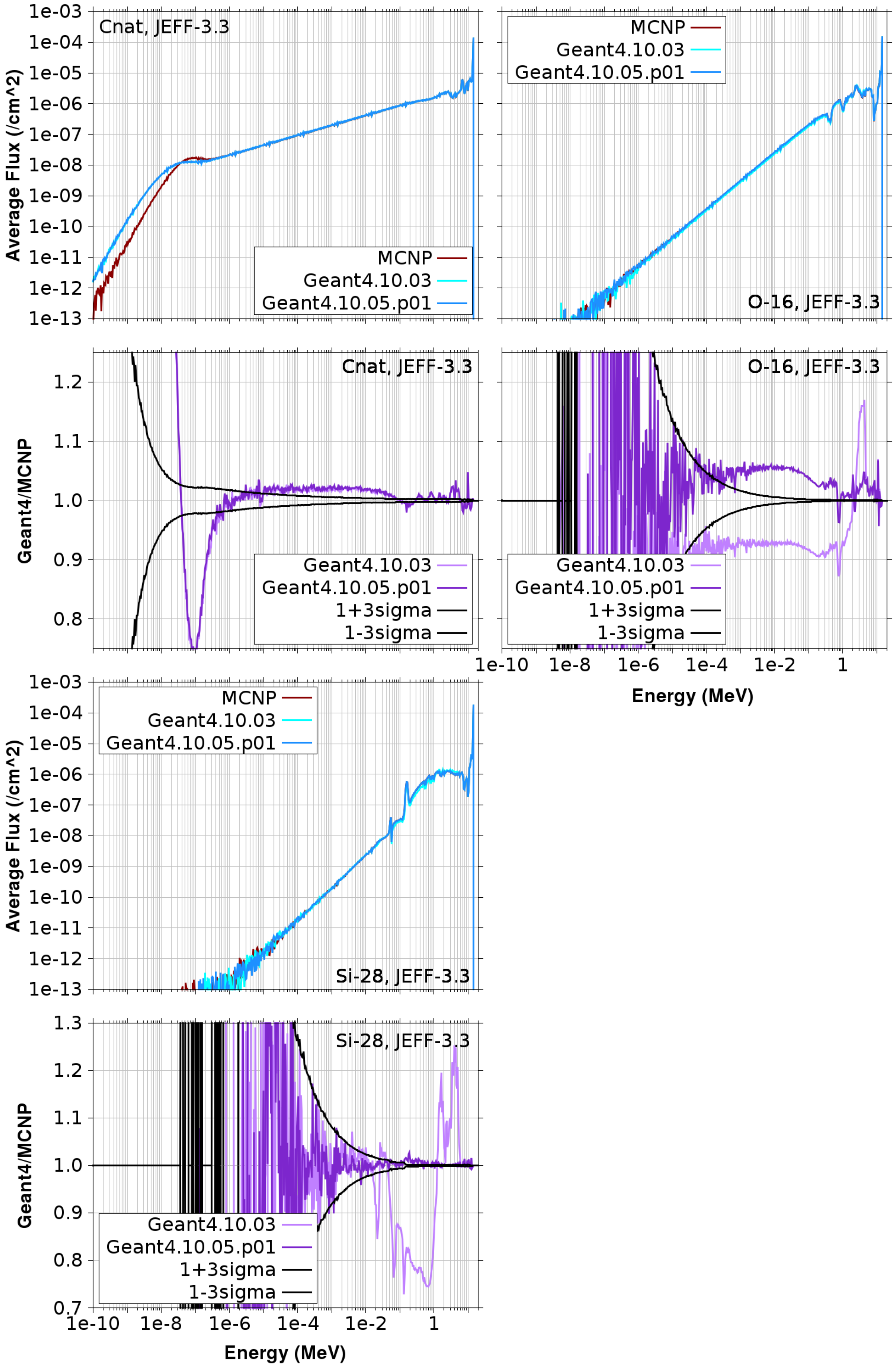

Figure 5.14: The Geant4 and MCNP result for the average neutron flux and the ratio between Geant4 and MCNP result plotted against the energy in a 30 cm sphere filled with Cnat (two upper left plots), O-16 (two upper right plots), and Si-28 (two lower left plots). The JEFF-3.3 nuclear data library is used.

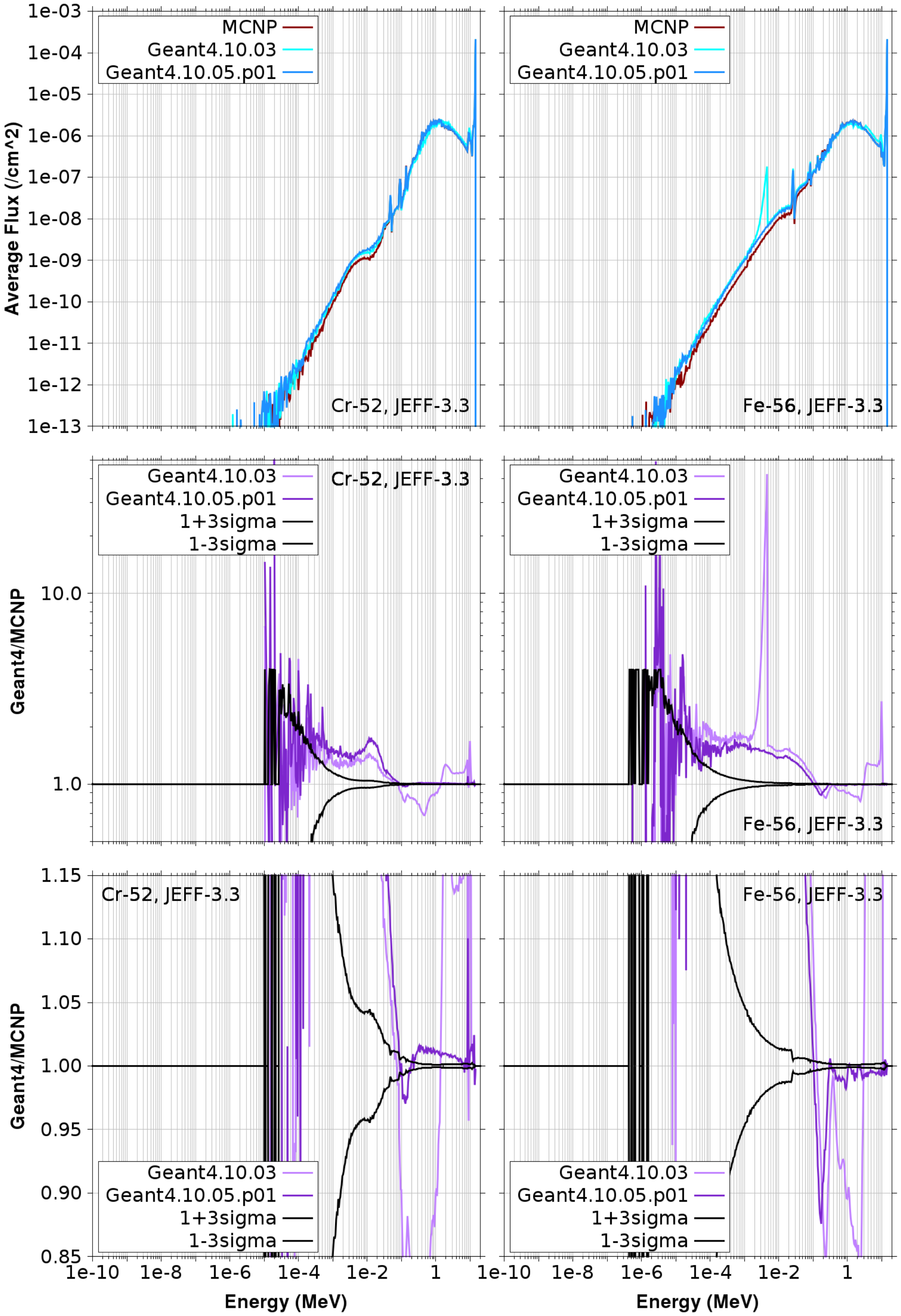

Figure 5.15: The Geant4 and MCNP result for the average neutron flux and the ratio between Geant4 and MCNP result plotted against the energy in a 30 cm sphere filled with Cr-52 (left plots), and Fe-56 (right plots). The JEFF-3.3 nuclear data library is used.

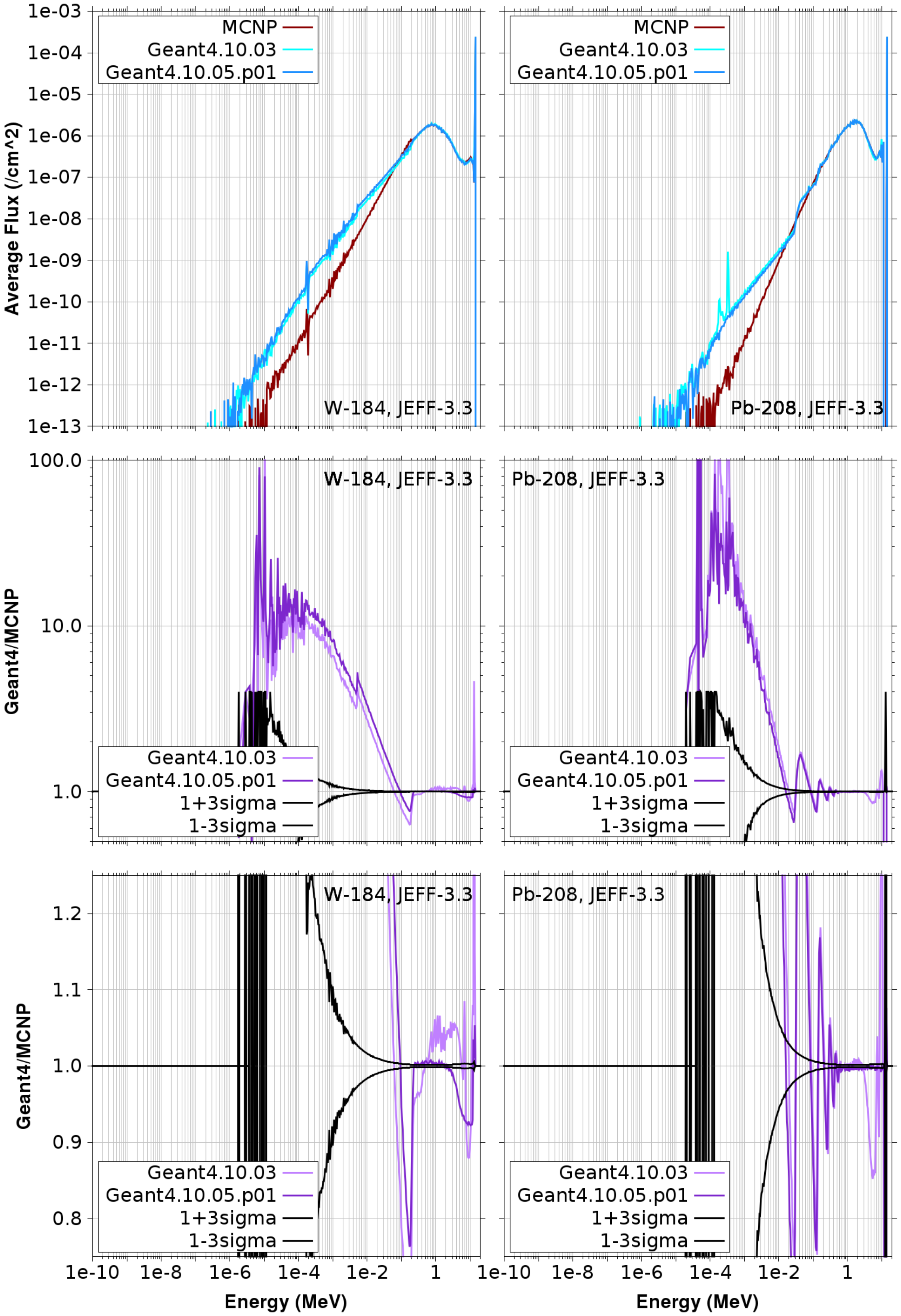

Figure 5.16: The Geant4 and MCNP result for the average neutron flux and the ratio between Geant4 and MCNP result plotted against the energy in a 30 cm sphere filled with W-184 (left plots), and Pb-208 (right plots). The JEFF-3.3 nuclear data library is used.

a peak near 0.15 MeV for Si-28, three combinations of peak and dip between 0.04 MeV and 0.2 MeV for Cr-52, a strong combination of peak and dip at 0.015 MeV for Fe-56, and a combination of peak and dip at $2 \cdot 10^{-4}$ MeV for W-184.

The strongly fluctuating cross-section in the resonance region also has an effect on the average flux spectrum. The features are slighter, because the peaks and dips in the cross-section are very narrow and can average out. They can be observed in the approximate range from 0.01 MeV till 3 MeV for Cr-52 and for Fe-56, from $5 \cdot 10^{-4}$ MeV till $5 \cdot 10^{-3}$ MeV for W-184, and from 0.1 MeV till 2 MeV for Pb-208.

Towards lower energies, the statistics become less good, which also leads to fluctuations. The size of these increases with increasing statistical error.

In the range between 0.1 MeV and below the uncollided neutron peak there are a number of relevant interaction types. The most dominant one is elastic scattering. It keeps the amount of available neutrons constant, just moves them down to lower energies. The amount of transferred energy per interaction depends on both the interaction angle and the mass of the nuclide. The maximum transferable energy ratio E_t/E_0 in a single elastic scattering interaction depending on the nuclide is displayed in table 5.1. It can be seen that for heavier nuclides only very little energy can be transferred, while a single interaction with H-1 can stop a neutron. Due to the dependence on the interaction angle, any amount of energy between 0 and E_t can be transferred per interaction.

There are a number of reactions which can only happen above an energy threshold, which is for all considered nuclides larger than 0.1 MeV, and often much larger than that. Some of these reactions such as (n,p), (n,d), and (n,α) remove neutrons. Since these interaction types only act above their threshold, there is more neutron removal happening at very high energies than at lower energies.

The threshold reactions also include the inelastic scattering (n,n'), and the (n,2n) reactions. These create secondary neutrons with considerably lower energies (especially compared to elastic scattering for heavy nuclides) and in case of (n,2n) the amount of available neutrons at lower energies is doubled. Except for Be-9, which has a low (n,2n) threshold of 1.8 MeV, the threshold for the (n,2n) reaction tends to be close to 10 MeV, while the (n,n') reaction generally has lower thresholds, in some cases close to 0.1 MeV.

As a result, the average flux for H-1 (see figure 5.13), is the only one which decreases smoothly without any local dips or peaks, because the hydrogen cross-section is dominated by a smooth elastic scattering without any resonance peaks and does not have any of the threshold reactions.

The average flux for the heavier nuclides (Cr-52, Fe-56, W-184, and Pb-208, see figures 5.15 and 5.16) has a dip at higher energies, which does not correlate with a peak in the total cross-section, and goes up again in a broad local peak around 1 MeV. It can be seen that the dip is below 10 MeV for Cr-52 and Fe-56, and above 10 MeV for W-184 and Pb-208. For these heavy nuclides, the elastic scattering reaction is having only a weak effect, even when its cross-section is dominant, because of the low amount of removed energy per interaction. In the absence of a strong influence from this reaction, the effect of the (n,n') and the (n,2n) reaction can be seen clearly. The dip at higher energies is due to the strong removal of neutrons. Its position correlates with the position of the (n,2n) threshold and the area where the (n,n') cross-section comes very close to the elastic scattering cross-section, which is below 10 MeV for Cr-52 and Fe-56, and above 10 MeV for W-184 and Pb-208.

The position of the local peak correlates with the energy range of the secondary neutrons of this reaction. The first code-to-code benchmark (see section 5.1), which observes the energy spectrum of secondary particles after a single interaction, also reveals a peak below 1 MeV for W-184 and near 2 MeV for Pb-208.

The neutron-removing reactions with thresholds such as (n,p) and (n,α) have significantly weaker cross-sections. They contribute to the dip at high energies, but to a lesser extent.

For the nuclides lighter than Cr-52, the dominant elastic scattering reaction can remove neutrons to lower energies with fewer interactions than for the previously discussed heavier nuclides. Therefore, the shape of the average flux curve correlates inversely with the shape of the cross-section for most of the nuclides with some slight additional effects of neutron removing reactions.

For O-16 and Si-28, the average flux curve shows a tendency towards the shape of the heavier isotopes: it has a dip at high energy, which does not correlate with the shape of the total cross-section. The broad peak around 1-2 MeV is much slighter than for the heavier isotopes. For these isotopes with intermediate weight, the relative strength of the elastic cross-section is already somewhat decreased. Since the (n,2n) reaction has too high thresholds for these isotopes, the dip is caused by the (n,n') cross-section being close to the elastic cross-section and the slight peak by the secondary neutrons with strongly decreased energy. Additionally, neutron removing reactions with thresholds such as (n,p) and (n,α) also act to remove neutrons in the dip region.

Of these nuclides, only Be-9 has an (n,2n) reaction with a threshold below 14.1 MeV. The resulting average flux curve (see figure 5.13) does not show the same behaviour as the heavy isotopes where (n,2n) is playing a part. This is on the one hand due to the fact that for the light Be-9 nucleus, elastic scattering is more dominant and on the other hand the (n,2n) reaction of Be-9 is a special case. Since the (n,2n) reaction dissolves the Be-9 nucleus into two very energetically favourable He-4 nuclei, this reaction can happen over a larger energy range down to a much lower threshold, which explains the lack of a sharp dip at higher energies. Consequently, the secondary neutron energies are also spread over a much wider range down to lower energies so that no broad peak near 1–2 MeV appears and the average flux is instead kept at a high level throughout.

Below 0.1 MeV, the Li-6 cross-section is dominated by the (n,t) reaction, which removes neutrons and therefore causes a particularly steep decline of the average neutron flux towards lower energies.

For all other nuclides the total cross-section is dominated by elastic scattering in the energy range between $1\,\text{eV}$ and 0.1 MeV. Apart from that, the (n,γ) reaction and in the case of Pb-208 the (n,α) reaction are happening in this energy range. The strength of the dominance of the elastic scattering reaction over these two reactions, which remove neutrons, varies between the nuclides.

For nuclides, which are close in mass, such as Li-7, Be-9, and Cnat, the strength of the dominance of the elastic scattering reaction appears to cause the steepness of the decline of the average flux towards lower energies. For Li-7, which has the steepest decline of the three, the (n,γ) cross-section is only between 2 and 4.5 orders of magnitude smaller than the elastic scattering cross-section. Meanwhile Be-9 and Cnat, which have a 3.5–5.5 orders of magnitude smaller (n,γ) cross-section, have a less steep decline.

In addition, the steepness of the average flux decline towards lower energies is increasing with the nuclide mass. The heaviest nuclide Pb-208 has the steepest decline, even though it has weaker (n,γ) and (n,α) cross-sections than Cr-52, Fe-56, and W-184. This can be explained by a combination of two previously discussed effects.

The first is the effect of setting up this benchmark with the same mass density for all nuclides. This causes the number density to scale opposite to the mass number of the nuclide. At lower number density, the macroscopic cross-section is lowered and therefore the travel distance of a neutron between material interactions is increased. Due to this, neutrons can escape a sphere filled with a heavier nuclide more easily and are then no longer counted towards the average neutron flux.

The second effect is that the amount of energy which can be lost in a single elastic scattering interaction depends on the mass of the nuclide: the heavier the nuclide the lower the energy which can be removed from the neutron this way. For a sphere filled with a heavier nuclide, it takes a neutron more interactions to reach the lower energy part of the average flux spectrum.

In combination, these two effects make it more likely for neutrons to escape from the sphere before reaching lower energies the heavier the nuclide is, causing a steeper average neutron flux decline for heavier nuclides.

Having discussed the underlying physics of the average flux spectrum curves, the agreement between Geant4 and MCNP results is analysed. To this end, the focus shifts to the $Geant4/MCNP$ ratio plots also included in figures 5.13-5.16, which make slight deviations in the average flux spectrum more visible.

One of the goals of this work is to make a suite of benchmark experiments available for monitoring the ongoing development of the Geant4 code. The use of this multiple interaction code-to-code benchmark for this purpose is illustrated by comparing the average flux spectrum results produced by the older version Geant4.10.03 with the results by the newer version Geant4.10.05.p01.

Again, the energy range below $1\,\text{eV}$ has to be disregarded, because the TSL treatment has been neglected. Furthermore, when the statistical error range becomes large, strong statistical fluctuations are to be expected and the results of MC codes become untrustworthy. For this reason, the discussion of the $Geant4/MCNP$ ratio results focuses only on parts where the 3σ error range is below $3\,\%$. Just as previously, the spectrum plots are discussed from high to low energy.

For a sphere filled with **H-1**, the $Geant4/MCNP$ ratio plot is displayed in figure 5.13. In the highest energy range from 0.4 MeV till 14.5 MeV, the deviation fluctuates between -1.9 $\%$ and the 3σ range. This is followed by a small energy range between 0.1 MeV and 0.4 MeV, where the deviation is within the 3σ range. In the following energy range from $3 \cdot 10^{-3}$ MeV till 0.1 MeV, the underestimation by Geant4 exceeds the 3σ range but is no larger than -1.9 $\%$.

In the energy range from 1 eV till $3 \cdot 10^{-3}$ MeV, the deviation between Geant4 and MCNP remains mostly within the range of the statistical 3σ error of $\approx 0.21\,\%$. No correlations between these features and the average flux spectrum or the cross-section, which are both smooth except for the uncollided neutron peak, can be found.

Overall, the deviation between Geant4 and MCNP is between $-1.9\,\%$ and $0.3\,\%$, which constitutes good agreement despite not always remaining within the 3σ range. The differences between Geant4.10.03 and Geant4.10.05.p01 are negligible.

For a sphere filled with **Li-6**, the $Geant4/MCNP$ ratio plot is displayed in figure 5.13. It can be seen that for this nuclide, the statistical error 3σ range already exceeds $3\,\%$ below the energy of $6.3 \cdot 10^{-3}$ MeV. At energies higher than 0.3 MeV, the $Geant4/MCNP$ ratio fluctuates around unity. At the characteristic peak in the cross-section between 0.2 and 0.3 MeV, which causes a dip in the average flux, Geant4 overestimates the MCNP result.

While the elastic scattering reaction is dominant at higher energies, below 0.1 MeV, the (n,t) reaction takes over and Geant4 underestimates the MCNP result. The deviations exceed the 3σ range in many energy bins, but remain between nearly identical $-4.2\,\%$ and 2.0 % for Geant4.10.03 and $-3.9\,\%$ and 2.7 % for Geant4.10.05.p01, which is good agreement. The differences between Geant4.10.03 and Geant4.10.05.p01 become visible only in the range with large statistical error as a result of strong fluctuations.

For a sphere filled with **Li-7**, the $Geant4/MCNP$ ratio plot is displayed in figure 5.13. For this nuclide, the 3σ range already exceeds $3\,\%$ below the energy of $1.6 \cdot 10^{-5}$ MeV. It can be seen in the $Geant4/MCNP$ ratio plot that there are fluctuations around unity at energies above $6 \cdot 10^{-2}$ MeV. In the small energy range between 10^{-2} MeV and $6 \cdot 10^{-2}$ MeV, there is a very slight overestimation. At lower energies, the underestimation only extends slightly below the 3σ range. These features do not correlate with features in the cross-section or average flux spectrum, such as the peak or dip at 0.25 MeV.

In the energy range where the inelastic scattering reaction is happening above just below 1 MeV, the fluctuations in the $Geant4/MCNP$ ratio plot are more pronounced. The deviations exceed the 3σ range in many energy bins, but remain between $-3.9\,\%$ and 1.8 % for Geant4.10.03 and $-4.1\,\%$ and 3.1 % for Geant4.10.05.p01, which is good agreement. The differences between Geant4.10.03 and Geant4.10.05.p01 become visible only in the range with large statistical error as a result of strong fluctuations.

For a sphere filled with **Be-9**, the $Geant4/MCNP$ ratio plot is displayed in figure 5.13. For this nuclide, the 3σ range does not exceed $3\,\%$ anywhere in the energy range above 1 eV. In the energy range above 0.5 MeV there are fluctuations between strong overestimations of up to 5.4 % and underestimations of up to $-11.5\,\%$. In this energy range, the elastic scattering cross-section has fine local peaks between 0.5 MeV and 1 MeV and a broader peak at 2.7 MeV, which both correlate with underestimations. Above its threshold of 1.8 MeV, the (n,2n) reaction is likely also an influence. There is more underestimation happening in this energy range, which means that Geant4 is removing more neutrons. Since the dominant reactions are elastic scattering and (n,2n), more neutrons end up at lower energies, which is likely the cause of the overestimation between 10^{-3} MeV and 0.5 MeV. For the single interaction benchmark, it is found that the effect of (n,2n) and other secondary neutron producing reactions is overestimated for many nuclides, though not for Be-9. This causes a pattern of underestimation at higher energies and overestimation in adjacent lower energies just as observed in the range between 10^{-3} MeV and 4 MeV. Therefore, this might be the cause of the observed deviations.

There is good agreement below 10^{-3} MeV, except for a smaller fluctuation near 7 eV, which does not correlate with any features of the cross-section or average flux spectrum. The overestimation at 1 eV and just above is likely affected by the neglected TSL treatment. This small deviation at this energy is also found in the single interaction benchmark for this nuclide and several others. There it is caused by an unexplained fluctuation in the MCNP-calculated neutron current. In the case of the multiple interaction benchmark, the average flux plot does not reveal the cause for the $Geant4/MCNP$ ratio deviation.

The overall deviations between Geant4 and MCNP are between $-11.5\,\%$ and 5.4 % which is not good. No differences can be observed between Geant4.10.03 and Geant4.10.05.p01.

For a sphere filled with **Cnat**, the $Geant4/MCNP$ ratio plot is displayed in figure 5.14. For this nuclide, the 3σ range does not exceed $3\,\%$ anywhere in the energy range above 1 eV. In the $Geant4/MCNP$ ratio plot, there is a narrow peak at 10 MeV, fluctuations around 1 above 0.1 MeV, and consistent overestimation below 0.1 MeV. The narrow peak correlates with the energy range where the neutron removing (n,α) cross-section is strongest, indicating an underestimation of the effect of this cross-section. Another factor for this could be an imprecise representation of the fluctuations in the elastic or inelastic scattering reaction in this energy range.

The consistent overestimation in the energy range below 0.1 MeV means that in the Geant4 calculation too few neutrons are removed. This could either be caused by a not strong enough (n,γ) reaction or by not enough escape out of the volume due to underestimation of the mean free path. Alternatively, the production of secondary neutrons in the low energy range may be overestimated. Overall, the deviations lie between $-2.0\,\%$ and $4.8\,\%$ for both Geant4 versions, which is good agreement.

For a sphere filled with **O-16**, the $Geant4/MCNP$ ratio plot is displayed in figure 5.14. For this nuclide, the 3σ range already exceeds $3\,\%$ below the energy of $2.75 \cdot 10^{-4}$ MeV. It can be seen in the $Geant4/MCNP$ ratio plot that for the first time there is a strong difference between the versions Geant4.10.03 and Geant4.10.05.p01. Geant4.10.03 has a strong overestimation around 4 MeV, which correlates with a dip in the average flux spectrum and a local peak in the elastic scattering dominated total cross-section; Geant4.10.05.p01 does not have this feature. Below this, Geant4.10.03 underestimates, and Geant4.10.05.p01 mostly overestimates the MCNP result, with smaller deviation than Geant4.10.03.

For Geant4.10.03 it is likely that the elastic scattering reaction is not strong enough in the range near 4 MeV. This leads to a too high flux in this range and causes fewer neutrons to be moved to lower energies, contributing to the underestimation in that range. Additionally, neutron removal through the (n,γ) reaction and escape out of the volume is likely overestimated. Geant4.10.05.p01's less pronounced overestimation at higher energies means that elastic scattering is less underestimated there and affects the amount of available neutrons at lower energies less. In contrast to Geant4.10.03, the neutron removal is underestimated.

Between 0.7 MeV and 0.8 MeV both Geant4 versions have a local dip overlaid on the general trend, which corresponds to a broader peak in the average flux spectrum and to the range between two peaks in the cross-section. In the code-to-code benchmark (see section 5.1), a stronger deviation fluctuation is also found near this energy. A possible cause for this is interpolation imprecision in the library conversion leading to Geant4 not quite reproducing the average neutron flux current feature.

Below this, the trend of going down to a dip at 0.2 MeV and rising again towards lower energies is similar for both Geant4 versions, which indicates a common influence, which is superseded by the effect that causes the Geant4.10.05.p01 $Geant4/MCNP$ result to be in the positive range and the Geant4.10.03 result to be in the negative range.

The benchmark allows to observe the improvement between the version Geant4.10.03 and Geant4.10.05.p01. Geant4.10.03 has deviations between $-12.80\,\%$ and $17.00\,\%$ in the energy range with $3\sigma < 3\,\%$, which are reduced to between $-4.32\,\%$ and $6.78\,\%$ for Geant4.10.05.p01. This still leaves room for further improvements.

For a sphere filled with **Si-28**, the $Geant4/MCNP$ ratio plot is displayed in figure 5.14. For this nuclide, the 3σ range already exceeds $3\,\%$ below the energy of $6.6 \cdot 10^{-3}$ MeV. A marked improvement between the Geant4 versions can be observed in the $Geant4/MCNP$ ratio plot: while the deviation ranges between $-27.14\,\%$ and $25.31\,\%$ for Geant4.10.03, it is decreased to between $-4.09\,\%$ and $2.77\,\%$ for Geant4.10.05.p01.

For Geant4.10.03, there is strong overestimation between 6 MeV and 1 MeV, and strong underestimation at lower energies down to 0.04 MeV. This can be explained by not enough neutrons being moved towards lower energies by elastic or inelastic scattering above 1 MeV, which leads to too little neutrons present at lower energies. Since the neutrons need to lose a significant amount of energy to be removed from the higher energy dip and end up in the broad lower energy peak, the culprit is likely primarily inelastic scattering. This does not account entirely for the quantity of the underestimation in the lower energy range, which indicates there is likely an additional effect in the lower energy range of too strong neutron removal by the (n,γ) reaction or escape from the volume.

Close to the position near 0.055 MeV and 0.15 MeV of dip/peak features in the cross-section and resulting peak/dip features in the average flux spectrum, there are also strong local dips in the $Geant4/MCNP$ ratio of Geant4.10.03, which indicates insufficient precision in reproducing these distinctive features.

For Geant4.10.05.p01, the deviations are much reduced throughout the part of the spectrum with energy above $6.6 \cdot 10^{-3}$ MeV. Only small fluctuations around 1 can be observed, which constitutes good agreement. Near 0.2 MeV, there is a small peak, which is close to the dip/peak features in the total cross-section. This indicates that the cross-section feature does not quite cause the same shape in the resulting peak/dip in the average flux result of Geant4 as for MCNP.

For a sphere filled with **Cr-52**, the $Geant4/MCNP$ ratio plot is displayed in figure 5.15. For this nuclide, the 3σ range already exceeds $3\,\%$ below the energy of $2.4 \cdot 10^{-2}$ MeV. It can be seen in the $Geant4/MCNP$ ratio plot, that there is strong improvement between Geant4.10.03 and Geant4.10.05.-p01. For Geant4.10.03, the $Geant4/MCNP$ ratio alternates between overestimation up to $68.3\,\%$ above 1.5 MeV, underestimation down to $-31.4\,\%$ between 0.08 MeV and 1.5 MeV. The cause for this is that in the average flux spectrum the broad peak of secondary neutrons produced by the (n,2n) and (n,n') reaction is shifted towards higher energies. In fact, the transition between overestimation and underestimation happens close to the threshold of the inelastic scattering reaction.

For Geant4.10.05.p01, the broad peak is no longer shifted. Instead, for a single energy bin near 10 MeV, there is an overestimation of $10.0\,\%$ and much better agreement in the energy range above 0.1 MeV. Between 0.2 MeV and 6 MeV, there is an overestimation rising towards lower energies up to $1.6\,\%$. This correlates with the position of the unresolved resonance region in the total cross-section, which indicates that Geant4.10.05.p01's handling of the unresolved resonances incurs slight deviations, which add up as neutrons slow down.

Additionally, there is a slight underestimation between 0.2 MeV and 0.1 MeV at one of the three strong features in the average flux spectrum which are caused by peaks in the cross-section. This means, Geant4.10.05.p01 is not reproducing this feature in exactly the same way as MCNP.

Below 0.1 MeV, both Geant4 versions strongly overestimate the MCNP result, but Geant4.10.05.-p01's overestimation is worse. In both cases, this indicates not enough neutron loss is happening due to underestimation of the escape out of the volume and the absorption via the (n,γ) reaction or there may be an overestimation of the production of secondary neutrons in this energy range.

Overall, the agreement with MCNP is much improved for Geant4.10.05.p01, but the overestimations of $10\,\%$ in the bin near 10 MeV and of $> 10\,\%$ below 0.1 MeV are still too large to constitute good agreement.

For a sphere filled with **Fe-56**, the $Geant4/MCNP$ ratio plot is displayed in figure 5.15. For this nuclide, the 3σ range already exceeds $3\,\%$ below the energy of $2.2 \cdot 10^{-3}$ MeV. It can be seen in the $Geant4/MCNP$ ratio plot, that there is again a strong improvement between Geant4.10.03 and Geant4.10.05.p01.

For Geant4.10.03, the broad peak is again shifted towards higher energies, which results in strong overestimations of up to $172.0\,\%$ between 3 MeV and 10 MeV and strong underestimations of down to $-18.8\,\%$ between 0.3 MeV and 3 MeV. This indicates that secondary neutrons produced by the (n,2n) and (n,n') reactions are shifted towards higher energies. In contrast to Cr-52, the transition between over- and underestimation does not happen at the threshold of the (n,n') reaction. For Geant4.10.05.p01, there are only very slight deviations fluctuating between an underestimation of down to $-1.8\,\%$ and agreement within the 3σ range in this energy range.

Between 0.1 MeV and 0.3 MeV, both Geant4 versions underestimate the MCNP result in a similar way, which is shifted slightly towards lower energies for Geant4.10.05.p01. In this range, the total cross-section has strong resonance features, which cause fluctuations in the average flux that both Geant4 versions do not fully recreate.

Below 0.1 MeV, there is an improvement for Geant4.10.05.p01, but still both Geant4 versions increasingly overestimate the average flux. This indicates an underestimation of neutron removal due to the (n,γ) reaction and escape out of the volume or there may be an overestimation of the production of secondary neutrons in this energy range.

Near $4.5 \cdot 10^{-3}$ MeV, Geant4.10.03 has a very strong peak in the $Geant4/MCNP$ ratio plot, which is difficult to explain, since there are no strong features in the cross-section, the MCNP average flux, or the $Geant4/MCNP$ ratio of the single interaction code-to-code benchmark in this energy range. It might be caused by an issue in the code, which gives this particular energy too many secondary neutrons, however, since Geant4.10.03 also overestimates the average flux in the adjacent energy range, these secondary particles do not appear to be missing there. This peak is no longer present for Geant4.10.05.p01.

Overall, after the improvement, Geant4.10.05.p01 produces good agreement at energies above 0.1 MeV and bad agreement below.

For a sphere filled with **W-184**, the $Geant4/MCNP$ ratio plot is displayed in figure 5.16. For this nuclide, the 3σ range already exceeds $3\,\%$ below the energy of $4.6 \cdot 10^{-3}$ MeV.

It can be seen in the $Geant4/MCNP$ ratio plot, that for Geant4.10.03, there is a strong overestimation at 13.2 MeV because Geant4.10.03 has a slightly broader uncollided neutron peak which coincides with the adjacent dip of the MCNP result. This is followed by a dip in the $Geant4/MCNP$ ratio down to $-12.0\,\%$ between 7.5 MeV and 11 MeV. As the (n,2n) reaction has its threshold near

7.5 MeV, it is likely that Geant4 overestimates the effect of this reaction. Since this reaction produces two neutrons at lower energies, this overestimation of the neutron removal at high energies has to result in an overestimation of the average neutron flux at the secondary neutron energy range. Indeed the broad peak near 1 MeV is slightly higher, in addition to being shifted towards higher energies just like for the previously discussed nuclides. An additional factor in the underestimation of the average flux in the range 7.5 MeV and 11 MeV is an overestimation of the effects of the various neutron removing reactions with thresholds such as (n,p) and (n,d).

For Geant4.10.05.p01, the overestimation near the uncollided neutron peak is decreased to only up to 5.4 $\%$. Between 2 MeV and 12 MeV, there is an underestimation down to $-7.8\,\%$ due to Geant4 underestimating the higher energy side of the secondary neutron peak. There is no corresponding overestimation at adjacent lower energies, so the deviation does not appear to be primarily caused by Geant4 overestimating reactions which produce secondary neutrons with significantly lower energies, such as inelastic scattering and (n,2n). Instead, it is likely that there is an overestimation of the effects of neutron removing reactions such as (n,p) and (n,α) despite their comparatively low cross-sections. Too much neutron removal at energies close to the uncollided neutron peak is depleting the available neutrons for other reactions so that the underestimation is carried downwards until 2 MeV. This is followed by good agreement between 0.2 MeV and 2 MeV.

Just like for the previous nuclides, the $Geant4/MCNP$ ratio plot has again a dip near 0.1 MeV, followed by a strong overestimation at lower energies. This is the case for both Geant4 versions and they follow the same rising trend, though the Geant4.10.05.p01 result is shifted more towards overestimation. Since for W-184, the resonance region only begins at lower energies than this, it cannot be the cause of this deviation. The underestimation of the neutron removal instead is likely caused by either underestimation of the effect of the (n,γ) reaction or the escape from the volume. Alternatively, there may be an overestimation of the production of secondary neutrons in this energy range.

Near $5 \cdot 10^{-3}$ MeV, the $Geant4/MCNP$ ratio for both Geant4 versions undergoes a step to a lower value, from which the rising trend is continued again. This correlates with the upper end of the resonance region in the dominant elastic scattering and second strongest (n,γ) cross-section. Apparently, the treatment of the resonance region somewhat improves the agreement in this case, but cannot counteract the general trend of increasing overestimation towards lower energies, which are caused by an underestimation of the neutron removal.

It can be seen in the average flux plot that despite the general overestimation at lower energies, both Geant4 versions still reproduce the features caused by the resonance region between $5 \cdot 10^{-3}$ MeV and $5 \cdot 10^{-2}$ MeV, and the peak near $2 \cdot 10^{-4}$ MeV in the total cross-section.

For a sphere filled with **Pb-208**, the $Geant4/MCNP$ ratio plot is displayed in figure 5.16. For this nuclide, the 3σ range already exceeds 3 $\%$ below the energy of $1.9 \cdot 10^{-2}$ MeV. Between 12 MeV and 13.2 MeV, the average flux is zero or very close to it, which causes the discontinuities in the average flux and $Geant4/MCNP$ ratio plot. It can be seen in the $Geant4/MCNP$ ratio plot that there is improvement for Geant4.10.05.p01 at energies above 1 MeV, while the results are nearly identical for both Geant4 versions at lower energies.

For Geant4.10.03, there is an overestimation of up to 34.0 $\%$ between 9 MeV and 10.5 MeV, followed by an underestimation of down to $-9.3\,\%$ between 8 MeV and 9 MeV, a slight overestimation of up to 3.9 $\%$ between 7 MeV and 8 MeV, a more prolonged underestimation of down to $-14\,\%$ between 3 MeV and 7 MeV, and a slight overestimation between 1 MeV and 3 MeV.

This energy range covers the average flux spectrum from the discontinuity, over the dip, and up onto the secondary neutron peak. The overestimation happens in the energy range below 10 MeV where (n,n') takes over from the (n,2n) reaction as second strongest cross-section and is followed by underestimation in the range down to the (n,n') threshold. Potentially, the (n,2n) reaction is underestimated, causing too little neutron removal in the higher energy range and not enough secondary neutrons in the lower energy range. This appears to affect only reactions which create secondary neutrons with comparatively high secondary neutron energy, which end up in the average flux spectrum dip instead of the peak. Additionally, there is underestimation of the average flux dip and overestimation of the secondary neutron peak. This effect is very weak, since the overestimation is not very strong and is caused by the (n,n') reaction.

For Geant4.10.05.p01, the agreement in the energy range above 0.6 MeV and up to the discontinuity is much improved and close to the 3σ range.

Below 0.6 MeV, both Geant4 versions show similar escalating fluctuations in the $Geant4/MCNP$ ratio between over and underestimating the MCNP average flux result until below $2 \cdot 10^{-2}$ MeV, there is only an increasing overestimation. The strong fluctuations can also be seen in the average flux plots: MCNP shows a straight downward trend towards lower energies, while the Geant4 results meander around the MCNP result in a way that appears not representative of realistic physics. There is no clear cause for the fluctuations to be found in the cross-section data: the resonance peaks in the total cross-section do not correlate with the $Geant4/MCNP$ ratio peaks and dips, but the treatment of the resonance region might still be a factor. The cause may lay with the sampling of secondary neutron energies after the elastic or inelastic scattering, or (n,2n) reaction, which produces too many neutrons in one energy range and too few in an adjacent one. Additionally, there may also be an underestimation of the neutron removal by escape or the (n,γ) reaction.

In conclusion, the agreement in the average flux spectrum is good between both Geant4 versions and MCNP for light nuclides, except Be-9 which has a discrepancy of up to $11.5\,\%$ in the energy range above 1 MeV. For O-16 and Si-28, the agreement has improved from version Geant4.10.03 to version Geant4.10.05.p01 to almost good agreement for O-16 and very good agreement for Si-28. For Cr-52, Fe-56, W-184, and Pb-208, Geant4.10.03 has large deviations throughout the energy spectrum. This has improved for Geant4.10.05.p01 to better agreement (good for Cr-52, Fe-56, and Pb-208, almost good for W-184) at energies above ≈ 0.5 MeV.

Below this energy, the $Geant4/MCNP$ ratio plot of these nuclides shows for both Geant4 versions an underestimation followed by an increasing overestimation towards lower energies, which indicates either an underestimation of the neutron removal by escape from the volume and (n,γ) reaction or an overestimation of the production of secondary neutrons in this energy range. In some cases, the treatment of the resonance region may also have an effect. Additionally, there are escalating fluctuations between over- and underestimation before the increasing overestimation for Pb-208. For this there is no clear explanation, but it might be related to the sampling of secondary neutron energies.

The multiple interactions in this benchmark cause a more complex interplay between the different reactions than for the single interaction benchmark. Another difference is that for the single interaction benchmark, the energy range of the primary neutrons reaches up to 20 MeV, which means additional reaction types with thresholds > 14.1 MeV are active. The single interaction benchmark reveals an underestimation of (n,n'), (n,2n) and similar reactions' impact resulting in overestimation of available neutrons at higher energies and underestimation at lower energies. This appears to affect the multiple interaction benchmark result calculated with Geant4.10.03 for Si-28, Fe-56, and Cr-52, while it is less clear for W-184 and Pb-208. For all these nuclides, Geant4.10.05.p01 has marked improvements in the affected energy range likely due to the underlying cause having been fixed for the newer version of the code.

5.2.2 Comparison of Geant4's Neutron Flux Agreement with other Alternative Codes

The multiple interaction benchmark has originally been developed by Pampin et al. (2012) (also published with more details in Davis (2012)) to evaluate alternative codes to MCNP. They have tested the codes Tripoli4, Serpent, Serpent-2, and COG11 against MCNP5. They have used the ENDF/B-VII.0 nuclear data library and 10^9 histories to test 390 nuclides. The nuclear data library format is ACE for MCNP, Serpent, and Serpent-2, while the nuclear data has to be pre-processed into the code's format for Tripoli4 and COG11.

In section 5.2.1, the agreement of the total neutron flux result is discussed. Geant4 produces the same level of integral deviation $\leq 1\,\%$ as the other codes.

Now the agreement throughout the energy spectrum is analysed. For this, the $Geant4/MCNP$ ratios are plotted with the same range as the $Code/MCNP$ ratio plots by Davis (2012). For the Geant4-plots, the relative error σ of the MCNP calculation is multiplied by three, added or subtracted from one and included in the $Geant4/MCNP$ ratio plot to give an indication of the statistical error range.

Davis (2012) has found very good spectral agreement with MCNP for Serpent-2 with on average $< 1\,\%$ of energy bin results being outside the 3σ range across all nuclides. Serpent has larger deviations only for fissionable nuclides due to issues with the delayed neutron treatment. Fissionable nuclides are not investigated in this dissertation due to the low relevance for fusion energy applications. This better agreement than between Geant4 and MCNP is likely due to Serpent, Serpent-2, and MCNP using very similar physics algorithms and the same nuclear data library format, which avoids acquiring interpolation inaccuracies and errors during the conversion process.

Since the multiple interaction code-to-code benchmark reveals that the newer version Geant4.10.05.p01 has marked improvements over the older version Geant4.10.03, Geant4.10.05.p01 is used for the comparison with the other alternative codes. In a previous Geant4.10.03 calculation with multiple libraries, it has been found that the $Geant4/MCNP$ ratio spectra for the nuclides chosen for the following discussion are nearly identical between the libraries JEFF-3.3 and ENDF/B-VII.0. These are the nuclides Li-6, O-16, and Si-28. For these nuclides, also the single interaction benchmark average relative deviation displayed in table 5.2 is nearly identical between the older JEFF version JEFF-3.1 and ENDF/B-VII.0. Therefore, Geant4.10.05.p01 JEFF-3.3 results can be used to compare with the other alternative codes' ENDF/B-VII.0 results.

It is found that Geant4.10.05.p01 has better agreement for some nuclides and worse agreement for others. For comparison, the $Geant4/MCNP$ ratio results already displayed in figures 5.13, 5.15, and 5.16 have been replotted with the same ranges as the ones by Davis (2012).

As example for worse agreement with MCNP for Geant4 than for the other codes, the $Code/MCNP$ ratios for a sphere filled with **O-16** can be seen in figure 5.17. Due to a problem with the JEFF-3.3 MCNP calculation, the library has been replaced with JEFF-3.1 for MCNP. This should not cause a significant difference, because calculations with the Geant4.10.03 code revealed a nearly identical $Geant4/MCNP$ ratio as for JEFF-3.1 and ENDF/B-VII.0.

It can be seen that the Tripoli $Code/MCNP$ ratio remains well below $5\,\%$ nearly everywhere except in a few bins in the low energy range where the statistical error is rising. The COG11 $Code/MCNP$ ratio is even closer to 1 throughout. For Geant4.10.05.p01, there is improvement towards Geant4.10.03, but the deviation is still larger than $5\,\%$ for significant parts of the energy range. In the rest of the energy range, the deviation is larger than for Tripoli and COG11 nearly everywhere.

As example for better agreement with MCNP for Geant4 than for the other codes, the $Code/MCNP$ ratios for a sphere filled with **Si-28** are displayed in figure 5.18. Here it can be seen that Geant4.10.03 has worse agreement than the other codes, but for Geant4.10.05.p01 this is improved to a $Code/MCNP$ ratio $< 3\,\%$ everywhere while the Tripoli4 and COG11 deviations are higher for most of the energy spectrum.

For those two examples, it becomes apparent that for the same nuclide different codes can have better and worse agreement in different energy ranges: despite generally worse agreement, Geant4 has better agreement than the other codes in the energy range near 1 MeV for O-16 and COG11 has the best agreement around 10 MeV for Si-28 despite having the worst agreement in most of the energy spectrum.

Another example for this behaviour is the result for a sphere filled with **Li-6**, which can be seen in figure 5.19. Tripoli and Geant4 have a similar level of agreement with deviations $< 2\,\%$ throughout most of the energy range between 0.1 MeV and 8 MeV. COG11 has significantly worse agreement in this range with deviations reaching beyond $10\,\%$, but in the energy range above and below this range,

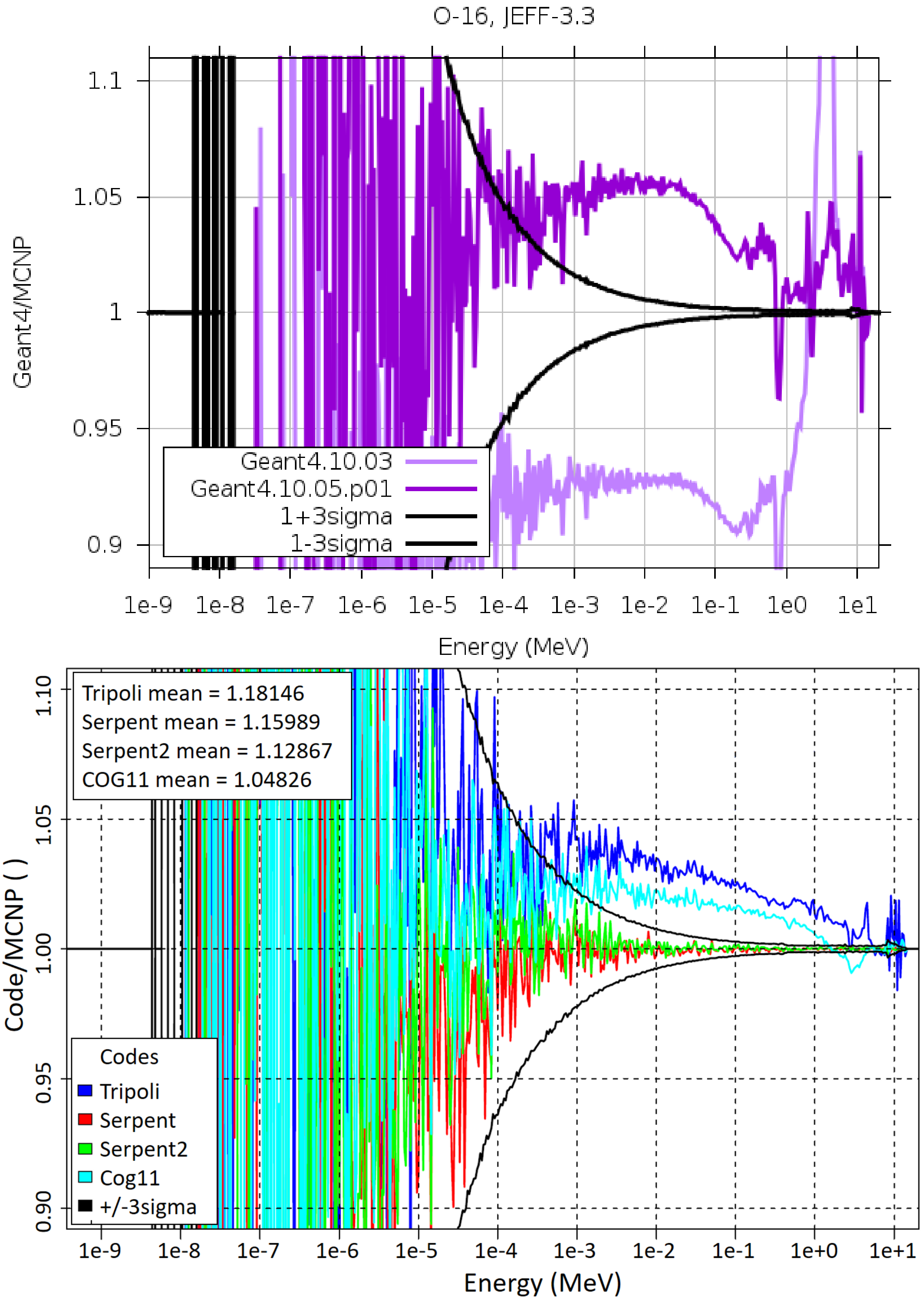

Figure 5.17: Comparison of the agreement between Geant4 (upper plot) and other codes (lower plot, edited from Davis (2012)) and MCNP for the average neutron flux in a 30 cm sphere filled with O-16 plotted against the energy. For the $Geant4/MCNP$ ratio, the JEFF-3.3 nuclear data library is used for the Geant4 calculation and JEFF-3.1 for the MCNP calculation. For the other codes, the ENDF/B-VII.0 nuclear data library is used.

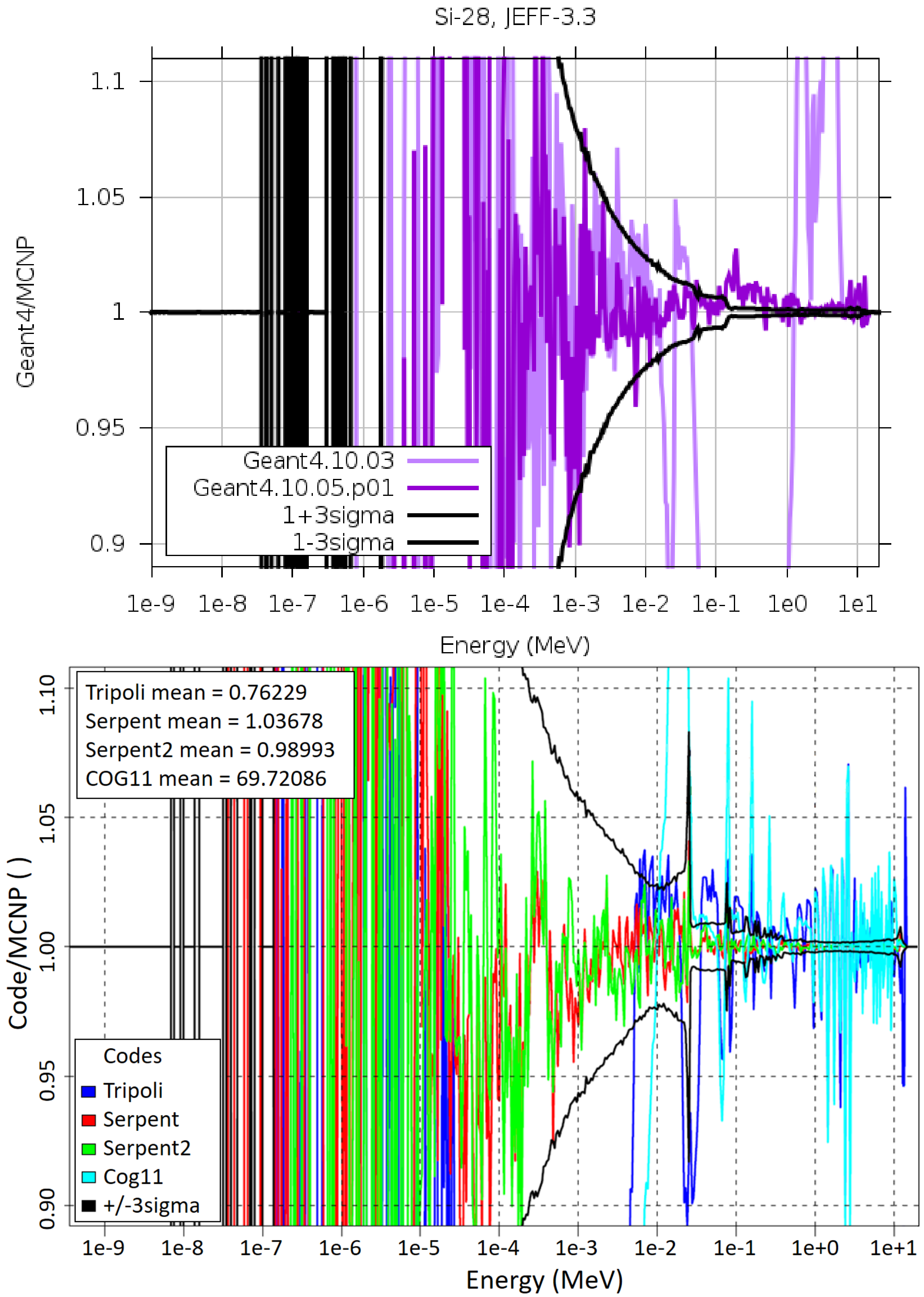

Figure 5.18: Comparison of the agreement between Geant4 (upper plot) and other codes (lower plot, edited from Davis (2012)) and MCNP for the average neutron flux in a 30 cm sphere filled with Si-28 plotted against the energy. For the Geant4 result the JEFF-3.3 nuclear data library and for the other codes the ENDF/B-VII.0 nuclear data library is used.

the COG11 deviation is the smallest. In the energy range $<$0.1 MeV, Geant4 has worse deviation than Tripoli, while in the energy range > 8 MeV, Geant4 has better deviation than Tripoli.

In conclusion, Geant4.10.05.p01 is approximately on a similar agreement level as Tripoli4 and COG11 for the considered isotopes, while Serpent and Serpent-2 have better agreement.

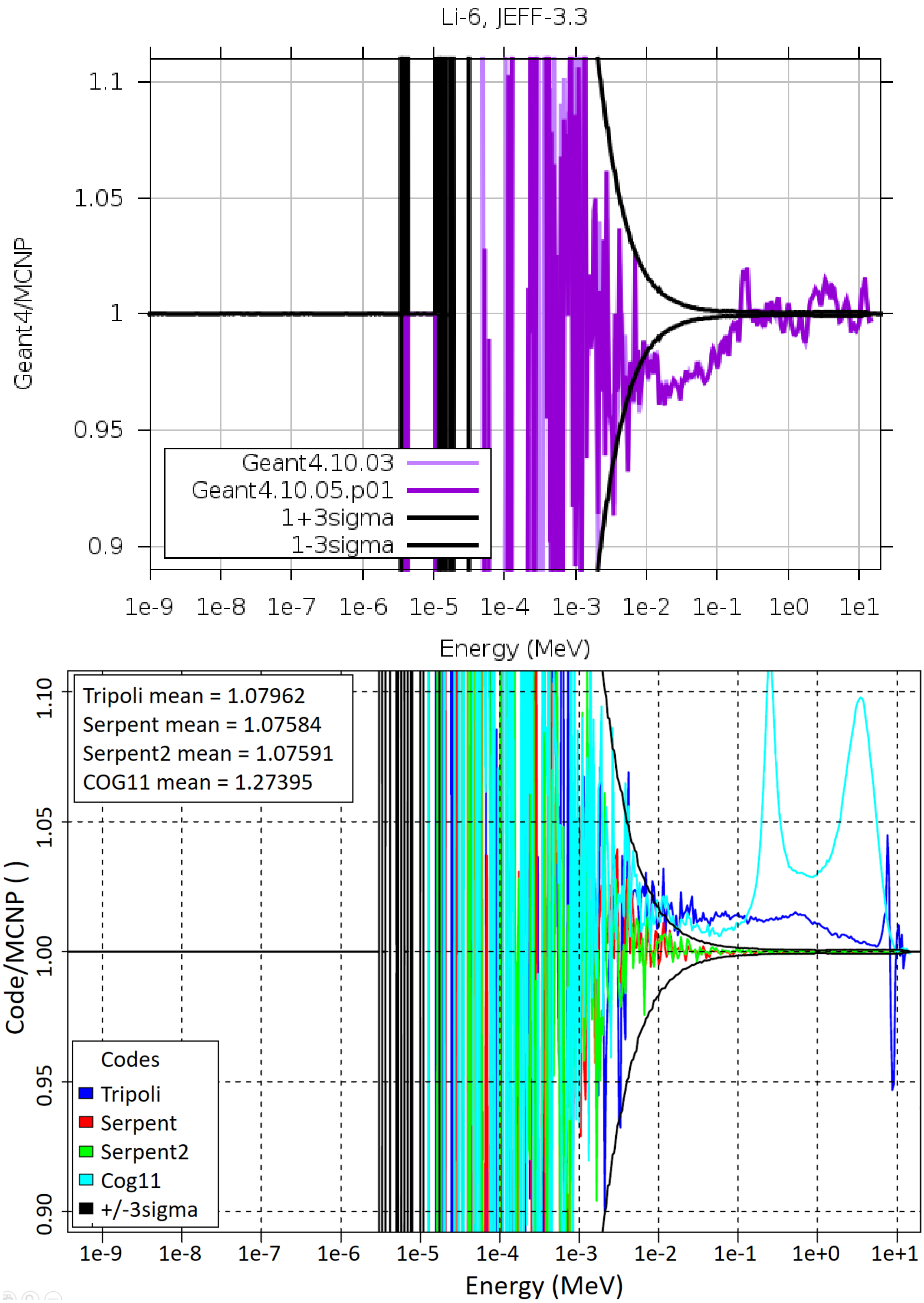

Figure 5.19: Comparison of the agreement between Geant4 (upper plot) and other codes (lower plot, edited from Davis (2012)) and MCNP for the average neutron flux in a 30 cm sphere filled with Li-6 plotted against the energy. For the Geant4 result the JEFF-3.3 nuclear data library and for the other codes the ENDF/B-VII.0 nuclear data library is used.

5.2.3 Analysis of Gamma Flux and Energy Deposition Agreement

For the gamma flux and energy deposition part of the benchmark, only the version Geant4.10.05.p01 is used, because the neutron flux part of the multiple interaction benchmark (see section 5.2.1) reveals a marked improvement over the earlier version Geant4.10.03. For H-1, 10^7 particle histories have been calculated and for all other isotopes 10^8 particle histories. The statistical errors are less than $1\,\%$.

Nuclear cross-section data is taken from the libraries JEFF-3.3, ENDF/B-VIII.0, and FENDL-3.1. The Geant4 library version of FENDL-3.1 is not an official release available on the IAEA website (`https://www-nds.iaea.org/geant4/`) (Mendoza and Cano-Ott, 2018b). It has been provided directly by Mendoza and Cano-Ott (2018a). For FENDL-3.1, Cnat is replaced with C-12.

In figures 5.20 and 5.21, the average total gamma flux and the total energy deposition in the sphere for different nuclides are displayed. Additionally, the ratios between Geant4 and MCNP results are shown. It can be seen that for light nuclides the gamma production varies strongly depending on the nuclide, while for heavier nuclides it mostly remains in the same order of magnitude. The energy deposition declines with rising nuclide mass number. This is likely due to the declining number density in the sphere due to the constant mass density.

For **H-1**, the gamma production and energy deposition have the highest values for all nuclides. The gamma flux and energy deposition agreement between Geant4 and MCNP is close to 1 for all libraries.

For **Li-6**, the total gamma flux calculated by MCNP is more than two orders of magnitude lower than for H-1, while the Geant4 result is only slightly lower. This leads to an extreme deviation between Geant4 and MCNP of $\approx 23000\,\%$ for all libraries. For the total energy deposition, the Geant4 value is instead lower than the MCNP value, but the underestimation is only $16\,\%$ for all libraries.

For **Li-7**, the total gamma flux is higher than for Li-6 for both libraries, but for Geant4 the difference is small, while it is several orders of magnitude for MCNP. Geant4 again overestimates the total gamma flux result; this time by $250\,\%$ for all libraries. For the energy deposition, the Geant4 value is again lower than the MCNP value: Geant4 underestimates the energy deposition result by $33\,\%$ for all libraries.

For **Be-9**, the total gamma flux is much lower than for Li-7 for both Geant4 and MCNP and all libraries. The agreement between Geant4 and MCNP is very good for JEFF-3.3 and ENDF/B-VIII.0, while there is an overestimation of $20\,\%$ for FENDL-3.1. For MCNP, the energy deposition result is lower than for Li-7. For Geant4, it rises for ENDF/B-VIII.0 and FENDL-3.1 to a result close to the MCNP result, while it sinks for JEFF-3.3 to an underestimation of $57\,\%$. Only the ENDF/B-VIII.0 library achieves good agreement for both gamma flux and energy deposition.

For **Cnat**, the total gamma flux is higher than for Be-9 for both Geant4 and MCNP and all libraries. Geant4 significantly overestimates the gamma flux for all libraries by $> 220\,\%$ with FENDL-3.1 being slightly worse than the other two. The energy deposition sinks compared to Be-9. Except for the ENDF/B-VIII.0 result of MCNP, which is $16\,\%$ higher, all code and library combinations arrive at nearly the same result.

In a sphere filled with **O-16**, the total gamma flux calculated by Geant4 is nearly the same as for Cnat for all libraries, while it approximately doubles for all libraries for MCNP. As a result, the overestimation by Geant4 decreases to $22\,\%$. The energy deposition falls slightly compared to Cnat and there is good agreement between Geant4 and MCNP for all libraries.

For **Si-28**, the total gamma flux rises more strongly for MCNP compared to O-16 to nearly the same value as for Geant4 for all libraries. The energy deposition falls slightly compared to O-16 and the agreement between Geant4 and MCNP remains good for all libraries.

For **Cr-52**, the gamma flux compared to Si-28 remains nearly constant for MCNP and JEFF-3.3 and FENDL-3.1, while rising slightly for ENDF/B-VIII.0, and slightly more strongly for all Geant4 and library combinations. As a result, there is good gamma flux agreement for ENDF/B-VIII.0, an overestimation by Geant4 of $21\,\%$ for JEFF-3.3, and an overestimation of $60\,\%$ for FENDL-3.1. The energy deposition in a sphere filled with Cr-52 is lower than for Si-28 for both Geant4 and MCNP. For MCNP, the value varies between libraries: it is lowest for FENDL-3.1, higher for ENDF/B-VIII.0 and highest for JEFF-3.3. The Geant4 results for JEFF-3.3 and FENDL-3.1 are even higher, while the Geant4 result for ENDF/B-VIII.0 is very close to the MCNP result for the same library. Accordingly, the deviation is only $2\,\%$ for ENDF/B-VIII.0, $21\,\%$ for JEFF-3.3, and $60\,\%$ for FENDL-3.1.

For **Fe-56**, the gamma flux remains nearly constant compared to Cr-52 and Si-28 for MCNP. For Geant4, the result for JEFF-3.3 and FENDL-3.1 also remains nearly constant compared to Cr-52 and the result for ENDF/B-VIII.0 rises slightly. As a result, the agreement for JEFF-3.3 and FENDL-3.1 improves to a deviation of $12\,\%$, while for ENDF/B-VIII.0 it worsens to $24\,\%$. The energy deposition agreement is good for all libraries.

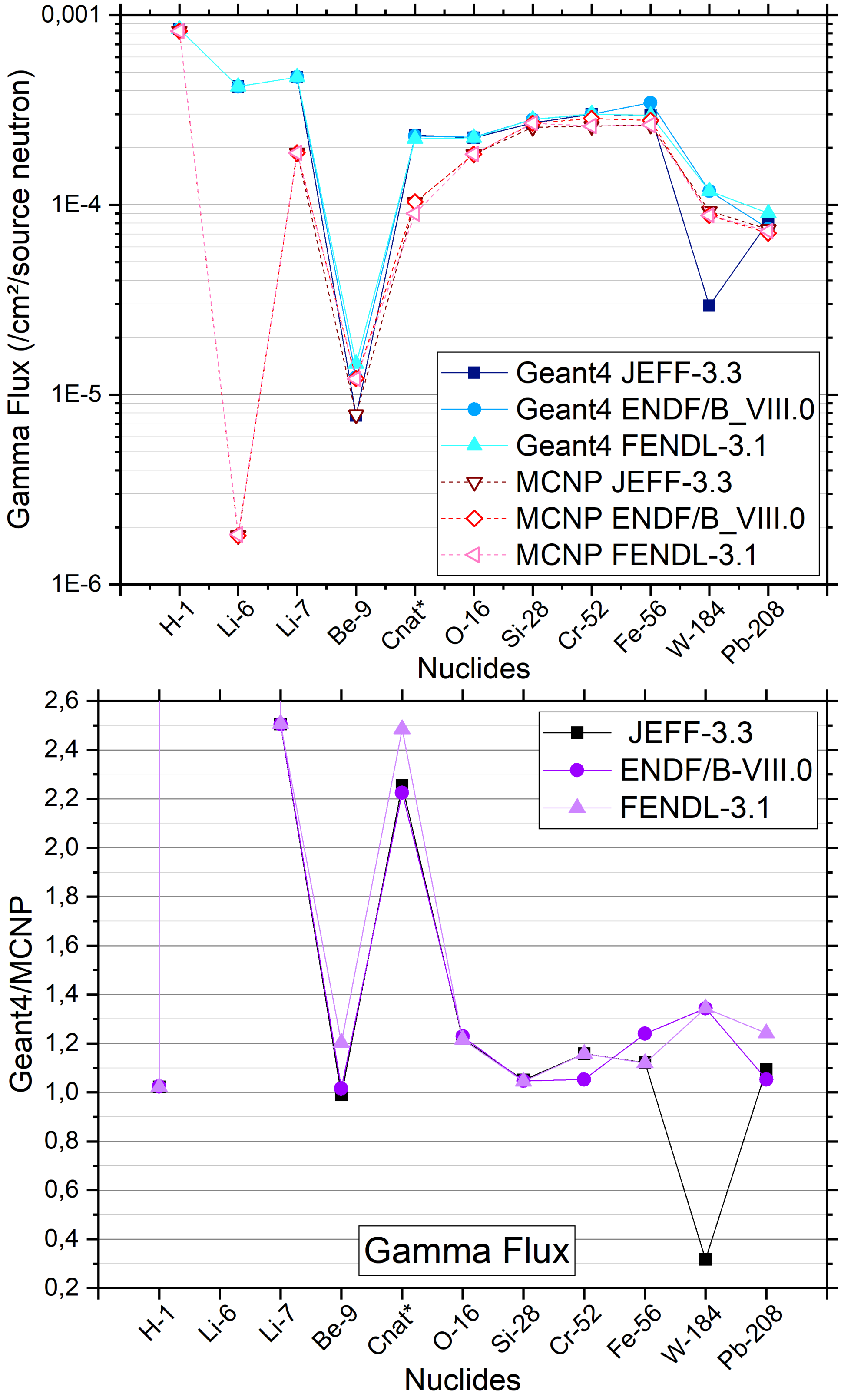

Figure 5.20: The average total gamma flux (top) and the ratio between Geant4 and MCNP result (bottom) in a sphere filled with a fusion-relevant nuclide at a time. The Li-6 gamma flux result for all libraries lies far out of range at ≈ 230. The error bars are too small to be visible.
(*) For FENDL-3.1, Cnat is replaced by C-12.

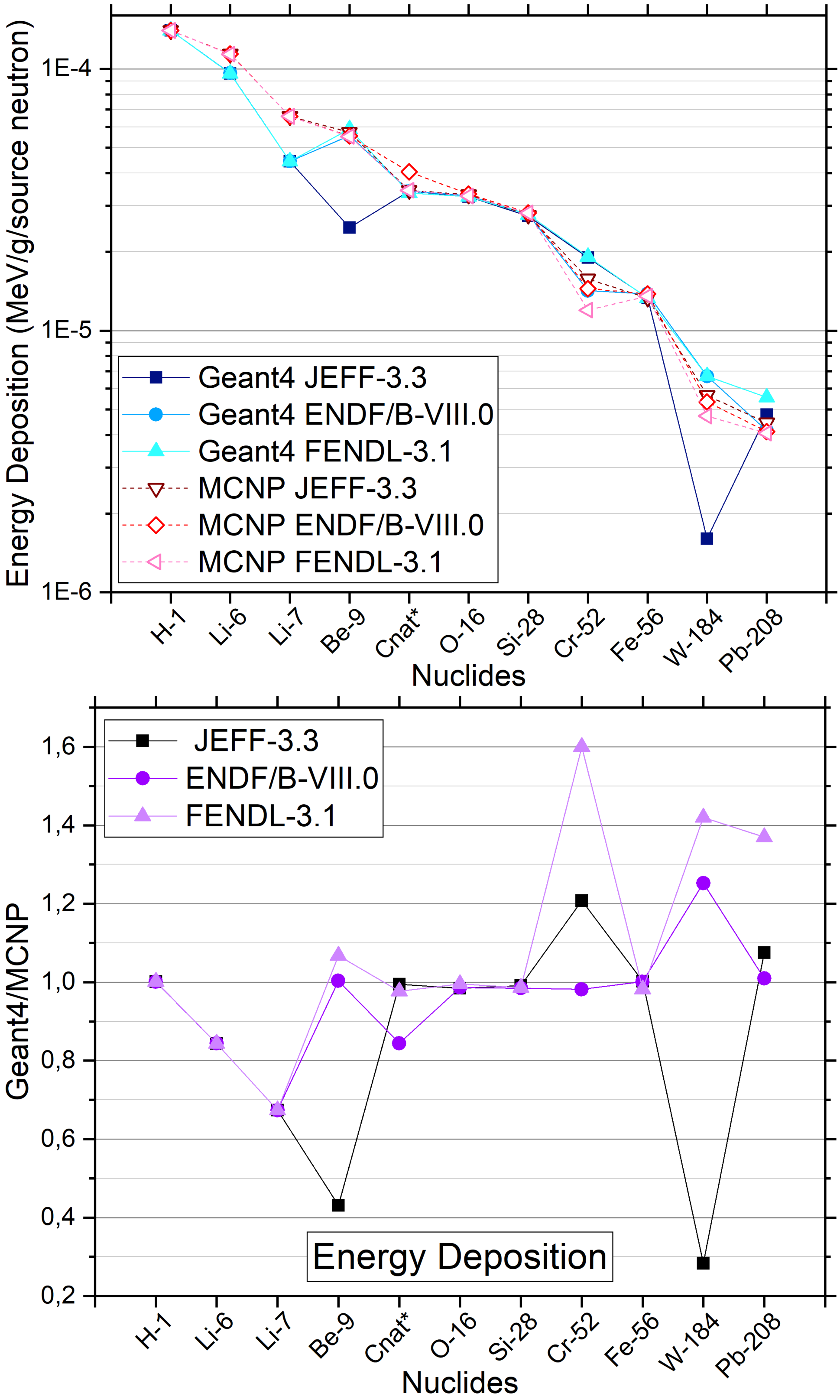

Figure 5.21: The total energy deposition (top) and the ratio between Geant4 and MCNP result (bottom) in a sphere filled with a fusion-relevant nuclide at a time. The error bars are too small to be visible. (*) For FENDL-3.1, Cnat is replaced by C-12.

For **W-184**, the total gamma flux sinks compared to Fe-56. It is overestimated by Geant4 by 34 % for ENDF/B-VIII.0 and FENDL-3.1, and underestimated by 68 % for JEFF-3.3. The energy deposition also sinks compared to Fe-56. Like for the gamma flux, Geant4 produces nearly the same result for ENDF/B-VIII.0 and FENDL-3.1, which is higher than the MCNP results for all libraries, while the JEFF-3.3 result of Geant4 is much lower. This causes a strong underestimation of 72 % for JEFF-3.3. Since the MCNP result for FENDL-3.1 is lower than for ENDF/B-VIII.0, the nearly identical Geant4 results for these libraries cause different overestimations: 25 % for ENDF/B-VIII.0 and 42 % for FENDL-3.1.

For **Pb-208**, the total gamma flux is slightly lower than for W-184. The Geant4 results are generally higher than the MCNP results. The deviation varies between 5 % for ENDF/B-VIII.0 and 24 % for FENDL-3.1. The energy deposition is lower for Pb-208 than for W-184. MCNP produces nearly identical results for ENDF/B-VIII.0 and FENDL-3.1, while the JEFF-3.3 result is slightly higher. For Geant4, the ENDF/B-VIII.0 result is very close to the MCNP result, while the JEFF-3.3 and FENDL-3.1 results have a deviation of 7 % and 37 %.

In conclusion, the agreement between Geant4 and MCNP is often very different for different libraries. Sometimes there are strong discrepancies for one or two libraries, while a third library has a ratio close to 1. For the isotopes H-1 and Si-28, all libraries produce ratios close to one for both gamma flux and energy deposition.

There is a correlation between the ratios of the gamma flux and the energy deposition: the size of the discrepancy varies, but the order of the libraries in over- or underestimation is similar. In some cases (e.g. for Cnat* and Cr-52), the results for different libraries are close together for Geant4 for both gamma and energy deposition, while there are stronger discrepancies between libraries for MCNP. In other cases (e.g. for Be-9, W-184, and Pb-208), the deviations between libraries are small for MCNP compared to Geant4.

To investigate this further, gamma flux and energy deposition spectra have been calculated for selected nuclide and library combinations:

- Fe-56 and JEFF-3.3, to establish the spectral agreement for a case were the integral agreement is very good for the energy deposition and good for the gamma flux.
- Li-6 and JEFF-3.3, to look into the extreme deviation between MCNP and Geant4 result for the total gamma flux.
- W-184 and JEFF-3.3 and FENDL-3.1, to investigate the strong discrepancies between libraries for both gamma flux and energy deposition.

The average gamma flux spectrum calculated by MCNP and Geant4 using the JEFF-3.3 library for a sphere filled with **Fe-56** and the spectrum of the ratio between Geant4 and MCNP result is displayed in figure 5.22. It can be seen that in the range between 0.5 MeV and 12 MeV there is very close agreement. At $7 \cdot 10^{-3}$ MeV, the MCNP spectrum has a peak, which Geant4 does not reproduce, which leads to a strong underestimation. In the rest of the energy range, Geant4 overestimates the MCNP result. This combines to the total 12 % overestimation.

Along with the library data itself, Mendoza and Cano-Ott (2018a) publish results of a calculation with the single interaction benchmark discussed in section 5.1 also for all secondary particle types, including gammas (Mendoza and Cano-Ott, 2018b). This benchmark serves to investigate the original gamma production for a nuclide without any transport. Here, the version Geant4.10.04.p01 is compared to MCNP6.1. The result for Fe-56 and JEFF-3.3 is displayed in figure 5.23. It can be seen that the Geant4 result follows the the basic curve of the MCNP spectrum, but does not represent the overlaying peaks well. There is an overestimation of the small peak near 9.5 MeV and the big peak near 7.5 MeV, while multiple peaks in the energy range between 0 MeV and 7.5 MeV are not reproduced at all or only to a lesser extent. In combination, the overestimation of some peaks and the lack of other peaks make it unclear whether there is an over- or underestimation by Geant4 of the gamma production in Fe-56 with a JEFF-3.3 library. Therefore it is also unclear whether the overestimation by Geant4 for the multiple interaction benchmark is caused only by this discrepancy in the gamma production or also by discrepancies in the gamma transport.

For a sphere filled with Fe-56, the energy deposition spectrum calculated by Geant4 and MCNP using the JEFF-3.3 library and the spectrum of the ratio between Geant4 and MCNP result is displayed in figure 5.24. For MCNP, the energy deposition contribution of neutrons and gammas can be distinguished and this is included in the plot. For Geant4, the energy deposition is calculated in a different way from all secondary particles, which makes such a distinction not possible.

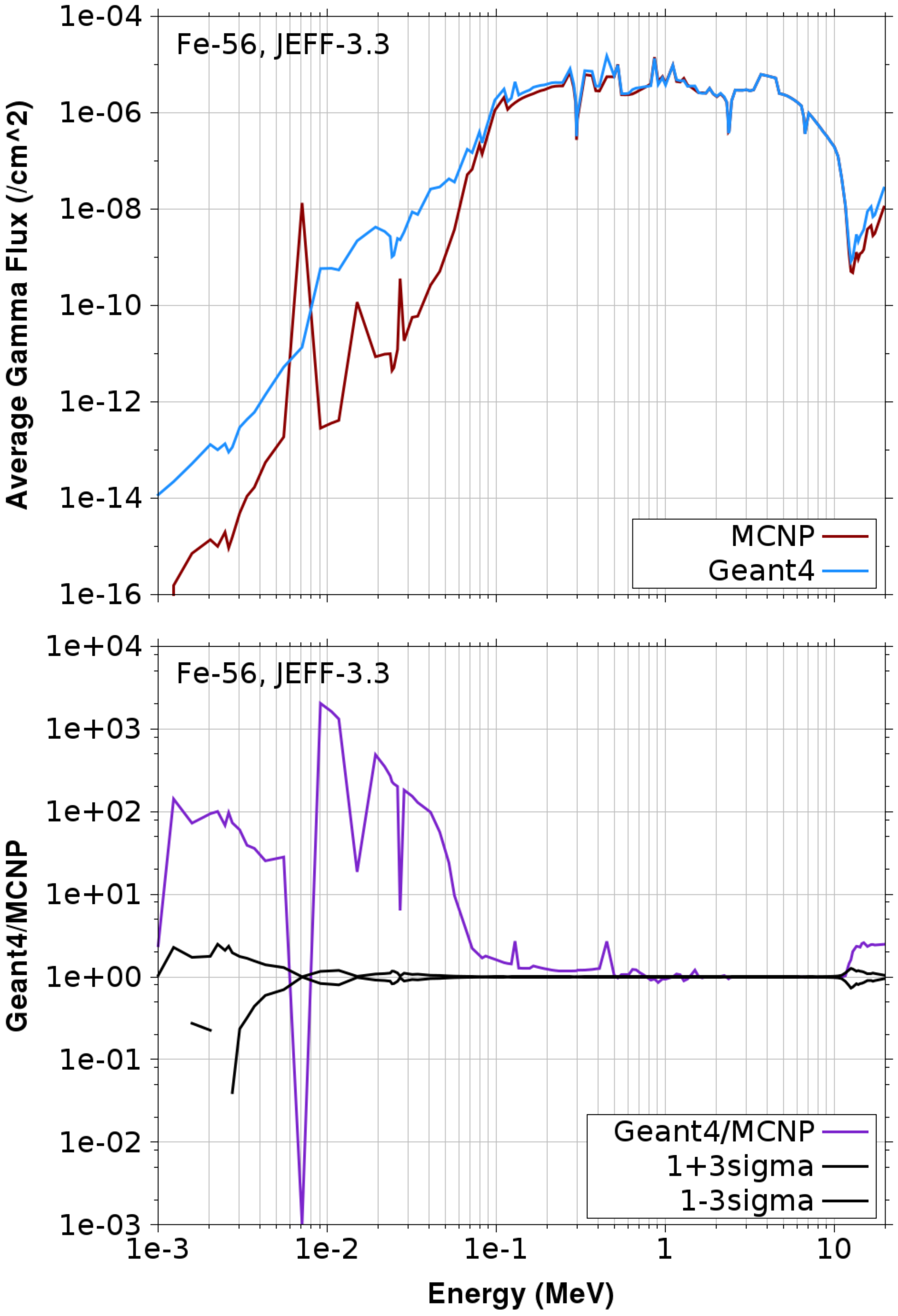

Figure 5.22: The gamma flux spectrum (top) and the ratio between Geant4 and MCNP result for the gamma flux spectrum calculated in a sphere filled with Fe-56 for the JEFF-3.3 library.

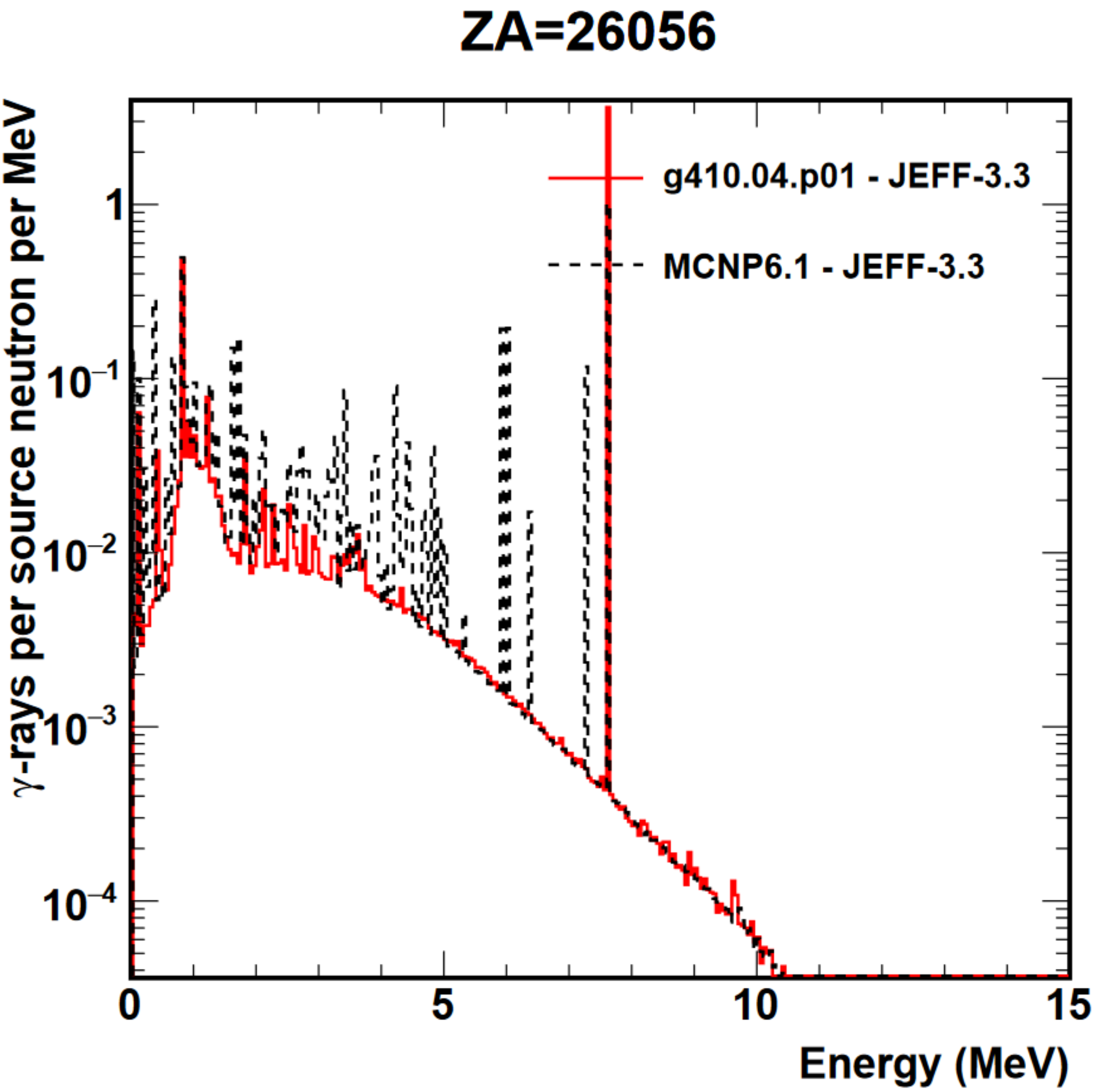

Figure 5.23: Comparison of Geant4 and MCNP result for the number of gamma rays per source neutron and energy plotted against the energy in the single-interaction benchmark, for a cylinder filled with Fe-56 using the JEFF-3.3 library (published by Mendoza and Cano-Ott (2018a) on the Geant4 library website (Mendoza and Cano-Ott, 2018b)).

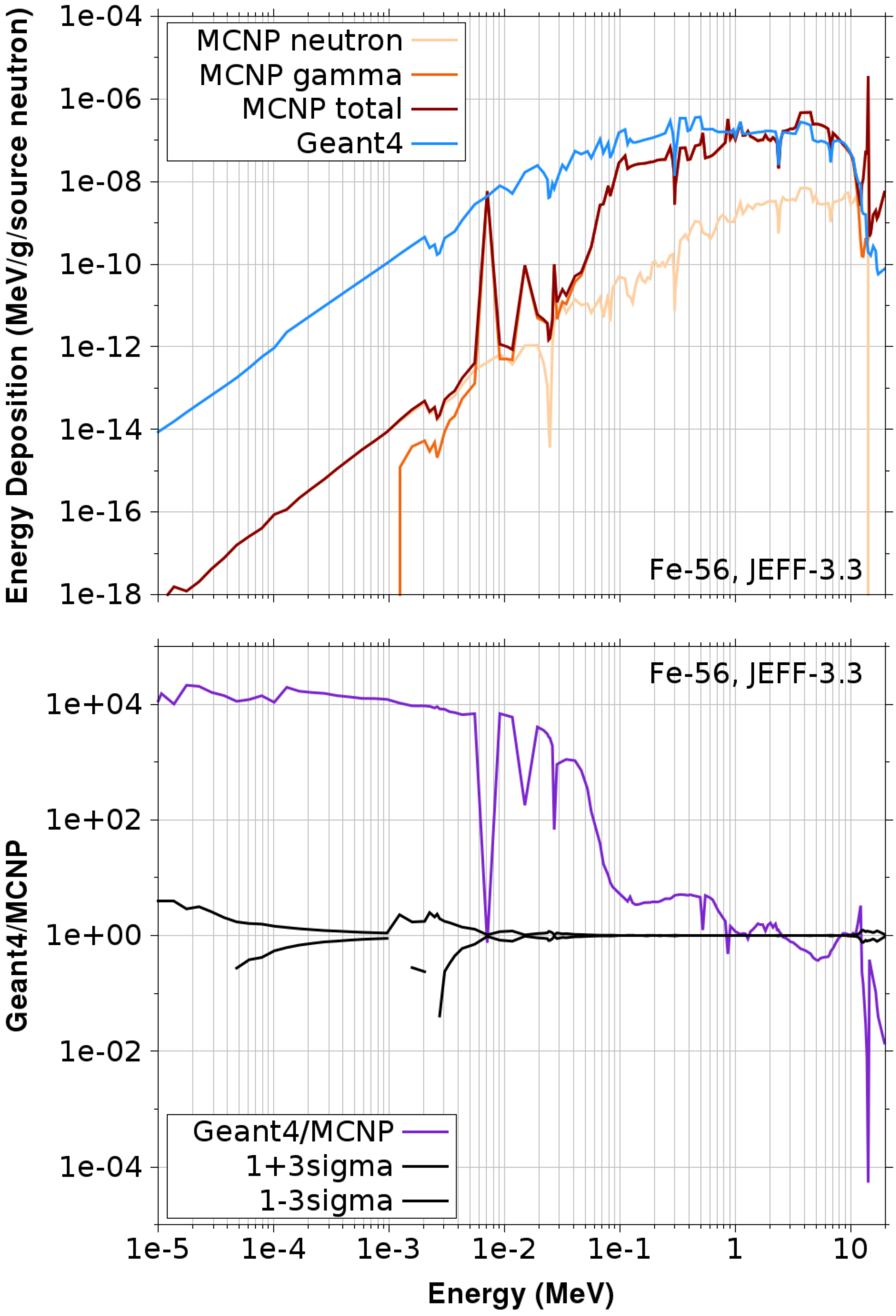

Figure 5.24: The energy deposition spectrum (top) and the ratio between Geant4 and MCNP result for the energy deposition spectrum calculated in a sphere filled with Fe-56 for the JEFF-3.3 library.

It can be seen that for MCNP, the energy deposition is dominated by neutrons around the 14.1 MeV peak and below $5 \cdot 10^{-3}$ MeV, and by gammas in the rest of the energy spectrum. Despite the very good integral agreement between Geant4 and MCNP there are strong deviations in the spectrum. Since for Geant4, the deposited energy is not related to the energy of the original neutron, but to that of the secondary particle which deposits it, the 14.1 MeV neutron heating peak is missing in the Geant4 spectrum. Instead, there is a higher level of energy deposition at lower energies.

Between 0.1 MeV and 10 MeV and near $3 \cdot 10^{-3}$ MeV, several distinctive peaks and dips in the MCNP spectrum are reproduced by Geant4. Just like for the gamma spectrum, the energy deposition spectrum calculated by MCNP has a strong peak near $7 \cdot 10^{-3}$ MeV, which comes from the gamma part of the energy deposition and does not exist in the Geant4 spectrum.

In conclusion, there are significant differences in the energy deposition spectrum for a sphere filled with Fe-56, despite both codes arriving at very consistent integral energy deposition results.

For a sphere filled with **Li-6**, the comparison of the total gamma flux reveals an extreme deviation between Geant4 and MCNP result for all libraries. To investigate this further, the gamma flux spectrum calculated with the FENDL-3.1 library and the spectrum of the ratio between Geant4 and MCNP result is displayed in figure 5.25. It can be seen that in the range between 0.01 MeV and 3 MeV the same series of peaks and dips are present in both spectra, however, the Geant4 result is shifted by a factor of ≈ 250 towards a higher gamma flux. Between 3 MeV and 4.5 MeV, the Geant4 result has additional peaks, until it closes in on the MCNP result with deviations below a factor of 12.2 up till 7 MeV. Even though the MCNP spectrum continues towards higher energies, the Geant4 spectrum stops at this point.

The large deviations and the consistent shift towards higher flux throughout most of the energy range indicates a major issue in Geant4's calculation of the gamma production from neutron interactions with Li-6. When installing one of the converted nuclear data libraries for Geant4, published online by Mendoza and Cano-Ott (2018a), the user has to copy some parts into it from the basic nuclear data library available with the code distribution. Therefore these parts of the library are identical between JEFF-3.3, ENDF/B-VIII.0 and FENDL-3.1. Since for all libraries, there is a similar deviation in the total gamma flux, it is likely that this issue may derive from the part all libraries have in common.

Again, the results of a calculation with the single interaction benchmark (discussed in section 5.1), which are published on the website (Mendoza and Cano-Ott, 2018b) along with the library data by Mendoza and Cano-Ott (2018a) are used to investigate the gamma production. The converted version of FENDL-3.1 is not an official release; therefore this data is not available for it. However, the large deviation happens the same way for JEFF-3.3, so instead the result for a calculation with JEFF-3.3 is displayed in figure 5.26. It can be seen that the Geant4 result reproduces all of the gamma peaks of the MCNP result. The peak near 3.5 MeV is overestimated and the peak near 7.25 MeV is slightly underestimated. Additionally, two strong peaks near 2.25 MeV and 4.25 MeV, and a small peak near 11.5 MeV appear in the spectrum produced with Geant4, which do not exist for MCNP, leading to a strongly increased gamma production.

The expected energies of gammas produced in Li-6 through interactions with high-energy are published by Demidov et al. (1978) and for thermal neutrons by Firestone et al. (2006). Demidov et al. (1978) do not distinguish between different isotopes of lithium and list a gamma energy of 0.478 MeV. The catalogue by Firestone et al. (2006) contains the energies 0.478 MeV, 6.769 MeV, and 7.246 MeV for Li-6. This accounts for the first, third and fourth peak in the MCNP spectrum, but not the second one. The additional peaks of the Geant4 spectrum do not appear in either list, which indicates that they do not represent realistic physics well. This is likely the cause for the strong shift towards higher values for the gamma flux in the multiple interaction benchmark.

In figure 5.27, the energy deposition spectrum in a sphere filled with Li-6 calculated with Geant4 and MCNP using the FENDL-3.1 library is displayed along with the spectrum of the ratio between Geant4 and MCNP result. It can be seen that just like for Fe-56, the Geant4 spectrum does not contain the peak near 14.1 MeV and is shifted towards higher or lower values than the MCNP spectrum, while maintaining distinctive peaks and dips. The deviation between Geant4 and MCNP is much smaller than for the gamma flux both for the integral result and observable in the spectrum. This indicates that Geant4 is calculating energy deposition in an independent way from the gamma production.

The analysis of the total gamma flux and energy deposition calculated by Geant4 reveals that for **W-184**, there are large discrepancies between the results for JEFF-3.3 and the other two libraries: the JEFF-3.3 result is significantly lower for both cases, leading to a strong underestimation of the MCNP result. To investigate this further, the gamma flux spectrum calculated by Geant4 and MCNP with the libraries JEFF-3.3 and FENDL-3.1 is displayed in figure 5.28.

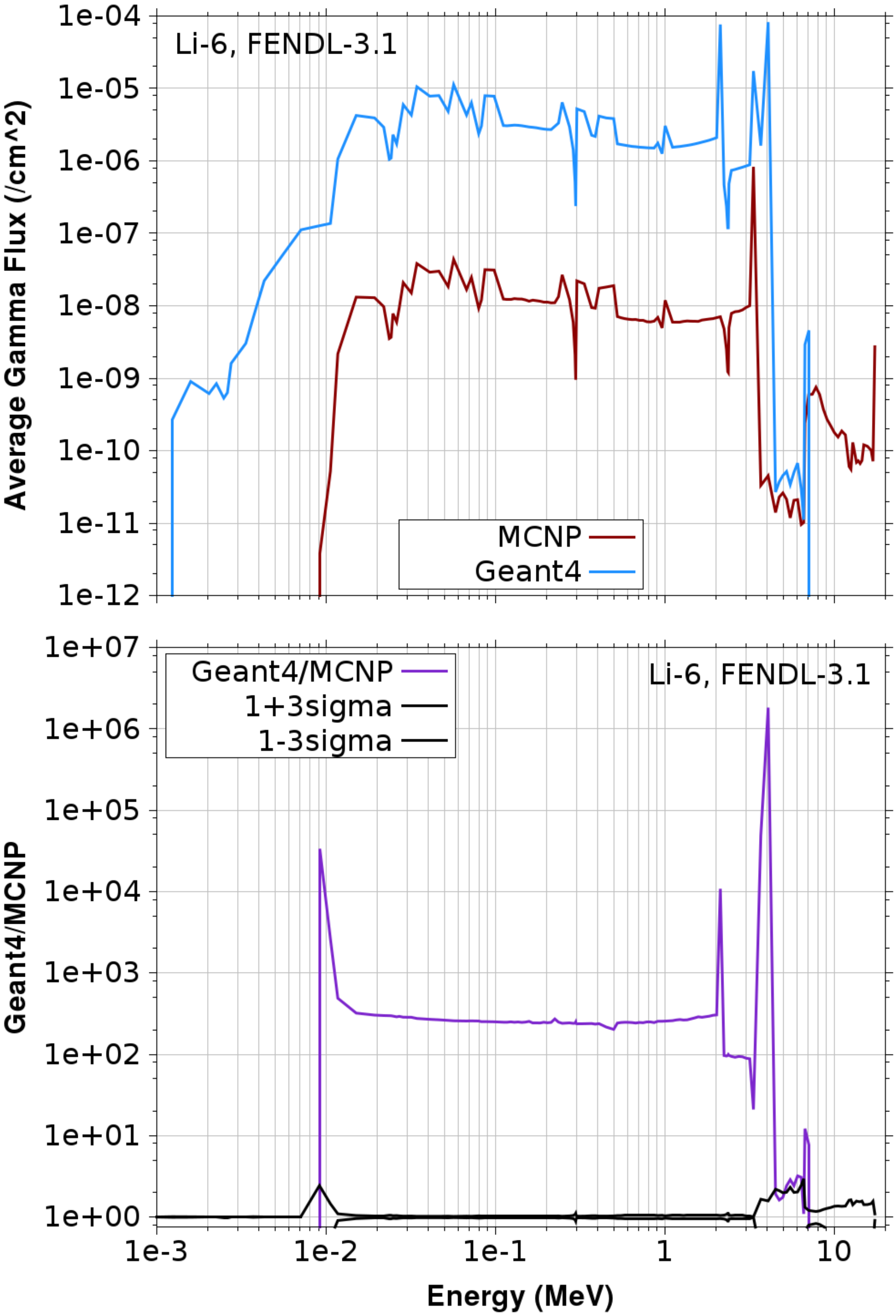

Figure 5.25: The gamma flux spectrum (top) and the ratio between Geant4 and MCNP result for the gamma flux calculated in a sphere filled with Li-6 for the FENDL-3.1 library.

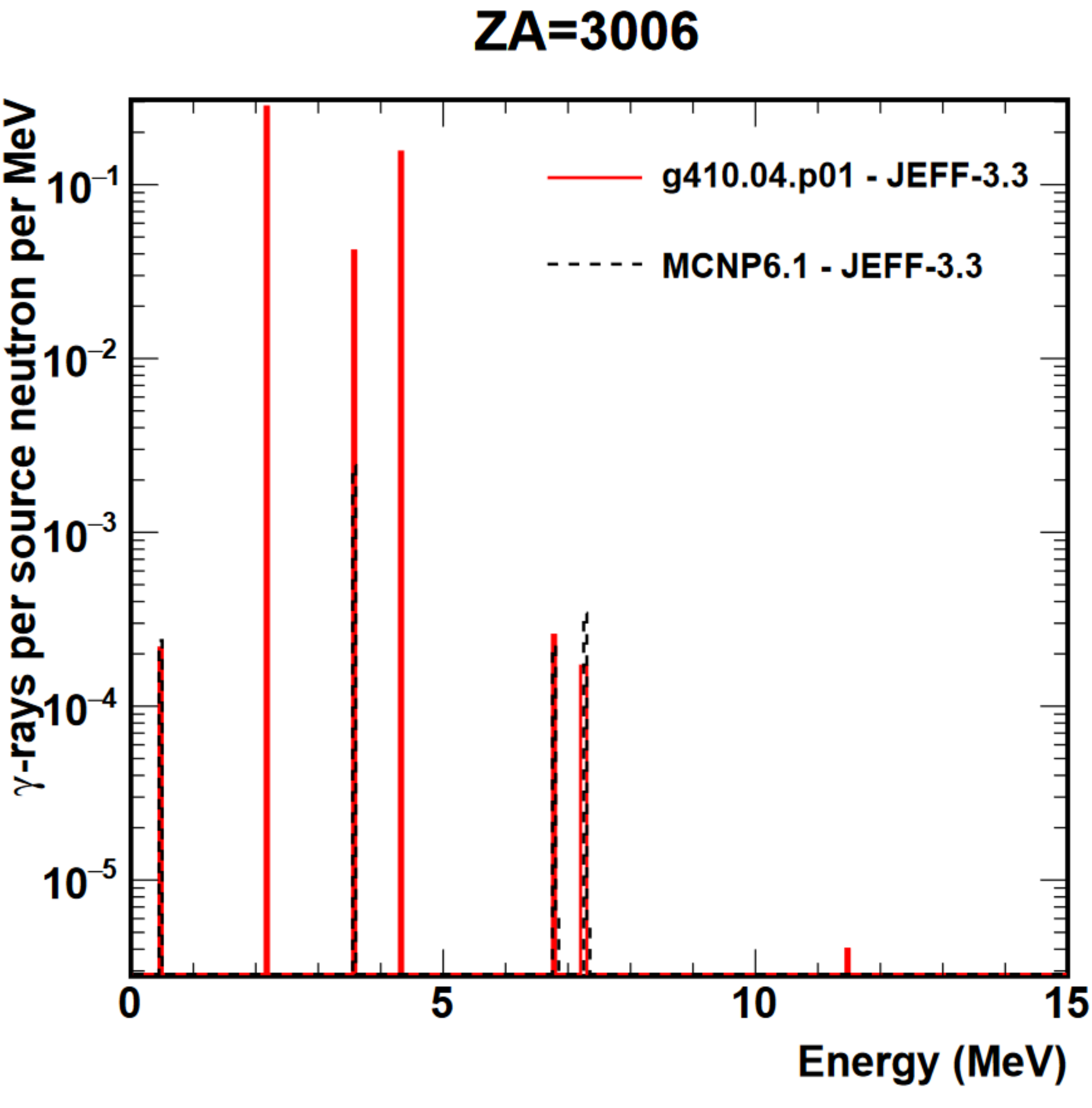

Figure 5.26: Comparison of Geant4 and MCNP result for the number of gamma rays per source neutron and energy plotted against the energy in the single-interaction benchmark, for a cylinder filled with Li-6 using the JEFF-3.3 library (published by Mendoza and Cano-Ott (2018a) on the Geant4 library website (Mendoza and Cano-Ott, 2018b)).

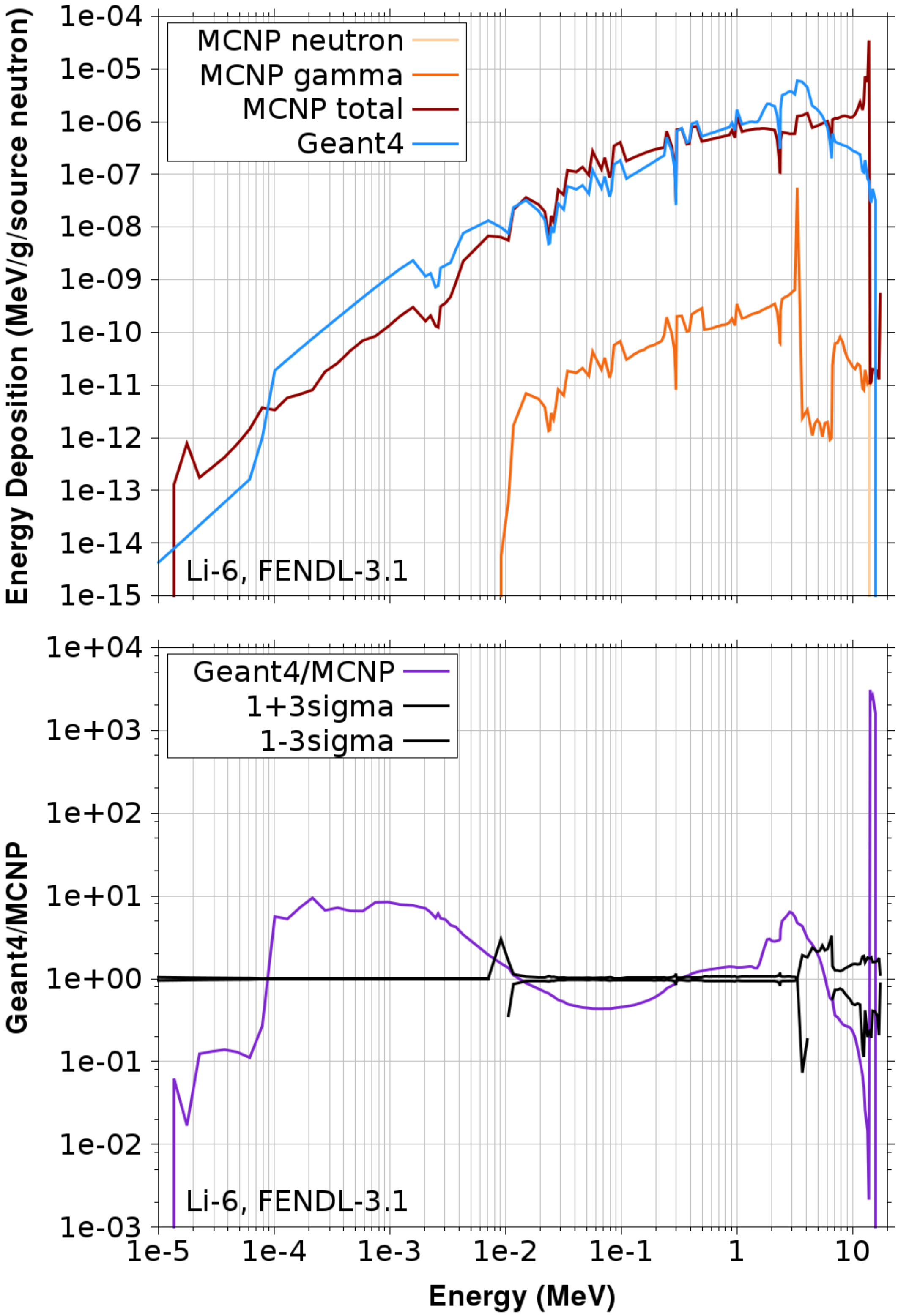

Figure 5.27: The energy deposition spectrum (top) and the ratio between Geant4 and MCNP result for the energy deposition spectrum in a sphere filled with Li-6 for the FENDL-3.1 library.

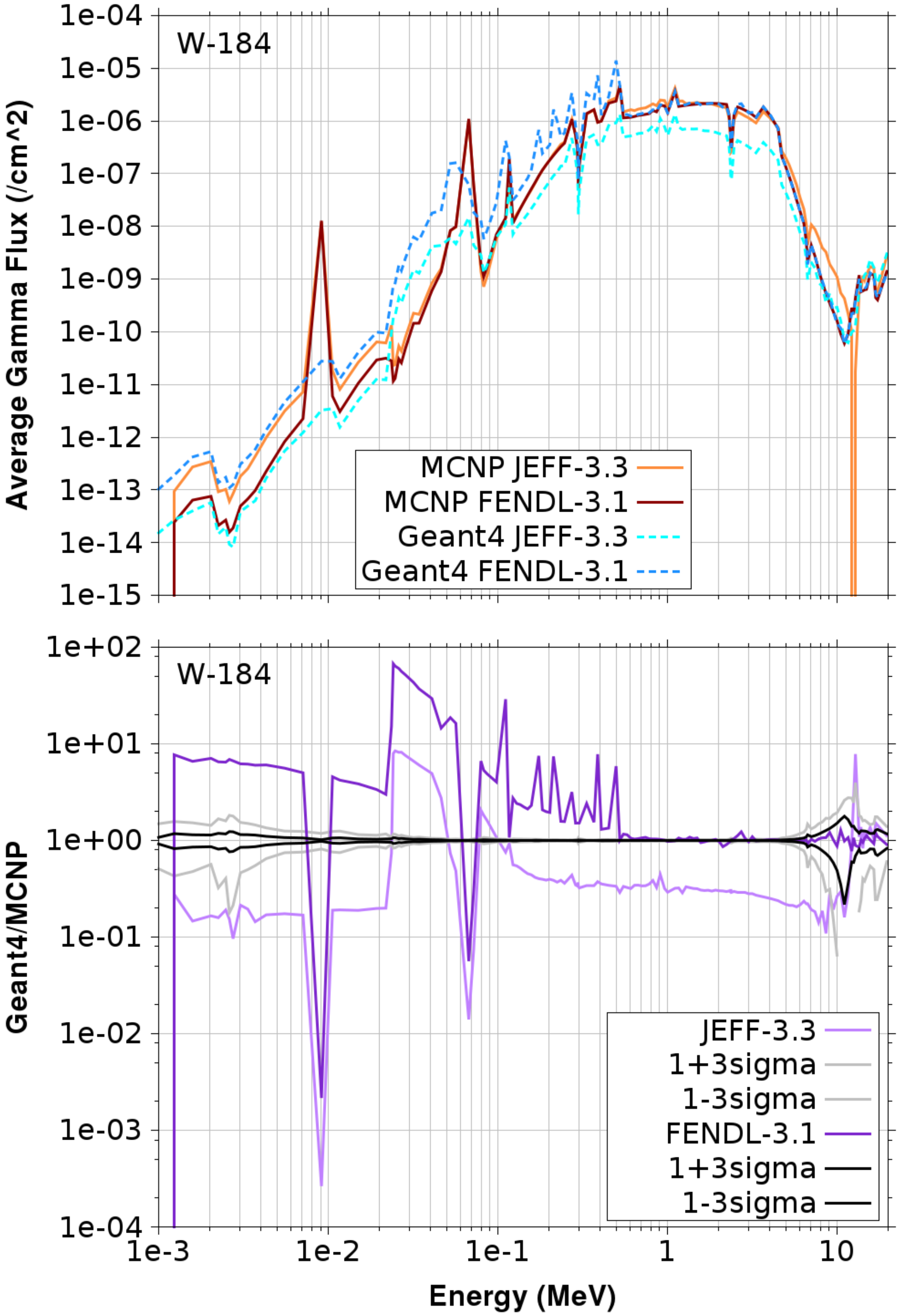

Figure 5.28: The gamma flux spectrum (top) and the ratio between Geant4 and MCNP result for the gamma flux calculated in a sphere filled with W-184 for the JEFF-3.3 and the FENDL-3.1 library plotted against the energy.

It can be seen that for MCNP, the spectrum produced for the JEFF-3.3 library has either slightly higher values than the FENDL-3.1 spectrum or follows the FENDL-3.1 spectrum closely. The only exception is a strong dip in the JEFF-3.3 spectrum near 13.5 MeV, which does not appear in the FENDL-3.1 spectrum.

The spectrum calculated by Geant4 for FENDL-3.1 is close to the MCNP result at energies above 0.5 MeV and mostly overestimates the MCNP result at lower energies. The spectrum produced by Geant4 for the JEFF-3.3 library is shifted towards lower values than the FENDL-3.1 spectrum in the energy range below 8 MeV. As a result, it underestimates the MCNP result throughout most of this energy range. At energies above 8 MeV, the Geant4 JEFF-3.3 spectrum is fluctuating slightly above and below the FENDL-3.1 spectrum calculated by Geant4 and the JEFF-3.3 spectrum calculated by MCNP. It does not contain the strong dip near 13.5 MeV of the MCNP JEFF-3.3 spectrum, which results in an overestimation.

At energies above 0.1 MeV, there are several peaks and dips which appear consistently in all spectra produced by both codes for both libraries. However, the spectrum produced by Geant4 with the FENLD-3.1 library has a series of additional peaks between 0.15 MeV and 0.5 MeV. Only some of these exist in the MCNP spectra and have different shapes. Using the JEFF-3.3 library, the shape of the peaks in the MCNP spectrum is reproduced more accurately and there are no additional peaks, but the entire spectrum is shifted towards lower values in this range. It is unclear what causes the additional peaks in the Geant4 FENDL-3.1 spectrum.

Near $7 \cdot 10^{-2}$ MeV, there is a strong peak in both MCNP spectra, which is reproduced only weaker and spread out towards lower energies in both Geant4 spectra. This causes a strong underestimation by Geant4 in the peak range and an overestimation in the spread range for both libraries. Near $9 \cdot 10^{-3}$ MeV, there is another strong peak in both MCNP spectra. The Geant4 spectra only have a much slighter peak here, which leads to a strong underestimation for both libraries.

Considering again the calculation of the gamma rays per source neutron and energy in the single interaction benchmark (discussed in section 5.1) published by Mendoza and Cano-Ott (2018a) along with the libraries on the website (Mendoza and Cano-Ott, 2018b), it can be seen in figure 5.29 that for W-184 and the JEFF-3.3 library there is an underestimation by Geant4. Both in the energy range above 5 MeV and below approximately 0.25 MeV, the Geant4 result is significantly lower than the MCNP result. This shows that Geant4 already has underestimation issues for the gamma production in W-184. It is likely, this effect becomes more pronounced in the multiple interaction benchmark and causes the underestimation which can be seen in figure 5.28.

The discrepancy between the Geant4 results for different libraries also happens for the total energy deposition in a sphere filled with W-184. To investigate further, the energy spectrum of the energy deposition calculated by Geant4 and MCNP for the libraries JEFF-3.3 and FENDL-3.1 has been calculated and is displayed in figure 5.30.

It can be seen that for MCNP, the energy deposition spectrum for JEFF-3.3 is shifted towards higher values than for FENDL-3.1 in nearly all energy ranges except for a dip near 13 MeV, which is also present in the gamma spectrum.

Same as for Li-6 and Fe-56, the Geant4 energy deposition has a different shape than the MCNP spectrum: The Geant4 spectrum again lacks the neutron energy deposition peak near 14.1 MeV and has higher values than MCNP at lower energies. Just like for Fe-56, strong peaks in the MCNP energy deposition spectrum (near $7 \cdot 10^{-2}$ MeV and $9 \cdot 10^{-3}$ MeV), which correlate to peaks in the gamma spectrum, are not reproduced by Geant4.

The deviation between the spectra calculated with Geant4 for the two libraries happens mainly in the energy range above 10^{-2} MeV: here the result for JEFF-3.3 is lower than for FENDL-2.1, which is opposite to the MCNP result. At lower energies, the JEFF-3.3 and the FENDL-3.1 spectrum are very close to each other. In the range between 0.1 MeV and 0.5 MeV, the spectrum calculated by Geant4 for the FENDL-3.1 library has a series of peaks, which don't appear in any of the other spectra, just like for the gamma spectrum.

An evaluation of the other alternative code Serpent-2 by Valentine et al. (2021) using an experimental benchmarks and the application to DEMO, which is further discussed in section 6.2, has found issues with the heating number part of the JEFF-3.2 library for tungsten isotopes. The cross-section ACE file contains negative values in the energy range 1–15 MeV. This causes a strong discrepancy between the Serpent-2 and MCNP results, because the codes deal differently with the physically implausible data.

As can be seen in figure 5.31, the issue persists for JEFF-3.3 with negative values in the energy range between 2 MeV and 10.5 MeV. FENDL-3.1 is not affected. There is no clear effect on the MCNP

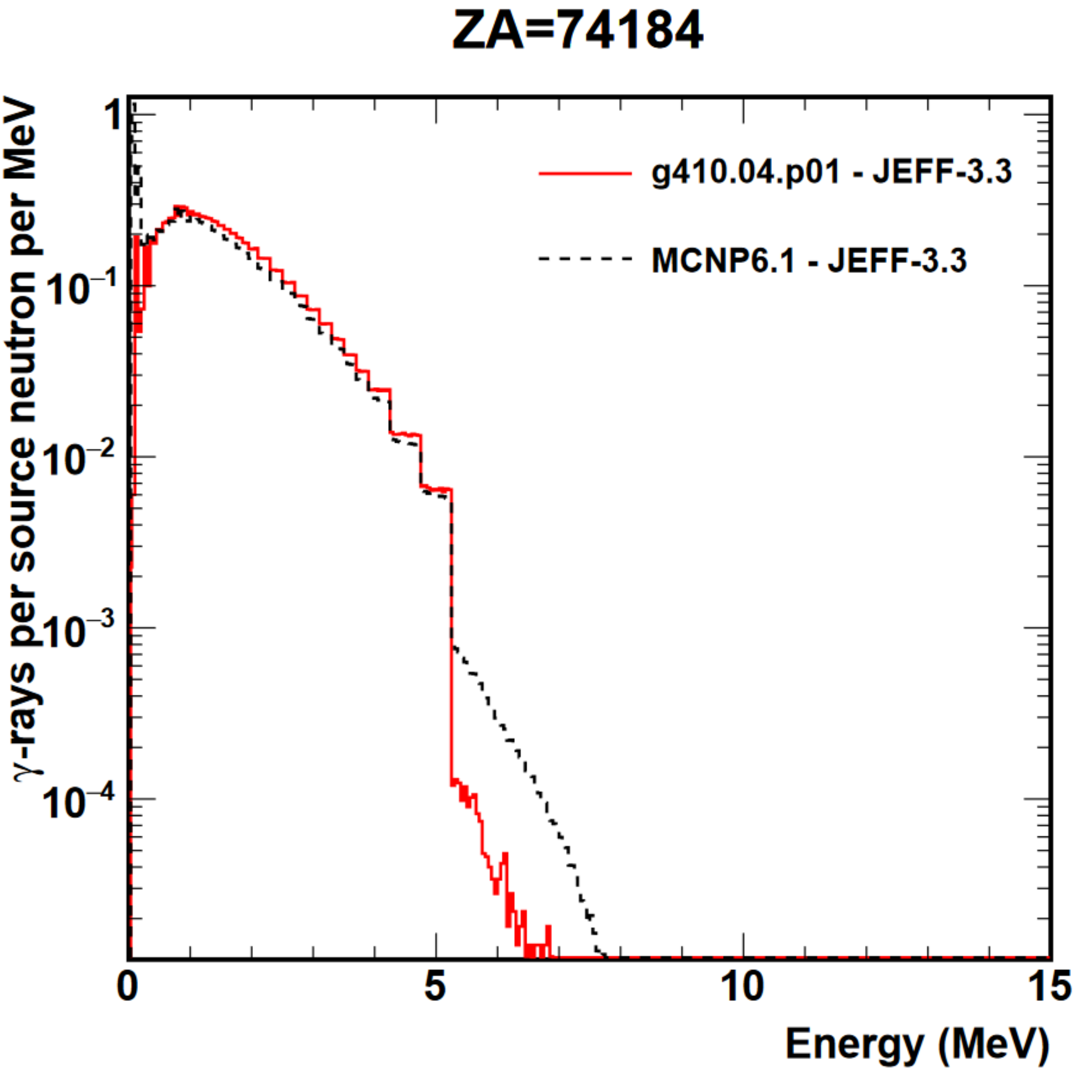

Figure 5.29: Comparison of Geant4 and MCNP result for the number of gamma rays per source neutron and energy plotted against the energy in the single-interaction benchmark, for a cylinder filled with W-184 using the JEFF-3.3 library (published by Mendoza and Cano-Ott (2018a) on the Geant4 library website (Mendoza and Cano-Ott, 2018b)).

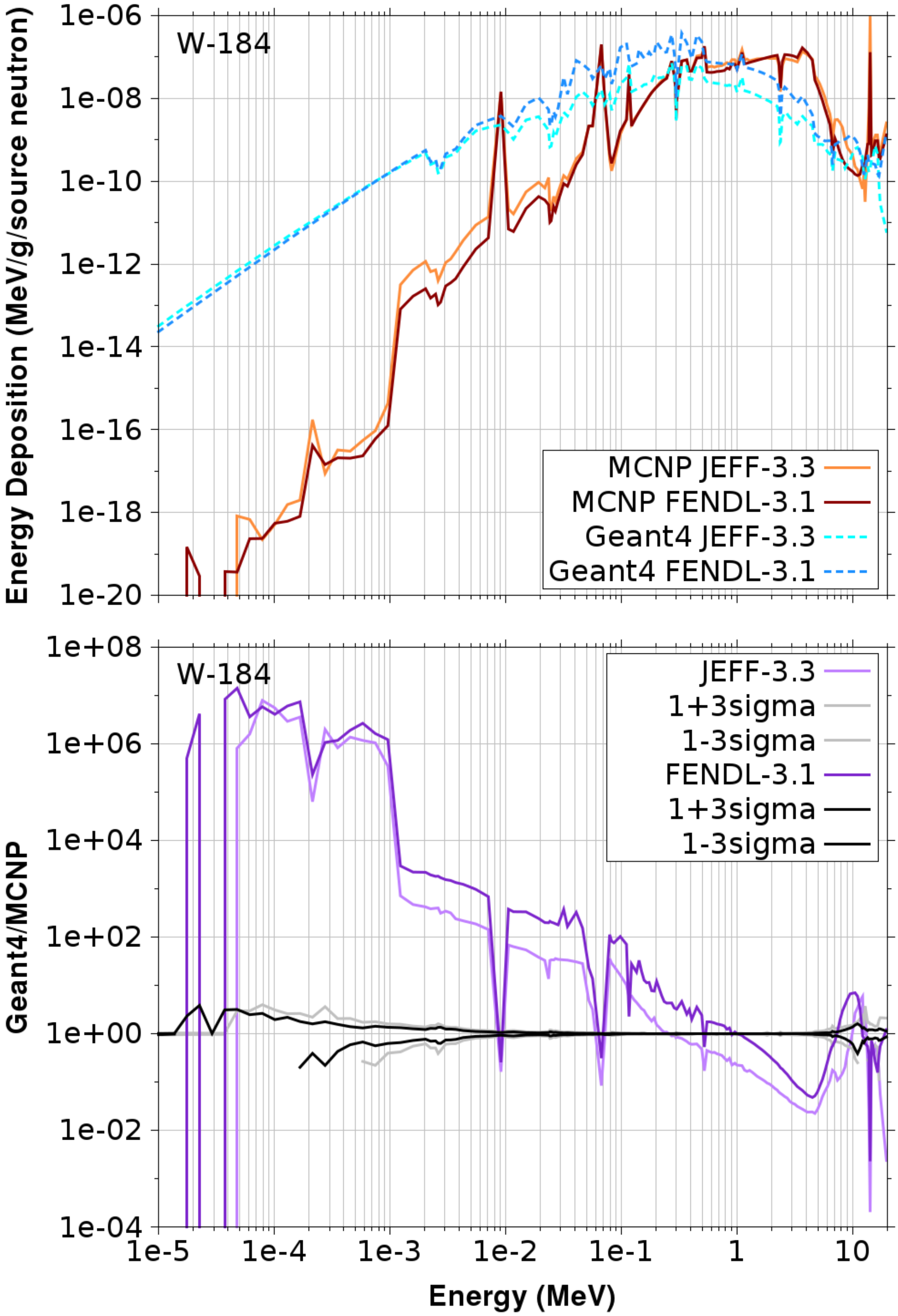

Figure 5.30: The energy deposition spectrum (top) and the ratio between Geant4 and MCNP result for the energy deposition spectrum in a sphere filled with W-184 for the JEFF-3.3 and the FENDL-3.1 library plotted against the energy.

spectra observable: the JEFF-3.3 results in the affected energy range are neither negative, nor zero, nor smaller than the FENDL-3.1 results. Valentine et al. (2021) assume that MCNP compensates for the faulty data, which might explain this outcome. Since the (n,heat) cross-section is not used at all in the library conversion for Geant4, and the MCNP result does not appear to be affected by the issue, the faulty JEFF-3.3 (n,heat) cross-section, is likely not the cause of the strong underestimation of the energy deposition by Geant4 for the JEFF-3.3 library.

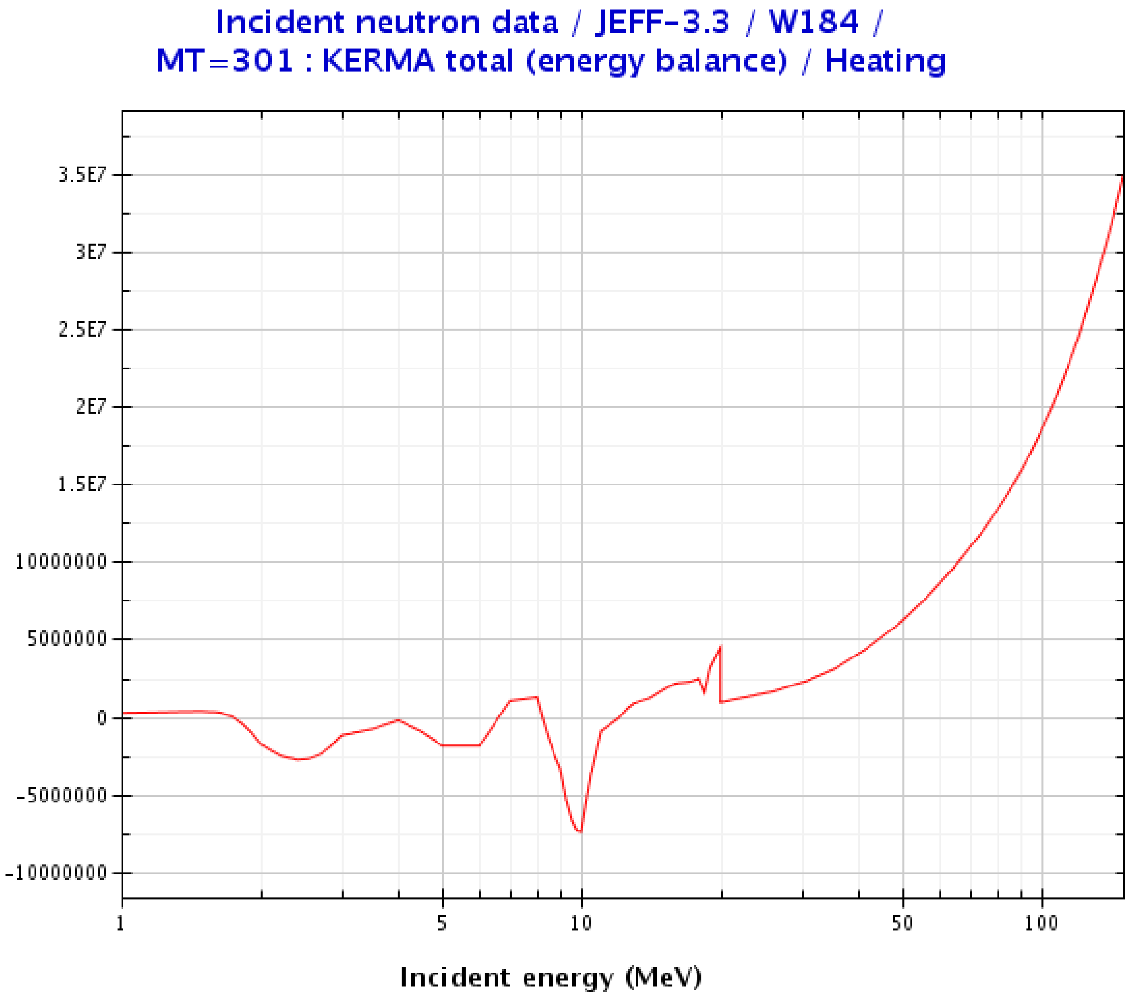

Figure 5.31: The (n,heat) cross-section of W-184 in the JEFF-3.3 library plotted with the JANIS cross-section plotter (Soppera et al., 2014).

In summary, for the MCNP calculation of the total gamma flux, there is good agreement between libraries for some nuclides (H-1, Li-6, Li-7, O-16, Si-28, W-184, and Pb-208) and discrepancies for other nuclides (Be-9: JEFF-3.3 much lower, Cnat: FENDL-3.1 lower, Cr-52: ENDF/B-VIII.0 slightly higher, and Fe-56: ENDF/B-VIII.0 slightly higher). For the Geant4 calculation of the total gamma flux, there are nuclides with good agreement with the MCNP result (H-1, Be-9 + JEFF-3.3, Be-9 + ENDF/B-VIII.0, Si-28, Cr-52 + JEFF-3.3, Cr-52 + FENDL-3.3, and Pb-208 + ENDF/B-VIII.0). For the nuclides with bad agreement overestimation is observed for Li-6, Li-7, Be-9 + FENDL-3.1, Cnat, O-16, Cr-52 + ENDF/B-VIII.0, W-184 + ENDF/B-VIII.0, W-184 + FENDL-3.1, Pb-208 + JEFF-3.3, and Pb-208 + FENDL-3.1, and underestimation is observed for W-184 + JEFF-3.3. The overestimation of the total gamma flux for Li-6 for all libraries is particularly strong and likely caused by a problem with the gamma production. This is also the cause for the strong underestimation of the total gamma flux for W-184 using the JEFF-3.3 library

For the MCNP calculation of the total energy deposition, there is good agreement between libraries for some of the same, but also different nuclides as for the total gamma flux (H-1, Li-6, Li-7, Be-9, O-16, Si-28, and Fe-56). Discrepancies can be seen for other nuclides (Cnat: ENDF/B-VIII.0 higher, Cr-52: FENDL-3.1 lowest, JEFF-3.3 highest, W-184: FENDL-3.1 lowest, JEFF-3.3 highest, and Pb-208: JEFF-3.3 higher). For the Geant4 calculation of the total energy deposition, there are nuclides with good agreement with MCNP (H-1, Be-9 + ENDF/B-VIII.0, Cnat + JEFF-3.3, Cnat + FENDL-3.1, O-16, Si-28, Cr-52 + ENDF/B-VIII.0, Fe-56, and Pb-208 + ENDF/B-VIII.0). The bad agreement is more evenly distributed among underestimation (Li-6 but not as bad as for gamma, Li-7, Be-9 + JEFF-3.3, and W-184 JEFF-3.3 especially strong), and overestimation (Be-9 + FENDL-3.1, Cr-52 + JEFF-3.3, Cr-52 + FENDL-3.1, W-184 + FENDL-3.1, W-184 + ENDF/B-VIII.0, Pb-208 + JEFF-3.3, and Pb-208 + FENDL-3.1). There are more nuclide + library pairs with good agreement for the energy deposition than for the gamma flux.

None of the libraries is consistently good for all nuclides. ENDF/B-VIII.0 produces the best overall agreement. There are nuclides for which the order in which the libraries appear in over- and underestimations are consistent between total gamma flux and energy deposition such as W-184 and Pb-208, but there are also nuclides for which an overestimation in the gamma flux is combined with an underestimation of the energy deposition such as Li-6 and Li-7. In general, the results are much less consistent between MCNP and Geant4 than for the total neutron flux where at least the integral values have very good agreement despite deviations in the spectrum.

5.3 Synopsis of the Major Verification and Validation Achievements

A code-to-code benchmark for single neutron interactions has been reproduced and employed to test the agreement between Geant4 and MCNP for particularly fusion relevant isotopes with the nuclear data libraries ENDF/B-VII.0 and JEFF-3.1. The Geant4.10.03 version of the code is used.

For nuclides including Si-28 and heavier, an underestimation of the neutron removal at high energies by reactions which produce one or more secondary neutrons with significantly lower energies and a resulting underestimation of the lower energy secondary neutron peak is observed. Additionally, neutron removal by reactions which create non-neutron secondary particles above high-energy thresholds appears to also be slightly underestimated.

For this benchmark, good agreement in the spectrum is defined as a $Geant4/MCNP$ ratio within the 3σ range or if not a deviation below $5\,\%$ between Geant4 and MCNP and an average relative deviation $d < 1\,\%$. Be-9 and JEFF-3.1 fails on both accounts, due to a major library translation issue which has been fixed by the library providers for newer JEFF library releases.

W-184 and JEFF-3-1 has a spectral deviation of $> 5\,\%$ for some energy bins, but $d < 1\,\%$. In the range with the large deviation, the neutron current curve has an unrealistic staircase-like shape at the secondary neutron peak. This might be explained by too large bins in the energy distribution data of the secondary neutrons for one or more of the relevant reactions (elastic and inelastic scattering, (n,2n), and (n,3n)).

For all other nuclide and library combinations, d is $< 1\,\%$, which verifies the newly developed Geant4 application produces results which comply with standard Geant4 for which the same level of agreement is reported.

Next, a **multiple interaction code-to-code benchmark** originally used to test other codes considered potential alternatives to MCNP has been reproduced. The same isotopes as for the single-interaction benchmark are used in combination with the JEFF-3.3 library. The Geant4 code is updated regularly, so that in the course of this work, improved versions have become available. Results are presented for the versions Geant4.10.03 and Geant4.10.05.p01. The total neutron flux shows good agreement with deviations $\leq 1\,\%$ for both Geant4 versions.

Considering the spectrum of the neutron flux, the agreement between Geant4 and MCNP is significantly better for the newer version Geant4.10.05.p01 in all nuclides including O-16 and heavier compared to the originally tested version Geant4.10.03. For the other nuclides it is nearly identical. However, even for Geant4.10.05.p01, the results are worse than for the single interaction benchmark: for both code versions, most of the spectra deviations are outside the 3σ range and the nuclides Be-9, O-16, Cr-52, Fe-56, W-184, and Pb-208 have deviations $> 5\,\%$ in their spectra. For Geant4.10.03, the deviations are significantly larger throughout the spectra, especially in the high energy range, and Si-28 has to be added to that list. This improvement between Geant4.10.03 and Geant4.10.05.p01 indicates that the underlying issue of the underestimation of reactions which produce secondary neutrons with significantly lower energies revealed by the single interaction benchmark has been fixed for the newer version of the code. The increased deviation compared to the single-interaction benchmark is likely due to slight deviations observed in the single interaction benchmark having the chance to add up in the multiple interaction benchmark.

In comparison with other codes considered to be an alternative to MCNP, Geant4 has the same level of agreement for the total neutron flux, but for the neutron energy spectrum it cannot compete with the near-perfect agreement of Serpent-2. The newer version Geant4.10.05.p01 is approximately on the same level of agreement as Tripoli4 and COG11 for the considered isotopes.

For the test of the **gamma flux and energy deposition agreement** in the same geometry set-up as the multiple interaction benchmark, only the version Geant4.10.05.p01 has been used with the libraries JEFF-3.3, ENDF/B-VIII.0, and FENLD-3.1. The total gamma flux has varied results from good agreement ($\leq 5\,\%$) to very bad agreement for different nuclide and library combinations. The largest deviation of $\approx 23000\,\%$ happens for all libraries for Li-6 and is likely caused by an issue with the gamma production. The ENDF/B-VIII.0 library has the closest agreement for the most nuclides, but for Fe-56, it still has the worst agreement of all libraries with a deviation of $24\,\%$.

For the energy deposition, the Geant4 energy spectrum is very different from the MCNP one due to a different calculation method. Despite this, there is good agreement ($\leq 5\,\%$) of the total result for some nuclides and libraries. The worst deviation of $72\,\%$ happens for W-184 and the JEFF-3.3 library. Same as for the gamma flux, the ENDF/B-VIII.0 library has the closest agreement for the most nuclides, but still has large deviations from MCNP for Li-6, Li-7, Cnat, and W-184.

Further improvements are necessary, for example a dedicated treatment of the unresolved resonance region to improve the neutron flux agreement and for several nuclides an investigation of the gamma production calculation by the Geant4 physics package, which governs the nuclear cross-section data library based transport of neutrons below 20 MeV (NeutronHP). The multiple-interaction benchmark presented in this thesis can be used to monitor the ongoing development of Geant4.

Chapter 6

Validation of Geant4 with Experimental Benchmarks

6.1 Analysis of Code Performance in the Structural Material Iron

This benchmark has originally been performed with the Geant4 version 10.03 and the JEFF-3.1 and ENDF/B-VII.0 nuclear data libraries (Nunnenmann and Fischer, 2019). Since the newer version Geant4.10.05.p01 produces improved results, in particular for Fe-56, the benchmark has been repeated with this version for the smallest and the largest of the iron spheres, using the JEFF-3.3 nuclear data library. Since the code-to-code benchmark compares the agreement for the two Geant4 versions for the same nuclear data library JEFF-3.3 and shows that the agreement is still bad for Geant4.10.3, it can be expected that any change observed in the IPPE benchmark experiment is mainly due to the code version and not due to the library change.

Simakov et al. (2000) reported multiple sources of experimental uncertainty in the supplementary material of the SINBAD benchmark. These include the stability of equipment, the Cf-252 fission spectrum, the Pu-238 α-intensity, the Cf-chamber scattering, and the TOF-to-energy conversion. All energy dependent values they used in the C/E analysis are included in the C/E plots.

The number of histories is chosen so that the relative statistical error is below $1\,\%$ in nearly all energy bins > 0.1 MeV and below $2\,\%$ everywhere else.

In figure 6.1 and 6.2, the leakage spectra and C/E results for the smallest and largest of the spheres are displayed. Since the geometry is similar to the multiple interaction code-to-code benchmark, it is not surprising that the shape of the experimental leakage spectra curve also has some similarities. It starts with a peak due to the uncollided neutrons near 14.1 MeV. This peak is higher for the smaller sphere, because fewer neutrons have interactions in the shorter distance to the outside.

The bigger sphere has nearly the same radius as the geometry of the code-to-code benchmark, however, it is not entirely filled with material. Additionally, the considered quantity here is the leakage spectrum, while for the code-to-code benchmark it is the flux averaged over the entire volume. Therefore it makes sense for the spectra to have some differences such as the relative height of the uncollided neutron peak compared to the rest of the spectrum.

At energies just below the uncollided neutron peak, there is a dip in the spectra of both the small and large sphere with the deepest point being at 8.5 MeV. In this energy range, a number of threshold reactions such as (n,n'), (n,2n), (n,p), and (n,α) are active. Interactions with those either remove neutrons entirely, or create one or two secondary neutrons with significantly lower energies. Elastic scattering is happening throughout the spectrum, moving neutrons from higher energies to lower energies.

Towards lower energies, the leakage spectra rise again. In this range, increasing numbers of secondary neutrons created by the threshold reactions are deposited. For the smaller sphere, a peak is reached already near 0.65 MeV and for the larger sphere near 0.3 MeV.

In the energy range below 1 MeV, the resonance range of the Fe-56 cross-section and other minor nuclides is causing fluctuations in the leakage spectrum. These are more pronounced in the larger sphere, because the longer path through the material and the additional interactions are allowing them to add up more.

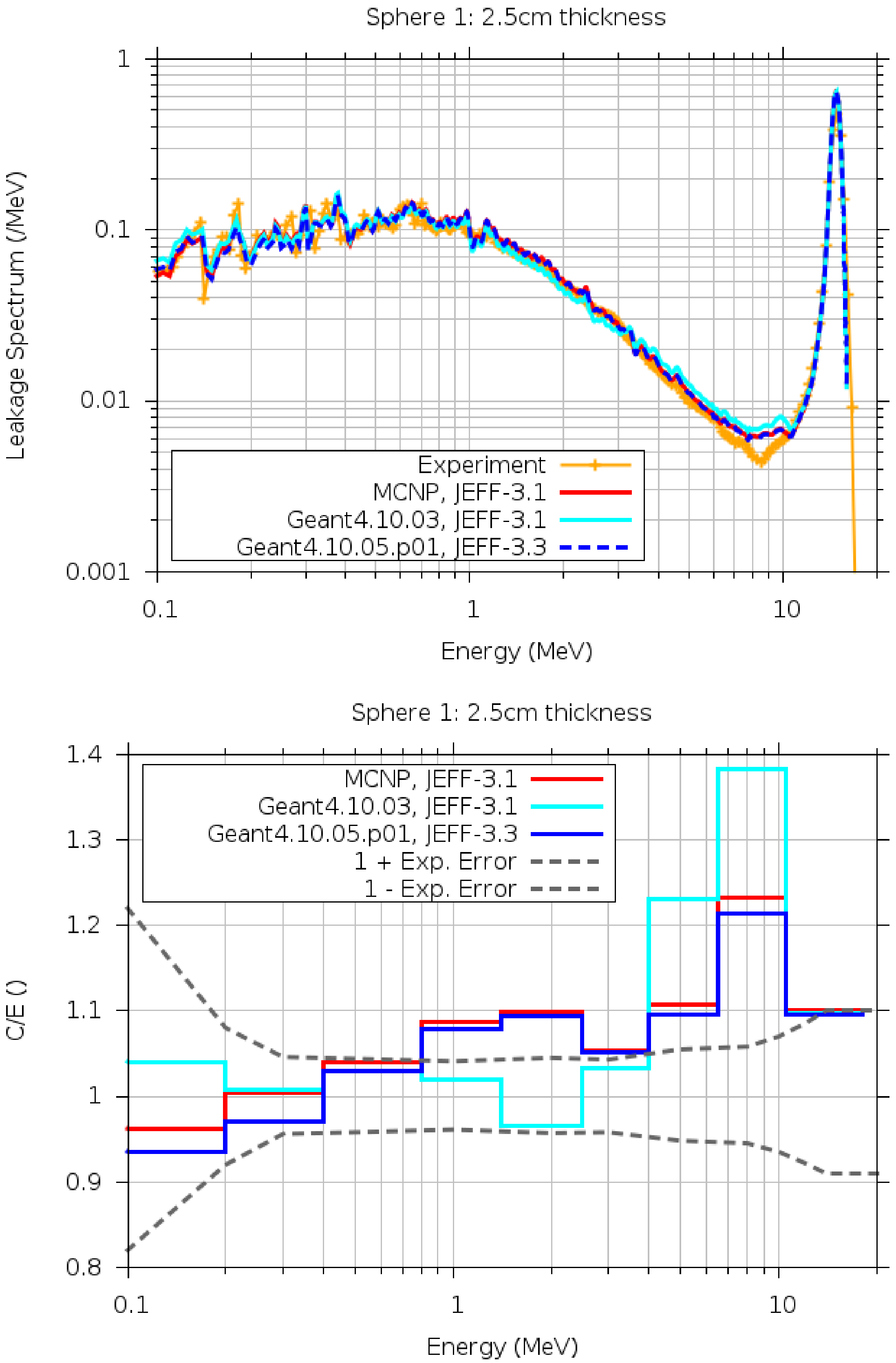

Figure 6.1: Comparison of the measured and simulated (with MCNP, Geant4.10.03, and Geant4.10.05.p01) leakage spectrum as function of energy for a 2.5 cm thick iron sphere (upper plot) and the resulting $Calculation/Experiment$ ratio (lower plot). For MCNP, 10^8 particle histories have been calculated, for each of the Geant4 evaluations $5 \cdot 10^{10}$.

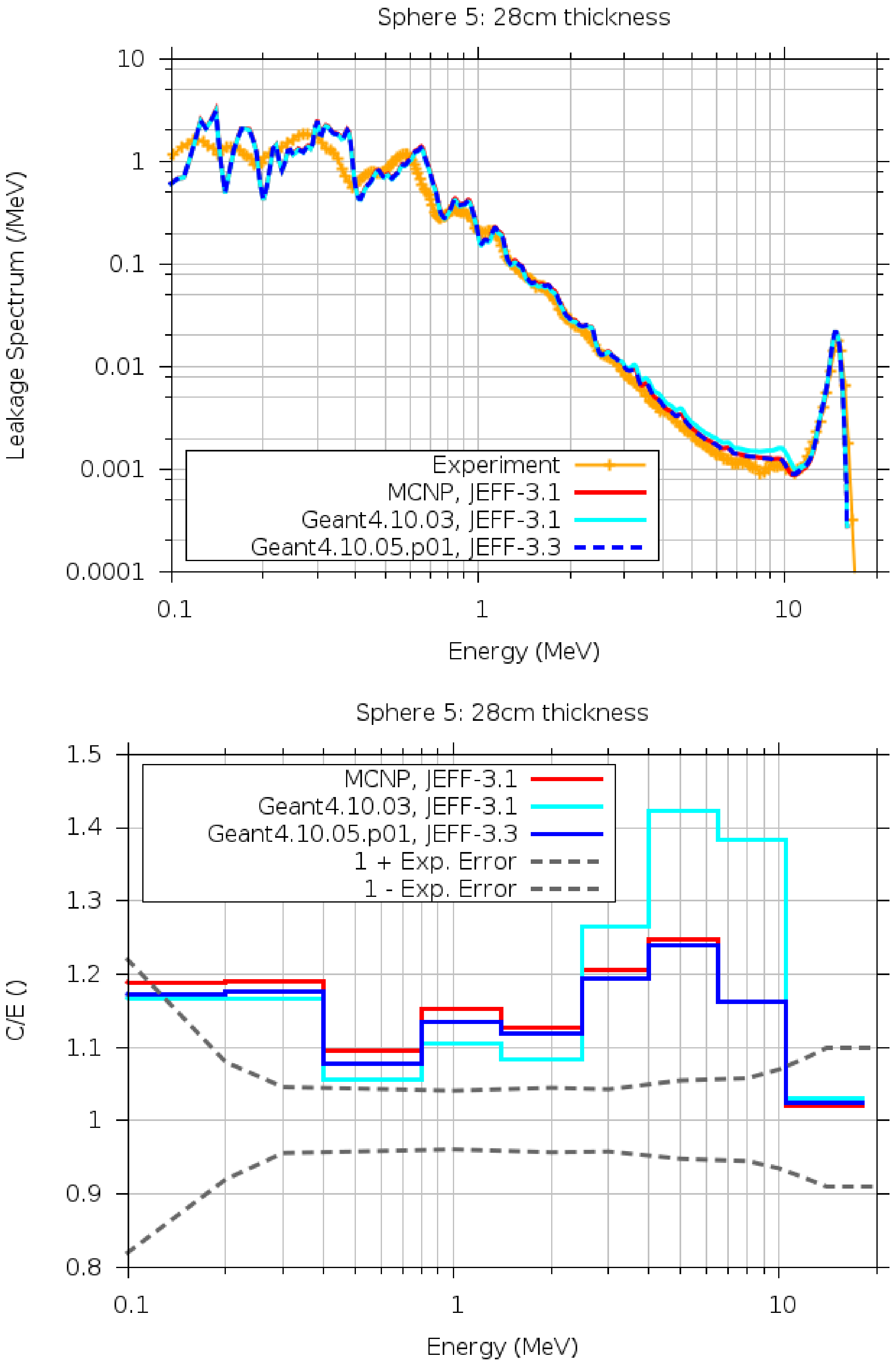

Figure 6.2: Comparison of the measured and simulated (with MCNP, Geant4.10.03, and Geant4.10.05.p01) leakage spectrum as function of energy for a 28 cm thick iron sphere (upper plot) and the resulting $Calculation/Experiment$ ratio (lower plot). For MCNP $2 \cdot 10^8$ particle histories have been calculated, for each of the Geant4 evaluations $5 \cdot 10^{10}$.

In general, the MCNP results are already outside the range of the experimental error in most of the energy range. This means even with the MCNP code, the experimental results cannot be exactly reproduced. This could be due to incomplete description of the experiment or flaws in the nuclear data. The original evaluation by Simakov et al. (2000) has deviations on the same level for the nuclear data libraries they used (FENDL-1, EFF-2.4, EFF-3.0/FENDL-2, EFF-3.1, and JENDL-FF).

It can be seen that for Geant4.10.03, the issue identified in the code-to-code benchmarks is again having an effect: in the leakage current dip, the impact of threshold reactions which produce secondary neutrons with significantly lower energies such as (n,n') and (n,2n) is underestimated. This causes an overestimation compared to the other codes of the leakage current in the energy range of the dip and an underestimation at lower energies. Since Geant4.10.03 has been superseded by the newer version Geant4.10.05.p01, for which this issue is fixed, it is not discussed in further detail.

Geant4.10.05.p01 and MCNP follow the shape of the uncollided neutron peak in the leakages spectrum well for both spheres. For the smaller sphere, the C/E ratio in the highest energy bin above 10.5 MeV reveals an overestimation of $\approx 10\,\%$ for all codes, which is on the same level as the experimental error in part of this energy range and slightly above in the other part.

In the energy range of the dip between 6.5 MeV and 10.5 MeV, all codes overestimate the leakage and do not reproduce the depth of the dip for both spheres. For the smaller sphere, the overestimation is 23 % for MCNP, and 21 % for Geant4.10.05.p01. For the larger sphere, the overestimation is 16 % for both MCNP and Geant4.10.05.p01.

In the energy range between dip and resonance range from 1.4 MeV till 6.5 MeV, the deviation is lower for both spheres. For the small sphere, the overestimation is close to or below 10 %. For the big sphere, the overestimation of $\approx 25\,\%$ in the range closest to the dip is larger than in the dip. From there it decreases towards lower energies down to $\approx 12\,\%$. For both spheres, the Geant4 results are slightly closer to the experimental results than the MCNP results. All results are outside the range of the experimental errors.

In the resonance range below 1.4 MeV, both codes follow the fluctuations in the leakage spectrum somewhat, but do not reproduce their shapes exactly. The deviation is more pronounced for the larger fluctuations of the larger sphere. For the smaller sphere, the integrated C/E results show a trend from an overestimation of $\approx 8\,\%$ for both codes at the highest energies to an underestimation of $3.8\,\%$ for MCNP and of $6.5\,\%$ for Geant4 at the lowest energies. Except for the first bin, this is within the experimental error range. For the larger sphere, the C/E deviation fluctuates between $7.8\,\%$ and $19.0\,\%$. This is only reaching within the experimental error range at the lowest energies. The Geant4 results are $\approx 1.5\,\%$ closer to the experimental results than the MCNP results.

The energy range covered in this benchmark does not extend below 0.1 MeV, so the larger deviations at lower energies identified for the code-to-code benchmark do not have an effect for this benchmark.

In conclusion, there are significant deviations from the experimental results for both codes. These are consistent with previous evaluations. Geant4 is following the MCNP results very closely. In many energy ranges for both spheres the Geant4 results are even slightly closer to the experimental results than the MCNP results. This shows, Geant4 can successfully calculate neutron flux spectrum results in bulk volumes of the important structural material iron in the energy range > 0.1 MeV.

6.2 Reliability of Tritium Breeding Estimationn

The results of this benchmark have first been published in Nunnenmann et al. (2020).

Activation Foil Results

The experimental results for the reaction rates in the activation foils are displayed in figure 6.3. For discussing these reaction rate results in the activation foils, the relevant nuclear cross-sections are displayed in figure 6.4.

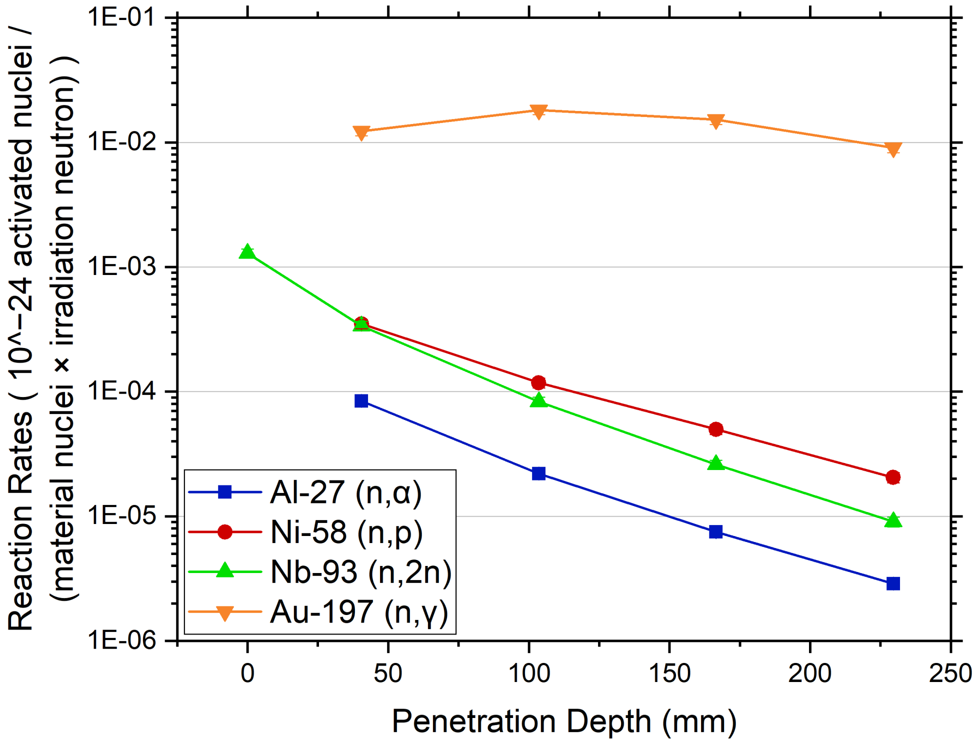

Figure 6.3: Measured normalised reaction rates in the activation foils as a function of the penetration depth for the HCPB TBM mock-up experiment at the FNG. The error bars denoting the total experimental uncertainty (1σ) are too small to be visible. Data is taken from SINBAD (Kodeli et al., 2014).

It can be seen that the activation foils made of Al-27, Ni-58, and Nb-93 have decreasing reaction rates with increasing penetration depth. The reason for this is that the activating reactions of these nuclides can only happen above a threshold energy (0.4 MeV for the (n,p)-reaction of Ni-58, 3.25 MeV for the (n,α)-reaction of Al-27, and 8.93 MeV for the (n,2n)-reaction of Nb-93). The 14.1 MeV neutrons produced by the source are slowed down by material interactions and when the neutron flux penetrates deeper into the material, fewer neutrons with high enough energy for one of those threshold reactions are available. The high threshold of the Nb-93 reaction can be used to observe the amount of uncollided neutrons and neutrons with slightly lower energies due to only few scattering interactions at different penetration depths. The reaction rate of this reaction has the steepest downwards slope. This shows that with increasing penetration depth the amount of uncollided neutrons decreases faster than the amount of neutrons with somewhat lower energies, which are still able to undergo the activating reactions of Ni-58 and Al-27.

The reaction rate in the gold foil does not decrease with penetration depth, because the Au-197 (n,γ) reaction has no threshold. Instead, it is lowest at 20 MeV, increases monotonically towards lower energies until the resonance region between 5 ev and 50 keV and below it again increases monotonically towards lower energies. Due to this, the (n,γ) cross-section is outcompeted by stronger Au-197 cross-sections at higher energies and only overtakes the dominant elastic scattering cross-section in the middle

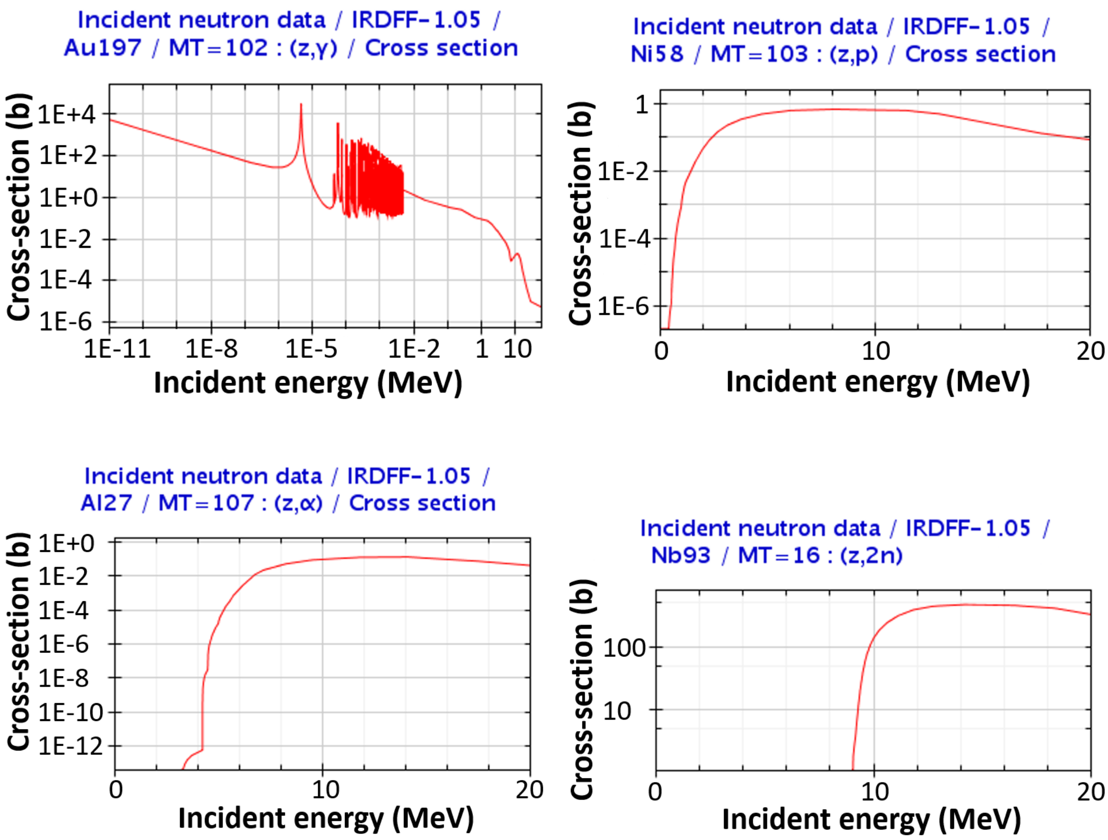

Figure 6.4: The relevant nuclear cross-sections of the activation foils plotted against the incident neutron energy: the (n,γ) reaction of Au-197 (upper left), the (n,p) reaction of Ni-58 (upper right), the (n,α) reaction of Al-27 (lower left), and the (n,2n) reaction of Nb-93 (lower right). The plots are created with the JANIS tool (Soppera et al., 2014) with IRDFF-v.1.05 data (Zsolnay et al., 2012).

of the resonance region. While the total amount of neutrons is decreasing with penetration depth due to absorption, their spectrum is shifted towards lower energies, which makes it more likely that they undergo an activating (n,γ) reaction. These opposing effects appear to be in balance resulting in a nearly constant reaction rate for all penetration depths.

To discuss the deviation between the experimentally measured reaction rates in the activation foils and the ones calculated by Geant4 and MCNP, the C/E results are displayed in figure 6.5. The error bars are calculated from the experimental errors described in section 3.2.2 and the statistical errors of the Geant4 or MCNP calculation. Due to the large number of calculated particle histories, the MC code statistical errors are negligible in most cases.

Looking first at the MCNP results, it can be seen that for two of the the activation foils with a threshold reaction (Ni-58 and Nb-93), the C/E is going down with penetration depth to $-8\,\%$ and $-4.4\,\%$, but is going up again at the deepest penetration to $0.2\,\%$ and $-2.6\,\%$. For Al-27, this effect is less pronounced: the decrease of the C/E only slows down towards deeper penetration and is nearly constant and close to $C/E = 1$ between the second deepest and deepest penetration.

There are both simulation and experiment-based potential causes for this behaviour. In the simulation, the reaction rates are calculated from the local neutron flux spectrum in the foil volume and the nuclear cross-section of the activating reaction. The activating reaction cross-section does not just go to $100\,\%$ above the threshold. Instead, Al-27, Ni-58, and Nb-93 have complex cross-sections with different reactions being more and less dominant throughout the energy range. For example in the JEFF-3.3 cross-section of Ni-58, the activating (n,p) reaction is superseded by elastic and inelastic scattering, (n,n+p), (n,γ), and (n,α) at different parts of its active energy range.

Due to this, the exact energy spectrum of the simulated neutron flux in the activation foil volume is relevant for the resulting reaction rate instead of just the decay of the total flux with increasing penetration depth. The local neutron flux spectrum is shaped by the cross-sections of all nuclides in the surrounding materials through which the neutrons travel on the way there, which is a random walk that

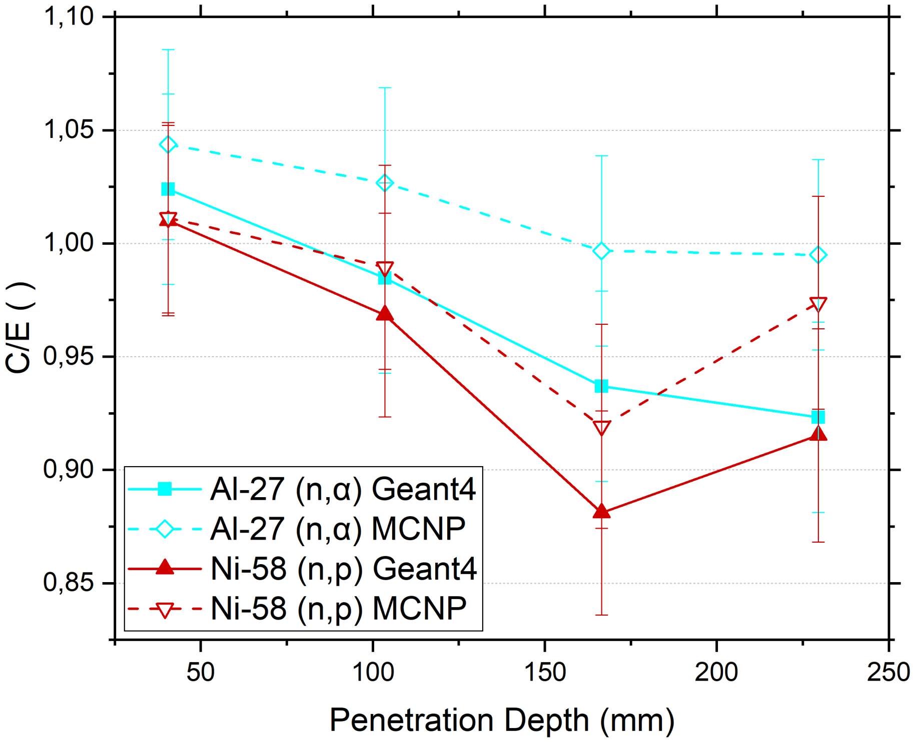

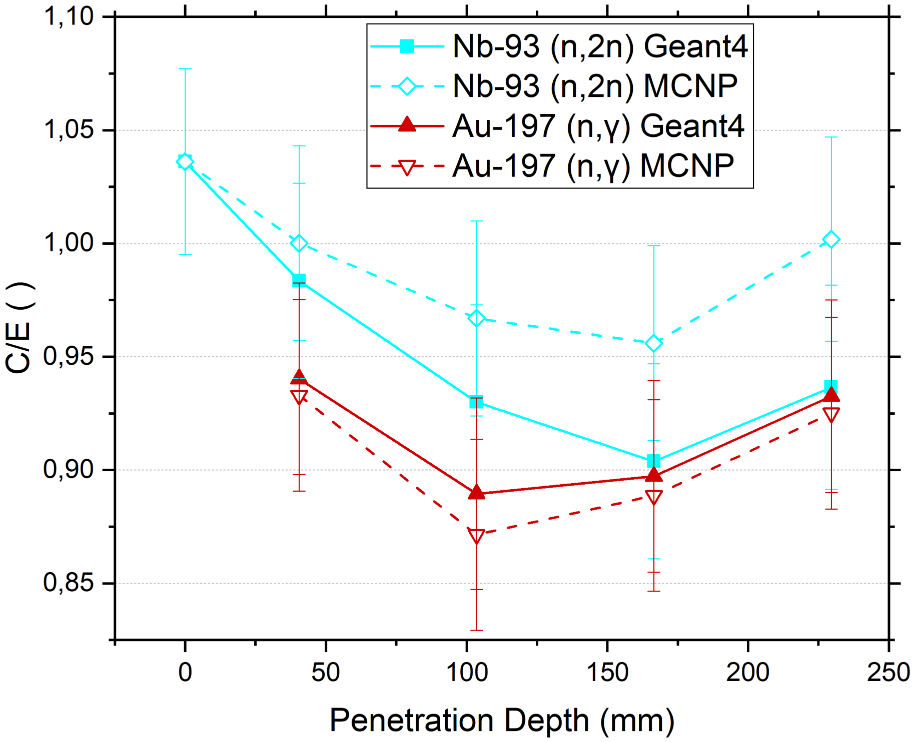

Figure 6.5: The C/E ratio between Geant4 and MCNP simulation results and measurements conducted by Batistoni et al. (2007) for the reaction rates in the activation foils made of Al-27 and Ni-58 (upper plot) and Nb-93 and Au-197 (lower plot, adapted from Nunnenmann et al. (2020)) as a function of penetration depth. The uncertainties (1σ) are combined out of experimental and statistical.

does not go straight from front to back. The relevant materials include beryllium, breeder material, steel, and all foil materials. Any deviation in JEFF-3.3 from the real-life cross-sections has an impact on the resulting local neutron flux spectrum at different penetration depths.

The slight deviations from reality in the local neutron flux spectrum in turn change the calculated reaction rates. Here, the deviations of the IRDFF-v1.05 activation reaction cross-sections from reality impact the consistency of the simulated result with the experimental result. Since the interplay of the reaction types within the cross-section varies between the considered nuclides Al-27, Ni-58, and Nb-93, this can affect some nuclides more than others, which explains how Ni-58 and Nb-93 both show a pattern of strongest deviation at second deepest penetration depth and then less deviation at deepest penetration depth, while for Al-27 the two deepest penetration depths have nearly the same deviation.

One of the main applications of the benchmarks collected in SINBAD is to quantify the deviation from experimental data for new versions of nuclear data libraries.

In addition to deviations introduced by the cross-section library, the deviation between simulated and experimental results is impacted by the precision of the geometric model, and the fact that materials are simulated as perfectly homogeneous throughout a volume in the model, but might be more heterogeneous in the real world.

In the experiment, there is also the possibility for errors. Batistoni et al. (2007) state counting statistics, detector calibration, and FNG source calibration as sources of errors. The observed deviations between C/E results at different penetration depths are not much larger than the given 1σ experimental errors. Potentially, the handling and measurement of foil stacks might also introduce deviations which affect different foil stacks differently. Aluminium, being the thickest foil, might be less affected by this than other foils.

However, considering the C/E results obtained by Batistoni et al. (2007) using FENDL-2.1 or JEFF-3.1 and IRDF-02, show different behaviour for some of the nuclides. For example for Al-27, the deviation is small for the second largest penetration depth for both FENDL-2.1 or JEFF-3.1 and then goes up to above $10\,\%$ for JEFF-3.1 and down to $\approx 2.5\,\%$ for FENDL-2.1 and for Nb-93, the largest deviation of $\approx -5\,\%$ happens at the third from last instead of the second to last penetration depth for FENDL-2.1. This indicates that the main factor driving the shape of the C/E curves are the nuclear cross-section libraries.

To compare the Geant4 and MCNP results, the $Geant4/MCNP$ ratio for the reaction rates in the activation foils is displayed in figure 6.6. For the three activation foils with a threshold reaction, there is good agreement between the Geant4 and MCNP C/E results at the front of the breeder box. For the niobium foil placed outside the box and the nickel foil at the first penetration depth step, the Geant4 and MCNP C/E results are nearly identical. Apart from this, the Geant4 C/E results are consistently lower than the MCNP results. With increasing penetration depth, the Geant4 C/E results increasingly deviate from the MCNP results up to 6.0–7.2$\%$ at the deepest penetration.

In contrast to the previously discussed deviation between MCNP and the experimental result, this deviation between Geant4 and MCNP is consistently increasing with penetration depth. This indicates that slight differences in individual particle interactions are adding up with the increased number of interactions. This straightforward increase is due to the two simulation models having less systematic deviations in material and geometry description than between simulation and experiment and both codes use the same nuclear data library albeit with some minor deviations due to the conversion for Geant4. Due to formatting issues, the cross-section data for the (n,2n) reaction of Be-9 has been replaced with JEFF-3.0 data for the Geant4 JEFF-3.3 library by the library producers Mendoza and Cano-Ott (2018a). Since there is a slight deviation between the JEFF-3.0 and the JEFF-3.3 version of this cross-section for the energy range above 12 MeV, this is likely to have a slight impact on the conformity between the Geant4 and the MCNP result.

On the one hand these deviations put the Geant4 result closer to the experimental result than MCNP for the two smallest penetration depth results of Al-27. On the other hand, in most cases MCNP already underestimates the experimental result, and the Geant4 result is even lower. For Ni-58 and Nb-93 and the second deepest penetration, the Geant4 result and its error range is more than 5% from the experimental result, while all the MCNP results reach closer than 5% with their error range.

For the (n,γ) reaction of Au-197, both Geant4 and MCNP significantly underestimate the experimental result for all penetration depths. In this case, the Geant4 result is slightly higher but within $2\,\%$ of the MCNP result and slightly closer to the experimental result throughout. Batistoni et al. (2007) have found better agreement for MCNP. While for this thesis, IRDFF-v1.05 dosimetry data is used for the activation foil reactions and JEFF-3.3 for the general particle transport, Batistoni et al. (2007) have

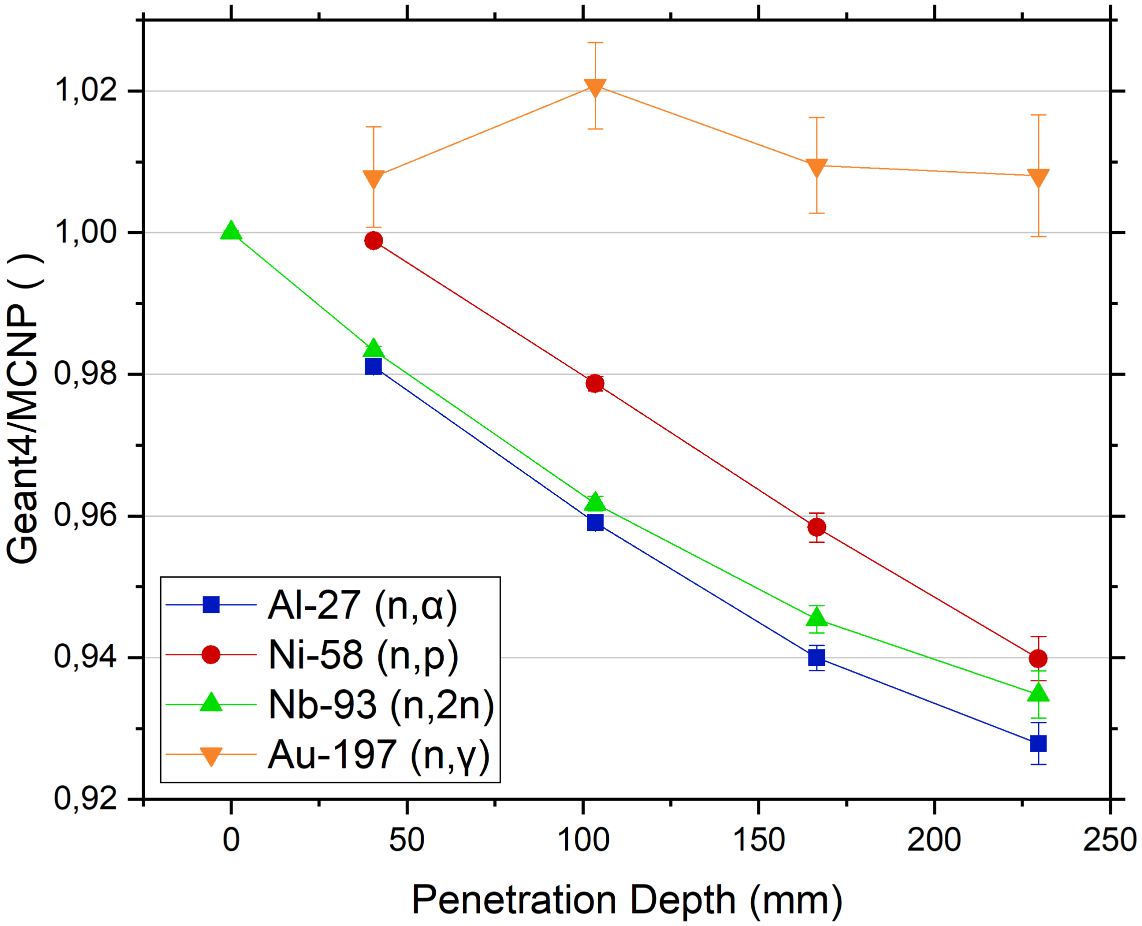

Figure 6.6: The ratio between Geant4 and MCNP simulation results for the reaction rates in the activation foils made of Al-27, Ni-58, Nb-93, and Au-197 as a function of penetration depth. The uncertainties are calculated from the statistical errors of both codes.

used IRDF-02 (Greenwood and Paviotti-Corcuera, 2002) dosimetry data and have calculated results for both JEFF-3.1 and FENDL-2.1 (Lopez Aldama and Trkov, 2004) as general particle transport library.

Exchanging IRDFF-v1.05 for IRDF-02 data does not improve the discrepancy between MCNP and experimental results so the treatment of the Au-197 (n,γ) reaction is not the cause of the discrepancy to the earlier evaluation by Batistoni et al. (2007).

Kodeli (2015) have used several shielding benchmarks from SINBAD to validate the IRDFF-v1.04 (Capote et al., 2012) dosimetry library. For the (n,γ) reaction of Au-197 in the HCPB TBM mock-up benchmark, they observe good agreement with experimental data for FENDL-2.1 and worse agreement similar to the result of this evaluation for FENDL-3 (Forrest et al., 2012). The results are barely affected by changing dosimetry data between IRDF-02 and IRDFF-v1.04. This indicates that the discrepancy between Batistoni et al. (2007)'s Au-197 reaction rate result and the one on this thesis is caused by the change in the general particle transport library.

Since the activation foils are embedded in the beryllium layer, the local neutron flux is strongly influenced by the Be-9 cross-section. Therefore it is a likely cause for the discrepancy. However, investigation of this cross-section revealed the JEFF-3.1 and JEFF-3.3 versions of this cross-section are identical, so this is not the reason for discrepancy towards the results by Capote et al. (2012).

As another likely cause for the discrepancy, the cross-sections of Au-197 and of the adjacent activation foils filled with Nb-93 and Al-27 have been investigated. While the reaction rates in the activation foils are calculated with dosimetry data, the neutron transport in those foils is calculated with cross-section data from the JEFF-3.3 library, and therefore these cross-sections exert an influence on the local neutron flux spectrum and intensity, which is in turn used to calculate the reaction rates.

In figure 6.7, the total, elastic and (n,γ) cross-sections of Au-197 of the libraries JEFF-3.1 and JEFF-3.3 are plotted against each other. The FENDL-2.1 cross-section is not shown, but is very close to the JEFF-3.1 cross-section. It can be seen that the elastic cross-section is slightly higher for JEFF-3.3 throughout the energy range below 5 eV, which has a slight impact on the total cross-section. For both elastic and (n,γ) cross-section, the resonance range extends only up to 0.002 MeV for JEFF-3.3, while for JEFF-3.1 it goes up to 0.005 MeV.

For Nb-93, the resonance region in the total, elastic and (n,γ) cross-section of JEFF-3.3 also extends to higher energies (up to 0.01 MeV), while for JEFF-3.1 and FENDL-2.1 it stops at 0.007 MeV. The Al-27 cross-section is identical for JEFF-3.1 and JEFF-3.3 and can therefore not be a cause of the discrepancy between the current Au-197 reaction rate results and the ones obtained by Batistoni et al. (2007). Likely there are also additional changes in the cross-sections of other materials further away from the gold foil, which are having some effect.

Since these cross-section changes between the libraries are in the energy range below 0.1 MeV, they do not affect the threshold reactions of the other activation foils.

Breeder Pellet Results

The experimental results for the tritium specific activity in the breeder pellets are displayed in figure 6.8. It can be seen that JAEA have measured slightly higher activities for their pellets, but Batistoni et al. (2007) have found the values are still consistent with the ones that have been measured by ENEA or TUD within the experimental error range. The difference between the upper and the lower breeder layer results has been assumed by Batistoni et al. (2007) to be caused by the previously discussed observation that the FNG-source has not been symmetrically aligned (3 mm vertically shifted) and the effect of the aluminium support on which the mock-up box rests. This is included in the geometrical model of the simulation.

The tritium specific activity at a certain penetration depth is lowest at the middle pellet range (4–8) and rising towards the outer edges of the breeder layer (1–3 and 9–12). This is likely caused by a self-shielding effect, which lowers the tritium production at the centre of the breeder layer, while the tritium production rises when getting closer to the neutron multiplier layer. For the lower box, the pellets 11 and 12 have a particularly high tritium specific activity compared to the other pellets at edge positions. This can be explained by the fact that at this edge of the breeder zone there is less parasitic absorption due to the removable steel tubes not extending further downwards.

The tritium specific activity at a certain pellet position decreases with larger penetration depth, except for the first two penetration depths (42 mm and 105 mm) which have results close to the same levels. There are multiple effects affecting this result. As discussed for the activation foils, the high energy neutron flux decreases with rising penetration depth, while more lower energy neutrons are produced. Absorption effects cause the low energy neutron flux to eventually decrease as well.

In the breeder material both Li-6 and Li-7 are producing tritium. The nuclear cross-sections of the tritium producing reactions of Li-6 and Li-7 are displayed in figure 6.9. It can be seen that the cross-section of Li-7 has a threshold and its tritium production is therefore expected to be stronger at small penetration depths. In contrast to this, the Li-6 tritium producing reaction has a cross-section which increases monotonically towards lower energies, which causes it to become stronger at larger penetration depths. These counteracting effects likely cause the low discrepancy for the two first penetration depths. The general tritium production decrease towards larger penetration depths is likely caused both by the decrease of high energy neutrons for the Li-7 reaction (due to natural enrichment 92.5 % of the contained lithium is Li-7) and by the loss of low energy neutrons for the Li-6 reaction to parasitic absorption.

The C/E results for the tritium activity in the breeder pellet stacks at different penetration depths of the upper and the lower breeder blanket boxes are displayed in figures 6.10 and 6.11. First, the agreement of MCNP results with the experimental results are discussed.

It can be seen that for all pellets measured by JAEA (cyan stars) the agreement is the lowest in the respective breeder stack due to JAEA having measured higher tritium activities than ENEA and TUD.

For the lower breeder box, the agreement between calculation and experiment rises with rising pellet numbers apart from fluctuations of individual pellets, reaching the best agreement at pellet number 12. This is consistent for all four penetration depths. This trend is not observed for the upper breeder box.

A difference in the geometry could be the explanation for this. The breeder pellets and activation foils are inserted into the mock-up box through steel inserts which stop at the lower breeder layer (see figure 3.6). Due to this, the upper and middle beryllium layer is interrupted by the steel insert, but not the lowest beryllium layer. This causes the beryllium layers adjacent to pellet 1 and 12 of the upper breeder layer to be structured in a symmetric way, while for the lower layer, there is more steel present next to pellet 1 than to pellet 12. From the fact that the agreement is better at pellet 12 of the lower

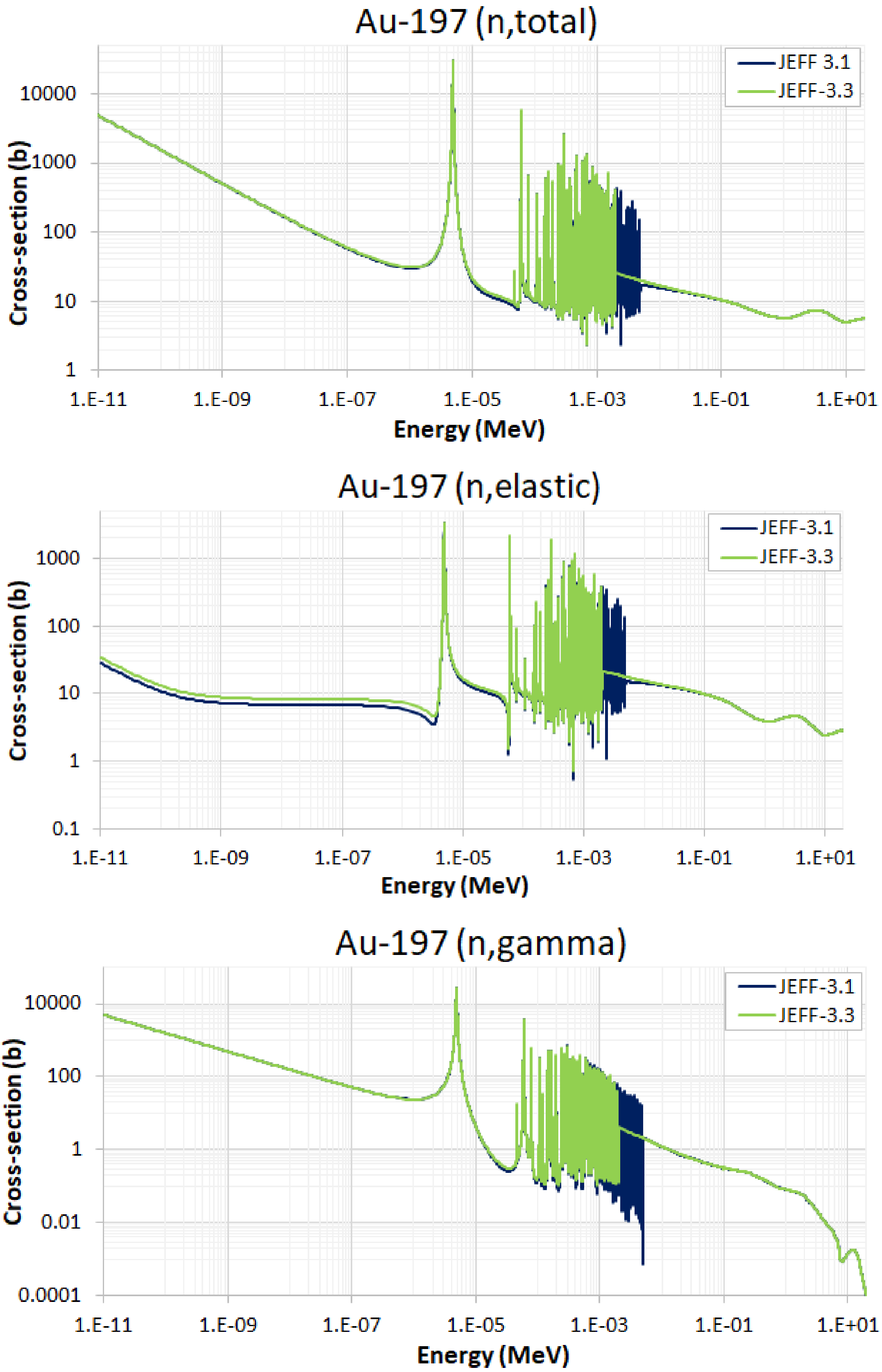

Figure 6.7: The total, elastic, and (n,γ) cross-sections of the JEFF-3.1 and the JEFF-3.3 library plotted against the energy. Data tables taken from JANIS (Soppera et al., 2014).

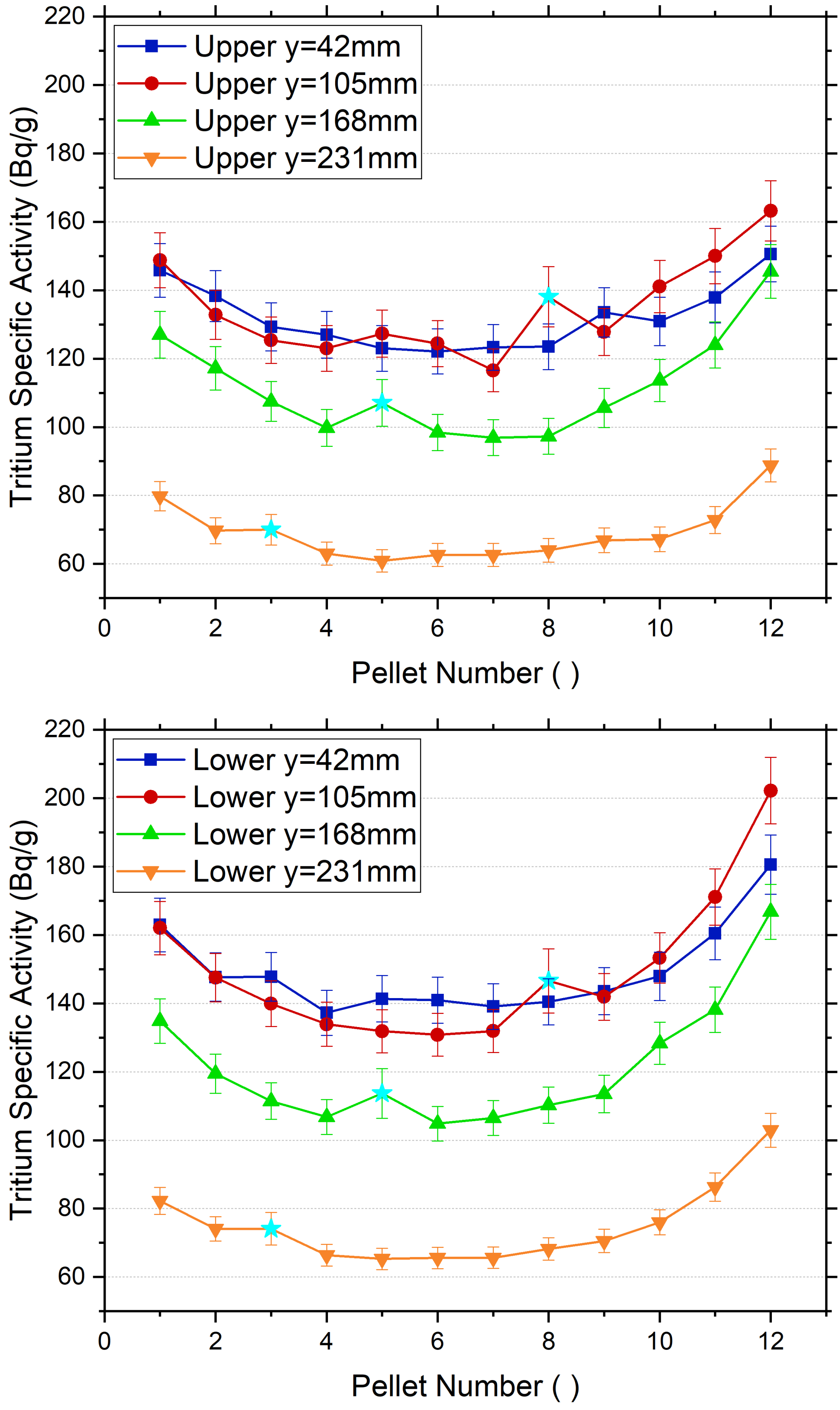

Figure 6.8: Measured tritium specific activity for four penetration depths as a function of pellet number in the breeder pellets in the HCPB TBM mock-up. The upper breeder stack (top) is measured by TUD, the lower breeder stack (bottom) is measured by ENEA and individual pellets in both stacks are measured by JAEA (marked by cyan stars). Error bars denote total experimental uncertainty (2σ). Data is taken from SINBAD (Kodeli et al., 2014).

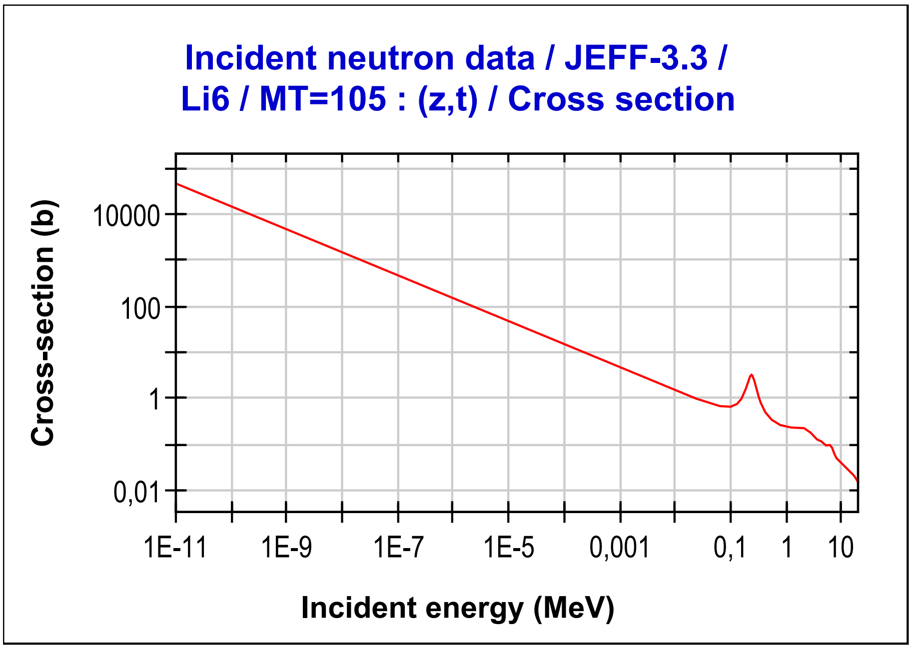

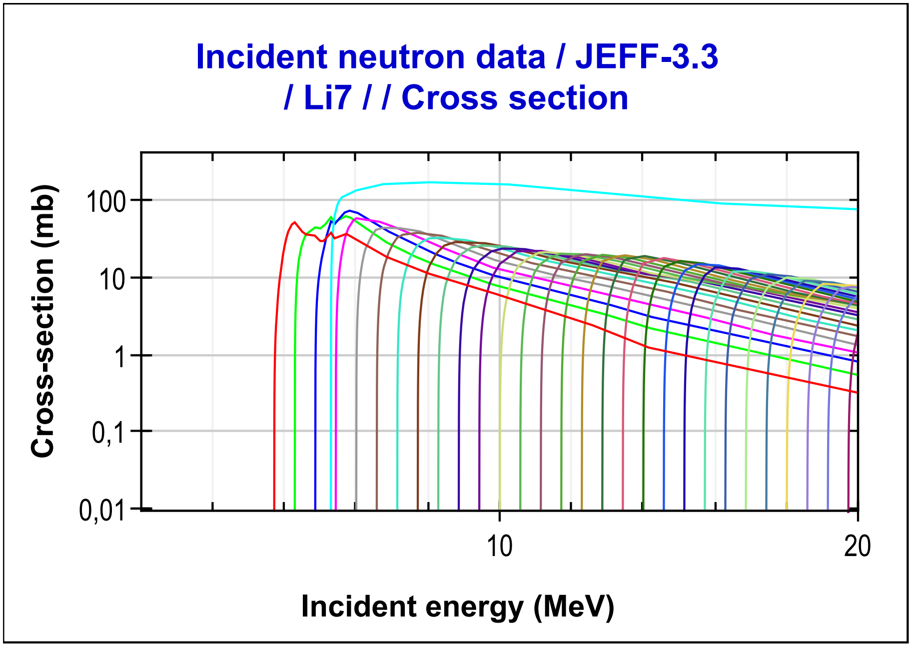

Figure 6.9: The reaction cross-sections of the tritium producing reactions of the lithium isotopes. The plots were created with the JANIS tool (Soppera et al., 2014) using the JEFF-3.3 nuclear cross-section library (Plompen et al., 2020).

breeder layer it can be deduced that either imperfections in the geometry description of the steel insert or the nuclear cross-section of steel is causing an increased discrepancy of the calculation results toward experimental observations.

It can be seen that MCNP underestimates the experimental result for nearly all breeder pellets, by up to about 15 %. In some cases the error range does not reach up to $C/E = 1$. This is consistent with the result obtained by the original evaluators (Batistoni et al., 2007). This uniform underestimation means that the simulation of the DEMO TBR is expected to give a conservative result (Fischer et al., 2020).

In the evaluation by Batistoni et al. (2007), the final uncertainty (2σ) of the tritium activity in the breeder pellets (9.2–10.6 %) has been calculated from the experimental error previously described in section 3.2.2, the uncertainty of the FNG absolute intensity (6 %), the statistical uncertainty of the MCNP calculation (3–3.2 %) and the uncertainty due to the nuclear cross-sections which has been estimated with a sensitivity/uncertainty analysis (4–5 %).

In the calculations done for this thesis, a larger number of particle histories are calculated, which cause the statistical errors of both MCNP and Geant4 to be much lower so that they are negligible compared to the other error sources. As different nuclear data libraries are used than in the original evaluation, the sensitivity/uncertainty analysis is no longer applicable. Due to this, this error source is left out of the calculation of the total uncertainty. It is very likely, however, that the uncertainty due to the nuclear cross-sections is still in the same order of magnitude, so the calculated total uncertainty slightly underestimates the actual uncertainty.

The total uncertainty is calculated by adding up the squares of the individual errors and taking the square root of the result. This yields a total relative uncertainty (2σ) of 7.7 % for pellets measured by ENEA, 8.1 % for pellets measured by TUD, and 8.8 % for pellets measured by JAEA.

As the tritium production cross-section of Li-6 increases towards lower neutron energies, Geant4's underestimation in the fast and uncollided neutron flux observed by the activation foils has little impact on the tritium activity in the breeder pellets. For both the upper and the lower blanket box, the Geant4 results follow the MCNP results closely, but are slightly lower. The deviation from MCNP increases with penetration depth up to 2.7 % in the upper blanket box and up to 2.1 % in the lower blanket box. This is outside the statistical error range but well within the experimental error range. Furthermore, this discrepancy between both codes is much less significant than the discrepancy between either code and the experimental result, which is likely caused by the nuclear data. Therefore, this benchmark calculation by Geant4 can be considered successful.

Comparison with Alternative Code Serpent-2

For the Serpent-2 code, which is one of the other considered alternative codes to MCNP, the same benchmark has been performed by Valentine et al. (2021) using the FENDL-2.1 nuclear data library and the same dosimetry data as in this thesis: IRDFF-v.1.05.

For the activation foils, the Serpent-2 results are consistent with MCNP within the experimental error with deviations of the same magnitude as observed for Geant4 in this thesis. There is no trend for larger deviations at deeper penetration though.

The ratio between MCNP and Serpent-2 results $MCNP/Serpent$ in all pellets of the four stacks in the lower breeder box is displayed in figure 6.12 and the $MCNP/Geant4$ results obtained in this thesis are displayed plotted in the same way for comparison in figure 6.13. It can be seen that the Serpent-2 results fluctuate around 1 with no observable effect of penetration depth, as opposed to Geant4's trend to underestimate the MCNP results more with increasing penetration depth. While all Geant4 results deviate less than 2.2 % and for the pellet stack closest to the source only less than 0.6 %, some of the Serpent-2 results exceed this with deviations up to 4.7 %. Consequently, both codes show compliance with MCNP in the same order of magnitude for this set-up. For different set-ups with deeper penetration the underestimation trend for the Geant4 results might lead to larger deviations.

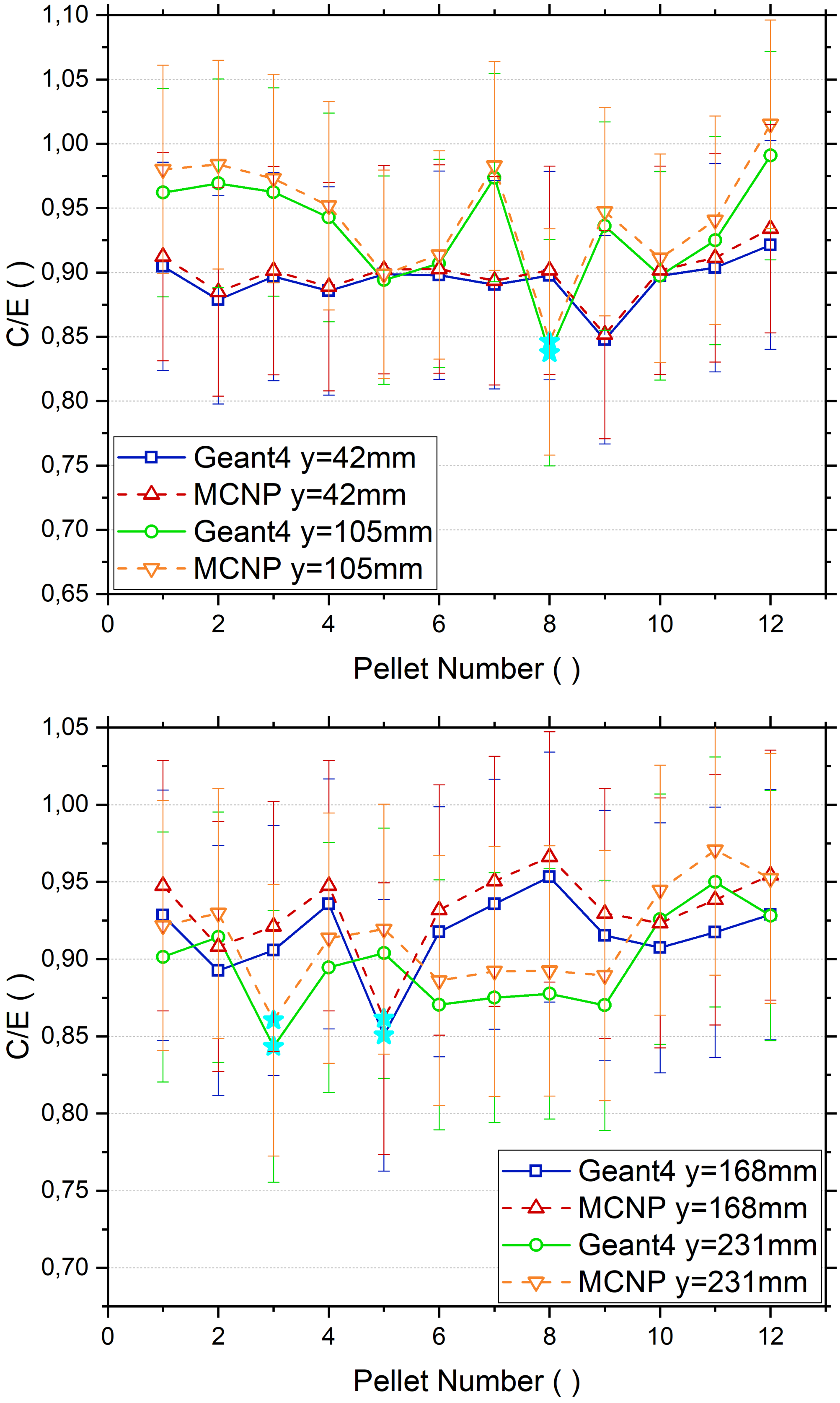

Figure 6.10: The C/E of Geant4 and MCNP with uncertainties (2σ) for the tritium activity in the breeder pellets at different penetration depths in the upper breeder box. Most pellets were measured by TUD, except for individual pellets measured by JAEA (cyan stars). Adapted from Nunnenmann et al. (2020).

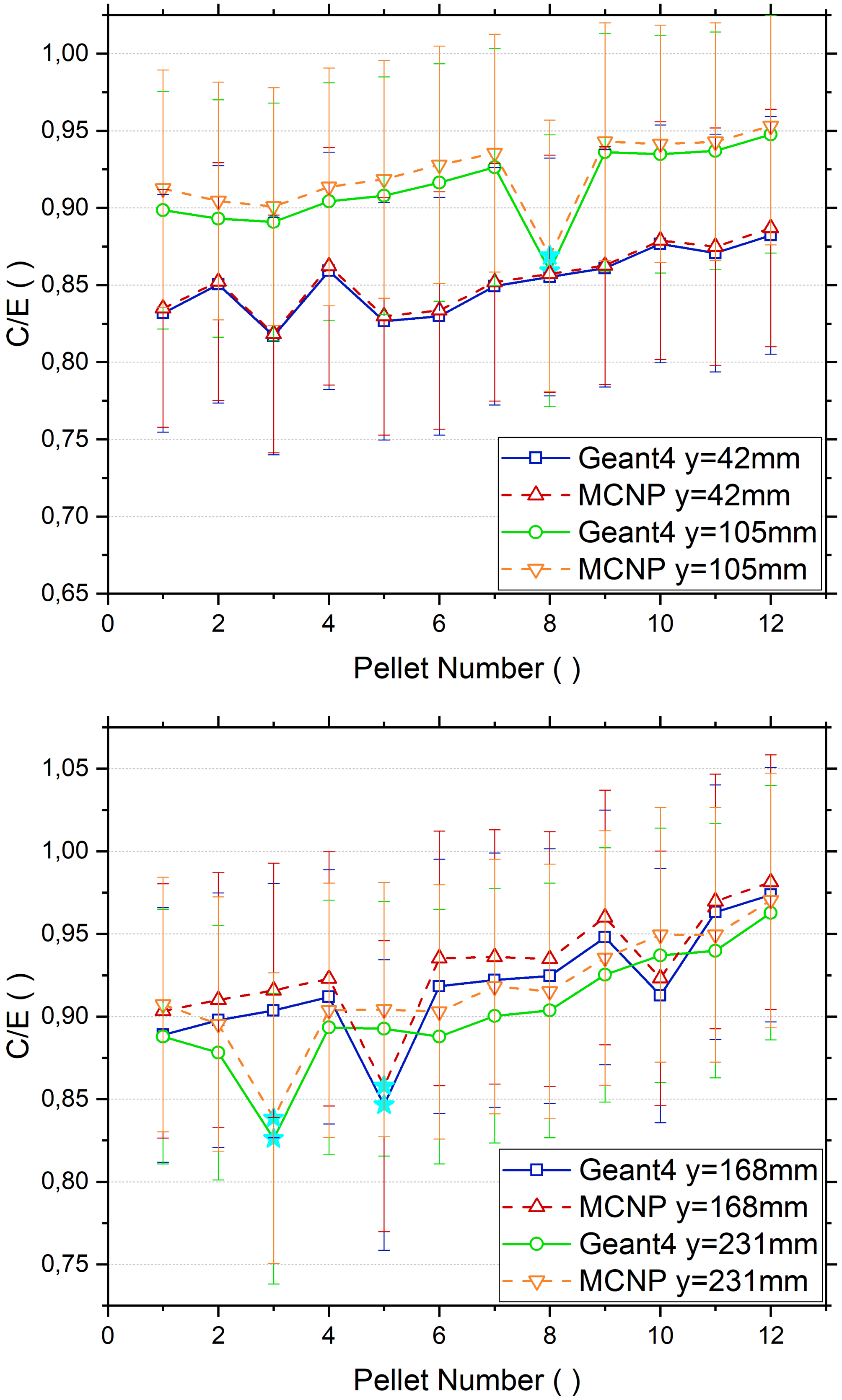

Figure 6.11: The C/E of Geant4 and MCNP with uncertainties (2σ) for the tritium activity in the breeder pellets at different penetration depths in the lower breeder box. Most pellets were measured by ENEA, except for individual pellets measured by JAEA (cyan stars). Adapted from Nunnenmann et al. (2020).

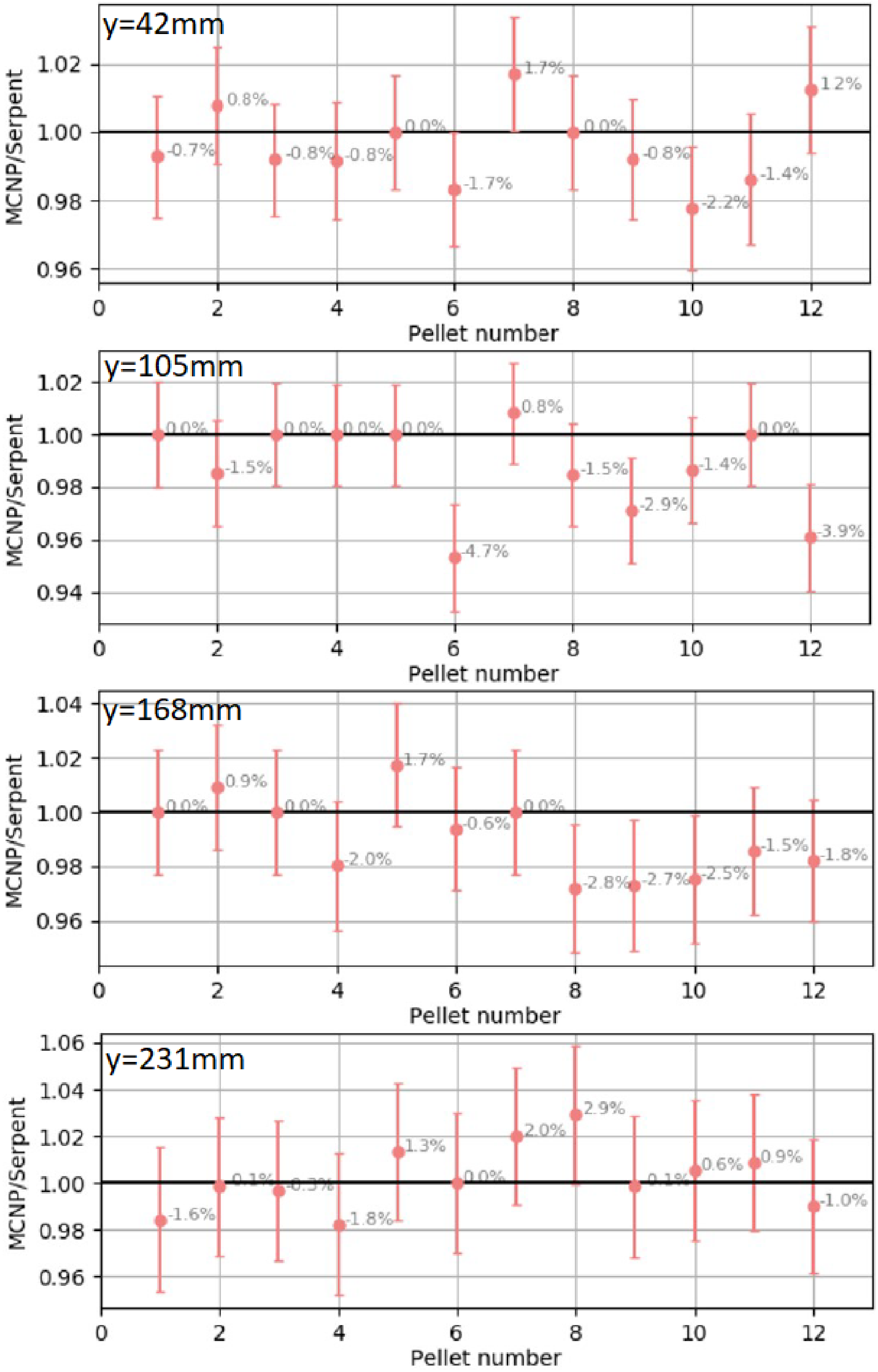

Figure 6.12: The ratio of MCNP and Serpent-2 for the tritium activity in the breeder pellets of the SINBAD HCPB experiment at different penetration depths in the lower breeder box plotted against the pellet number (modified from Valentine et al. (2021)).

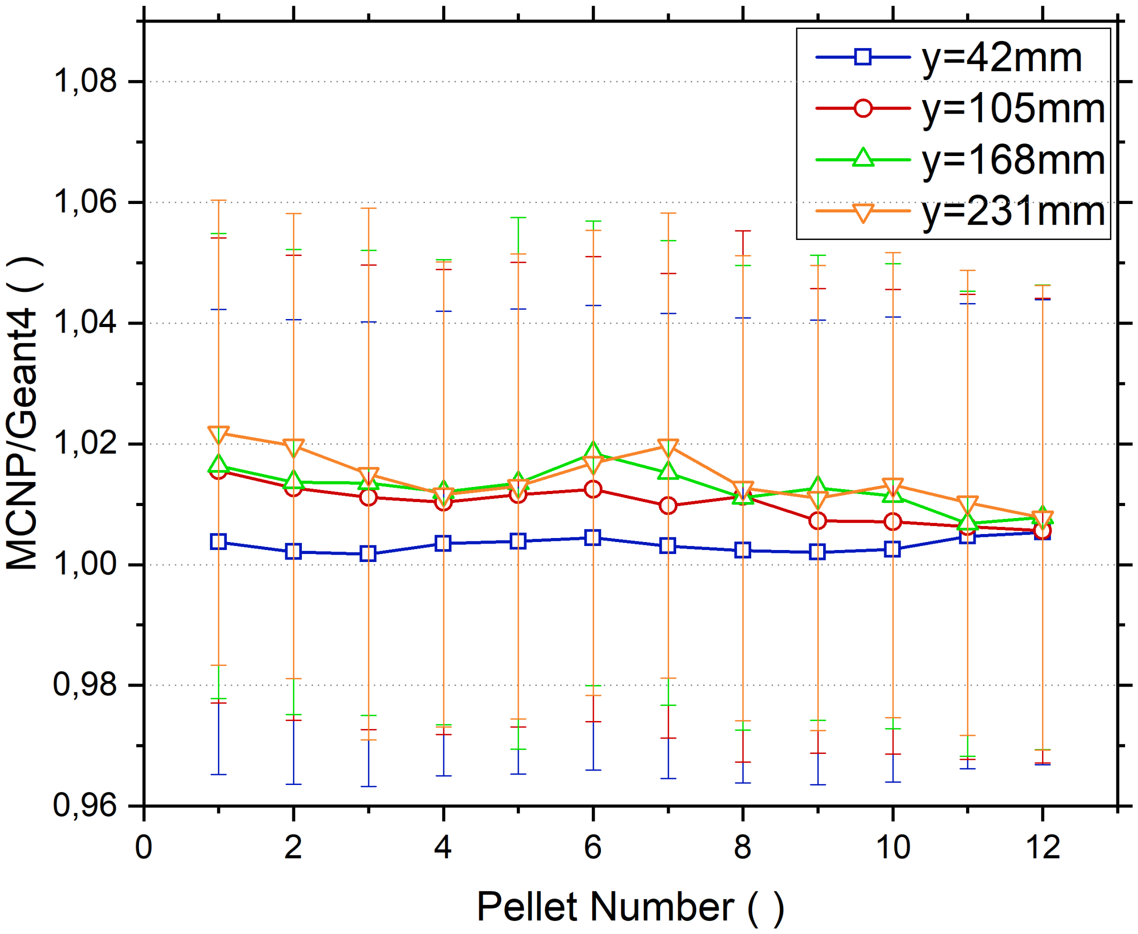

Figure 6.13: The ratio of MCNP and Geant4 with experimental uncertainties (1σ) for the tritium activity in the breeder pellets of the SINBAD HCPB experiment at different penetration depths in the lower breeder box plotted against the pellet number.

6.3 Test of Coupled Neutron-Photon Transport and Variance Reduction

A benchmark on a deep penetration shielding calculation using a mock-up of the ITER bulk shield is used for testing both Geant4's variance reduction and coupled neutron-photon transport capabilities.

There is no standard Geant4 executable. Instead, the user has to build their own code package out of available modules and own implementation. To assist with this process, Geant4 provides a suite of example implementations. For variance reduction, a number of examples are provided in the "/extended/biasing" directory. The results shown in the following are from an implementation with the general biasing approach based on the example "GB03". This implementation still has issues which affect the results.

For MCNP, $2 \cdot 10^8$ particle histories are used. For Geant4 it has become apparent that the relative errors are still too large, so the number is increased to 10^9 particle histories. The results for 10^7 histories are also shown as a reference point to discuss the convergence behaviour.

The neutron fluence spectrum at position A (41.5 cm penetration depth) is displayed in figure 6.14. First the experimental neutron fluence spectrum is discussed. The peak near 14.5 MeV is produced by uncollided neutrons. This shows that a significant number of neutrons penetrate until the representation of the back plate of the shielding blanket without having any material interactions.

The centre of the uncollided neutron peak is slightly higher than the 14.1 MeV of the fusion reaction, because the neutron energy produced in a neutron source such as the FNG is shifted to slightly higher energies in the direction of the deuteron acceleration. An example of this can be seen for the IPPE neutron source of similar build in figure 4.2. The way the neutron source is aligned in this experiment causes the neutrons to have the maximum possible energy.

All lower energy ranges are populated by neutrons losing energy through interactions with the material. Perspex consists of carbon, oxygen, and is rich in hydrogen, which are all light nuclei. This effectively slows down neutrons with elastic scattering interactions. The steel consists mainly of iron, chromium, and nickel. For these nuclides, elastic scattering is also dominant throughout nearly all of the energy spectrum. However, the slowing down is less effective, because these nuclides are heavier.

All nuclides except H-1 also have threshold reactions with varied strengths and threshold energies. These either remove neutrons entirely (e.g. (n,p) and (n,α)) or they create secondary neutrons with much lower energies (e.g. (n,n') and (n,2n)). This is causing the broad dip below the uncollided neutron peak down to ≈ 7 MeV, after which the fluence is rising towards lower energies. Since there are many nuclides involved with varying relative strengths of the threshold reactions, there are small local peaks and dips overlaid on the broad dip region.

Another neutron removing reaction, but without a threshold, is the (n,γ) reaction. It is several orders of magnitude lower than the total cross-section at energies above 1 MeV for all considered nuclides, and therefore has little effect in this range. For the Perspex nuclides, it remains this low throughout the whole considered energy range. For the steel nuclides, there is a resonance region below 1.5 MeV, where both the dominant elastic scattering and the (n,γ) reaction have strong fluctuations. In this range, some of the narrow peaks of the (n,γ) reaction reach high enough to have a relevant effect. Due to this, there are some fluctuations in the neutron fluence in this range.

The neutron fluence calculation is using larger bins than the experimental results. Therefore it cannot follow strong gradients as effectively. The neutron fluence calculated by MCNP is close to the experimental fluence in the uncollided neutron peak. MCNP slightly overestimates the fluence in the transition between uncollided neutron peak and threshold reaction dip between 12 MeV and 14 MeV. The larger energy bins for the simulation do not allow to reproduce the smaller features such as the local dip near 7.75 MeV or the small peak below 12 MeV, but the broader local peak centred around 9.5 MeV is well reproduced.

Between 1 MeV and 7 MeV, the MCNP result is following the experimental result quite well with only a very slight underestimation. In the resonance region below 1 MeV, the MCNP result is generally lower than the experimental result and does not quite reproduce the fluctuation features.

The Geant4 result has strange fluctuations. These are not caused by poor statistics, because they exist very similarly for both the 10^7 histories result and the 10^9 histories result. On average, the Geant4 curve fluctuates around the MCNP and experimental curves. Often a strong overestimation in one bin is followed by a strong underestimation in the next bin.

There are energy ranges where the Geant4 result is close to the MCNP result without any strong fluctuations such as between 1 MeV and 2 MeV, between 4.5 MeV and 7 MeV, between 9 MeV and 12 MeV, and between 14 MeV and 15 MeV. The Geant4 result is mostly slightly higher in these ranges.

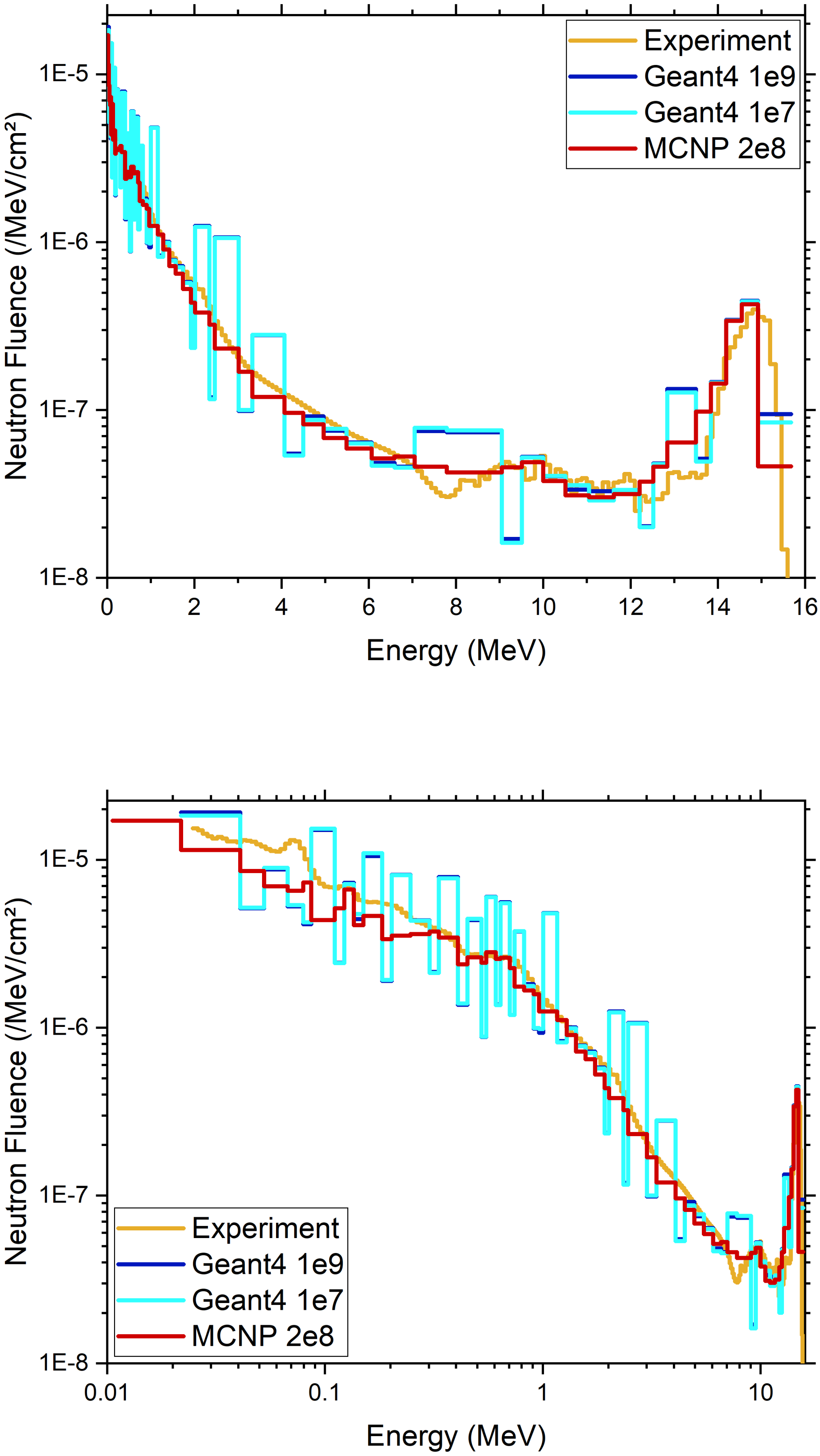

Figure 6.14: The neutron fluence measured experimentally and simulated with Geant4 and MCNP plotted against the neutron energy at position A (penetration depth: 41.5 cm) of the ITER bulk shield benchmark with a linear (top) and a logarithmic (bottom) energy scale.

The cause for the strong fluctuations is likely a compability issue between the importance biasing variance reduction algorithm and the HalfSpaceSolid geometry description. When particles hit the boundary between two geometry volumes, the HalfSpaceSolid geometry description defines them as belonging to neither the previous nor the current volume, but instead the World Volume. As the World Volume is set to importance of 1 and in the rest of the geometry, the importances rise with penetration depth, it can for example happen that a particle moving from volume 1 with importance 5000 to volume 2 with importance 10000 hits the boundary with importance 1. Instead of splitting the particle into 10000/5000=2 with half the previous weight, the particle will be killed in the Russian Roulette with the high probability of 1-1/5000. Any surviving particle is given the enormous weight of 5000.

The result collected for the neutron fluence is a combination of a reasonable result produced by particles which never stopped on a boundary with an underestimation due to particles having been killed prematurely and an overestimation due to some particles arriving with too large weights.

The neutron fluence spectrum at position B (penetration depth: 87.6 cm) is displayed in figure 6.15. The experimental neutron fluence in this representation of a position close to the boundary between vacuum vessel and toroidal field coils is significantly lower than at position A (penetration depth: 41.5 cm). At position A, the neutron fluence is between 10^{-8} /MeV/cm^2 and $2 \cdot 10^{-5}$ /MeV/cm^2 and the maximum of the uncollided neutron peak is at $4{\cdot}10^{-7}$ /MeV/cm^2. At position B, the neutron fluence is between 10^{-11} /MeV/cm^2 and $5 \cdot 10^{-8}$ /MeV/cm^2 and the maximum of the uncollided neutron peak is at $4 \cdot 10^{-10}$ /MeV/cm^2. This means, the additional penetration into the shielding has caused the neutron fluence to be 2–3 orders of magnitude lower in general and 3 orders of magnitude lower for the uncollided flux maxima.

Even at this depth, some neutrons penetrate without any prior material interactions. However, the relative strength of the uncollided neutron peak compared to the lower energy tail of the spectrum near 0.1 MeV is lower than at position A. For position A, the maximum of the peak is 50 times lower than the lower energy tail and for position B this increases to 125 times lower.

The shape of the spectrum is similar: the uncollided neutron peak is centred at 14.5 MeV followed by the broad threshold reaction dip down to ≈ 7 MeV, which is overlaid with minor local peaks and dips at similar positions: a local dip near 12 MeV and 7.75 MeV, and a broad higher area between these dips. Towards lower energies, the neutron fluence rises and below 1.5 MeV the resonance regions in the steel nuclides are causing fluctuations.

Again, the larger energy bins of the simulation do not allow the MCNP simulation result to follow the experimental neutron fluence to perfectly reproduce the uncollided neutron peak. There is an overestimation in the following upper end of the threshold reaction dip and at the local dip near 7.75 MeV similar as for position A.

Between 1 MeV and 7 MeV, the MCNP result is following the experimental result quite well with a very slight underestimation, which is slightly larger than for position A. Also in the resonance region below 1 MeV, the MCNP result is deviating more strongly from the experimental result than for position A and already at 0.7 MeV instead of 0.3 MeV.

The Geant4 result still has strong fluctuations. In the deeper position B, these fluctuations no longer average out to the MCNP and experimental result. Instead they are mostly too high. As far as it is possible to separate the general trend out from the fluctuation issue, Geant4 appears to overestimates the neutron fluence throughout most of the energy range of this deeper penetration.

It does not look like the accuracy of the result is improved between 10^7 and 10^9 histories. Only for some energy bins, the 10^9 result is better such as for the largest deviations of the 10^7 result at 2 MeV, 0.6 MeV, and 0.1 MeV. For other ranges, such as the range between 4.5 MeV and 7 MeV, the 10^7 result is following the MCNP and experimental result very closely, while the 10^9 result has a large overestimation.

At this deeper penetration, likely more neutron histories which have interacted with a geometry boundary on their way there are reaching the detector volume, causing there to be more and stronger fluctuating deviations than for position B. Instead of achieving better convergence, the 10^9 result includes more particle histories with boundary interactions than the 10^7 result, producing worse agreement with MCNP and the experimental result in many energy bins.

When looking at the relative statistical errors displayed in figure 6.16, it can be seen that the Geant4 result for 10^9 histories is not lower than the MCNP result as it is for position A and as one would expect due to the five times larger particle history number. Instead, it fluctuates around only 0.1, and only goes down to below 0.01 above 13 MeV. In fact, in the energy range of 3.3–10 MeV, the statistical error for 10^7 histories is mostly lower than for 10^9 histories. In part of this energy range, the 10^7 result follows the experimental result quite well and much better than the 10^9 result.

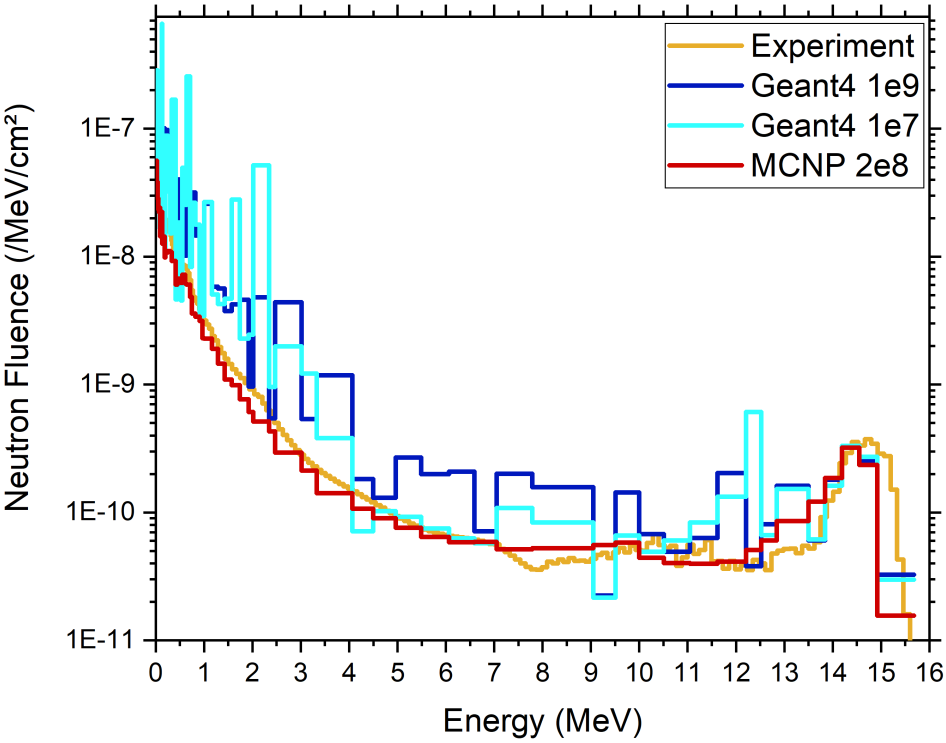

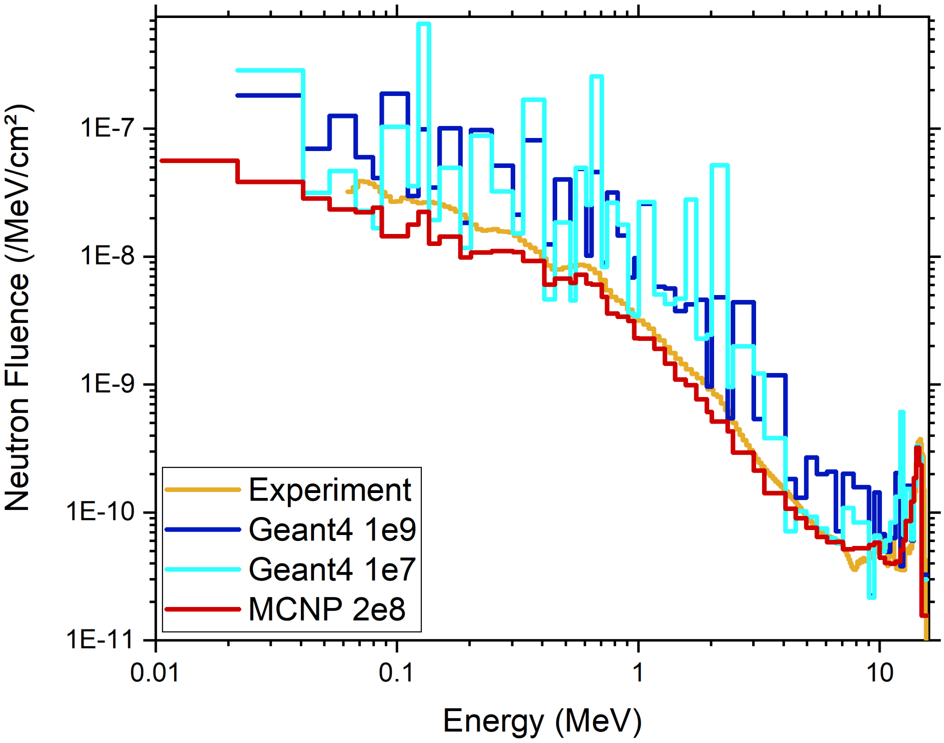

Figure 6.15: The neutron fluence measured experimentally and simulated with Geant4 and MCNP plotted against the neutron energy at position B (penetration depth: 87.6 cm) of the ITER bulk shield benchmark with a linear (top) and a logarithmic (bottom) energy scale.

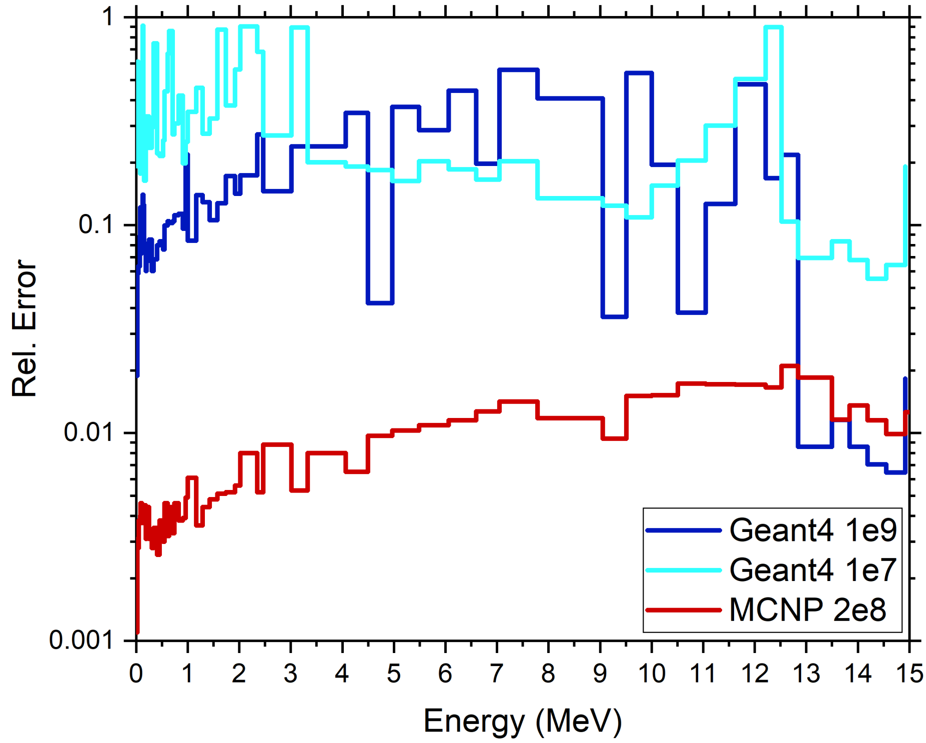

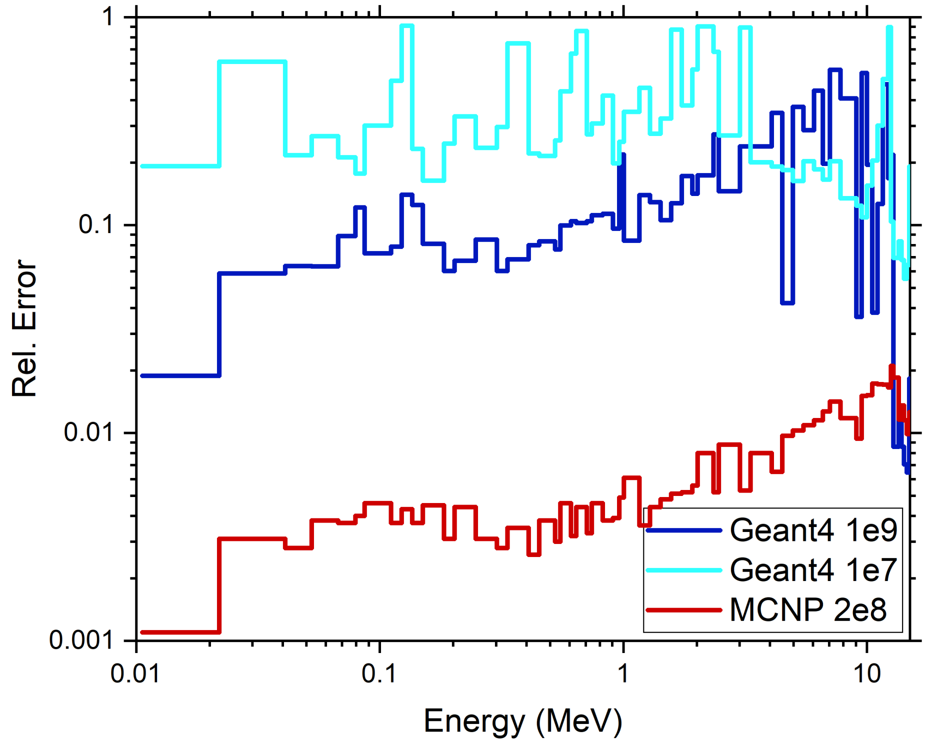

Figure 6.16: The statistical error of the neutron fluence plotted against the energy in position B of the ITER bulk shield benchmark.

All of this indicates major problems with the variance reduction procedure, which causes the calculation to fail to reach convergence. This effect compounds with penetration depth, since the results for position A are still on average consistent with the experimental and MCNP results. It is unclear whether the geometry boundary issue for the importance sampling in the HalfSpaceSolids is the only cause of these problems or if there is an additional cause. It is also interesting that > 13 MeV neutrons which have the fewest material interactions before reaching the detector volume appear to be least affected.

The gamma fluence spectra at position A and position B are displayed in figure 6.17. Both neutrons and gammas penetrate deeply through the material. One part of the gamma spectrum detected at a specific penetration depth is the spectrum of gammas created nearby by neutrons penetrating to this depth and interacting with the local material. Another contribution comes from neutron interactions further away at different penetration depths and from different material interactions. Only part of the gammas produced further away reach the detection point. Another part is scattered to lower energies by the Compton effect and the last part is removed by processes such as the photoelectric effect. Other processes such as pair or triplet production can introduce new peaks into the gamma spectrum such as at 0.511 MeV due to positron annihilation.

The gammas are produced at various characteristic energies due to neutrons interacting with the material. According to Batistoni et al. (1999), the copper with density 8.96 g/cm^3 and the perspex with density 1.18 g/cm^3 and molecular formula $(\mathrm{C_5O_2H_8})_n$ have a high degree of purity (< 10 appm of any trace materials). The steel with density 7.89 g/cm^3 mainly consists of Fe (weight fraction 68.1 %), Cr (16.8 %), and Ni (10.7 %). The polyethylene (PE) of the rear shield has the molecular formular of $(\mathrm{CH_2})_n$.

In table 6.1, the most important neutron induced characteristic gamma energies of these elements are displayed. Both interactions with thermal neutrons and with high energy neutrons can produce characteristic gammas. The gamma lines produced by thermal neutrons are taken from Firestone et al. (2006) and the gamma lines produced by fast neutrons are taken from Demidov et al. (1978).

For the thermal gamma lines, Firestone et al. (2006) also reports microscopic cross-sections. Using molar mass and isotopic composition data taken from Coursey et al. (2015), the material density, and the composition of the materials, the macroscopic cross-sections for the most important gamma lines of the isotopes contained in copper, steel and perspex have been calculated and are also displayed in table 6.1. They indicate the relative likelihood of these reactions. The PE not considered for the macroscopic cross-sections as it is further away produces an additional contribution to the carbon and hydrogen lines. For the fast gamma lines, Demidov et al. (1978) contains no cross-section data, only relative intensity, which is given in the table instead.

Position A is located at a penetration depth of 41.5 cm from the front, directly behind a 6 cm thick Perspex layer and represents the back plate of the shielding blanket. Position B is located at a penetration depth of 87.6 cm and represents a position close to the boundary between vacuum vessel and toroidal field coils. Gammas can scatter randomly in the material and therefore gammas produced further back than the measurement position can contribute to the detected gamma flux. Since the neutron flux decreases from front to back and in directions away from the central axis, these contributions are likely to be somewhat lower than contributions from the front and near the central axis.

Comparing the gamma spectra in figure 6.17, it can be seen that the gamma fluence in position B is generally close to three orders of magnitude lower than in position A. The shape and position of the peaks is mostly similar. The broadness of the detected peaks cover several gamma line energies.

Looking at the individual peaks in detail, in the spectrum of position B, there is a smaller peak around 9.8 MeV which correlates with the Cr-53 peak at 9.7 MeV. For position A, this peak is not as well separated from the next peak at lower energy but also present.

The next peak around 9.0 MeV correlates with strong lines by Ni-58 and Cr-53 at 9.0 MeV and 8.9 MeV. Weaker lines of Fe-54 at 9.3 MeV and Cr-50 at 8.5 MeV are positioned close to the edge of the peak. The peak is followed by a dip near 8.4 MeV despite there being another fairly strong line of Ni-58 close-by at 8.5 MeV. The dip is less pronounced for the spectrum of position A.

The fact that the dips near 9.5 MeV and 8.4 MeV are less pronounced in the spectrum of position A can be explained by the presence of the thick perspex layer with low atomic numbers $Z = 1 - 8$ directly in front. In contrast, position B has a thinner perspex layer and instead more steel with atomic numbers $Z = 24 - 28$ in front of it and only steel and copper ($Z = 29$) behind it.

The area diagram of the most important relative parts of the photon interaction probability depending on photon energy and atomic number Z of the interaction material in figure 2.1 shows that at

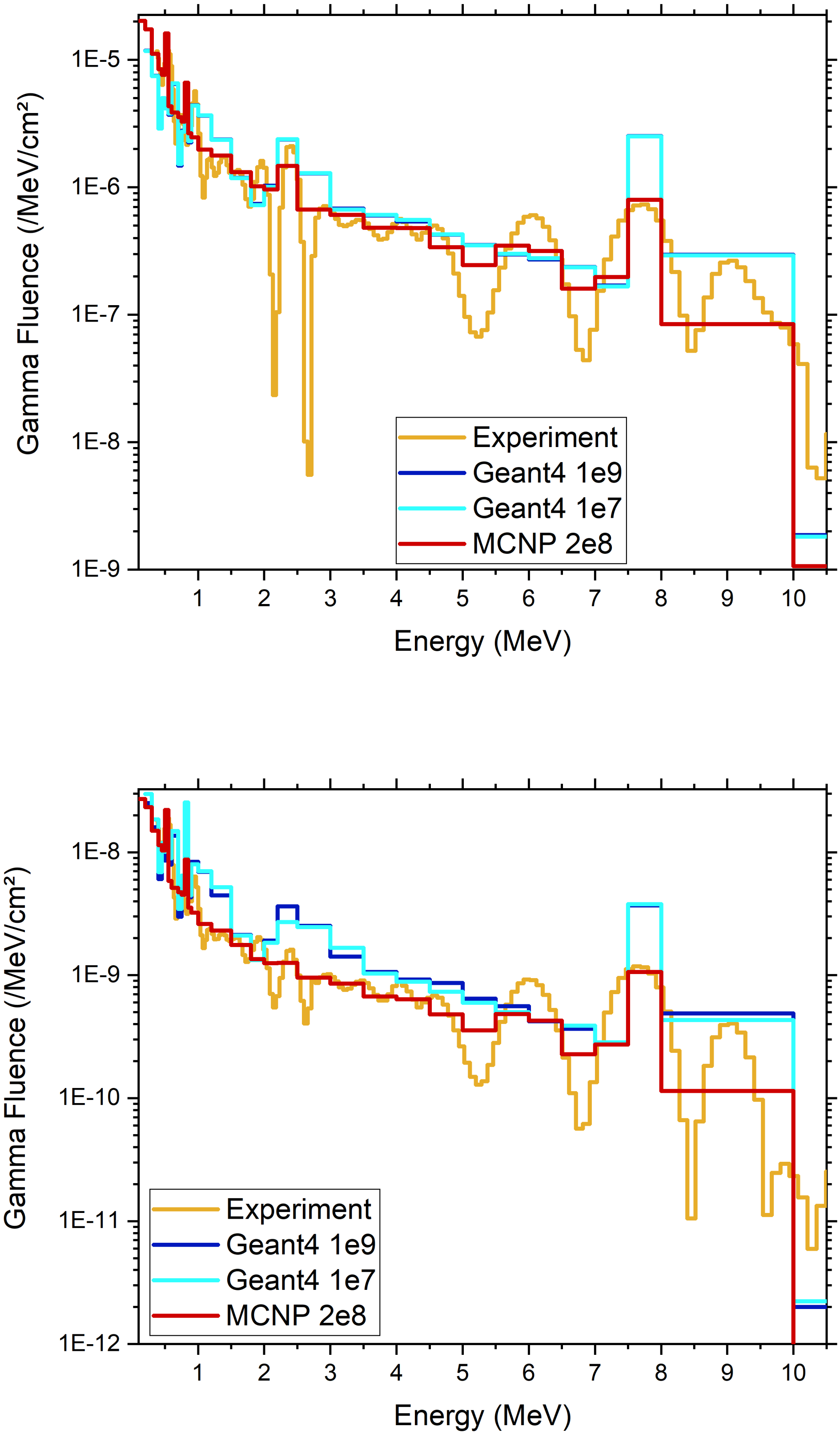

Figure 6.17: The gamma fluence measured experimentally and simulated with Geant4 and MCNP plotted against the neutron energy at position A (top, penetration depth: 41.5 cm) and at position B (bottom, penetration depth: 87.6 cm) of the ITER bulk shield benchmark.

Table 6.1: A list of the strongest neutron induced gamma lines of the most abundant isotopes in the ITER bulk shield mock-up. Lines of the same isotopes with the same energy after rounding to one decimal have been merged. Lines produced by thermal neutrons are from Firestone et al. (2006). The macroscopic cross-sections in the materials steel, perspex and copper have been calculated. Lines produced by fast neutrons are marked in bold and are from Demidov et al. (1978).

Element	Energy (MeV)	Macro. cross-section (/cm)	Rel. Intensity
Cu-63	0.6	$2.7 \cdot 10^{-02}$	-
Fe-56	0.7	$7.6 \cdot 10^{-03}$	-
Cr-50	0.7	$4.0 \cdot 10^{-04}$	-
Cr-53	0.8	$2.1 \cdot 10^{-03}$	-
Fe-56	0.8	-	100
Ni-58	0.9	$1.5 \cdot 10^{-03}$	-
Cu-63	1.0	-	100
Fe-56	1.3	$3.8 \cdot 10^{-03}$	-
Ni-60	1.3	-	60
Cr-52	1.4	-	100
Ni-58	1.5	-	100
Fe-56	1.6	$8.5 \cdot 10^{-03}$	-
Fe-56	1.7	$1.0 \cdot 10^{-02}$	-
Cr-53	1.8	$2.7 \cdot 10^{-04}$	-
O-18	2.0	-	100
H-1	2.2	$1.3 \cdot 10^{-03}$	-
Cr-53	2.2	$2.8 \cdot 10^{-04}$	-
Fe-56	4.2	$5.5 \cdot 10^{-03}$	-
Cnat	4.4	-	109
Fe-56	5.9	$1.3 \cdot 10^{-02}$	-
Fe-56	6.0	$1.3 \cdot 10^{-02}$	-
O-16	6.1	-	595
Cr-53	6.6	$2.8 \cdot 10^{-04}$	-
Ni-62	6.8	$1.5 \cdot 10^{-04}$	-
Cu-63	7.0	$7.4 \cdot 10^{-03}$	-
Cr-53	7.1	$2.2 \cdot 10^{-04}$	-
Cu-63	7.2	$5.4 \cdot 10^{-03}$	-
Cu-63	7.3	$2.8 \cdot 10^{-02}$	-
Fe-56	7.3	$7.6 \cdot 10^{-03}$	-
Ni-60	7.5	$4.5 \cdot 10^{-04}$	-
Fe-56	7.6	$6.7 \cdot 10^{-02}$	-
Cu-63	7.6	$3.2 \cdot 10^{-02}$	-
Ni-60	7.8	$8.0 \cdot 10^{-04}$	-
Cu-63	7.9	$5.1 \cdot 10^{-02}$	-
Cr-52	7.9	$5.7 \cdot 10^{-03}$	-
Cr-50	8.5	$2.8 \cdot 10^{-04}$	-
Ni-58	8.5	$4.4 \cdot 10^{-03}$	-
Cr-53	8.9	$1.2 \cdot 10^{-03}$	-
Ni-58	9.0	$9.2 \cdot 10^{-03}$	-
Fe-54	9.3	$2.6 \cdot 10^{-04}$	-
Cr-53	9.7	$4.0 \cdot 10^{-04}$	-

energies close to 10 MeV, the Compton effect is clearly dominant for perspex, but for steel and copper, pair production is close to taking over.

The Compton effect is causing gammas of the characteristic peaks to lose part of their energy in material interactions producing a continuum of lower energy gammas and thereby filling up the dips between the peaks. As it is more dominant in position A, this explains the less pronounced dips near 9.5 MeV and 8.4 MeV.

Pair production produces no continuum of lower energy gammas, causing the dips near 9.5 MeV and 8.4 MeV in the gamma spectrum of position B to be more pronounced. No clear difference can be observed between the spectra of the two positions at 0.511 MeV, which is the energy of the annihilation gammas produced by pair production.

The difference in Z is only relevant at energies close to 10 MeV. At lower energies, the Compton effect is dominant irrespective of Z, so the effect on the spectrum is similar for both positions. Since the Compton effect causes secondary gammas whose energy is continuous but always lower than their original energy, it produces a continuous background which rises towards lower energies.

The next lower peak covers a number of gamma lines between 7 MeV and 7.9 MeV produced by steel and copper isotopes. It has to be noted that despite the strong macroscopic cross-section, the copper lines are likely to be weaker than the steel lines. For position A this is because copper is only present in a thin layer at the very front of the box while steel makes up a large part of the bulk volume. For position B this is because the closest copper is at deeper penetration depth where the further attenuated neutron flux is producing less gamma rays than in the steel at less penetration depth. The measured peak is centred near 7.6 MeV, which is the position of a strong Fe-56 gamma line. The next lower dip is positioned near an energy with only very weak gamma lines produced by Cr-53 and Ni-62 nearby.

The next lower peak covers the energy range between 5.2 MeV and 6.7 MeV and is centred at 6.0 MeV. It is caused by two strong gamma lines by Fe-56 at 5.9 MeV and 6.0 MeV. Additionally, there is the first gamma line produced by fast neutrons: at 6.1 MeV due to interaction with O-16.

No strong gamma lines are present near the next lower dip at 5.2 MeV.

Between 2.7 MeV and 4.8 MeV there is a range of several small peaks with nearly no dips between then. The upper two are shifted towards slightly higher energies than the gamma lines by Cnat at 4.4 MeV and by Fe-56 at 4.2 MeV. Table 6.1 does not contain any lines in the range between 2.7 MeV and 4.2 MeV, however several of the steel and copper isotopes have multiple lines in this range which are too weak for the table.

The next lower experimental peak is centred near 2.4 MeV. It is likely also shifted to slightly higher energies and correlates to the H-1 and weaker Cr-53 lines at 2.2 MeV. According to Batistoni et al. (1999), the energy calibration has been performed with multiple Compton edges with energy of 1.116 MeV and below, so a slight shift at higher energies is possible. For the peaks near 6.0 MeV, 7.6 MeV, and 9.0 MeV, this is not relevant, because they are broader.

In position A, this peak is slightly higher compared to the rest of the spectrum than in position B. This is due to position A being directly behind the thick perspex layer, which contains hydrogen. In the spectrum for position A this peak is surrounded by very deep dips, which are not present for position B. This might be caused by the increased presence of steel and copper in position B, whose isotopes have multiple weak gamma lines close to the dip energies.

The next experimental peak is centred near 1.9 MeV. This is likely the upwards shifted Fe-56 gamma line at 1.7 MeV. Below there are several weak and closely set peaks down to 1 MeV. These are caused by gamma lines both in table 6.1 and weaker lines by steel and copper isotopes not included in there.

The baseline of the peaks continues to rise due to the Compton scattering continuum and on top of it, peaks are positioned at 0.97 MeV, 0.7 MeV, and 0.5 MeV correlating to Cu-63, Cr-50 and Fe-56 gamma lines. Part of the peak at 0.5 MeV is likely caused by the annihilation gammas of pair production.

When comparing the experimental result with the MCNP simulation, it can be seen that the larger energy bins of the calculations are not resolving the strong peaks and dips very well.

The MCNP result includes a strong peak near 7.6 MeV and a slight peak near 6 MeV for both position A and B. In position A, there is additionally a peak at 2.4 MeV, which is not apparent for position B. In both positions, the MCNP result is following the general trend of the experimental result below the 6 MeV peak.

The Geant4 result also reproduces the peak at 7.6 MeV, but overestimates it strongly for both position A and B. Below it for position A, it fluctuates between slightly under- and overestimating the MCNP result without reproducing the peak near 6 MeV down until the 2.4 MeV peak, which it overestimates. For position B, the Geant4 result increasingly overestimates the experimental and the MCNP result down until the 2.4 MeV peak, which it overestimates more strongly than for position A. This is followed at lower energies by briefly getting close to the MCNP results for both positions. Stronger fluctuations above and below the MCNP result in adjacent energy bins such as observed for the neutron fluence only appear below 1 MeV for both positions. To a degree a deviation from the MCNP result is to be expected, considering that the photon transport is handled by Geant4's own physics package G4EmStandardPhysics.

The multiple interaction code-to-code benchmark (see section 5.2), reveals discrepancies in the gamma production and transport between Geant4 and MCNP. For the JEFF-3.3 library and the most abundant elements in this bulk shield benchmark, there is good agreement for H-1, a slight overestimation for Fe-56 and a strong overestimation for Cnat.

There is barely any difference between the 10^7 and 10^9 history result for position A. In position B, the difference increases slightly but does not become as pronounced as for the neutron fluence result. There are again multiple energy bins where the 10^9 result has worse agreement than the 10^7 result and only few where the 10^9 result has better agreement. The statistical error of the Geant4 result for 10^9 histories is in the range between 0.01 and 0.1. It is mostly lower than for 10^7 histories but not as low as the MCNP result for $2 \cdot 10^8$ histories. Since the gamma particles are produced by neutrons interacting with the material, the problems in the neutron fluence at position B also affect the gamma result and likely cause the overestimation.

Neutron and Gamma fluence results are also obtained integrated over larger energy ranges. The experimental versions have been processed from the spectra, while the codes have tallies with integral energy bins. In table 6.2, the C/E ratios for Geant4 and MCNP are displayed.

Table 6.2: Integral C/E results for the neutron and gamma fluence calculated with Geant4 (10^9 histories) and MCNP ($2{\cdot}10^8$ histories) at the positions A and B. The relative error is a combination of experimental and statistical calculation error.

	Geant4		MCNP	
Energy (MeV)	C/E	Rel. Error	C/E	Rel. Error
Neutron Fluence, Position A				
0.1–1	0.88	0.10	0.90	0.10
1–5	0.93	0.06	0.93	0.06
5–10	1.03	0.05	1.02	0.05
10–15	0.97	0.03	0.96	0.03
0.1–15	0.91	0.08	0.92	0.08
Neutron Fluence, Position B				
0.1–1	2.67	0.11	0.75	0.10
1–5	2.89	0.08	0.83	0.05
5–10	2.56	0.18	1.08	0.05
10–15	1.07	0.10	0.86	0.03
0.1–15	2.63	0.11	0.78	0.08
Gamma Fluence, Position A				
0.4–1	1.70	0.03	1.03	0.03
1–10.5	1.32	0.03	1.09	0.03
0.4–10.5	1.49	0.03	1.06	0.03
Gamma Fluence, Position B				
0.4–1	2.60	0.03	0.98	0.03
1–10.5	1.59	0.04	0.98	0.03
0.4–10.5	2.01	0.04	0.98	0.03

The displayed errors have been obtained by combining the experimental and the statistical calculation errors. In most cases, the statistical errors can be neglected. Only for the Geant4 neutron fluence at position B, the problem with the variance reduction causes statistical errors large enough to be significant. The experimental error for the gamma fluence is only given for the total range. The same relative error has been assumed for the other energy bins.

It can be seen that for the neutron fluence in position A, Geant4 produces C/E results on the same level as MCNP. As could already be observed for the spectra, for the neutron fluence in position B and for the gamma fluence in both positions, Geant4 significantly overestimates the experimental result. The best agreement with the experimental neutron results in position B is produced in the highest energy range, which involves the fewest material interactions.

6.4 Summary of the Major Results of the Validation Procedure

Geant4 performs on the same level as MCNP within the scope of the SINBAD IPPE iron sphere benchmark experiment. This shows it can produce reliable results for neutron interactions with the important structural material iron even in a thick bulk context.

Despite underestimating the high-energy neutron flux with increasing penetration depth, Geant4 manages to produce good results for the tritium production in the HCPB breeder blanket module mock-up benchmark experiment. The Geant4 results are very consistent with MCNP, with only a slight underestimation increasing towards higher penetration depths. This demonstrates Geant4 can be used to reliably predict the important fusion quantity of tritium production in breeder blankets. A comparison with the results of the same benchmark performed by Valentine et al. (2021) with the Serpent-2 code showed that both codes have comparable deviations from MCNP.

When setting up the ITER bulk shield benchmark, there have been issues in the implementation of the variance reduction. This causes stronger discrepancies and overestimation of the neutron fluence results for the detector position at deeper penetration. The variance reduction does not work well enough to achieve low enough relative errors. For less deep penetration, the effect is not as strong. Strange nonstatistical fluctuations can be observed in the neutron fluence results, but they average out into good integral neutron fluence agreement at the less deep penetration position.

At this position, the gamma fluence results visibly follow the MCNP result, but with an integral overestimation of 32–70 %. This matches up with the results for the multiple interaction code-to-code benchmark (see section 5.2), which reveals for the gamma flux close agreement, and slight and strong overestimations for the most relevant isotopes of the ITER bulk shield geometry (H, Cnat, and Fe-56). At deeper penetration, where the effects of the variance reduction issues on the underlying neutron flux are more severe, even stronger overestimations (59–160 %) in the gamma results can be observed.

It is unclear whether the identified HalfSpaceSolid boundary issue is the full cause for the discrepancies or if there are any additional problems in the variance reduction implementation in Geant4. In the current state, the variance reduction procedure cannot be considered reliable.

The gamma fluence calculation also yields too high overestimations. It is unclear how much of this is a secondary effect of the issues with the variance reduction. Considering that the multiple interaction benchmark also yields significant discrepancies for the gamma flux with several combinations of nuclide and library, it is likely that the gamma production and/or transport also has issues and can therefore not be considered reliable at this point.

Chapter 7

Application to DEMO Nuclear Analyses in Comparison with MCNP

In this final step, Geant4 is applied to a nuclear design analysis of the DEMO reactor. For a DEMO reactor equipped with a HCPB tritium breeding blanket, the TBR is calculated and analysed in comparison with MCNP.

For DEMO nuclear analyses, two different geometry set-ups are used. In the *heterogeneous* set-up, the layered inner structure of the breeder volumes, which consists of neutron multiplier zones filled with beryllium and breeding zones filled with lithiumorthosilicate separated by steel cooling plates, is represented. In the *homogenised* set-up, the inner structure is replaced by a uniform material, which is a mixture of the materials making up the heterogeneous model according to their share. For Geant4, it is not possible to fill the breeder volumes entirely with the heterogeneous representation. The left-over 8.4 $\%$ of the volume, which are located close to the surface of the breeder volume parts, are filled with the homogenised material mixture, making the Geant4 set-up only *mostly heterogeneous*.

The convergence testing developed for Geant4 is passed for $2 \cdot 10^9$ particle histories for the homogenised set-up and for 10^9 particle histories for the mostly heterogeneous set-up. For MCNP, the included statistical checks are passed for 10^9 particle histories for the homogenised and 10^8 particle histories for the heterogeneous set-up. The results discussed in the following are obtained using these particle history numbers.

The JEFF-3.3 nuclear data library is used in these calculations. The TSL data for beryllium is taken from JEFF-3.3 for MCNP, and for Geant4 from the standard G4NDL4.5 data, which is based on the ENDF/B-VII library.

7.1 Analysis of DEMO Neutron Flux Spectrum

The TBR is an integral quantity, but because it is calculated with the energy-dependent tritium production cross-sections of Li-6 and Li-7, it still depends on the energy spectrum of the neutron flux. Therefore the nuclear analyses are started with the calculation of the average neutron flux spectrum in the breeder volumes.

In figure 7.1, the average neutron flux results for Geant4 and MCNP for both the homogenised and the (mostly) heterogeneous set-up and the ratio between the heterogeneous and the homogenised result are displayed. Due to the different geometry, the results are obtained only in the breeding material layers for the heterogeneous model, and for the whole breeder volume for the homogeneous model. The results are comparable, since the average flux contains a volume normalisation.

It can be seen that in the homogenised set-up the results for Geant4 and MCNP are nearly identical, while the differences in the heterogeneous set-up cause the Geant4 result to be higher and closer to the result of the homogenised set-up. Later on, the deviations between the Geant4 and MCNP results are examined in more detail.

First, the underlying physics and the differences between the homogenised and the heterogeneous average flux results are discussed. The average flux is calculated in a time-invariant way for a steady-state state plasma neutron source. It has a strong, narrow peak at 14.1 MeV, which is caused by the neutrons coming directly from the plasma without losing any energy in material interactions. The width of the peak comes from Gaussian broadening due to the thermal motion in the plasma. It can be seen

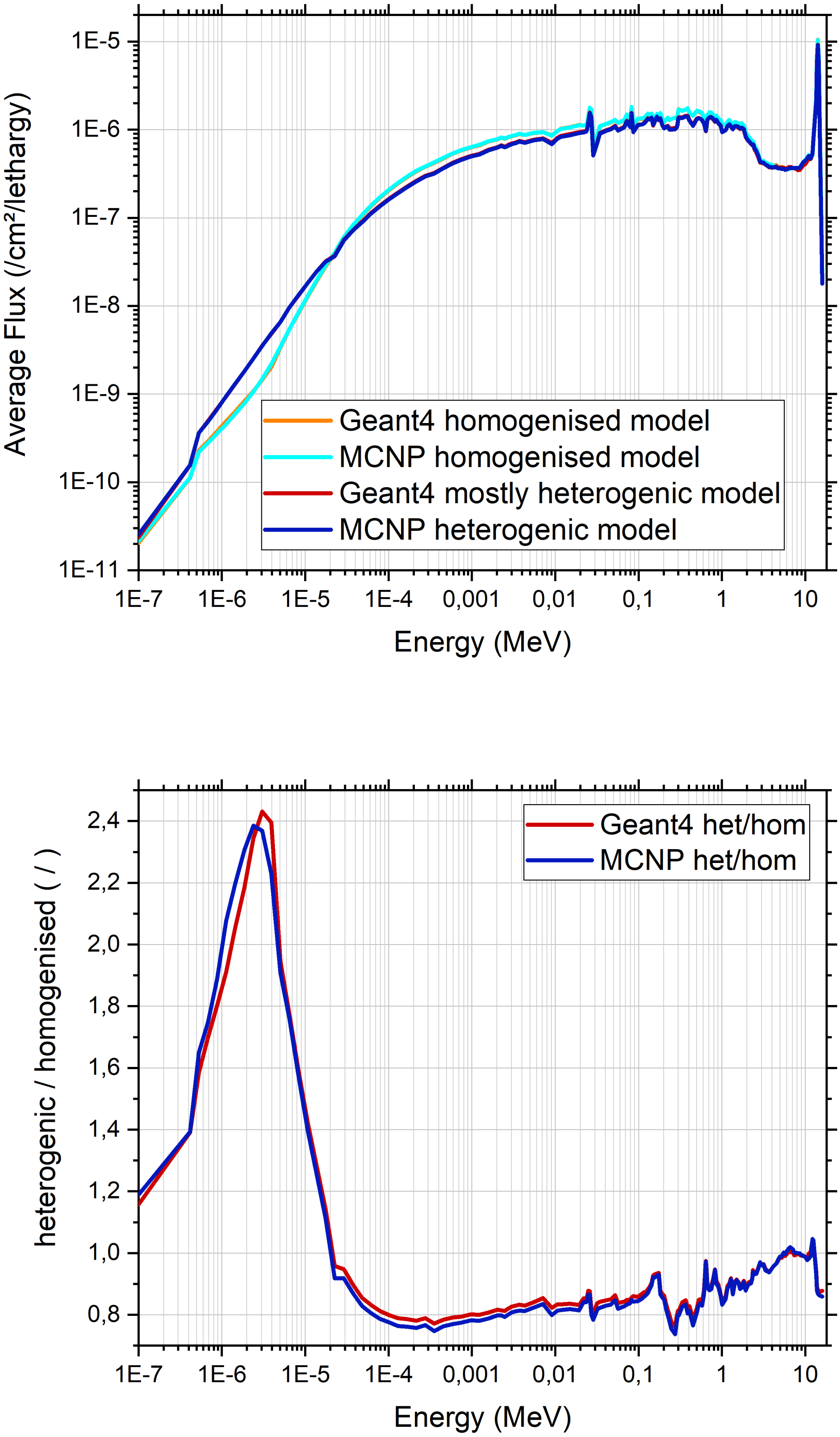

Figure 7.1: The neutron flux spectrum in the breeder blankets of the DEMO reactor produced by Geant4 and MCNP for the geometry set-up with breeders filled with homogenised material and for the geometry set-up with heterogeneous breeder models.

that in the heterogeneous set-up, the peak is slightly lower, which means that slightly more neutrons have undergone material interactions before reaching the breeding zone.

The rest of the flux spectrum is populated by neutrons, which have undergone one or more material interactions. The average flux result Φ_i in the energy bin i depends on the amount N_i of neutrons with energies in the range ΔE_i between the lower and upper energy thresholds of the bin i passing through the designated volume. This amount N_i depends on the one hand on reactions, which change the energy of neutrons from higher or lower energies to the range ΔE_i. This happens through elastic and inelastic scattering and reactions which produce more than one secondary particle and at least one neutron, such as (n,2n), (n,3n), (n,nα), and many others. In most of the energy range, elastic scattering reactions remove energy from the neutrons. Only in the thermal neutron energy range, energy can be transferred from the material onto the neutrons. This is only relevant at very low energies < 1 eV. On the other hand, the amount N_i is affected by reactions, which remove neutrons of the energy range ΔE_i, either through the previously discussed reactions which change their energy, or through absorption reactions such as (n,p) or (n,α) which remove the neutrons entirely.

Neutrons are moving through lots of different materials before reaching the breeder zone. Due to this, the shape of the flux spectrum is caused by a combination of the effects of many different cross-sections. In the following the impact of the most important reactions is discussed. Since the neutron flux spectrum is populated from high energies down to low energies, the discussion is following that direction.

Beryllium is used to increase the total available neutron flux via its (n,2n) reaction. The cross-section of the (n,2n) reaction of Be-9 is highest between 3 and 10 MeV and only works above the energy threshold of 1.8 MeV. The reaction decreases the neutron flux in this energy range and increases it at lower energies. In the average flux spectrum of the homogenised set-up, the dip next to the peak of the uncollided neutrons is likely caused by this reaction removing neutrons to lower energies. This dip can also be seen in the average flux result of the heterogeneous set-up due to the adjacent beryllium layers impacting on the flux spectrum inside those breeder layers.

In addition to the (n,2n) reaction, many reactions can only happen above high thresholds and are therefore only active in the energy range of the dip next to the uncollided neutron peak or higher. These threshold reactions either remove neutrons entirely by producing other secondary particles such as (n,p), or they create one or more secondary neutrons with significantly reduced energies. They also participate in creating the dip next to the uncollided neutron peak, and increasing the neutron flux at lower energies. One of these reactions is the tritium producing reaction of Li-7 with a threshold of 3.15 MeV, which produces a secondary neutron.

The elastic scattering reaction is active throughout the entire energy range and dominates the cross-section of most nuclides. Neutrons are being moved from higher to lower energies by it. As displayed in table 5.1, the energy transfer in the individual interaction depends on the mass of the nuclide. For heavier nuclides, the energy transfer per interaction is low. Therefore, the elastic scattering reaction is moving neutrons to lower energies through many small steps, which enacts a somewhat smoothing effect on the resulting flux spectrum.

In the energy range 20 eV–5 MeV, the homogenised set-up has a slightly higher average flux. This is likely caused by the beryllium acting as more effective neutron-multiplier when it is distributed throughout the whole breeder volume as for the homogenised model, instead of in separate layers as for the heterogeneous model. The homogeneous model is avoiding self-shielding effects this way.

In the energy range 0.01 MeV–2 MeV, very similar fluctuations can be seen in the average flux for both the heterogeneous and the homogenised set-up. These are likely caused by the resonance region in the cross-section of Fe-56 and other isotopes. In this region, both the elastic scattering cross-section and the (n,γ) absorption cross-section fluctuates strongly. At the peaks, more neutrons are removed from the current energy, while at the valleys less neutrons are removed. This leaves the imprint of a negative of the cross-section on the average flux. The resulting peaks and valleys in the average flux are less strong and sharp than in the individual cross-sections. This is due to the overlapping effects of multiple isotopes. Furthermore, there is the usual removal by absorption and addition of neutrons from higher energies by scattering or (n,2n) reactions.

Towards low energies, the neutron flux declines more steeply. In this energy range, the (n,t)-reaction of Li-6 becomes very strong and removes neutrons. Li-6 is an unusual nuclide, since its (n,t)-reaction is active throughout the whole energy range and also is stronger than elastic scattering below $\approx 5 \cdot 10^{-2}$ MeV. Furthermore, another neutron removing reaction, the (n,γ) reaction, rises in strength towards lower energies for most nuclides. Due to this, the average flux decreases exponentially towards lower energies.

Below 20 eV, the average flux is higher in the heterogeneous set-up than in the homogenised set-up even though in the intermediate energy range it is the other way around. Potential causes for this include slightly stronger scattering reactions in the intermediate energy range for the heterogeneous model, which cause a slightly lower neutron flux in this range, but a higher flux in the lower energy area. At low energies, thermal neutron scattering also becomes relevant. Both could be affected by the different material distributions. The ratio plot shows that the discrepancy between homogenised and heterogeneous set-up in the low energy range is the strongest throughout the average flux spectrum. It reaches a factor of ≈ 2.4 at 2 eV–4 eV.

Since the agreement between the Geant4 results is so good that discrepancies can barely be seen in the average flux plot in figure 7.1, the ratio between the Geant4 and MCNP result for the average flux for the homogenised and the heterogeneous set-up is displayed in figure 7.2.

During the code-to-code benchmark discussed in section 5.2, the $Geant4/MCNP$ ratio for the average flux in a 30 cm sphere filled with pure Be-9 has been calculated (see figure 5.13). When comparing this sphere $Geant4/MCNP$ ratio plot with the DEMO ratio plots, it becomes apparent that Be-9 is dominating the agreement between Geant4 and MCNP for the average flux in a large energy range down to $\approx 10^{-3}$ MeV. In this range, strong features in the sphere $Geant4/MCNP$ ratio plot can all also be found in the DEMO versions: a strong underestimation around 10 MeV, an overestimation around 6–8 MeV, an underestimation with three dips between 1.5 MeV and 4 MeV, a narrow peak at 1 MeV, followed by a dip, another peak at 0.3 MeV, fluctuations around 0.1 MeV, and finally a broad peak centred near 0.01 MeV. Since the (n,2n) reaction has a higher threshold than part of this pattern, this means that other Be-9 reactions are also involved in creating these discrepancies. The code-to-code benchmarks yielded better agreement for other investigated isotopes in the high energy range, so it is plausible that Be-9 is dominating the discrepancy.

In the intermediate energy range below 0.01 MeV and down to 5 eV, the $Geant4/MCNP$ ratio result shows that Geant4 underestimates the average neutron flux in the homogenised set-up by up to 2.5 %. This observation cannot be readily explained by the results of the sphere benchmark. On the one hand, the results for spheres filled with strong neutron absorbers such as Li-6 have large relative errors for this energy range or part of it despite the high number of particle histories that have been used so that no information on the deviation between Geant4 and MCNP is available. On the other hand, for many isotopes such as Cnat, O-16, Cr-52, Fe-56, and W-184, an overestimation can be observed instead. The experimental benchmarks with more realistic material mixtures than the sphere benchmark also fail to provide an explanantion. The iron sphere benchmark only covers a higher energy range, and in the HCPB benchmark, the activation foil reaction, which happens at lower energies, shows higher neutron flux for Geant4 than for MCNP.

In an overlapping energy range below 0.01 MeV and down to 20 eV, the $Geant4/MCNP$ ratio for the average flux in the heterogeneous set-up shows an overestimation instead. This can be explained by the fact that the Geant4 set-up contains a contribution by the homogenised parts, which is larger in this energy range.

In the $Geant4/MCNP$ ratio for the average flux result in the homogenised set-up, there is an underestimation at 4 eV and an overestimation at 1 eV, which both deviate approximately 8 %. For the heterogeneous set-up, the peaks and dips in the lowest energy range of the $Geant4/MCNP$ ratio are less pronounced. The combination of those features indicate that in the Geant4 version more scattering happens at 4 eV, which leads to a higher neutron population in the adjacent lower energies. The effect extends until there is another underestimation by Geant4 at the lowest energy bin, which might be caused by slightly stronger absorption effects in the slightly higher energy range. In this low energy range, thermal scattering effects also play a part, which makes it less clear, because neutrons can also be scattered towards higher energies. Discrepancies between Geant4 and MCNP could be caused by differences in the thermal neutron treatment.

7.2 Analysis of DEMO Tritium Breeding Ratio Results

The TBR results for DEMO with a HCPB breeder blanket are displayed in table 7.1. The deviation d between the Geant4 and MCNP TBR result is calculated like this:

$$d = \frac{TBR_{Geant4} - TBR_{MCNP}}{TBR_{MCNP}} \quad . \tag{7.1}$$

The simulated homogenised TBR is larger and the inaccurate modelling leads to an overestimation of the TBR for both Geant4 and MCNP. The Geant4 result is $\approx 1\,\%$ smaller than the MCNP result.

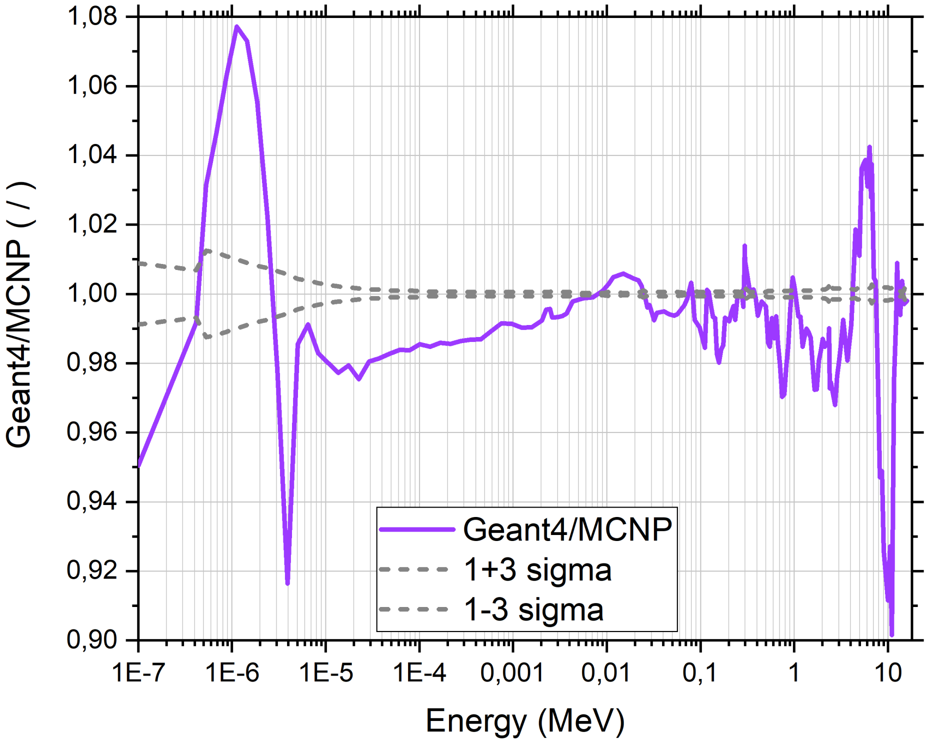

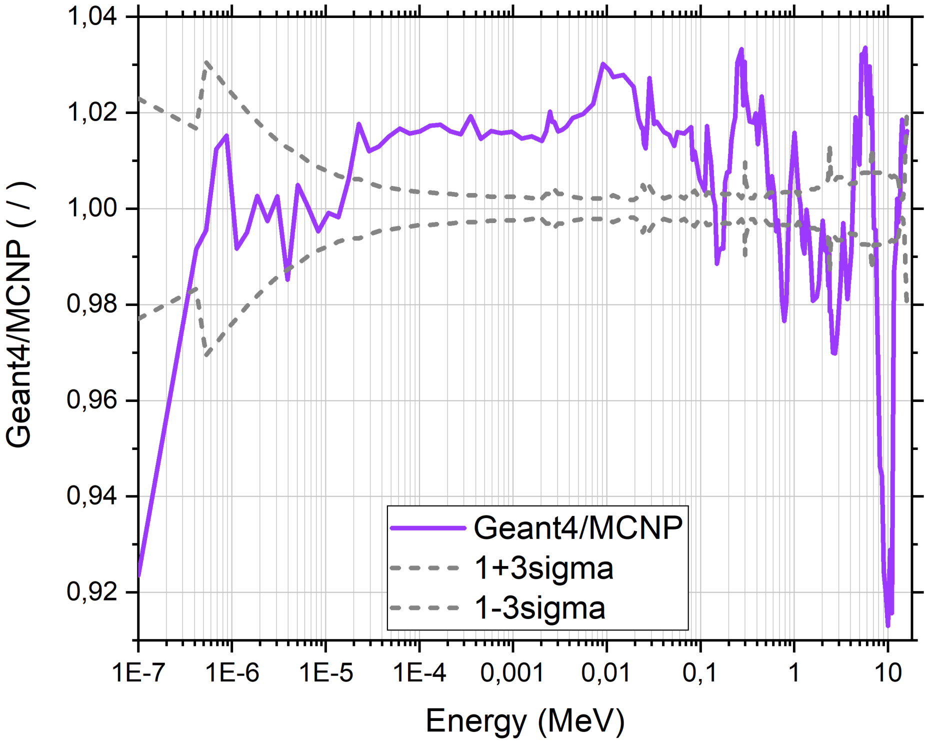

Figure 7.2: The ratio between the Geant4 and the MCNP result for the average flux in the breeder units in the homogenised (top) and heterogeneous (bottom, (Nunnenmann et al., 2020)) set-up.

This follows the tendency to slightly underestimate the tritium production observed already in the HCPB Mock-Up experiment discussed in section 6.2. This evaluation is independent of the issues with the modelling of the internal structure of the breeder modules.

In the mostly heterogeneous model, the Geant4 result is $\approx 1.5\,\%$ larger than the MCNP result. In the homogenised part of the model, a higher TBR value is produced: the homogenised part fills 8.4 % of the volume and contributes 10.2 % to the mostly heterogeneous TBR result. This counteracts the previously observed tendency of Geant4 to slightly underestimate the tritium production.

Table 7.1: The DEMO TBR results for the homogenised and the mostly heterogeneous breeder blanket set-up with TSL (previously published in Nunnenmann et al. (2020)). The relative statistical errors for all results are 10^{-4} or less.

homogenised	Geant4	MCNP	Deviation
Li-6	1.366	1.380	-0.97 %
Li-7	0.014	0.014	-0.87 %
total	1.380	1.394	-0.97 %

heterogeneous	Geant4	MCNP	Deviation
Li-6	1.169	1.152	1.48 %
Li-7	0.013	0.013	-0.25 %
total	1.181	1.164	1.46 %

To discuss the physics of the tritium production, the contribution of individual energy bins to the total TBR result calculated by MCNP in the heterogeneous set-up is displayed in figure 7.3. This TBR spectrum shows that Li-7 dominates the tritium production in the higher energy range above the threshold of its tritium producing reaction. In this energy range, the Li-6 (n,t) reaction cross-section has its lowest range. At the peak of the uncollided neutrons, the production by Li-7 is about 7.5 times higher than from Li-6.

The effect of the Li-7 tritium production is counteracting most of the dip in the energy range 3–10 MeV of the flux spectrum. At 5.5 MeV, the tritium production by the Li-6 (n,t) cross-section takes over. This cross-section (see figure 6.9) follows an exponential increase towards lower energies. Combined with the flux which is rising to a plateau, the tritium production is rising with decreasing energy until there is a local peak at 0.25 MeV, which is caused by the local peak in the Li-6 (n,t) cross-section.

The fluctuations, which are observed for the average flux spectrum in the energy range 0.01 MeV–2 MeV and are likely caused by the resonance region of Fe-56 and other isotopes, have also left their imprint on the spectral TBR.

Moving further towards lower energies, the rising Li-6 (n,t) cross-section counteracts the increasingly falling neutron flux, resulting in rising tritium production until at $\approx 2 \cdot 10^{-4}$ MeV a turning point is reached. From then on, the decrease in the flux outweighs the rise in the cross-section leading to the tritium production falling with decreasing energy from then on.

In general, it can be seen that the most tritium is being produced by neutrons with intermediate energies between 10 eV and 0,5 MeV in addition to directly from the uncollided neutrons at 14.1 MeV.

In figure 7.4, the TBR spectrum for the (mostly) heterogeneous and homogenised set-up of Geant4 and MCNP is displayed. It can be seen that the behaviour is the same as for the average flux: in the homogenised set-up, there is a higher TBR contribution in the energy range 20 eV–2 MeV and at the uncollided neutron peak. In the energy range below 20 eV there is a lower TBR contribution. In total, the higher tritium production at higher energies outweighs the lower production at lower energies and causes a higher total TBR result for the homogenised set-up

In figure 7.5 the ratio between the Geant4 and the MCNP result for the TBR throughout the energy bins is displayed for the homogenised and the mostly heterogeneous blanket set-up. It can be seen that the shape of the curves is nearly identical to the result for the $Geant4/MCNP$ ratio of the average flux displayed in figure 7.2: In the highest energy range above 1 MeV, the behaviour of the $Geant4/MCNP$ ratio is similar between the homogenised and the heterogeneous set-up. As discussed for the flux, the deviations between Geant4 and MCNP in the energy range above $\approx 10^{-3}$ MeV are dominated by the Be-9 cross-section.

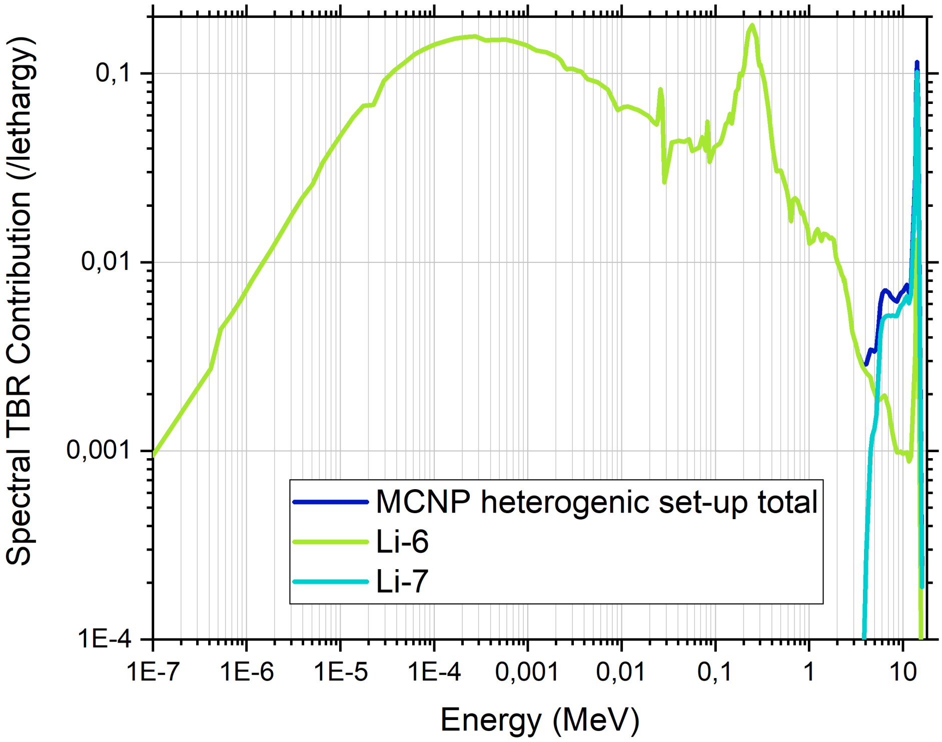

Figure 7.3: The spectral contribution to the TBR result of the DEMO reactor by the tritium producing reactions of Li-6, Li-7, and both together for the heterogeneous set-up calculated by MCNP (top).

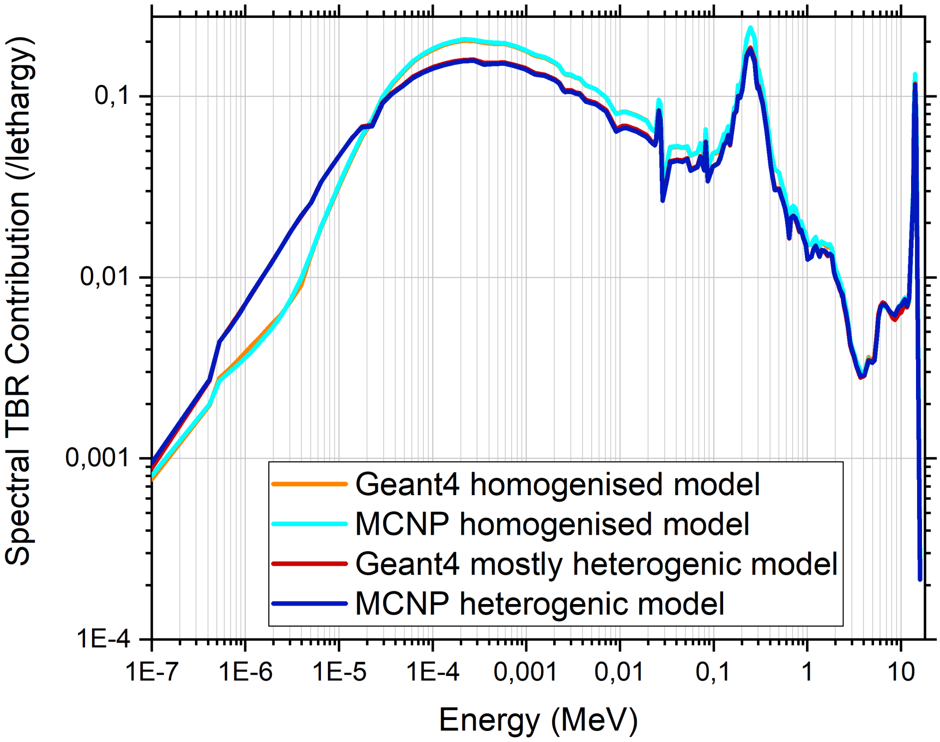

Figure 7.4: The contribution of the energy bins to the total TBR result of the DEMO reactor for the homogenised and (mostly) heterogeneous geometry set-up calculated with Geant4 and MCNP.

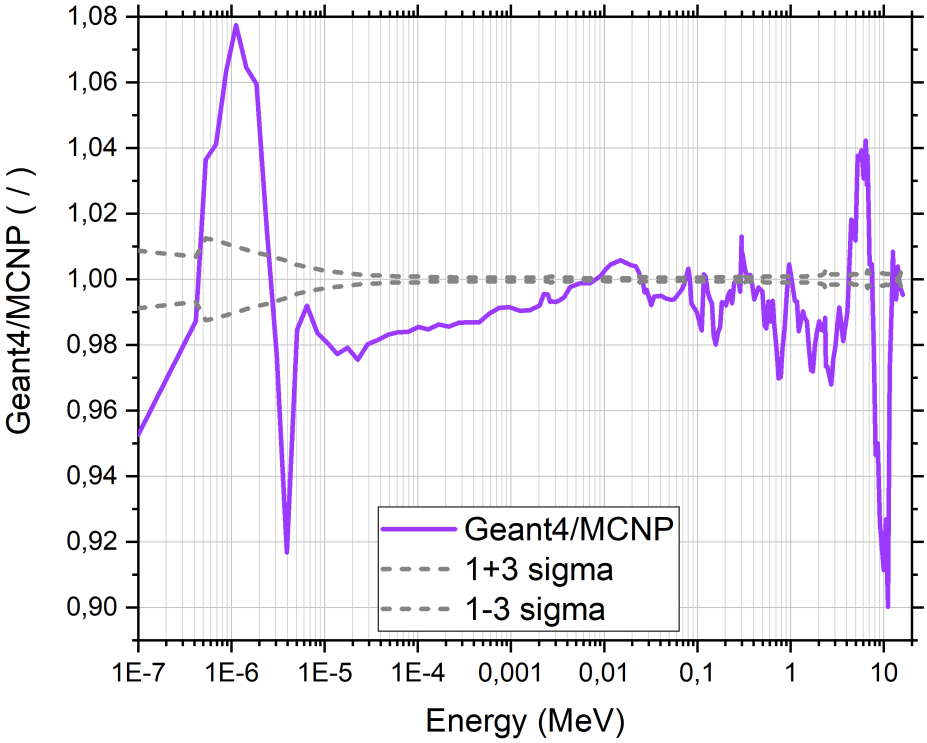

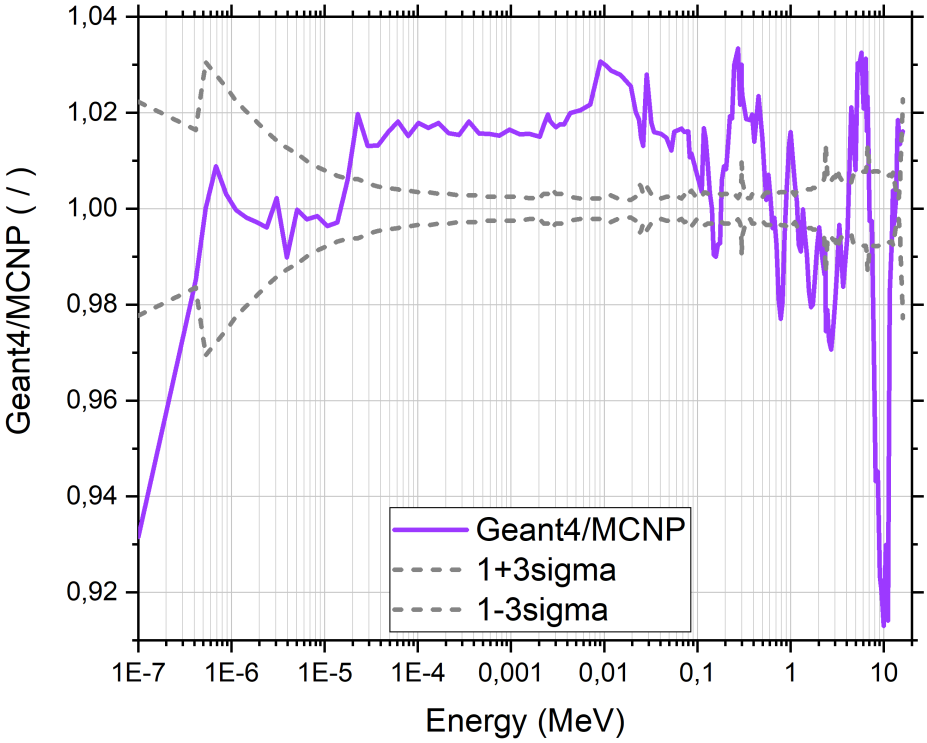

Figure 7.5: The $Geant4/MCNP$ ratio for the spectral contributions to the TBR in a homogenised blanket (top) and a mostly heterogeneous blanket (bottom, result previously published in Nunnenmann et al. (2020)).

Between 10^{-5} MeV and 0.1 MeV the homogenised result nearly always underestimates the MCNP result, while the Geant4 result consistently overestimates it. This likely causes the observed deviations between Geant4 and MCNP in the integral results (see table 7.1).

Overall, the deviations are mostly larger than the combined statistical errors from the two codes. However, the deviations are within $3\,\%$ for most energy bins.

In conclusion, Geant4 successfully produces TBR results consistent with MCNP for both the homogenised and the mostly heterogeneous model of the DEMO reactor equipped with a HCPB blanket. The good compliance of the Geant4 results with the MCNP results also proves that the reflective boundary function works as intended. The treatment of the Be-9 cross-section dominates the deviations between Geant4 and MCNP in the higher energy range. Accordingly, the consistency of the Geant4 TBR result for a beryllium-based breeding blanket would benefit from improvements in the baseline code and library treatment affecting this cross-section.

7.3 Evaluation of the Suitability of Geant4 for DEMO Nuclear Analyses

The DEMO neutron source representation has successfully been converted and applied. The complex geometry has been converted from CAD format and the reflective boundary functionality has been used successfully. With this set-up, TBR results consistent with MCNP can be calculated.

The lack of a repeating structure functionality causes problems with the representation of the internal blanket structure for which no CAD representation exists. This is solved for this thesis with a time-intensive work-around, but for future applications, better solutions still need to be developed.

Due to major issues in the variance reduction functionality and strong discrepancies in the gamma flux results revealed by the experimental benchmarks, no deep penetration shielding calculations have been attempted. Further development is necessary to open up these kinds of calculations. Therefore, the Geant4 code cannot replace MCNP for all applications at this stage.

Chapter 8

Summary and Outlook

The objective of this thesis was to investigate Geant4's suitability for the application in fusion neutronics analyses of the DEMO reactor and to extent the code with additional functionalities where necessary.

8.1 Summary of New Developments

In the course of this thesis, Geant4 applications have been created for several typical fusion neutronics problems. This involves the new development or conversion of geometry, source, and tally descriptions.

A track length tally functionality with multiple energy bins, which can be read in from a file, was developed. Based on this, another version for additional tally multiplication with cross-section data read in from a file was created. These were edited for detection based on a particle type given upon initialisation and to support multiplication with the weight during variance reduction runs.

The reflective boundary functionality for simplifying symmetric geometries was developed based on an existing Geant4 optical photon reflection function.

An existing Geant4 convergence testing subroutine was extracted to be used in post-processing. It was edited to be more consistent with the 10 statistical checks used by MCNP.

Variance reduction with the importance biasing method was only available for one particle type at a time. This was expanded for multiple particle types to enable the use in coupled neutron-photon transport. However, problems persisted with this development, which could not be solved in the timeframe of this thesis.

8.2 Summary of Verification and Validation Results

Good agreement with the standard code MCNP is found for the single interaction code-to-code benchmark. This serves to verify that the Geant4 application created out of toolkit parts for this thesis produces results consistent with previously published Geant4 results.

For the multiple interaction code-to-code benchmark, good agreement is found for the total neutron flux. Throughout the neutron flux energy spectrum, stronger deviations between Geant4 and MCNP are found for some isotopes. In comparison with other alternative codes, the multiple interaction benchmark yields the same level of agreement with MCNP as COG11 and Tripoli4, and less good agreement with MCNP than Serpent-2.

When repeating the multiple interaction benchmark for the calculation of total gamma flux and energy deposition, strong deviations are found for some combinations of nuclides and libraries. Therefore, the gamma production and transport capabilities and nuclear heating results are considered less reliable.

Next, Geant4 has been validated with experimental data from SINBAD. The IPPE neutron transmission through iron spheres benchmark shows that Geant4 performs on the same level as MCNP and can reliably treat thick bulk objects of the most important structural material iron.

In the HCPB TBM mock-up benchmark experiment, the activation foil evaluation shows an underestimation by Geant4 of the fast neutron flux with increasing penetration depth. Despite this, the tritium production results are very consistent with the MCNP results. There is again an underestimation increasing with penetration depth, but it is very slight and does not exceed 2.7 %. This is much smaller than the deviation of either code from the experimental results, which reaches beyond 15 % for some pellets. This deviation is likely caused by the nuclear data. When the same benchmark has been performed with the other alternative code Serpent-2, some slightly stronger deviations up to 4.7 % have been observed, but no trend with increasing penetration depth. Thus, the compliance with MCNP is on the same order of magnitude for the investigated set-up, but Geant4 might get larger deviations for a set-up with deeper penetrations.

The ITER bulk shield benchmark reveals issues when combining variance reduction and HalfSpaceSolid geometry description. It is unclear whether the strange fluctuations in the neutron result and the lack of reduced variance at deeper penetration is caused only by this or whether there are additional problems. For the neutron results at less deep penetration, good integral agreement is observed. The gamma results follow the trend of the experimental and MCNP results with an additional overestimation of 32–70 % at the depth where the neutron results show good agreement. Therefore, the gamma treatment in Geant4 cannot be considered reliable. Due to the time constraints for this thesis work, it has not been possible to further improve the variance reduction implementation. In the current state it cannot be considered reliable. This makes the application of the code to deep penetration problems doubtful.

For a 10° sector DEMO reactor model with integrated HCPB blanket and the newly developed reflecting boundary functionality, Geant4 calculates TBR results consistent with MCNP.

In the course of these benchmarks, it is also demonstrated that Geant4 possesses the ability to accurately represent complex neutron sources like the DEMO plasma source subroutine, or the FNG SDEF source description. Furthermore, it is shown that complex CAD-based geometry descriptions can be converted for Geant4 and used to obtain results consistent with experiments and MCNP.

In conclusion, in the course of this thesis many code capabilities have been created, which are required for fusion neutronics applications, and it is shown that Geant4 is not yet suitable for a general application to design analyses for fusion reactors like DEMO. Only for neutron transport and related nuclear responses, which are not too affected by deep penetration transport such as the tritium production in the blankets, Geant4 can be used with confidence. The issues revealed in the benchmarks for reliable photon production and variance reduction prevent the application to nuclear heating and shielding calculations, which are both crucial to the reactor operation. However, this thesis has paved the way to enable the confident application to DEMO design analyses provided the open issues discussed in the next section will be resolved.

The applications developed for verification and validation in this thesis can be used to monitor further Geant4 and cross-section library conversion development. It is the aim of the developers of SINBAD to expand their database to include other nuclear transport codes. The source code and input files of the SINBAD-based Geant4 applications developed in this thesis will be contributed to this effort.

8.3 Open Issues and Suggestions for Improvement

The main issue which could not be solved in the course of this thesis, is the successful importance biasing variance reduction application in a GDML-based HalfSpaceSolid geometry. To figure out whether the issue is even caused by a clash with the geometry description, further investigations should test Geant4's variance reduction methods with a baseline Geant4 geometry set-up.

Since both automatic CAD conversion and variance reduction are necessary for future DEMO application, this problem has to be resolved. In section B.5, several approaches are described for making the combination of variance reduction and HalfSpaceSolid geometry work. Once the issues of the importance biasing method are resolved, other variance reduction methods such as weight windows need to be tested.

The validation efforts in this thesis reveal some discrepancies towards MCNP in the neutron flux spectrum for some isotopes in the multiple interaction benchmark. A potential improvement of the baseline code would be to include a dedicated treatment of the unresolved resonance region.

Furthermore, in the multiple interaction benchmark, strong discrepancies are found for the gamma flux and energy deposition for some nuclide and library combinations. The ITER bulk shield experimental benchmark, while already suffering from the variance reduction issues, also revealed a significant overestimation of the photon flux.

Since the widely used Geant4 physics-list for electromagnetic physics G4EmStandardPhysics is doing the gamma transport the issues likely stem from the gamma production calculated by the relatively newly-developed NeutronHP package and its converted libraries. This is also confirmed by the fact that the evaluation by the library developers, on which the single-interaction benchmark is based, yielded discrepancies in the gamma production for several nuclides. Therefore an investigation of the NeutronHP package with respect to bugs or clashes with the format of different libraries could lead to improvements.

This thesis focuses more on prototype development and proof of concept. In the future, some of the developed functionalities could be improved with added automation to increase user-friendliness and decrease time-consuming pre-processing. For example, the sensitive detector with tally multiplier function could be enhanced with a function to automatically read-in the required cross-section data from ENDF formatted files according to the user's specifications. Furthermore, more MCNP-equivalent sensitive detector types could be developed to simplify the conversion of established MCNP-based experimental benchmarks and design concepts.

A very important future development is a better way to replicate MCNP's repeated structure geometry function, since the approach utilised in this thesis did not manage to fill 100 % of the volume and is too time-consuming to be feasible for general usage.

At the current development stage, the DEMO model contains fewer details than the ITER model. As development progresses, this can be expected to change. Therefore, it would make sense to test Geant4's ability to support a progressed DEMO with versions of the current ITER model.

Furthermore, mesh-based evaluation is not covered in this thesis. Geant4 does provide functionalities for this, but it needs to be investigated and combined with the developed applications.

References

Atzeni, S. and Meyer-ter-Vehn, J. (2004). *The Physics of Inertial Fusion: Beam Plasma Interaction, Hydrodynamics, Hot Dense Matter*. International Series of Monographs on Physics; 125 Oxford Science Publications. Clarendon Press, Oxford, UK. ISBN: 0-19-856264-0.

Barros, R. C. (1997). On the Equivalence of Discontinuous Finite Element Methods and Discrete Ordinates Methods for the Angular Discretization of the Linearized Boltzmann Equation in Slab Geometry. *Annals of Nuclear Energy*, 24(13):1013–1026.

Batistoni, P., Angelone, M., Bettinali, L., Carconi, P., Fischer, U., Kodeli, I., Leichtle, D., Ochiai, K., Perel, R., Pillon, M., et al. (2007). Neutronics Experiment on a Helium Cooled Pebble Bed (HCPB) Breeder Blanket Mock-up. *Fusion Engineering and Design*, 82(15-24):2095–2104.

Batistoni, P., Angelone, M., Fischer, U., Freiesleben, H., Hansen, W., Pillon, M., Petrizzi, L., Richter, D., Seidel, K., and Unholzer, S. (1999). Neutronics Experiment on a Mock-up of the ITER Shielding Blanket at the Frascati Neutron Generator. *Fusion Engineering and Design*, 47(1):25–60.

Brown, F. et al. (2003). MCNP–A General Purpose Monte Carlo N-Particle Transport Code, Version 5. Technical Report LA-UR-03 1987, Los Alamos National Laboratory, Los Alamos, New Mexico, United States.

Capote, R., Zolotarev, K., Pronyaev, V., and Trkov, A. (2012). Updating and Extending the IRDF-2002 Dosimetry Library. *J. ASTM International*, 9(4):197–209.

Chadwick, M., Obložinskỳ, P., Herman, M., Greene, N., McKnight, R., Smith, D., Young, P., MacFarlane, R., Hale, G., Frankle, S., et al. (2006). ENDF/B-VII.0: Next Generation Evaluated Nuclear Data Library for Nuclear Science and Technology. *Nuclear Data Sheets*, 107(12):2931–3060.

Conlin, J. L. and Romano, P. (2019). A Compact ENDF (ACE) Format Specification. Technical Report LA-UR-19-29016, Los Alamos National Lab (LANL), Los Alamos, New Mexico, United States.

Coursey, J., Schwab, D., Tsai, J., and Dragoset, R. (2015). Atomic Weights and Isotopic Compositions (version 4.1). *URL http://physics.nist.gov/Comp*, 2023-04-15.

Čufar, A., Lengar, I., Kodeli, I., Milocco, A., Sauvan, P., Conroy, S., and Snoj, L. (2016). Comparison of DT Neutron Production Codes MCUNED, ENEA-JSI Source Subroutine and DDT. *Fusion Engineering and Design*, 109:164–168.

Cullen, D. (2017). PREPRO 2017 ENDF/B Pre-processing Codes (ENDF/B-VII or Proposed VIII Tested). Technical Report IAEA-NDS-39, Rev 17, International Atomic Energy Agency.

D'Auria, S. (2019). *Introduction to nuclear and particle physics*. Springer, 6330 Cham, Switzerland. ISBN: 978-3-319-93855-4.

Davis, A. (2012). Validation Report of a Subset of Available Monte Carlo Codes Using ENDF/B-VIIR.0 Data. Technical Report EFDA task WP12-DTM04-T11-D12., CCFE, Abingdon, UK.

Demidov, A., Govor, L., Cherepantsev, Y. K., Ahmed, M., Al-Najjar, S., Al-Amili, M., Al-Assafi, N., and Rammo, N. (1978). *Atlas of gamma-ray spectra from the inelastic scattering of reactor fast neutrons*. Atomizdat, Moscow, Russia.

Donné, A. (2019). The European Roadmap towards Fusion Electricity. *Philosophical Transactions of the Royal Society A*, 377(2141):20170432.

Ellis, D. V. and Singer, J. M. (2008). *Well Logging for Earth Scientists*. Springer, Dordrecht, The Netherlands, 2. [revised and enlarged], reprinted with corrections edition. ISBN: 978-1-4020-3738-2.

Fahrmeir, L., Künstler, R., Pigeot, I., and Tutz, G. (2007). *Statistik - Der Weg zur Datenanalyse, 6. Auflage*. Springer, Berlin, Germany. ISBN: 978-4-540-69713-8.

Fausser, C., Puma, A. L., Gabriel, F., and Villari, R. (2012). Tokamak DT Neutron Source Models for Different Plasma Physics Confinement Modes. *Fusion Engineering and Design*, 87(5-6):787–792.

Firestone, R., Choi, H., Lindstrom, R., Molnar, G., Mughabghab, S., Paviotti-Corcuera, R., Revay, Z., Trkov, A., Zhou, C., and Zerkin, V. (2006). Database of prompt gamma rays from slow neutron capture for elemental analysis. Technical report, International Atomic Energy Agency, Vienna, Austria.

Fischer, U., Boccaccini, L., Cismondi, F., Coleman, M., Day, C., Hörstensmeyer, Y., Moro, F., and Pereslavtsev, P. (2020). Required, Achievable and Target TBR for the European DEMO. *Fusion Engineering and Design*, 155:111553.

Forrest, R., Capote, R., Otsuka, N., Kawano, T., Koning, A., Kunieda, S., Sublet, J.-C., and Watanabe, Y. (2012). FENDL-3 Library-Summary Documentation. Technical Report INDC(NDS)-0628, International Atomic Energy Agency, Vienna, Austria.

Freiesleben, H., Hansen, W., Richter, D., Seidel, K., Unholzer, S., Fischer, U., Wu, Y., Angelone, M., Batistoni, P., and Pillon, M. (1998). Neutron and Photon Flux Spectra in a Mock-up of the ITER Shielding System. *Fusion Engineering and Design*, 42(1-4):247–253.

Geant4 Collaboration (2019a). Book for Application Developers. *URL https://geant4.web.cern.ch/support/user_documentation, accessed: 02/09/2020*, Release 10.5.

Geant4 Collaboration (2019b). Book for Toolkit Developers. *URL https://geant4.web.cern.ch/support/user_documentation, accessed: 02/09/2020*, Release 10.5.

Geant4 Collaboration (2019c). Physics Reference Manual. *URL https://geant4.web.cern.ch/support/user_documentation, accessed: 02/09/2020*, Release 10.5.

Geant4 Collaboration (2020a). Geant4 Installation Guide Documentation. *URL https://geant4.web.cern.ch/support/user_documentation, accessed: 10/02/2021*, Release 10.7.

Geant4 Collaboration (2020b). Introduction to Geant4. *URL https://geant4.web.cern.ch/support/user_documentation, accessed: 10/02/2021*, Release 10.7.

Greenwood, L. and Paviotti-Corcuera, R. (2002). Summary Report of the Technical Meeting on 'International Reactor Dosimetry File: IRDF-2002'. Technical Report INDC(NDS)-435, International Atomic Energy Agency, Vienna, Austria.

Häußler, A., Fischer, U., and Warmer, F. (2016). Neutronics source modeling for stellarator power reactors of the helias-type. In *Compact at the 47th Annual Meeting on Nuclear Technology (AMNT)*.

Herman, M., Trkov, A., et al. (2021). ENDF-6 Formats Manual. Technical Report NL-203218-2018-INRE, Brookhaven National Laboratory, Upton, New York, United States.

Hernández, F., Pereslavtsev, P., Kang, Q., Norajitra, P., Kiss, B., Nádasi, G., and Bitz, O. (2017). A new HCPB breeding blanket for the EU DEMO: Evolution, rationale and preliminary performances. *Fusion Engineering and Design*, 124:882–886. Proceedings of the 29th Symposium on Fusion Technology (SOFT-29) Prague, Czech Republic, September 5-9, 2016.

Hernández, F., Pereslavtsev, P., Zhou, G., Kang, Q., D'amico, S., Neuberger, H., Boccaccini, L., Kiss, B., Nádasi, G., Maqueda, L., Cristescu, I., Moscato, I., Ricapito, I., and Cismondi, F. (2020). Consolidated Design of the HCPB Breeding Blanket for the Pre-Conceptual Design Phase of the EU DEMO and Harmonization with the ITER HCPB TBM Program. *Fusion Engineering and Design*, 157.

Kodeli, I. (2015). Validation of IRDFF-v1. 04 (&v1. 05) Dosimetry Library Using SINBAD Shielding Benchmark Experiments. Technical Report INDC(SLO)-0002, International Atomic Energy Agency International Nuclear Data Committee, Vienna, Austria.

Kodeli, I., Milocco, A., Ortego, P., and Sartori, E. (2014). 20 Years of SINBAD (Shielding Integral Benchmark Archive and Database). *Progress in Nuclear Science and Technology*, 4:308–311.

Koning, A., Forrest, R., Kellett, M., Mills, R., Henriksson, H., Rugama, Y., Bersillon, O., Bouland, O., Courcelle, A., Duijvestijn, M., et al. (2006). The JEFF-3.1 Nuclear Data Library - JEFF Report 21. Technical Report NEA No. 6190, Organisation for Economic Co-operation and Development, Paris, France. ISBN: 92-64-02314-3.

Kovari, M., Coleman, M., Cristescu, I., and Smith, R. (2017). Tritium Resources Available for Fusion Reactors. *Nuclear Fusion*, 58(2):026010.

Krieger, H. (2019). *Grundlagen der Strahlungsphysik und des Strahlenschutzes*, volume 6. Springer Spektrum, Berlin. ISBN: 978-3-662-60583-7.

lcl (Username) (31 May, 2014). *Website: Wayback Machine Recording of Deactivated Geant4 Message Board. Post Title: "Re: how to get the RMS error of cellFlux scoring by mesh_box?"*. Internet Archive. `https://web.archive.org/web/20160605030843/http://hypernews.slac.stanford.edu:80/HyperNews/geant4/get/biasing_scoring/101/2.html`, accessed: 11/05/2021.

Li, S., Jiang, H., Ren, Z., and Xu, C. (2014). Optimal Tracking for a Divergent-type Parabolic PDE System in Current Profile Control. *Abstract and Applied Analysis*, 2014, Article ID 940965:1–8.

Lopez Aldama, D. and Trkov, A. (2004). FENDL-2.1: Update of an Evaluated Nuclear Data Library for Fusion Applications. Technical Report INDC(NDS)-467, International Atomic Energy Agency, Vienna, Austria.

Lu, L., Qiu, Y., and Fischer, U. (2017). Improved Solid Decomposition Algorithms for the CAD-to-MC Conversion Tool McCad. *Fusion Engineering and Design*, 124:1269–1272.

Masterson, R. E. (2017). Nuclear Fuels, Nuclear Structure, the Mass Defect, and Radioactive Decay. In *Introduction to Nuclear Reactor Physics*. CRC Press, Taylor and Francis Group, Boca Raton, Florida, United States. ISBN: 9781315118055.

Mendoza, E. and Cano-Ott, D. (2018a). Update of the Evaluated Neutron Cross Section Libraries for the Geant4 Code. Technical Report INDC(NDS)-0758, International Atomic Energy Agency, Vienna, Austria.

Mendoza, E. and Cano-Ott, D. (2018b). *Website: Evaluated neutron cross section libraries for the Geant4 code (v2.0)*. International Atomic Energy Agency - Nuclear Data Section. https://www-nds.iaea.org/geant4/, accessed: 30/09/2019.

Mendoza, E., Cano-Ott, D., Guerrero, C., and Capote, R. (2012). New Evaluated Neutron Cross Section Libraries for the Geant4 Code. Technical Report INDC(NDS)-0612, International Atomic Energy Agency, Vienna, Austria.

Mendoza, E., Cano-Ott, D., Koi, T., and Guerrero, C. (2014). New Standard Evaluated Neutron Cross Section Libraries for the Geant4 Code and First Verification. *IEEE Transactions on Nuclear Science*, 61(4):2357–2364.

Milocco, A. and Trkov, A. (2008). Modelling of the Production of Source Neutrons from Low-Voltage Accelerated Deuterons on Titanium-Tritium Targets. *Science and Technology of Nuclear Installations*, Volume 2008, Article ID 340282:1–7.

Nunnenmann, E. and Fischer, U. (2019). V&V Analyses of the Geant4 Monte Carlo Code Toolkit with Computational and Experimental Fusion Neutronics Benchmarks. *Fusion Engineering and Design*, 146:1579–1582.

Nunnenmann, E., Fischer, U., and Serikov, A. (2020). Verification and Validation of the Geant4 Monte Carlo Code Toolkit for DEMO TBR Evaluations. *Fusion Engineering and Design*, 161:111927.

Pampin, R., Davis, A., Zheng, S., Porton, M., Jaboulay, J.-C., Trama, J.-C., Drozdowicz, K., Dworak, D., Bienkowska, B., and Prokopowicz, R. (2012). T11: Comparison of Monte Carlo Codes D12: Generic Evaluation of Alternative Monte Carlo Codes. Technical Report Report for TA WP12-DTM-04 Task 11 Deliverable 12, EFDA_D_XXXXXX, v.1.0, EFDA-Power Plant Physics & Technology.

Pereslavtsev, P., Fischer, U., Hernandez, F., and Lu, L. (2017). Neutronic Analyses for the Optimization of the Advanced HCPB Breeder Blanket Design for DEMO. *Fusion Engineering and Design*, 124:910–914.

Plompen, A., Cabellos, O., De Saint Jean, C., Fleming, M., Algora, A., Angelone, M., Archier, P., Bauge, E., Bersillon, O., Blokhin, A., et al. (2020). The Joint Evaluated Fission and Fusion Nuclear Data Library, JEFF-3.3. *The European Physical Journal A*, 56(7):1–108.

Qiu, Y. (2016). *Development of a Coupling Approach for Multi-Physics Analyses of Fusion Reactors*. PhD thesis, Department of Mechanical Engineering, Karlsruhe Institute of Technology.

Qiu, Y., Lu, L., and Fischer, U. (2016). A New Geant4 Modeling Solution Based on CAD Geometries. In *2016 IEEE Nuclear Science Symposium, Medical Imaging Conference and Room-Temperature Semiconductor Detector Workshop (NSS/MIC/RTSD)*, pages 1–5, Strasbourg, France. IEEE. DOI: 10.1109/NSSMIC.2016.8069638.

Rubinstein, R. Y. and Kroese, D. P. (2016). *Simulation and the Monte Carlo Method*, volume 10. John Wiley & Sons, Hoboken, New Jersey, United States. ISBN: 978-1-118-63238-3.

Simakov, S., Devkin, B., Kobozev, M., Talalaev, V., Fischer, U., and von Möllendorff, U. (2000). Validation of Evaluated Data Libraries Against an Iron Shell Transmission Experiment and Against the Fe (n, xn) Reaction Cross Section with 14 MeV Neutron Source. Technical Report EFF-DOC-747, Nuclear Energy Agency Data Bank, Paris, France.

Soppera, N., Bossant, M., and Dupont, E. (2014). JANIS 4: An Improved Version of the NEA Java-based Nuclear Data Information System. *Nuclear Data Sheets*, 120:294–296.

Stuart, A., Kendall, M. G., et al. (1973). *The Advanced Theory of Statistics - Volume 2: Inference and Relationship*. Griffin London, London, UK. ISBN: 0-85264-215-6.

Valentine, A., Colling, B., Worrall, R., and Leppänen, J. (2021). Benchmarking of the Serpent 2 Monte Carlo Code for Fusion Neutronics Applications. In *EPJ Web of Conferences*, volume 247, page 04015. EDP Sciences.

Wu, Y. (2017). *Fusion Neutronics*. Springer Nature Singapore, Singapore. ISBN: 978-981-10-5469-3.

Wu, Y., Song, J., Zheng, H., Sun, G., Hao, L., Long, P., Hu, L., Team, F., et al. (2015). CAD-based Monte Carlo Program for Integrated Simulation of Nuclear System SuperMC. *Annals of Nuclear Energy*, 82:161–168.

Zsolnay, E. M., Capote Noy, R., Nolthenius, H. J., and Trkov, A. (2012). Summary Description of the New International Reactor Dosimetry and Fusion File (IRDFF Release 1.0). Technical Report INDC(NDS)-0616, International Atomic Energy Agency, Vienna, Austria.

Appendix A

The Particle Transport Code Geant4

Geant4 is described by Geant4 Collaboration (2020b) as a free Monte Carlo particle transport simulation toolkit written in C++. It contains multiple physics models which are able to describe the interaction of different kinds of particles with matter across a wide energy range. The object-oriented structure with uniform interfaces and common organisational principles in all physics models allows to combine or replace physics models. At the start, the focus has been on high-energy particle physics, and later also nuclear, accelerator, space, and medical physics have been included.

The first production release was delivered in December 1998. The code is produced in a collaboration of many international institutes and universities. The different components of the code are individually managed by working groups of experts, which handle the continued code development and user support.

Multiple user manuals are provided, which are updated along with code updates, and can be downloaded from the website `https://geant4.web.cern.ch/support/user_documentation`:

- Introduction to Geant4 (Geant4 Collaboration, 2020b)
- Geant4 Installation Guide Documentation (Geant4 Collaboration, 2020a)
- Book for Application Developers (Geant4 Collaboration, 2019a)
- Book for Toolkit Developers (Geant4 Collaboration, 2019b)
- Physics Reference Manual (Geant4 Collaboration, 2019c)

Geant4 defines a set of standard data types, which in some cases replace the C++ data types. For example G4double replaces double. In contrast to MCNP, which uses a standard set of units such as centimetre for length, Geant4 allows the user more freedom. Geant4 uses a set of basic units internally such as millimetre (mm) or nanosecond (ns) (Geant4 Collaboration, 2019a), but there is a large variety of derived units available as well and the user can also define additional units. Any value should be entered along with its unit. For example the value of 15 km of the variable $distance$ could be defined like this:

$$\mathrm{G4double}\ distance = 15 * \mathrm{km} \quad , \tag{A.1}$$

because "km" is one of the defined derived variables.

A.1 Explanation of the Toolkit Structure and Provided Examples

Geant4 serves a wide range of physics fields which require different functionalities from the code. Consequently, Geant4 exists as a toolkit which offers a variety of options. The user can mix and match these options to create an application tailored to their own needs.

First, the main code has to be installed. CMake is used to configure the installation. Not all options are installed by default, but can be added via CMake variables during the installation process. This includes functionalities such as multi-threading support or various graphical output options. A basic set of material interaction data libraries can also be downloaded and installed. An existing installation can be modified later on by changing the CMake variables with CMake (Geant4 Collaboration, 2020a).

Next, the user can create their own application out of parts of the toolkit. For this, two directories are set up: one for the source code and a build-directory where the result of the compilation is stored. The user builds an application out of different subroutines. CMake is used again to link the application back to the main installation. Then, it is compiled into an executable. The executable can be run in an interactive mode, which in this work has only been used for geometry visualisation, or it can be run in batch mode with an input file, which contains a set of commands, and if necessary also a GDML file which contains an external geometry description.

When setting up a new application, a good starting point is the suite of examples provided by the toolkit. The examples complement the explanations given in the user manuals and illustrate ways to implement many different use cases. Each of them consists of a directory with a README file with explanations, source code files, input files, and reference output files. The user has to compile them linked back to the main code installation and can run them usually both in interactive mode or in batch mode using the provided input files.

The examples are divided into three groups. The **basic** examples serve as introduction for new users and illustrate the most basic principles. The **extended** examples illustrate functionalities such as biasing, or the use of specific physics packages such as for electromagnetic or hadronic physics. The **advanced** examples consist of implementations of Geant4 for various realistic applications. These include medical applications such as proton or ion therapy and a human phantom, CERN detector applications, and astronomical applications such as x-ray or gamma-ray telescopes (Geant4 Collaboration, 2019a).

Here is a list of the most important examples for this thesis:

- **/extended/hadronic/Hadr04** introduces the < 20 MeV neutron transport physics package NeutronHP, which is the main physics package used in this work.
- **/extended/runAndEvent/RE02** served as an example on how to set up the data collection with the DetectorConstruction and the Run subroutines, equivalent to the MCNP tally functionality.
- **/basic/B4c** introduces a different data collection method to the one from RE02 based on so-called SensitiveDetectors.
- **/extended/persistency/gdml** includes multiple examples for using the GDML external geometry format.
- **/extended/biasing/B01** implements variance reduction based on the importance biasing method.
- **/extended/biasing/GB01** till /GB06 introduce more generic biasing options.

Unfortunately, the different parts do not always work like puzzle pieces which can simply be slotted together. The large number of options has the effect that the examples represent different combinations of options which often do not directly fit in with the application the user has developed so far. However, with growing user experience, it becomes easier to extract the desired option from an example and modify the user application so that it ties in properly. One of the aims of this work is to create a set of fusion neutronics examples which implement the required functionalities and can be used by future users as is or as a less difficult jumping off point than the existing examples.

A.2 Physics and Nuclear Data Treatment

According to Geant4 Collaboration (2019a), Geant4 has seven major categories of physics processes: electromagnetic, hadronic, transportation, decay, optical, photolepton-hadron and parameterisation. The design principle is that all physics processes are generalised to the point that they can be treated the same by the particle tracking. All processes have two groups of methods: GetPhysicalInteractionLength (GPIL) and DoIt. The GPIL methods calculate the length of the step until the next interaction happens from the interaction probability based on the process's cross-section data. The DoIt methods implement the details of this interaction including the change of the particle's energy, momentum, direction, and position, and the creation of any secondary particles.

In a Geant4 application, a PhysicsList class has to be implemented based on the G4VUserPhysicsList base class, in which all required physics processes and particles are registered. In this thesis, G4NeutronHP, which is part of the hadronic category, is used nearly exclusively. Only when photon transport is used, G4EmStandardPhysics of the electromagnetic category is used additionally.

Geant4 also allows the user to implement their own physics processes, however, the scope of this thesis is to test and validate the existing standard physics processes, not to create new ones.

To fit in with the general hadronic physics process interface, G4NeutronHP splits the < 20 MeV neutron transport into four parts: radiative capture, elastic scattering, fission, and inelastic scattering (Geant4 Collaboration, 2019c).

Both Geant4 and MCNP perform neutron transport calculations based on data from evaluated nuclear data libraries. This data is published in ENDF-6 format and has to be processed into a format the codes can interpret before use.

Geant4 offers a standard nuclear cross-section library called G4NDL4.5. Other converted libraries are available. The conversions are performed by a group at CIEMAT (Centro de Investigaciones Energéticas, Medioambientales y Tecnológicas), Spain (Mendoza et al., 2012), (Mendoza et al., 2014) (Mendoza and Cano-Ott, 2018a). They advice to set several additional environment variables:

- G4NEUTRONHP_SKIP_MISSING_ISOTOPES=1: In the case that cross-section data is missing for an isotope, Geant4 usually looks for cross-section data from another isotope close in Z and A. Since such an isotope is likely to have completely different nuclear properties, the setting of this variable prevents Geant4 from doing this. Instead, it only looks for the natural composition data from the element and if this is not successful, the particular cross-section is set to zero. Additionally, a warning appears in the output file to alert the user to the issue.

- G4NEUTRONHP_DO_NOT_ADJUST_FINAL_STATE=1: The ENDF-6 library data does violate energy and momentum conservation. Without setting this variable, Geant4 would counteract this by generating unphysical gamma rays. Setting this variable makes the result compatible to the ENDF-6 library data.

- AllowForHeavyElements=1: This variable activates the physics for isotopes with $Z > 92$.

These variables are used throughout the calculations.

A.3 Implementation of MC Transport and Data Collection

This part strongly simplifies a very detailed description given by Geant4 Collaboration (2019a). The particle transport in Geant4 is structured in a hierarchy which goes from most generic down to the finest detail. The highest level of this tracking hierarchy is G4Run, which includes a user-defined number of G4Events. A G4Event is equivalent to a particle history from creation until all secondary particles are killed. A G4Event includes one or more G4Tracks. A G4Track is a particle from creation till destruction and its secondary particles are new G4Tracks. The next level down is the G4Step which is the movement from one interaction to the next within one G4Track. This is where the communication with the physics processes and calculation of distances within the geometry happens. There are manager classes (G4RunManager, G4EventManger, G4TrackingManager, and G4SteppingManager), which manage what is happening at different levels of the hierarchy.

Off to the side of the tracking hierarchy is the creation of initial particles. The user can derive their own PrimaryGeneratorAction class based on G4UserPrimaryGeneratorAction and implement the calculation or definition of the required variables such as particle type, position, and energy. There are many versions of PrimaryGeneratorAction classes in the examples which can be used to get started. Alternatively, Geant4 also provides the General Particle Source, which is a ready-made set of routines for calculating these variable, which the user can control through the input file via a set of commands.

Also to the side of the tracking is the G4Stack class, which stores particles which are not currently tracked. One G4Track is tracked at a time and when a physics process creates secondary particles, these new G4Track objects are stored in the G4Stack until the current G4Track has been killed. Then, a new G4Track is taken out of the G4Stack according to the "last in first out" principle and is tracked next.

The order in which things are happening, is from the top down until the lowest level like a set of nested loops: higher levels start iterations of the next lower level. Once a level has finished it goes one hierarchy level up. This iteration continues until all the steps of all primary and secondary particles of the initially set number of particle histories have finished.

The user can define their derived versions of the standard User Action Classes G4UserRunAction, G4UserEventAction, G4UserStackingAction, G4UserTrackingAction, and G4UserSteppingAction. These optional classes provide methods which make it possible to implement actions to be performed at particular stages of the tracking hierarchy. In this thesis, G4UserStackingAction was used to kill all secondary particles except neutrons instead of putting them in the G4Stack to be tracked next, and the EndOfRunAction method of G4UserRunAction was used to print out the collected data at the end of a run. A derived version of the G4VUserActionInitialization subroutine is used to define the chosen User Action Classes. PrimaryGeneratorAction is also set up here.

Additionally to moving particles through the geometry according to the principles of the physics processes, tallying data is collected. There are a set of available classes called Primitive Scorers and the user can also set up their own tallying class. On the most basic level, such a tallying class has to describe the structure of the data container being used and which data should be recorded. During the set-up of the geometry in the DetectorConstruction subroutine (mentioned already in section 2.4.4), any of the defined tallying classes can be chosen and associated with specific cells of the geometry. It is possible to assign more than one tallying class to a volume and to set up multiple instances of the same tallying class which are distinguished by name-tags given during this initialisation.

During the particle transport, for each new particle history (G4Event) and each initialised tallying class, the data container is set up. When eventually a particle of this G4Event performs a step into or within a volume with an associated tallying class, the tallying class is turned on and receives a pointer to the current G4Step object.

The different hierarchy levels each store a set of data relevant to this level. This is required for the physics processes and the particle movement, but the data can also be collected as part of the tallying. For example G4Track stores permanent information about the particle such as mass or charge. Information about changing properties such as energy, momentum, position, or time is kept from the beginning of a step until the step is finished. Then, the values are updated with the results from the step. G4Step stores transient information during a step. Its starting point is called PreStepPoint and its end point is called PostStepPoint. G4Track, G4Step, and the associated PreStepPoint and PostStepPoint objects have Get methods, which can retrieve the stored information at the different levels.

In a tallying class it is defined, which information should be retrieved with these Get methods using the pointer to the G4Step object and the Get methods and how it should be stored in the data container. For example, the tallying class could retrieve the $track\ length$ from the current G4Step object and the $particle\ type$ from the current G4Track object and in the case that it is a $neutron$ store the $track\ length$ in the data container to act as a track length tally for neutrons.

The data containers created and filled with data on the G4Event level have to be collected on the G4Run level. For this, the user has to overwrite two virtual methods: RecordEvent() for collecting event-level data containers into run-level data containers during a thread-local run, and Merge(), which is used during multi-threading and handles the merging of the thread-local data containers to the global run-level data containers.

Appendix B

New Geant4 Developments for Fusion Nuclear Analyses

B.1 Development of Application out of Toolkit Parts

As explained in section A.1, in Geant4 there is no standardised code which the user can use directly. Instead, the user has to build their own application out of the parts of the toolkit and if necessary own developments. As also laid out in that section, Geant4 provides a large number of example applications, which the user can use as jumping off points. The application built for this thesis is mainly based on the /extended/hadronic/Hadr04 example, except its Run subroutine, which is based on the /extended/RunAndEvent/RE02 example. Some unnecessary parts are removed and some additional parts are added.

A schematic of the used subroutines can be seen in figure B.1. The configuration was changed for the different set-ups discussed in this thesis, which is denoted by different colours in the schematic.

Hadr04 is the main program which calls the subroutines of the next level. It also reads in the input file and any additional data files and sets up the use of multi-threading.

DetectorConstruction defines the geometry of the problem including the materials. The geometry definition can be hard-coded in this subroutine or defined by a GDML file is read-in by the Hadr04 main routine. The detectors, which define the macroscopic quantity to be tallied up during a run, are also created here and assigned to a volume in the geometry.

DetectorMessenger is a messenger class, which governs the communication with the compiled executable through commands in an input file. It allows the user to change the geometry set-up for each run using a set of input commands defined in this subroutine. For example it is possible to choose a material for the current run out of the ones defined in the DetectorConstruction subroutine. This is used in chapter 5 for the verification and validation of Geant4 with code-to-code benchmarks to switch between nuclides.

TrackLengthBinsSD, TracklengthBinsHit, ActTLBinsSD, and ActTLBinsHit are subroutines which define new types of detectors. They are further explained in section B.3.

PhysicsList defines the physics processes to be used in the problem.

NeutronHPphysics is the set of physics routines for neutron transport at energies below 20 MeV using converted data from standard nuclear cross-section data libraries.

NeutronHPMessenger is another messenger class allowing to turn the neutron thermal scattering law treatment on and off with a command in the input file.

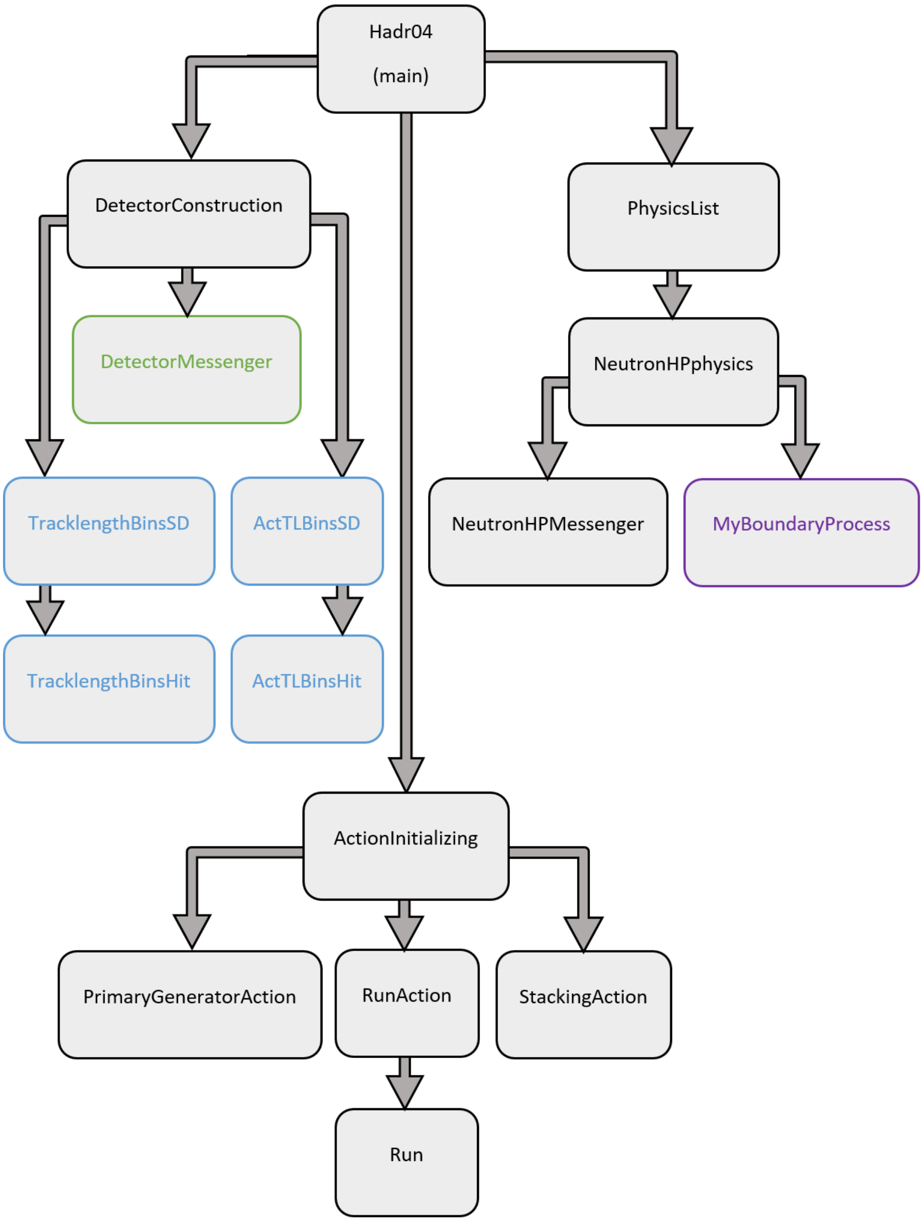

Figure B.1: The schematic of the subroutines of the Geant4 application developed for this thesis. The black marked subroutines are always present; the coloured ones are only present in specific set-ups.

MyBoundaryProcess is a newly implemented subroutine which allows the use of reflective boundaries. It is only used for the DEMO applications and is further discussed in section B.6.

ActionInitializing calls run-time subroutines, which are called UserActionClasses.

PrimaryGeneratorAction is the subroutine which defines the initial conditions of every new particle created during the run. It is possible to use a set of pre-defined source subroutines through commands in the input file, or to hard-code the calculation of the initial energy, momentum direction, and velocity of the source particle. Different versions of this subroutine were created to treat data from MCNP SDEF input cards and to represent the DEMO plasma source subroutines. These developments are described in sections 4.2 and 4.3.

RunAction governs the start and end of individual runs.

Run controls the tallying up of the hits to the detectors, including the adding up of results from different multithreading threads. For this, it refers back to the list of the detectors which are defined in the DetectorConstruction subroutine. A change of the kind of detector set-up in DetectorConstruction can require a rewrite of the Run subroutine. It contains a method for writing the results into a file which is called by RunAction at the end of a run.

StackingAction allows the user to implement an action which happens when newly created secondary particles are stored in G4Stack so that they can later be retrieved and tracked as well. For example it can be used to kill all secondary particles which are not neutrons in a neutron-only run to conserve computational resources.

B.2 Geometry Conversion

The different geometry description approaches of Geant4 and MCNP are described in section 2.4.4. In this section the methods for converting geometry descriptions are discussed.

For the computational benchmarks described in section 5.1 and 5.2, the simple geometry is set up by hand for both MCNP and Geant4. Also the first experimental benchmark described in section 6.1 has relatively simple geometry, which is converted by hand from the MCNP input file version into a Geant4 version. For this, the volume types and their dimensions and materials are hard-coded into the DetectorConstruction subroutine.

In this thesis, the CAD conversion method previously developed by Qiu (2016) is applied to the more complex geometries of the mock-up of a tritium breeding module for the second experimental benchmark described in section 3.2.2 and of the sector model of the DEMO reactor described in section 3.3. The CAD-formatted geometry is loaded into the SpaceClaim program, edited if necessary, and sorted by material. Next, a python script version of McCad is used to decompose the geometry. Then the parts of all materials are saved individually and imported into the McCad program, where the conversion into the GDML format takes place.

The Half-Space-Solid functionality had been developed for Geant4.10.02 and included some additions to the main Geant4 source code. This needed to be ported to the version Geant4.10.05-p01 used in this thesis.

Using a GDML-based geometry description requires several changes to the Geant4 application. Geant4 provides some example implementations. The version used in this thesis is based on `/examples/extended/persistency/gdml/G04`.

In the main subroutine, the interaction with the input files is defined. Without GDML, the application is executed in the command line like this:

$>$ *executable input-file* .

In the main subroutine, it is defined that interactive mode is started if no input-file is given ($arg < 1$). For GDML, a GDML-file is entered additionally like this:

$>$ *executable GDML-file input-file* .

Due to this additional argument, the main subroutine needs to be changed to launch interactive mode in the case $arg < 2$.

To interact with the GDML-file, Geant4 provides the G4GDMLParser functionality. It is initialised in the main subroutine and is used to read the GDML-file entered in the command line. The main subroutine passes on the parser object onto the DetectorConstruction subroutine and through ActionInitialization and RunAction onto the Run subroutine.

In DetectorConstruction, the GetWorldVolume() function of the GDML parser is used to construct the geometry. As the geometry is no longer hard-coded, the geometry and material definition part of DetectorConstruction is left empty.

When defining detectors for tallying, they need to be associated with specific volume cells of the geometry. In case of the hard-coded geometry, a pointer to the chosen logical volume, which is defined in the geometry definition part is used. Since this part does not exist anymore and the geometry definition happens within the GDML file instead, another technique has to be used.

For this, the GDML format offers the functionality of auxiliary information. In the GDML file, the user adds an additional line into the volume definition of the chosen volume cell. The syntax is:

$$<\textit{auxiliary auxtype="SensDet" auxvalue="detector name"}/> \quad . \tag{B.1}$$

This way, the user can define keywords in $auxtype$ and $auxvalue$, which are associated with a specific volume. In DetectorConstruction, the GDML parser functionality GetAuxMap() is used to retrieve an iterable data structure of all auxiliary information existing in the GDML file. This data structure makes it possible to iterate over all volumes with aux-info and retrieve volume name, $auxtype$ and $auxvalue$ for each iteration step. The keyword "SensDet" is defind to mean "place a detector here". If the $auxtype$ has this keyword, the also retrievable volume name and the detector name encoded in $auxvalue$ can be used to initialize a detector. The detector names placed as $auxvalue$ in the GDML file can be used to distinguish between different types of detectors. In section B.3, it is described how different detector types can be used to calculate reaction rates such as the Au-197 (n,γ) reaction in the activation foils of the HCPB mock-up benchmark described in section 6.2.

This method simplifies the procedure of setting up a large number of detectors. In the HCPB mock-up case, detectors have to be set up in eight breeder stacks with 12 breeder pellets each. For this, the line in equation B.1 with $auxvalue = "breeder"$ is placed in the volume definition of all 96 breeder pellet volumes. In DetectorConstruction, the conditional clause $auxvalue = "breeder"$ is set to place a pure flux detector and a Li-6 and Li-7 tritium producing reaction detector. Other $auxvalue$-keywords are used to denote the different activation foil reactions and place their detectors in the same way.

In the Run subroutine, again GetAuxMap() is used to retrieve the iterable data structure of all auxiliary information, which then allows to set up the data containers to collect the data produced during the run in the same way as the detectors are created in DetectorConstruction.

B.3 Detector Conversion and Development

As explained in section 2.4, the user can specify which macroscopic quantities should be detected during a Monte Carlo run. In MCNP, this functionality is called "tally". Geant4 offers a set of standard so-called "Primitive Scorer" classes. This includes some which are nearly equivalent to the MCNP standard tallies. An overview is displayed in table B.1.

For surface current and flux, Geant4 has different Primitive Scorers depending on the geometry type of the volume the surface is a part of. The detection also only happens on one surface of the volume: For Flat it is the -z surface of a G4Box volume, for Cylinder it is the inner surface of a G4Tubs volume and for Sphere it is the inner surface of a G4Sphere volume. Furthermore, it can be chosen to only detect particles, which are crossing the surface in the "in", "out", or both directions. This information is given in the beginning of the " .cc"-files of the different scorer types.

Table B.1: Geant4 primitive scorers equivalent to MCNP tallies (except for normalisation factors).

MCNP	Geant4
Surface current (F1)	G4PSFlatSurfaceCurrent G4PSCylinderSurfaceCurrent G4PSSphereSurfaceCurrent
Average surface flux (F2)	G4PSFlatSurfaceFlux G4PSCylinderSurfaceFlux G4PSSphereSurfaceFlux
Average cell flux (F4)	G4PSCellFlux

Different normalisation procedures have to be taken into account when comparing Geant4 and MCNP results. MCNP uses its standard unit of cm and automatically divides by the number of particle histories, while Geant4 offers a choice of units but calculates internally in mm and does not divide by the number of particle histories. These additional normalisation processes can be implemented either in the Run subroutine before the output of the data or have to be done in the post-processing of the data.

In MCNP, the detected particle type and the energy bins can be set in the tally and tally modification cards of the input file. The Geant4 equivalent are the filter classes G4SDParticleFilter, G4SDKineticEnergyFilter, and G4SDParticleWithEnergyFilter which allow the user to specify a particle type, an energy range, or both at the same time which is detected in the associated primitive scorer. Since the filter classes only set lower and upper energy thresholds, a list of energy bins has to be translated into one primitive scorer instance per energy bin.

The G4VPrimitiveScorer classes use the G4THitsMap storage type. In this type of storage, a G4THitsMap is associated with each instance of G4VPrimitiveScorer and can collect a single value. For example, the user can create a G4VPrimitiveScorer of the type G4PSCellFlux and a G4SDParticleWithEnergyFilter with particly type "neutron", lower energy threshold "10 MeV", and upper energy threshold "15 MeV", which is associated to a specific cell in the geometry. During the run, every time a neutron with the right kinetic energy crosses the chosen cell, its track length divided by the volume of the cell will be added to the value stored in the G4THitsMap object.

For accumulating the scored quantities during the run, a modified version of the Run subroutine based on the RE02 (Run and Event 02) example is incorporated in the basic Geant4 application created mostly based on the Hadr04 example. It consists of the following methods:

- **Constructor** uses global vectors to store detector names, detector ID values, and G4THitsMaps. It iterates over all G4VPrimitiveScorer detectors created in the DetectorConstruction subroutine and adds their name, ID and a newly created G4THitsMap into the respective vector.

- **RecordEvent()** accumulates G4THitsMaps of all events into a G4THitsMap of the run for each detector.

- **Merge()** accumulates G4THitsMaps from different threads during multithreading into a G4THitsMap of the master thread for each detector.

- **DumpAllScorer()** is called by the RunAction subroutine at the end of the run and dumps the output data. It iterates over all G4HitsMaps contained in the global vector and retrieves the data collected therein. The same energy bin list as in the DetectorConstruction subroutine is used to write out the energy bins along with the results and their relative errors.

- **Destructor** clears up all storage vectors.

According to Brown et al. (2003), the Monte Carlo method obtains results by sampling possible random walks and recording the contribution x_i of each random walk i to the sampled mean $\bar{x}$. The statistical precision, which is also called the relative error, of $\bar{x}$ is calculated during the run using equation 2.17.

To include this relative error calculation in the Run subroutine, this means that for each primitive scorer, additionally to the recorded value itself x_i, the square of the value x_i^2 has to be summed up for every particle history i in a run. This makes it possible to calculate the relative error at the end. Accordingly, an additional data container is created, which is filled with the square of the current value and otherwise treated like the data container for the actual value.

The error calculation is implemented in the DumpAllScorer() method based on an implementation found in the Geant4 message board (this message board has since been deactivated, but the thread can still be found in the wayback machine using this link: `https://web.archive.org/web/20160605035801/http://hypernews.slac.stanford.edu/HyperNews/geant4/get/biasing_scoring/101/2.html` (lcl (Username), 2014)), which is modified according to equation 2.17.

The set-up based on Primitive Scorer is used for the code-to-code benchmarks (section 5) and the SINBAD transmission through iron spheres experimental benchmark (section 6.1).

For the other experimental benchmarks (section 6.2 and 6.3) and the application to DEMO (section 7), the G4VSensitiveDetector class is used. G4VSensitiveDetector is an abstract base class which gives the user a basic structure for setting up their own detector type and defining which data should be recorded when a particle track is passing through an associated geometry volume during particle transport.

In combination with this, G4VHit is used, which is another abstract base class from which the user can derive their own type of hit class. In the hit class, snapshots of an interaction of a track in a sensitive volume are recorded. The user can specify which physical quantities should be stored such as position, time, momentum, energy, track length, energy deposition, and any combination of these. The G4VHit class contains variables for the physical quantities which should be collected and the methods for adding new values to and returning the contained values of the variables. This allows a lot more flexibility than the single stored value of the Primitive Scorer based tallying method.

G4THitsCollection is a template class, which the user can use to set up a storage container in the form of a vector collection for the G4VHit objects created during the run.

The new sensitive detector type needs to implement three methods:

1. **Initialize()** which is called at the beginning of each new particle history and sets up the storage in the G4THitsCollection.

2. **ProcessHits()** which gets called when a particle track is passing through the associated sensitive volume, defines which physical quantities to fetch out of the particle tracking information to record, and creates a G4VHit object associated with the previously created G4THitsCollection to store any data.

3. **EndOfEvent()** which is called at the end of each particle history and can be used to set up processes which should happen at this point such as to print out results.

In the following, the two new sensitive detector and hit classes created for missing functionalities in Geant4 are described.

B.3.1 Track Length Detector with Multiple Energy Groups

The new sensitive detector type TracklengthBinsSD detects track length for neutrons in a variable energy bin list which can be created or read in elsewhere in the code and is passed on during initialisation.

In Geant4, usually G4THitsCollection is used to just collect all hits during a run and print out a table of all hits and their data at the end. In contrast to this, MCNP only has the option to create energy bins in which the contribution of individual hits is added up, which loses the information of the individual hit. Since this additional information is not relevant and requires more storage, the G4THitsCollection is used in a way that creates an energy bin structure.

The example /basic/B4c provided by Geant4 and its implementation of a G4VSensitiveDetector called B4cCalorimeterSD served as basis for this. Instead of in energy bins, data is collected for different copies of a volume. B4cCalorimeterSD gets the number of volumes N passed during initialisation. Then, a G4THitsCollection object is created in the Initialize() method and filled with $N+1$ newly created G4VHit objects implemented as B4cCalorHit. The additional G4VHit object is for the total over all cells. In the ProcessHits() method, the necessary information about the current particle track including which copy number i it is in are retrieved. In the case that the particle fulfils the requirements to be detected, the vector to the G4Hit-object of bin i and the total bin $N+1$ is taken out of the G4THitsCollection object and used to add the values onto the values of both bins via the Add() method.

Instead of creating a new G4VHit object for every time a new value is detected, G4VHit objects are only created once in the beginning for every copy of a volume. Later during the particle tracking, newly detected values get sorted into the G4VHit object associated with the current copy number.

For the new implementation of a G4VSensitiveDetector called TracklengthBinsHit this is modified. This implementation takes a list of energy bins with length L. This list can be read in from a file.

B4cCalorHit is used as basis for the TracklengthBinsHit implementation. It collects track length in a variable and has an Add() and GiveTracklength() method for adding the track length values of new hits and returning the stored track length value.

In TracklengthBinsSD, the structure for the volume copies with the energy bin list is replaced: In the Initialize() method, a new G4THitsCollection object is created and a new TracklengthBinsHit for every energy bin of the energy bin list and an additional one for the total bin is inserted. In the ProcessHits() method, particle type, track length and kinetic energy of the current particle are retrieved. In case the particle type is "neutron" and the track length nonzero, a binary search is used to find the energy bin into which the kinetic energy falls. Then, the vector to the G4Hit-object of this bin and the total bin is taken out of the G4THitsCollection and used to add the current track length onto the values of both bins via the Add() method. The EndOfEvent() method is left empty.

The Run subroutine organises the combining of data collected during each particle history/event and by each individual thread in a multi-threading application into the final data of a run and writing the output. Changing from G4VPrimitiveScorer to G4VSensitiveDetector necessitates the modification of the Run subroutine to accommodate G4THitsCollection instead of the G4THitsMap data storage structure.

The B4c example does not have a Run subroutine and implements the read-out of the data collected during the run differently. Therefore the modification of the Run subroutine is not based on a template.

Run uses four vectors which collect detector names, detector IDs, sum of the values, and sum of the square of the values. The latter two were modified to store TracklengthBinsHitsCollection instead of G4THitsMap. In the beginning of each run, an iteration over all detectors happens. For each detector, its name, ID, and for each of the value-sum and the square-sum a newly created TracklengthBinsHitsCollection is added to the respective vector.

During the run, when the results of events are combined into the results of the run and when the results of threads are combined into the results of the master thread in multithreading, additions are performed. The G4THitsMap data container has a method for additions. Based on this, a new method Add() is implemented to add a TracklengthBinsHitsCollection to another TracklengthBinsHitsCollection. Furthermore, a slight variation of this method called Add2() is created, which adds the square of the values in a TracklengthBinsHitsCollection to another TracklengthBinsHitsCollection. The RecordEvent() and Merge() methods are modified with this new addition method.

At the end of the run, in DumpAllScorer(), the data retrieval is modified for TracklengthBinsHitsCollection and error calculation and data dumping performed as usual.

To get the average flux in a volume from the track length, it has to be divided by the volume of the detector cell. It would have been possible to include this in the TracklengthBinsSD subroutine or in the DumpAllScorer() method. Instead it was done in data post-processing, saving the computation time for these calculation operations during the run.

This sensitive detector set-up can easily be modified to record other additive physical quantities than track length such as energy deposition. It can also be modified to detect a specific particle type given upon initialisation.

B.3.2 Track Length Detector with Tally Multiplier Function

MCNP has the tally multiplier feature, which allows the multiplication with energy dependent factors before the energy binning is performed. In this way, a physical quantity like the reaction rate R can be calculated from the neutron fluence Φ using the conversion constant C and the cross-section of the reaction σ:

$$R = C \int \Phi(E)\sigma(E)\mathrm{d}E \quad . \tag{B.2}$$

This functionality is necessary to calculate tritium activity and activation foil reaction rates in the SINBAD HCPB TBM Mock-up experiment which is discussed in section 3.2.2 and for calculating the tritium breeding ratio (TBR) in a DEMO model which is discussed in section 3.3.

For the (n,α) reaction of Al-27, the (n,p) reaction of Ni-58, the (n,2n) reaction of Nb-93, and the (n,γ) reaction of Au-197 the data is taken from IRDFF-v.1.05 (Zsolnay et al., 2012) dosimetry data, which can be retrieved from `https://www-nds.iaea.org/IRDFFv105/`. For the tritium producing cross-sections of Li-6 (n,t) and Li-7 (n,n') data is taken from JEFF-3.3 (Plompen et al., 2020) cross-section library files. The required data are extracted by hand from the ACE data file. This data consisting of energy points and corresponding cross-section values is saved as lists in basic text files.

The Li-7 (n,n') cross-section data consists of different excitation levels. Here the cross-section values from the second till the highest excitation level are added up before creating the list file.

The main subroutine of the Geant4 application is modified to read-in these lists, neglecting any energy-cross-section pair with energy above 20 MeV, since this energy range iss not required for the current calculations. The data are stored internally in vector format.

For the implementation of the tally multiplier functionality, new classes are created based on the ones discussed in the previous section. TracklengthBinsSD is modified and renamed ActTLBinsSD which stands for "Activation Track Length energy Bins Sensitive Detector". The associated G4VHit class TracklengthBinsHit is renamed ActTLBinsHit, and the associated G4THitsCollection data container TracklengthBinsHitsCollection is renamed ActTLBinsHitsCollection. For ActTLBinsHit and ActTLBinsHitsCollection only their names are changed.

For ActTLBinsSD, TracklengthBinsSD is modified to additionally accept an energy and a cross-section data point vector upon initialisation. When setting up the detectors of the simulation in the DetectorConstruction subroutine, the user initializes new instances of TracklengthBinsSD. At this point, they can pick which type of reaction rate (for example Al-27 (n,α)) should be calculated by passing along the associated cross-section and energy data vectors.

In the ProcessHits() subroutine, as for TracklengthBinsSD, the particle type, current kinetic energy E_{kin}, and track length TL in the detector volume of a detected particle are recorded and if found worth of detection, the bin M_{energy} for the energy binning is found with a binary search.

Here, the tally multiplier feature is implemented: another binary search is used to find the energy bin M_{multi} of the cross-section data into which the kinetic energy E_{kin} of the particle fits. All the cross-section data used in this work for multiplication required linear-linear interpolation between the energy/cross-section points. The exact cross-section value corresponding to the kinetic energy E_{kin} of the particle is calculated from a linear interpolation between the energy/cross-section points M_{multi} and $M_{multi}+1$. Afterwards, the track length TL is multiplied with the interpolated cross-section value and the result tallied up according to the energy bin M_{energy}. As for TracklengthBinsSD, the result is also added to the total energy bin.

The data collection in the Run subroutine remains unchanged compared to TracklengthBinsSD. A TracklengthBinsHitsCollection data container is used, which poses no issue in adding up the ActTLBinsHitsCollection data container derived from the same base G4THitsCollection. Using both TracklengthBinsSD and ActTLBinsSD in the same simulation poses no issue for the data collection in the Run subroutine, since the data is structured the same way.

The ActTLBinsSD sensitive detector type can be modified just like TracklengthBinsSD. Currently, a change of the used cross-section or library means the user has to process the new data by hand. Going forward, it would be possible to add a routine which interprets ACE/ENDF-formatted files and extracts and processes the required data automatically into the energy and cross-section vector pairs which are used in the ActTLBinsSD class. A variable interpolation feature for switching between linear and logarithmic interpolation depending on what the used data requires would also be an option.

B.4 Statistical Checks for Convergence Testing

Geant4 has a subroutine containing some MCNP-equivalent statistical checks and some different checks called G4ConvergenceTester. This subroutine is extracted and set up to run on data written out by the code as a post-processing step and modified to be in better agreement with MCNP.

The reason it could not be used at run-time is the lack of parallelisation in Geant4. When performing a run with a large number of particle histories, the required time can become very long, sometimes exceeding the time limits on a cluster node imposed by the providers of computing infrastructure. Therefore, the calculation has to be split up and distributed among multiple nodes. In MCNP, such parallelisation is available as part of the code. In Geant4 only multi-threading, which utilizes multiple computing threads on special nodes for this purpose, is available as a standard, but not parallel computation on multiple nodes.

This issue is circumvented by using a scripted parallelisation in Geant4. For this, runs are started on multiple nodes using a different random seed for each run. After the run, the results of the different nodes are added up and divided by the total number of histories to arrive at a total result. Bash-scripts and simple Fortran90 programs are used to automate the tasks of creating the input and job submit files, starting the runs, and after the runs finished, gathering and processing the data from the output.

As each run only has a partial number of particle histories, a Geant4 subroutine which performs the statistical checks during run-time does not work. Instead, the data required for the quantities used for the statistical checks are collected and written out for each run. Additionally to the already collected $\sum x_i$ and $\sum x_i^2$ for calculating the estimated mean $\bar{x}$ and its relative error R as described in section B.3, for calculating the estimated variance of the variance VOV it is also necessary to collect $\sum x_i^3$ and $\sum x_i^4$ during the run. With these values, VOV can be calculated according to equation 2.20. Furthermore, the 201 largest scores for every tally are collected as a list sorted from biggest to smallest during the run for the $SLOPE$ calculation.

During post-processing, the modified G4ConvergenceTester subroutine reads in the data from one run after the other. The $\sum x_i^n$ values are summed up, and the largest scores for the current run are inserted into the sorted list of the 201 total largest scores. Then, the quantities mean $\bar{x}$, relative error R, figure of merit FOM, variance of variance VOV, and current slope $SLOPE$ are calculated and written out together with the combined particle histories N of the runs added up so far. This allows the user to examine the behaviour of these quantities throughout the adding up process.

It is necessary to monitor how the quantities evolve with N. When using MCNP, it can be observed in the MCNP output that the number of steps in N, for which $\bar{x}$, R, FOM, VOV, and $SLOPE$ values are printed, vary between 10 and 20 depending on the number of particle histories in the run. The G4ConvergenceTester subroutine of Geant4 is always using 16 steps. Since this falls within the range used by MCNP, the 16 steps for evaluating the quantities $\bar{x}$, R, FOM, VOV, and $SLOPE$ are kept. For the criteria fulfilment, the last nine, which denote the second part of the total calculation, are considered. For these points, the results for $1/N$ and $1/\sqrt{N}$ are also calculated.

According to notes in the source code, G4ConvergenceTester uses the Bravais-Pearson correlation coefficient r combined with the Student t-test to check if the values of $R(N)$ and $VOV(N)$ follow $1/\sqrt{N}$ and $1/N$ respectively. According to Fahrmeir et al. (2007) the correlation coefficient is calculated like this:

$$r = \frac{\sum_{i=1}^{N}(x_i - \bar{x})(y_i - \bar{y})}{\sqrt{\sum_{i=1}^{N}(x_i - \bar{x})^2 \sum_{i=1}^{N}(y_i - \bar{y})^2}} \quad , \tag{B.3}$$

with x_i being the $1/\sqrt{N}$ or $1/N$ steps and y_i being the $R(N)$ or $VOV(N)$ values. The values of r lie between -1 and $+1$ and mean

$$\begin{array}{cc} r < 0 & \text{negative linear correlation,} \\ r = 0 & \text{no linear correlation,} \\ r > 0 & \text{positive linear correlation.} \end{array}$$

Next, a Student t-value is calculated from the correlation coefficient r and the degrees of freedom n like this (Stuart et al., 1973):

$$t = r\frac{\sqrt{n-2}}{\sqrt{1-r^2}} \quad . \tag{B.4}$$

The zero hypothesis of the t-test is no correlation ($r = 0$). This hypothesis is rejected in favour of an alternative hypothesis by comparing the calculated t-value with a critical value t_{crit}. The t_{crit} values are tabulated for different degrees of freedom n and different confidence intervals α. In the case of a one-sided hypothesis of $r > 0$, which means a positive linear correlation between the x and y distributions, the zero hypothesis is rejected if $t \geq t_{crit} = t_{n-2;1-\alpha}$. Setting the confidence interval $\alpha = 5\,\%$ and using $n = 9$, this value is looked up to be $t_{7;95} = 1.8946$ (Fahrmeir et al., 2007). The original setting of Geant4 has been using eight steps and the value $t_{crit} = 1.090546$, which could not be found in the tabulated t-values. Therefore it is replaced with the newly looked up one. In the output, the calculated t and r values are printed out, so that the user can check them.

G4ConvergenceTester posits the requirement of a "random" distribution for the mean $\bar{x}$ and the FOM. This is replaced by the MCNP requirement that the mean $\bar{x}$ should be nonmonotonic and FOM should be statistically constant and nonmonotonic. The nonmonotonic requirement is passed if there is at least one $\bar{x}(N)$ or $FOM(N)$ that deviates from a decreasing or increasing trend. The statistically constant requirement is defined as all $FOM(N)$ values are within 5% of the average FOM calculated from the values at the 9 N steps.

Furthermore, the requirement $VOV < 0.1$ is added and the $SLOPE$ requirement is changed to be > 3 not ≥ 3.

B.5 Importance Biasing Variance Reduction Method

During the validation of Geant4 with the ITER Bulk Shield experimental benchmark (see section 3.2.3), the variance reduction method of importance biasing is used in MCNP. To translate this for Geant4, the importance value for each volume of the geometry is extracted from the MCNP input file. A list of the importances of the corresponding volumes after the conversion of the geometry into GDML format is created. Then, the importance values are entered into the GDML file as auxiliary information for every volume which can be read out by Geant4.

Geant4 includes standard functions for importance biasing. An example implementation of an application is given in the "/extended/biasing" directory. It is called "B01". It involves registering an importance biasing method ("G4ImportanceBiasing") to the current physics list in the main subroutine and the creation of a store of the importance values in the DetectorConstruction subroutine. The function for creating the importance store is modified to read in the importance value from the auxiliary information in the GDML file and assign it to each physical volume.

The track length detector described in section B.3 is modified for variance reduction so that it multiplies the detected track length of every hit with the current weight of the particle retrieved from the G4Track object before adding it to the result of the current energy bin.

Unfortunately, this implementation supports importance sampling only for one particle type at a time. As both neutrons and gammas have to be biased for the ITER Bulk Shield experimental benchmark, the approach has to be modified.

B.5.1 Support for Multiple Particle Types

Geant4 also includes the generic biasing scheme which offers more flexible biasing options. There are six example implementations available in the "/extended/biasing/" directory: "GB01"–"GB06". The example "GB03" has a simplified geometry based biasing scheme with a geometry consisting of a stack of slabs where particles are split when moving forward through the slabs and killed when moving backwards. Here, it is possible to turn on the biasing for more than one particle type.

The "GB03" example has the subroutines GeometryBasedBiasing and SplitOrKillOnBoundary which implement the split and kill behaviour when a particle crosses from one geometry volume into the next. These are replaced with splitting and Russian roulette according to the importance values of the two volumes. For this, the relevant part is extracted out of the G4ImportanceAlgorithm and G4ImportanceProcess subroutines. These are part of the standard Geant4 code which usually runs in the background of the importance sampling. Furthermore, the already modified importance store function from B01 is added, which reads in importance values from auxiliary information in the GDML files.

B.5.2 Attempts at Resolving the Clash of Compatibility with HalfSpaceSolid Geometry

There is an issue with particles hitting the exact boundary between two geometry volumes. The geometry description HalfSpaceSolid defines them as belonging to neither the previous nor the current volume, but instead the World Volume. As the World Volume is set to importance of 1 and in the rest of the geometry, the importances rise with penetration depth, it can for example happen that a particle moving from volume 1 with importance 5000 to volume 2 with importance 10000 hits the exact boundary with importance 1. Instead of splitting the particle into 10000/5000=2 with half the previous weight, the particle is killed in the Russian Roulette with the high probability of 1-1/5000.

This issue has not been resolved. All attempts such as implementing a functioning method of retrieving the importance value of the next entered volume for a particle sitting exactly on a boundary have failed so far.

The results of the SINBAD Bulk Shield benchmark are discussed in section 6.3. There are fluctuating discrepancies between Geant4 and experimental and MCNP results. It is unclear whether these are caused by the importance on boundary issue just discussed or whether there is another unknown issue either on the side of the baseline code or caused by the implementation for this thesis.

An alternative approach to an implementation using Geant4's parallel geometry feature has been attempted. It is possible to define a parallel geometry with different cell boundaries. The idea is to define the importance values on classic Geant4 solids in the parallel geometry and therefore potentially to avoid the boundary issue encountered in the HalfSpaceSolid geometry. The parts of the original geometry which do not describe the bulk shield box itself, such as the table, the room, and the source set-up, all have importance one or zero. Inside of the box, the importance rises in layers with penetration depth. Due to this, the parallel geometry can be a simplification of the original geometry consisting of G4Box volumes. If this were not the case, another geometry conversion by hand would be necessary for the parallel geometry, which would render the HalfSpaceSolid conversion unnecessary. Unfortunately, problems have been encountered when trying to place the detectors and this issue has not been resolved so far. Therefore it is unclear, whether this approach would remove the deviations from MCNP and experimental results.

Another approach which has not been implemented successfully, is to move the current particle a small step forward along its momentum vector any time it is in the World Volume when it is not supposed to be. Then, the standard Geant4 methods could be used for checking the current volume and its importance. Since interfering in the basic particle tracking algorithm like this could be quite risky, a clone of the current particle is created and killed after the volume retrieval. Unfortunately, the volume retrieved this way, is still the World volume, no matter how far the particle is pushed and therefore does not resolve the issue.

A further idea, which was attempted to implement, is to create a list of lower and upper boundary values in x, y, and z-direction for all volumes with important values other than 1. Since the volumes are mostly rectangular slabs these values could easily be taken from the GDML surface description. If a particle ends up in the World Volume, the current position can be used to find if it is in the relevant volume area and then the corresponding volume using several logical branches.

Depending on how often a boundary is being hit, this approach is likely computationally intensive. It would not scale up well for an application in a larger, more complex volume such as in DEMO. However, it could be useful to find out if the bulk shield results could be improved this way, thereby determining whether the boundary issue is the only problem causing discrepancies in the Geant4 results which are discussed in section 6.3. Unfortunately, this implementation runs only for smaller particle histories up to 10^6 and crashes with segmentation fault at some point during the run for all attempts with 10^7 particle histories.

B.6 Reflective Boundaries

Fusion reactors are rotationally symmetric. This fact is routinely used in neutronics simulations by representing the geometry of the whole reactor by just a slice and using reflective boundaries at the side surfaces of the slice. Tokamaks can be represented by fairly small slices. The DEMO model which is used in this thesis is a 10° slice, which means only $\frac{1}{36}$th of the reactor volume has to be covered. This method allows to calculate results in a fraction of the run-time it would take for a complete reactor representation and is therefore very useful.

In standard Geant4, a reflective boundary function is not available for neutron transport. However, there is a standard Geant4 subroutine, which governs the reflection and transmission behaviour of optical photons at material boundaries called G4OpBoundaryProcess. This subroutine is modified to work on any type of particle and to perform a specular reflection at the surface of any volume with a trigger name. The subroutine is renamed MyBoundaryProcess and can be called from the NeutronHPphysics subroutine.

In the usual reactor case, there are two reflective boundary surfaces at the sides of the slice. The geometry description of the reactor has to be modified to include two box volumes placed so that their side surfaces are at the two planes where the reflection is required. The box volumes have to be named "Reflector1" and "Reflector2" which are the trigger names which will be picked up by MyBoundaryProcess.

Originally, the subroutine had a function which automatically calculated the normal vector of the boundary surfaces required for reflection, but there are issues with this calculation at the point when combining this with detector meshes for a nuclear heating calculation. As there are only two boundary surfaces in the usual reactor case, the normal vector of the currently used surfaces are hard-coded . If other reactor configurations with a different placement of boundary surfaces are used in the future, these normal vectors have to be changed.

The correct behaviour of MyBoundaryProcess is tested for different incidence angles in a simple geometry set-up using a point source and a reflecting box and also observed for a number of individual particles in the final DEMO reactor set-up. The final validation is the use in the DEMO TBR calculation, which is discussed in section 7, during which results consistent with MCNP are produced.

Danksagung / Acknowledgments

An dieser Stelle möchte ich zuerst meine Dankbarkeit gegenüber meinem ursprünglichen Hauptreferenten Professor Robert Stieglitz ausdrücken, der leider kurz vor der Fertigstellung dieser Arbeit verstorben ist. Seine Kommentare zum ersten Entwurf haben mich auf dem letzten Stück weiter begleitet.

Mein großer Dank gilt Professor Thomas Müller, der kurzfristig und unkompliziert als Hauptreferent eingesprungen ist und mir ermöglicht hat, die Arbeit erfolgreich zu Ende zu bringen. Desweiteren danke ich Professor Anton Möslang, der schon länger als Korreferent dabei war, und Professor Xu Cheng, der ebenfalls sehr kurzfristig dazu kam, für Ihre hilfreichen Hinweise zum Abschluss dieser Arbeit.

Vielen Dank an Ulrich für die langjährige Betreuung, Unterstützung und Begleitung auch noch im Ruhestand!

Außerdem gilt mein besonderer Dank meinen ehemaligen Kollegen beim INR, insbesondere Alexandre für das hilfreiche Feedback zu meinem zweiten Entwurf, SuperMC Super-User Arkady für die Hilfe bei der Konvertierung der HCPB CAD-Geometrie, Dieter für die Organisation besonders nachdem ich nicht mehr persönlich vor Ort war, Pavel für die Hilfe bei DEMO-Fragen, Stanislav für die Hilfe bei SINBAD-IPPE-Fragen und Yuefeng für die Hilfe bei HalfSpaceSolid-Fragen und bei Rechenclusterproblemen. Außerdem danke ich meinem netten Zimmernachbarn Christian und meinen Kantinenbegleitern André, Axel, Prasoon, Bastian, Jin Hun, Moataz und Lei für die interessanten Gespräche.

Outside of INR, I would like to thank Aljaž Čufar of JSI, Slovenia, for the support with FNG SDEF files, Maurício Pazianotto of the Technological Institute of Aeronautics, Brazil, for his helpful suggestion on how to implement a reflective boundary function in Geant4, and Jonathan Shimwell of First Light Fusion, UK, for his useful online nuclear cross-section plotting tool XSPlot.

Mein herzlicher Dank gilt den Sekretärinnen des INR, Ingeborg, Birgit und Petra, die mir immer mit viel Engagement und Kompetenz zur Seite standen.

Danke auch an die Interpreten meiner Instrumental-Playlist: Vangelis, Murray Gold, Percival Schuttenbach, Soman, Juno Reactor, Enigma, Front Line Assembly, Abel Korzeniowski, Schiller, Go_A u.v.m..

An Christoph und unsere beiden Kater, danke für alles! ♡